

# **Registration of prone and supine CT colonography images and its clinical application**

Holger R. Roth

A dissertation submitted in partial fulfilment  
of the requirements for the degree of  
**Doctor of Philosophy**

Centre for Medical Image Computing  
Department of Medical Physics and Bioengineering  
**University College London**

July 11, 2013

I, Holger R. Roth, confirm that the work presented in this thesis is my own. Where information has been derived from other sources, I confirm that this has been indicated in the thesis.

London, July 11, 2013

---

Holger R. Roth



# Abstract

Computed tomographic (CT) colonography is a technique for detecting bowel cancer and potentially precancerous polyps. CT imaging is performed on the cleansed and insufflated bowel in order to produce a virtual endoluminal representation similar to optical colonoscopy. Because fluids and stool can mimic pathology, images are acquired with the patient in both prone and supine positions. Radiologists then match endoluminal locations visually between the two acquisitions in order to determine whether pathology is real or not. This process is hindered by the fact that the colon can undergo considerable deformation between acquisitions. Robust and accurate automated registration between prone and supine data acquisitions is therefore pivotal for medical interpretation, but a challenging problem.

The method proposed in this thesis reduces the complexity of the registration task of aligning the prone and supine CT colonography acquisitions. This is done by utilising cylindrical representations of the colonic surface which reflect the colon's specific anatomy. Automated alignment in the cylindrical domain is achieved by non-rigid image registration using surface curvatures, applicable even when cases exhibit local luminal collapses. It is furthermore shown that landmark matches for initialisation improve the registration's accuracy and robustness. Additional performance improvements are achieved by symmetric and inverse-consistent registration and iteratively deforming the surface in order to compensate for differences in distension and bowel preparation.

Manually identified reference points in human data and fiducial markers in a porcine phantom are used to validate the registration accuracy. The potential clinical impact of the method has been evaluated using data that reflects clinical practise. Furthermore, correspondence between follow-up CT colonography acquisitions is established in order to facilitate the clinical need to investigate polyp growth over time.

Accurate registration has the potential to both improve the diagnostic process and decrease the radiologist's interpretation time. Furthermore, its result could be integrated into algorithms for improved computer-aided detection of colonic polyps.

# Acknowledgements

I would like to sincerely thank all the following individuals, without whom this thesis would not have been possible. Firstly my supervisors Professor David Hawkes and Professor Sebastien Ourselin, and my co-supervisors Dr. Jamie McClelland and Dr. Mingxing Hu. Their passion for research and excellence were always a source of inspiration. I am very grateful for their unfaltering enthusiasm, expertise and dedication which have been very constructive in the development of this thesis; working with them has been a privilege.

I am also grateful for working together with a number of great colleagues at the Centre for Medical Image Computing. Firstly, Thomas Hampshire with whom I worked closely on this project and whose work showed major contribution in combination with the algorithms developed by myself. Marc Modat for his support and for contributing the *NiftyReg* package, Jorge Cardoso for his help with topological correction and segmentation, Yipeng Hu for his help and providing various Matlab functions, Lianghao for his effort in building a bio-mechanical model of the colon. Furthermore, I would like to thank everyone else at the *Centre for Medical Image Computing* for their good collegiality. They made *University College London* an excellent environment to work in.

Professor Hawkes has established a close link with clinicians at *University College Hospital London* and *Centre for Medical Imaging* alongside whom I felt honoured to have worked. I would like to extend my sincere thanks to Professor Steve Halligan, Shonit Punwani and Dr. Andrew Plumb. In particular, I would like to thank Dr. Darren Boone and Dr. Emma Helbren who made it possible to show the clinical relevance of the developed methods and who did extensive radiological assessment of the methods' accuracies.

I am very grateful to *Medicsight PLC* (London, UK), in particular Greg Slabaugh, Xujiong Ye, Xiaoyun Yang, Topraj Gurung and Justine McQuillan, for providing software and test cases used for these studies.

Image data for external validation were obtained from *The Cancer Imaging Archive* sponsored by the *Cancer Imaging Program, DCTD/NCI/NIH*. Professor Perry Pickhardt provided data of follow-up CTC patients. I thank them for making these cases available.

This thesis was funded by *MedicEndo Ltd* and the UK *National Institute for Health Research (NIHR)* under its Programme Grants for Applied Research funding scheme (*RP-PG-0407-10338*). Without their financial support, this thesis would not have been possible.

I also would like to thank my family and the friends I have made during these years in London, especially Jonas Minet Kinge, Daniel Heanes and Baptiste Allain. Finally, my thanks go to my dear girlfriend Georgina Oliver for her patience, understanding, proof-reading and encouragement over the course of writing this thesis.

# Contents

<b>Abstract</b>	<b>3</b>
<b>Acknowledgements</b>	<b>4</b>
<b>Table of contents</b>	<b>5</b>
<b>Publications</b>	<b>8</b>
<b>List of figures</b>	<b>10</b>
<b>List of tables</b>	<b>16</b>
<b>1 Introduction</b>	<b>17</b>
1.1 Motivation . . . . .	17
1.1.1 Computed tomographic colonography . . . . .	17
1.1.2 Current state of CTC in clinical practice . . . . .	20
1.1.3 Registration of CT colonography images . . . . .	22
1.2 Contributions of this thesis . . . . .	23
1.3 Structure of this thesis . . . . .	24
<b>2 Literature review and proposed solution</b>	<b>25</b>
2.1 Registration of prone and supine images . . . . .	25
2.1.1 Centreline-based registration . . . . .	25
2.1.2 Landmark-based registration . . . . .	27
2.1.3 Extraction of haustral folds . . . . .	28
2.1.4 Extraction of teniae coli . . . . .	28
2.1.5 Voxel-based registration . . . . .	29
2.1.6 Matching prone and supine polyps . . . . .	29
2.2 Proposed solution . . . . .	30
2.3 Methods of unfolding . . . . .	31
2.3.1 Ray casting methods . . . . .	31
2.3.2 Conformal mapping methods . . . . .	32
2.3.3 Unfolding for prone-to-supine registration . . . . .	34
<b>3 Prone-to-supine registration in cylindrical space</b>	<b>35</b>
3.1 Registration principle . . . . .	35
3.2 Colon segmentation . . . . .	35
3.3 Topological correction . . . . .	39
3.4 Colonic surface extraction . . . . .	41
3.5 Cylindrical representation of the endoluminal colonic surface . . . . .	43

3.5.1	Discrete Ricci flow . . . . .	43
3.5.2	Gradient descent method . . . . .	44
3.5.3	Newton's method . . . . .	45
3.5.4	Embedding into two-dimensional space . . . . .	46
3.5.5	Conformality . . . . .	48
3.5.6	Generating cylindrical images . . . . .	49
3.6	Establishing spatial correspondence between prone and supine datasets . . . . .	56
3.6.1	Cylindrical B-spline registration . . . . .	56
3.6.2	Objective function . . . . .	58
3.7	Dealing with collapsed colons . . . . .	61
<b>4</b>	<b>Evaluation of registration accuracy</b>	<b>63</b>
4.1	Validation using polyps . . . . .	64
4.2	Validation of spatial correspondence along the entire length of the colon . . . . .	67
4.3	Influence of segmentation quality on the registration result . . . . .	70
4.3.1	Results and conclusion . . . . .	70
4.4	Discussion . . . . .	72
<b>5</b>	<b>Clinical application of prone-to-supine registration</b>	<b>74</b>
5.1	Estimation of registration accuracy using a porcine phantom . . . . .	75
5.1.1	Methods and Materials . . . . .	75
5.1.2	Piece-wise linear initialisation . . . . .	79
5.1.3	Results . . . . .	81
5.1.4	Conclusion . . . . .	83
5.2	External clinical validation of prone and supine CT colonography registration . . . . .	84
5.2.1	Introduction . . . . .	84
5.2.2	Prone-to-supine registration . . . . .	85
5.2.3	Methods and materials . . . . .	85
5.2.4	Assessment of clinical utility . . . . .	86
5.2.5	Results . . . . .	88
5.2.6	Conclusion . . . . .	90
5.3	Summary . . . . .	92
<b>6</b>	<b>Inverse consistency in the registration of prone and supine CTC</b>	<b>93</b>
6.1	Introduction . . . . .	93
6.2	Inverse consistency error . . . . .	94
6.3	Evaluation of inverse consistency . . . . .	94
6.3.1	Inverse consistency without feature initialisation . . . . .	95
6.3.2	Initialisation using B-Spline approximation . . . . .	96
6.3.3	Inverse consistency after feature initialisation . . . . .	103
6.4	Inverse-consistent symmetric registration . . . . .	104
6.4.1	Motivation . . . . .	104
6.4.2	Related work . . . . .	105
6.4.3	Symmetric prone-to-supine transformation model . . . . .	105
6.4.4	Optimisation . . . . .	106
6.4.5	Inverse-consistent results . . . . .	107
6.5	Conclusions . . . . .	110

<b>7</b>	<b>Temporally separated CT Colonography cases</b>	<b>111</b>
7.1	Introduction . . . . .	111
7.2	Methods . . . . .	112
7.3	Results . . . . .	113
7.3.1	Initial feasibility study . . . . .	113
7.3.2	Results on external CTC data . . . . .	113
7.4	Discussion . . . . .	115
<b>8</b>	<b>Registration of cases with different distensions</b>	<b>116</b>
8.1	Introduction . . . . .	116
8.2	Methods . . . . .	116
8.2.1	Extraction of good quality point correspondences . . . . .	116
8.2.2	Surface deformation using thin plate splines . . . . .	117
8.2.3	Re-establishing correspondence in cylindrical space using a deformation relaxation approach . . . . .	120
8.3	Results . . . . .	122
8.4	Discussion . . . . .	122
<b>9</b>	<b>Future work</b>	<b>124</b>
9.1	Improving prone-to-supine surface registration . . . . .	124
9.1.1	Bio-mechanical modelling of colonic inflation . . . . .	124
9.1.2	Reduction of different features introduced by tight bends . . . . .	125
9.1.3	Improving colon segmentation . . . . .	126
9.1.4	Increasing the surface detail to allow finer alignment . . . . .	127
9.1.5	Alternative and multiple similarity measures . . . . .	127
9.1.6	Integration of features in the registration optimisation . . . . .	128
9.1.7	Patient-specific registration . . . . .	128
9.2	Using the registration result . . . . .	129
9.2.1	False-positive reduction in computer-aided-detection . . . . .	129
9.2.2	Registration of follow-up studies . . . . .	130
9.2.3	Providing more information to the colonoscopist . . . . .	130
9.2.4	Data fusion for optical colonoscopy guidance . . . . .	132
<b>10</b>	<b>Summary, discussion and conclusion</b>	<b>133</b>
10.1	Summary . . . . .	133
10.1.1	Chapter 1: Introduction . . . . .	133
10.1.2	Chapter 2: Literature review and proposed solution . . . . .	133
10.1.3	Chapter 3: Prone-to-supine registration in cylindrical space . . . . .	133
10.1.4	Chapter 4: Evaluation of registration accuracy . . . . .	133
10.1.5	Chapter 5: Clinical application of prone-to-supine registration . . . . .	134
10.1.6	Chapter 6: Inverse consistency in the registration of prone and supine CTC . . . . .	134
10.1.7	Chapter 7: Temporally separated CT Colonography cases . . . . .	134
10.1.8	Chapter 8: Registration of cases with different distensions . . . . .	135
10.1.9	Chapter 9: Future work . . . . .	135
10.2	Discussion . . . . .	136
10.3	Conclusion . . . . .	137
	<b>Bibliography</b>	<b>138</b>

# Publications

## Peer-reviewed journal articles

Boone D, Halligan S, **Roth H**, Hampshire T, Slabaugh G, McQuillan J, McClelland J, Hu M, Punwani S, Taylor S, Hawkes D, *CT Colonography: External Clinical Validation of an Algorithm for Computer-assisted Prone and Supine Registration*, Radiology, online, May 2013.

Hampshire T, **Roth H**, Helbren E, Plumb A, Boone D, Slabaugh G, Halligan S, Hawkes D, *Endoluminal Surface Registration for CT Colonography using Hausstral Fold Matching*, Medical Image Analysis, April 2013.

**Roth H**, McClelland J, Boone D, Modat M, Cardoso M, Hampshire T, Hu M, Punwani S, Ourselin S, Slabaugh G, Halligan S, Hawkes D, *Registration of the endoluminal surfaces of the colon derived from prone and supine CT colonography*, Medical Physics, 38, 6, 3077-3089, June 2011.

## Peer-reviewed conference proceedings

**Roth H**, McClelland J, Modat M, Hampshire T, Boone D, Hu M, Ourselin S, Halligan S, Hawkes D, *CT colonography: inverse-consistent symmetric registration of prone and supine inner colon surfaces*, SPIE Medical Imaging 2013.

Hampshire T, **Roth H**, Hu M, Boone D, Slabaugh G, Punwani S, Halligan S, Hawkes D, *Automatic prone to supine hausstral fold matching in CT colonography using a Markov random field model*, 14th International Conference on Medical Image Computing and Computer Assisted Intervention (MICCAI), Oct 2011.

**Roth H**, McClelland J, Modat M, Boone D, Hu M, Ourselin S, Slabaugh G, Halligan S, Hawkes D, *Establishing Spatial Correspondence between the Inner Colon Surfaces from Prone and Supine CT Colonography*, 13th International Conference on Medical Image Computing and Computer Assisted Intervention (MICCAI), Oct 2010.

**Roth H**, McClelland J, Boone D, Hu M, Ourselin S, Slabaugh G, Halligan S, Hawkes D, *Conformal Mapping of the Inner Colon Surface to a Cylinder for the Application of Prone to Supine Registration*, 14th conference on Medical Image Understanding and Analysis (MIUA), Jul 2010.

## Peer-reviewed workshop proceedings

**Roth H**, Boone D, Halligan S, Hampshire T, Slabaugh G, McQuillan J, McClelland J, Hu M, Punwani S, Taylor S, Hawkes D, *External Clinical Validation of Prone and Supine CT Colonography Registration*, Abdominal Imaging. Computational and Clinical Applications, Lecture Notes in Computer Science, 7601, 10-19, Oct 2012.

Hampshire T, **Roth H**, Boone D, Slabaugh G, Halligan S, Hawkes D, *Prone to Supine CT Colonography*

*Registration Using a Landmark and Intensity Composite Method, Abdominal Imaging. Computational and Clinical Applications*, Lecture Notes in Computer Science, 7601, 1-9, Oct 2012.

**Roth H**, Hampshire T, McClelland J, Hu M, Boone D, Slabaugh G, Halligan S, Hawkes D, *Inverse consistency error in the registration of prone and supine images in CT colonography*, MICCAI Workshop on Computational and Clinical Applications in Abdominal Imaging 2011, Lecture Notes in Computer Science, 7029, 1-7, 2012.

## Peer-reviewed abstracts

Helbren E, **Roth H**, Hampshire T, Pickhardt P, Hawkes D, Halligan S, *CT colonography: clinical evaluation of novel software to automatically co-register polyps between follow-up surveillance studies*, ESGAR 2013.

Hampshire T, **Roth H**, Hu M, Boone D, Slabaugh G, Punwani S, Halligan S, Hawkes D, *CT colonography: Accurate registration of prone and supine endoluminal surfaces of the colon*, ECR 2013.

**Roth H**, McClelland J, Modat M, Hampshire T, Boone D, Hu M, Ourselin S, Halligan S, Hawkes D, *Inverse-consistent symmetric registration of inner colon surfaces derived from prone and supine CT colonography*, AAPM 2012

Ye X, **Roth H**, Hampshire T, et al. *Computer-aided Detection for CT Colonography: False-Positive Reduction Using Surface-based Prone-Supine Registration*, RSNA 2011.

Boone D, **Roth H**, Hampshire T, et al. *CT Colonography: Development and Validation of a Novel Registration Algorithm to Align Prone and Supine Scans*, RSNA 2011.

Boone D, **Roth H**, Halligan S, et al. *CT colonography: development and validation of a novel registration algorithm to align prone and supine scans. Insights into Imaging*, ESGAR 2011.

Boone D, **Roth H**, Hampshire T, et al. *CT colonography: development and validation of a novel registration algorithm to align prone and supine scans. Insights into Imaging*, ECR 2011

## Award

Roth et al. 2012: *Outstanding Paper Award at the 4th International Workshop on Computational and Clinical Applications in Abdominal Imaging*, held in conjunction with MICCAI, in Nice, France (2012).

## Patent

MCCLELLAND J, **Roth H**, Hu M, Hawkes D, Halligan, S, *Apparatus and Method for Registering Medical Images Containing a tubular organ*, WO/2011/110867, PCT/GB2011/050488, **2010**

# List of Figures

1.1	Spiral CT colonography of patient in supine position (left). The patient couch is moved while the x-ray tube rotates in the transaxial plane. A 10 mm polyp in the transverse colon (arrow) as visible in a CTC scan with the patient lying in prone position (right). The large intestine is inflated with air which enables a sharp contrast between the surrounding abdominal soft tissues and the colonic lumen. [Figures courtesy of Halligan and Fenlon (1999)] . . . . .	18
1.2	The <i>colon</i> or <i>large intestine</i> is a very flexible organ. It is about 1.5 metres long from the <i>caecum</i> (or <i>cecum</i> ) to the <i>rectum</i> and <i>anus</i> . Starting from the <i>caecum</i> , where the <i>small intestine</i> fuses with the colon at the <i>ileo-caecal valve</i> , four parts can be differed: The <i>ascending</i> , the <i>transverse</i> , the <i>descending</i> and <i>sigmoid colon</i> which lead to the <i>rectum</i> (Gray, 1858). The above illustration further shows different stages of <i>colorectal diseases</i> : <i>polyps</i> in the <i>sigmoid colon</i> are likely to develop into <i>colorectal cancer</i> at a later stage (Cappell et al., 2005). Furthermore, several other diseases in the colon are illustrated, e.g. <i>irritable bowel syndrome</i> in the <i>ascending colon</i> and <i>diverticulitis</i> in the <i>transverse colon</i> . At the <i>hepatic</i> , <i>splenic flexures</i> , the colon remains more stable when the patient changes between prone and supine positions (Punwani et al., 2009). [Drawing courtesy of Georgina L. Oliver] . . . . .	19
2.1	The colonic centreline (blue line), running virtually from the caecum (green circle) to the rectum (red circle) trough the middle of the colonic lumen. . . . .	25
2.2	Plots of the x (blue), y (green), and z (red) co-ordinates of one of the centrelines against the distance along the centreline, from the prone (left) and supine (right) CT volumes. The black vertical lines indicate the corresponding points that have been detected by matching local maxima. . . . .	26
2.3	Internal (left) and external (right) view of segmented haustral folds with marked fold centres [Images courtesy of Thomas Hampshire]. . . . .	28
2.4	Ray casting using linear (a) and non-linear (b) rays in order to avoid self-intersections. [Figure based on Bartolí et al. (2001)] . . . . .	31
2.5	A one-to-one conformal mapping $f$ that preserves the angle between any local intersection of curves: $\vartheta^* = \vartheta$ [Figure based on Lévy et al. (2002)]. . . . .	33
2.6	One-to-one mapping $f$ that is not conformal [Figure based on Floater and Hormann (2005)]. . . . .	33
3.1	The principle of colon surface registration between prone ( $_p$ ) and supine ( $_s$ ) CTC using a cylindrical 2D parametrisation, where the colour scale indicates the shape index (see equation (3.25)) at each coordinate of the surface computed from the 3D endoluminal colon surfaces $S$ . Both surfaces are parametrised in 2D on regular cylinders $P$ between which a transformation $\mathbf{T}_{\text{cyl}}$ can be estimated using non-rigid registration. Hence, the transformation $\mathbf{T}_{\text{ps}}$ between the 3D surfaces $S_p$ and $S_s$ can be derived as shown in the figure. The hepatic and splenic flexures are marked as $\text{hf}_{p/s}$ and $\text{sf}_{p/s}$ respectively ( $_p/_s$ denotes prone and supine, respectively); see Figure 1.2 in Chapter 1. . . . .	36
3.2	Segmentation of the colonic lumen by thresholding. The segmented voxels are overlaid in red above an original axial slice of a CTC image. Left: Any voxels representing air are found with an intensity smaller than $t_{\text{air}} = -750$ HU (Hounsfield units). Middle: Any voxels representing fluids are found with an intensity greater than $t_{\text{fluids}} = 300$ HU. Right: Both segmented air and fluids voxels are shown in red, illustrating the boundary between air and fluids caused by partial volume effects. . . . .	36



3.3	Rendering of all gas-filled regions and regions detected to include fluids. Each connected object is displayed in a different colour. Because the intensities of bones and fluids are similar, bones are also rendered. The large intestine is then manually selected when start and end points of each colonic segment are chosen (see Section 3.3 and 3.7). . . . .	37
3.4	A flow chart of the proposed colon surface registration between prone and supine CTC: After the prone and supine colonic lumina have been segmented, topological correction is applied in order to allow the extraction of genus-zero surfaces. After using cylindrical 2D parametrisation (unfolding) and hepatic and splenic flexures for initialisation, a non-rigid intensity-based image registration performs aligns the surfaces in cylindrical space. The primary contributions of this thesis are highlighted (in purple) as the last two steps. .	38
3.5	Left: Schematic view of a “handle” which erroneously connects two sides of a haustral fold, resulting in incorrect topology that would allow the creation of two separated “loops” along the surface and therefore a surface of higher genus than that shown on the right. Right: the same surface region after topological correction by cutting through the handle (and the loop) [Schematic after (Hong et al., 2006)]. . . . .	39
3.6	Centreline extraction using the fast marching method on a 2D CT image slice of a porcine colon phantom: the original segmentation of the colon lumen (left); a map of the distance to the endoluminal surface (middle) is used as a speed function $F(x)$ . After wave propagation through the colon (right); the centreline path can be extracted by following the steepest gradient of the wave function (from blue to red colour coding). . . . .	40
3.7	Left: Enlarged view of “handles” and an erroneous connection caused by limitation of the segmentation quality, resulting in incorrect topology. Right: the same surface region after topological correction. Comparison of the highlighted surface areas shows that the handles are now removed and the endoluminal surface is of genus zero. . . . .	41
3.8	A colonic surface triangulation from the marching cubes algorithm (left). The smoothed and decimated triangulation $S$ (right). The original marching cubes output can generate about one million triangles for a standard CTC image (left), while the mesh on the right consist of about 60,000 triangle faces. The decimation and smoothing parameters to generate the mesh on the right have been chosen such that details of the colonic surface (such as folds and polyps) are still clearly visible after simplification. However, redundant triangles in mesh representation of the colon surface have been removed. . . .	42
3.9	Ricci flow on a genus zero 2-manifold with topology equal to sphere, generated as a manifold of revolution. The figure shows several stages of Ricci flow at different time intervals of the <i>geometry flow</i> . All shapes are drawn at equal scale. [Generated using software provided by Rubinstein and Sinclair (2005)] . . . . .	43
3.10	Circle packing metric on a mesh in two-dimensional space after Ricci flow convergence (left) and on an individual triangle (right). Each vertex $v_i$ is circumscribed by a circle of radius $\gamma_i$ , defined by the geometry of the surface mesh $S$ . The angles $\theta_i$ are the inside corner angles of the triangle. . . . .	45
3.11	Comparison of convergence speed of Ricci flow using gradient descent (blue) and Newton’s method (green) for optimisation. The curvature error is plotted in logarithmic scale. Computations were executed using a C++ implementation on a CPU with 2.13 GHz and 12.0 GB RAM. For both optimisation methods, Ricci flow was minimised until the error criterion, $E_{\max} \leq 1e^{-6}$ , was fulfilled. In this case, the gradient descent minimisation converged after 10.5 hours computation time (off the horizontal graph limits). . . . .	46
3.12	Computed planar embeddings $P$ of the endoluminal colonic surface $S$ with convergence errors $E_{\max} = 1e^{-4}$ (left), $E_{\max} = 1e^{-6}$ (middle) and the averaged planar embedding (right) with $E_{\max} = 1e^{-6}$ . . . . .	47
3.13	Conformality of parametrisation illustrated by mapping a chequerboard onto the colonic surface (renderings with <i>Alice Graphite</i> ). Right angles of the 2D squares are preserved in 3D. The histogram of angle ratios is concentrated around one. . . . .	48
3.14	Sampling the unfolded mesh to generate rectangular raster-images $I$ suitable for image registration. Each band represents a shifted copy of the planar embedded meshes $P$ which are sampled between the horizontal lines to cover a full $360^\circ$ of endoluminal colon surfaces $S$ . . . . .	49

3.15	Supine (top), prone (middle) and deformed supine deformed to match prone (bottom) raster images of patient 7 where each pixel has the value of the corresponding shape index ( $SI$ , see Equation 3.25) computed on the endoluminal colonic surface. The $x$ -axis is the position along the colon, while the $y$ -axis is its circumferential location. The $x$ -positions for the detected hepatic and splenic flexures are marked as $x_{\text{hepatic}}$ and $x_{\text{splenic}}$ . The location of a polyp is marked before (top) and after registration (middle, bottom) and in a zoom-in section. Corresponding 3D renderings are illustrated in Fig. 3.1. . . . . .	50
3.16	Normal planes, defining the principal curvatures on a saddle surface. . . . .	51
3.17	Computation of surface curvature: the base $\{1, 2, 3, 4\}$ is a square with side length of 1. The vertex 0 is centred above the square at a height of 0.5. Therefore, the area of each side triangle is $\sqrt{2}/4$ and the angle $\alpha$ is $2 \arctan \sqrt{2}/2$ at each face adjacent to $v_0$ . Hence, $K_0 = 2\pi - 4\theta \approx 1.3593$ . The area $A$ is used for computation of the mean curvature $H(e)$ (see equation 3.24. $A$ is 1/3 of the area of the two faces sharing $e_{ij}$ . [Figure and text based on Batchelor et al. (2002) and Castellano (1999)]. . . . .	52
3.18	The shape index $SI$ is a normalised shape measurement to describe local surface structures [Figure based on (Yoshida and Nappi, 2002)]. . . . .	52
3.19	A simulated profile of three anatomically corresponding haustral folds of the prone and the supine colonic surface. The folds move markedly between both views. While the mean curvature varies markedly between prone and supine, the shape index profile is virtually identical and therefore invariant to these changes. In this example, I assume the profiles to be ‘perfect ridges’. Therefore, the shape index instantly steps between 0.25 ( <i>rut</i> ) and 0.75 ( <i>ridge</i> ) as one of the principal curvatures will always be zero. . . . .	53
3.20	Interpolation of pixel values on a 2D triangle. The value $SI$ at a pixel position $(x, y)$ can be derived from the $SI_1$ , $SI_2$ and $SI_3$ (computed at the 3D vertices) as $SI = Ax + By + C$ . It is known that $SI_1 = Ax_1 + By_1 + C$ , $SI_2 = Ax_2 + By_2 + C$ and $SI_3 = Ax_3 + By_3 + C$ . Hence, $A$ , $B$ and $C$ can be computed by solving a system of three equations and hence computing $SI$ . . . . .	54
3.21	Flow chart illustrating the process of generating cylindrical raster images that represent the entire colonic surface: after extracting the triangulated surface mesh representing the colonic surface, the shape indices are computed on the 3D surface based on local discrete curvatures (see Sec. 3.5.6.2). In a next step, the mesh is parametrised in 2D using Ricci flow (see Sec. 3.5.1). Then, the 2D parametrisation is sampled on a regular pixel raster covering the entire cylindrical space (see Sec. 3.5.6). The shape index value at each pixel location is interpolated using linear interpolation (see Sec. 3.5.6.3). . . . .	55
3.22	The hepatic flexure is detected as the first local maximum, coming from the caecum, to be above $t_{\text{hepatic}}$ of the maximum centreline $z$ -coordinate. The splenic flexure is detected as the local maximum which is the first to lie above $t_{\text{splenic}}$ of the maximum centreline $z$ -coordinate, relative to the rectum. Both pairs of landmark matches can be used to initialise the registration by linear scaling the cylindrical images between the landmark matches as illustrated in Fig.3.23. The hepatic and splenic flexures are marked as $hf_{p/s}$ and $sf_{p/s}$ respectively ( $p/s$ denotes prone and supine, respectively) . . . . .	57
3.23	Both pairs of prone and supine landmark matches are used to initialise the registration by linear scaling along the $x$ -direction of the cylindrical images between the landmark matches. The corresponding $x$ -positions for the hepatic and splenic flexures are marked as $x_{\text{hepatic}}$ and $x_{\text{splenic}}$ in the figure before (top) and after linear scaling (middle) of the source image; the target cylindrical image is shown at the bottom. . . . .	58
3.24	Standard lattice of control points $\{\vec{\phi}\}$ for a 2D cubic B-Splines deformation model (left): the control point grid extends outside the image by one control point spacing in each direction. The cylindrical control points only extend in the ‘Along colon’ direction ( $x$ ) and loop around in $y$ direction. The deformation is therefore cylindrical. . . . .	58
3.25	Deformation field on a section of the colon at the final control point spacing level. The deformation field has been used to deform a regular grid and been overlaid on top of the deformed supine $T_{cyl}(I_s)$ (red) and target $I_p$ (cyan) cylindrical images. Red and cyan pixels of the same intensity are displayed in grey after registration. . . . .	60
3.26	A case where the descending colon is collapsed in the supine position (marked, right image) but fully distended in the prone (left). . . . .	62

3.27	Cylindrical representation as raster images of the collapsed supine (top), prone (middle) and deformed supine (bottom) endoluminal colon surface of patient 17. The location of a polyp is marked before (top) and after registration (middle, bottom) with an arrow. Note, the polyp is not visible in Fig. 3.26 . . . . .	62
4.1	Widely different distension changes the shape index of the cylindrical representations in supine (top) and prone (bottom). 3D renderings are shown in Fig. 4.2 . . . . .	63
4.2	Different amounts of distension in prone and supine view cause differences of local features in the cylindrical images. . . . .	64
4.3	Masking of polyps to ensure they do not influence subsequent registration: polyps in unfolded view (left). Masked polyps (right) to be ignored in registration. The centre of mass $c$ which is used as a reference point is marked with a cross. . . . .	65
4.4	Overlay of masked out polyps before (left) and after (right) establishing spatial correspondence. The prone image is coloured red with a yellow polyp mask, and the supine is coloured cyan with a blue polyp mask. After establishing spatial correspondence, aligned features display grey and the overlapping region of polyp masks in green. . . . .	65
4.5	Polyp localisation for patient 7 after registration using the prone (left) and supine (right) virtual endoscopic views. The black dot shows the resulting correspondence in the 2D (bottom) and 3D (top) renderings. . . . .	66
4.6	Normalised distributions of reference points normalised along the centreline from caecum to rectum for un-collapsed and collapsed cases. . . . .	68
4.7	Normalised histograms of the Fold Registration Error ( $FRE$ ) distributions in mm using reference points spread over the endoluminal colon surface for un-collapsed and collapsed cases. . . . .	69
4.8	A supine endoluminal surface extracted from a segmentation that included residual fluids (left); and a supine surface that excluding residual fluids, simulating insufficient fluid tagging for accurate colonic surface extraction (right). Note that not including the fluids in the right image caused a short section of collapse in the ascending colon and several ‘flat’ areas that are artefacts caused by the surface boundaries of the residual fluids (right). . . . .	70
4.9	Cylindrical representations of prone (top) and supine (2nd from top) endoluminal surfaces extracted from a segmentation that included residual fluids. The cylindrical representations of the prone (3rd from bottom) and supine (2nd from bottom) surfaces that excluded residual fluids, simulating insufficient fluid tagging for accurate colonic surface extraction. After each pair of cylindrical images, the respective registration result is overlaid over the target image. The target image is coloured in red and the floating image in cyan. Pixels of the same intensity after registration are displayed in grey. The less accurate registration result in the case of excluded residual fluids can be observed in the bottom row image. . . . .	71
5.1	Unprepared porcine colonic specimen with gastrointestinal tract. The animal was slaughtered for human consumption. At this stage, the colonic specimen remains distended due to retained residue. Note the haustral fold pattern is not dissimilar to the human colon [Image courtesy of Darren Boone]. . . . .	76
5.2	Pig phantom filled with water for cleaning purposes (left). One of twelve 5 mm metal clips is marked by an arrow. Phantom submerged under water using stockings (right) in front of CT scanner. . . . .	77
5.3	Cross-sections of a CT scan acquired of the segmented porcine colon submerged under water. Deformations were induced by applying weights to different external areas of the colon and by relocation of the air inside. Some of the metal markers (clips) and bags of saline are marked. . . . .	77
5.4	Pig phantom segmentations of 5 CT scans. This results in 10 combinations for registration between any two of the scans. . . . .	78
5.5	Haustral fold matches between two surface representations of the porcine phantom (a matched pair of folds is indicated by a connecting line between both surfaces). These matches can be used to provide a simple piece-wise linear initialisation along the length of the colon (shown in Fig. 5.6). The shown feature matches correspond to the combination of scans 1 and 5. . . . .	79

5.6	Piece-wise linear initialisation along the the length of the colon. A 3D feature is mapped to its corresponding location along the length of the cylinders (vertical lines). The top and bottom images correspond to the original cylindrical image. The middle image is the top image, after applying a piece-wise linear scaling in order to initialise it with the bottom image, prior to non-rigid cylindrical registration. Note that the vertical lines are now aligned between the middle and bottom images. The shown feature matches correspond to the combination of scans 1 and 5. . . . .	80
5.7	3D rendering of the porcine surface. The registration errors after feature-based Clip Registration Error ( $CRE_2$ ) are plotted as green lines between the transformed points (blue) and reference points at the 12 metal marker positions (red) in the space of the endoluminal surface. The shown errors correspond to the combination of scans 1 and 5. . . . .	81
5.8	Comparison of clip registration errors before (blue) and after (red) feature-based initialisation for the 10 possible combinations of pig colon scans, using the 12 metal clips as reference points; leading to 120 pairs of reference to test the algorithm. A marked increase in registration error can be observed when registering with surface number 2 is likely, due to an ‘unrealistic’ artefact introduced by the bags of saline during deformation of porcine phantom. However, feature-based initialisation (red) compensates for this artefact and reduces the error significantly. . . . .	82
5.9	Example of polyp conspicuity score of 5 (‘direct hit’). The registration prompt (black dot) marks the polyp indicated by the observer in the supine dataset (left). Following registration, the algorithm centres the prone view to point towards the endoluminal coordinates calculated by the algorithm (right). [Images courtesy of Darren Boone] . . . . .	87
5.10	Example of polyp conspicuity score of 4 (‘near miss’). The registration prompt (black dot) marks the polyp indicated by the observer in the prone dataset (left). Following registration, the algorithm centres the supine 3D field of view to point towards the coordinates calculated by the algorithm (right). The algorithm fails to indicate the polyp (arrow) correctly but the polyp is clearly visible in the same field of view. [Images courtesy of Darren Boone] . . . . .	87
5.11	Example of polyp conspicuity score of 2 or 3 (‘partially successful’). The polyp is only visible after rotation around the camera centre, but without navigation along the centreline when using virtual fly-through visualisation. [Images courtesy of Darren Boone] . . . . .	88
5.12	Example of polyp conspicuity score of 1 (‘registration failure’). The polyp comes only visible after navigation along the colonic centreline. The algorithm places the registration prompt to a neighbouring fold close to the polyp (only 11 mm away). However, the fold is obstructing the view of the polyp and navigation along the centreline was required. This illustrates that the Euclidean distance alone is not enough when assessing the clinical usefulness of the registration method. [Images courtesy of Darren Boone] . . . . .	88
5.13	Scatter plot of the observer’s conspicuity scores versus the 3D registration errors of the proposed method. An inverse relationship can clearly be seen and is illustrated by the line fitted in the least squares sense. . . . .	90
6.1	Computing the inverse consistency error ( $ICE$ ). The prone-to-supine direction is denoted as the forward transformation $T_{ps}$ , e.g. with prone as source and supine as target image. The supine image as source and prone image as target is denoted as the inverse (supine-to-prone) transformation $T_{sp}$ between the colon surfaces $S_s$ and $S_p$ . Any point $p$ is transformed in both directions such that the Euclidean distance $\ \cdot\ $ between point $p$ and $p'$ in 3D space gives the value of $ICE$ . . . . .	94
6.2	Difference between forward (top) and inverse (middle) registrations. The registration results are shown using a colour scheme which displays source features as blue and target features as red. After non-rigid alignment, overlapping features are displayed in grey. The forward (top) and inverse (middle) registrations show areas of inconsistency, especially around 2500 pixels in $x$ -direction (along the colon). This is reflected in larger $ICE$ values in these areas (bottom). The colour scale is in mm. . . . .	95
6.3	$ICE$ values mapped onto the colon surface. The colour scale is in mm. . . . .	96

6.4	A cylindrical image with arrows depicting the displacements $v_c$ computed from the prone and supine fold correspondences. The top image illustrates the ambiguity of these displacements in $y$ . The middle image illustrates the sorted displacements after minimising the error $e_y$ and the bottom image shows the image shifted in $y$ in order to minimise the total displacement in $y$ -direction. [Images courtesy of Thomas Hampshire] . . . . .	100
6.5	B-spline approximation of the deformation field used for initialisation. The top image shows the sorted displacements and the initial uniform control point lattice (indicated by the grid lines). After approximation, the entire cylindrical image is deformed using the final control point lattice (2nd from top). This provides good initialisation for a subsequent intensity-based B-spline registration in cylindrical domain which provides further alignment (3rd from top). The target image (supine) is shown in the bottom row. [Images courtesy of Thomas Hampshire] . . . . .	101
6.6	The inverse difference metric ( $ICE$ ) before (top) and after (bottom) initialisation using feature correspondences for a fully connected case. . . . .	103
6.7	The inverse difference metric ( $ICE$ ) before (top) and after (bottom) initialisation using feature correspondences for a collapsed case. . . . .	103
6.8	Symmetric prone-to-supine transformation model. The colour indicates the local shape indices. The prone-to-supine direction is denoted as the forward transformation $T_{ps}$ , e.g. with prone as source and supine as target image. The supine image as source and prone image as target is denoted as the inverse (supine-to-prone) transformation $T_{sp}$ between the colon surfaces $S_s$ and $S_p$ . . . . .	106
6.9	Local squared-differences ( $SD$ ) of registration result where no reference standard was provided. The $SD$ is measured between the floating and the reference image using the non-symmetric (left) and the inverse-consistent symmetric approach (right). Reduction in $SD$ indicates an improved registration (right). . . . .	109
7.1	Virtual fly-through renderings of a polyp in prone position (left) and prone position scanned 43 months later (right), now grown to about 11 mm in size. . . . .	111
7.2	Establishing correspondence between the follow-up prone ( $P$ ) and supine ( $S$ ) data sets acquired on the first or second occasion is superscripted with $_1$ or $_2$ respectively. . . . .	112
8.1	Principle of the proposed iterative thin plate spline deformation process . . . . .	117
8.2	Determining areas of good registration quality using a multi-resolution approach of local SSD computation . . . . .	117
8.3	Extraction of point correspondences (white dots). Right hand side shows better local correspondences and therefore a much higher concentration as in the middle section (magenta dots) . . . . .	118
8.4	Colon surface deformation using thin plate splines. Left: source (red) and target (blue) surfaces. Right: deformed source (red) and target (blue) surfaces. Overlaid with the target surface on the right, a good match can be seen in the sigmoid and descending colon segments which were previously detected as areas of successful registration, resulting in good spatial correspondence (between the arrows). . . . .	119
8.5	Top: Deformation field in beginning. Bottom: deformation after relaxation. This step keeps the good parts of the deformation but “relaxes” the control points where the registration is bad. This relaxing can be achieved by minimising the bending energy in the bad regions in order to provide a re-initialisation for a subsequent cylindrical registration. . . . .	120
8.6	Flow chart of the proposed iterative thin plate spline deformation process. . . . .	121
8.7	Evolution of registration error in mm over several iterations of the proposed optimisation method. . . . .	122
9.1	Virtual inflation of the colon using a bio-mechanical model of the ascending colon surface. Before inflation (left surface) and after applying a constant internal pressure to the inside of the colon (right surface). It can be observed how the shape index values change with the more inflated surface on the right. . . . .	125
9.2	False-positive reduction in computer-aided-detection [After Xujiong Ye]. . . . .	130

# List of Tables

1.1	Comparison of three clinical trials studying the diagnostic performance of CT colonography (CTC). CTC in all trials was validated with colonoscopy that was performed on the same day. [Table courtesy of Darren Boone] . . . . .	20
4.1	Registration error in mm for 13 polyps in the 13 patients used for validation of the registration method. These included 8 fully connected cases (patients 9 to 16) and 5 cases with local colonic collapse (patients 17 to 19). The Polyp Parametrisation Error ( $PPE$ ) gives the error in aligning the polyps after cylindrical parametrisation but before registration, the Polyp Registration Error ( $PRE$ ) gives the error after cylindrical registration. . . . .	67
5.1	This table summarises the mean Clip Registration Error $\overline{CRE}_1$ using only the cylindrical B-spline registration (see Chapter 3) and after $\overline{CRE}_2$ feature-based initialisation with subsequent intensity-based B-spline registration for the 10 possible combinations of pig colon scans using the 12 metal clips as reference points; leading to 120 pairs of reference points to test the algorithm. . . . .	82
5.2	Segmental distribution of polyps in the validation set and the total ACRIN CTC study. . . . .	86
5.3	1D registration error, measured as displacement along centreline [mm]. . . . .	89
6.1	Number of inverse-consistent haustral fold matches that can be used for a feature-based initialisation. The segmental locations of local colonic collapse are indicated with DC (descending colon) and SC (sigmoid colon). . . . .	97
6.2	The mean fold registration error ( $\overline{FRE}$ ) and mean inverse consistency error ( $\overline{ICE}$ ) in mm just using the B-spline registration as in Chapter 3 ( $_1$ ), after just using the feature-based initialisation as registration ( $_2$ ) and after initialisation followed by a subsequent intensity-based B-spline registration ( $_3$ ). $\overline{ICE}$ is only computed after intensity-based registration without ( $_1$ ) and with ( $_3$ ) feature-based initialisation. The locations of where the colon is collapsed are given (DC: descending colon, SC: sigmoid colon). Cases which were previously excluded due to vast differences in distension are now included. . . . .	102
6.3	Mean inverse consistency errors ( $\overline{ICE}$ ), registration accuracy ( $\overline{FRE}$ ) and mean-of-squared-differences ( $MSD$ ) without ( $_3$ ) and with ( $_4$ ) using the symmetric approach for the validation set of 17 CTC cases. The locations of where the colon is collapsed are given (DC: descending colon, SC: sigmoid colon). . . . .	109
7.1	Registrations of follow-up studies in an initial feasibility study. The number of days separating each colonography study are listed together with <i>longitudinal registration errors</i> (averaged over the number of polyps per case). . . . .	113
7.2	Registrations of follow-up studies on external CTC data. The number of days separating each colonography study are listed together with <i>longitudinal</i> and <i>consistency registration errors</i> (averaged over the number of polyps per case). . . . .	114

## Chapter 1

# Introduction

### 1.1 Motivation

Colorectal cancer is the second-largest cause of cancer mortality in the West, responsible for more than 1 million cases and 610,000 deaths each year (WHO, 2011). Early detection and removal of potentially precancerous polyps (adenomas) arising from the endoluminal colonic surface has been shown to significantly reduce the incidence of subsequent colorectal cancer and thus mortality (Atkin et al., 2010). Optical colonoscopy (insertion of a video-endoscope into the cleansed colon) is the reference-standard whole-colon diagnostic test and combines diagnosis and treatment; since polyps can be removed by endoscopic resection using a ‘snare’ (Deyhle, 1980). However, the procedure is uncomfortable for the patient, technically difficult to perform, and is occasionally associated with significant adverse events, including colonic perforation (Lohsiriwat, 2010). Furthermore, colonoscopy can be associated with the risk of serious complications such as internal bleeding and possible death, especially in older patients and patients with increased comorbidity (Rabeneck et al., 2008).

#### 1.1.1 Computed tomographic colonography

Computed tomographic (CT) colonography (CTC) is a relatively new alternative technique for imaging the colorectum. It was first described by Gene Coin et al. (1983) using full laxative bowel preparation and insufflation with gas. However, its wide usage was only promoted as an alternative to barium enemas in frail and elderly patients (Day et al., 1993) in the early and mid 1990s (Fink et al., 1994, Vining et al., 1994). CTC utilises computed tomography (CT), described by Hounsfield (1973) in 1970s, as a technology for 3D imaging of the abdomen. CT imaging enables three-dimensional imaging of the patient while also enabling the visualisation of internal organs and anatomical structures. This makes this technology especially interesting for medical applications as it can be used in order to diagnose diseases inside the human body. While CT is also used in many other applications, such as non-destructive testing or security applications, medical imaging applications have always been a major motivation for developing CT and had a great worldwide effect in diagnostic medicine – revolutionising the medical field of radiology (Herman, 2009).

CT imaging of the colorectum (CTC) has been shown in large comparative studies to be as sensitive as colonoscopy for larger polyps and cancer (Pickhardt et al., 2003, Johnson et al., 2008). Moreover, studies have shown CT colonography to be more acceptable to patients than colonoscopy (Taylor et al., 2003), and to be relatively safe (Burling et al., 2006). As for colonoscopy, the patient usually undergoes full cathartic bowel preparation (cleansing) prior to imaging: the patient’s bowel is typically prepared by taking laxatives or other oral agents Hara et al. (2011). Typically, the patient is administered a contrast agent orally that increases the intensities of any faecal remains in the reconstructed CTC images, compared to the surrounding tissues. This procedure is known as *faecal tagging* and allows the *electronic* or *digital cleansing* of faecal remains by subtraction from the CTC images (Zalis and Hahn, 2001).

Subsequently, a multi-detector helical CT is carried out with carbon dioxide colonic insufflation

of the bowel (via a small rectal catheter) to maximize the attenuation contrast between the endoluminal surface and the colonic lumen (see Fig. 1.1). Image rendering software is used to reconstruct a 3-dimensional representation of the endoluminal bowel surface; hence the alternative title, *virtual colonoscopy* (Fenlon et al., 1999). An additional advantage of CTC imaging is that it can be combined with other modalities (Boone et al., 2011) such as PET for improved specificity in the diagnosis, showing the increased uptake of  $^{18}\text{F}$ -FDG<sup>1</sup> by colonic neoplasia (Taylor et al., 2010). Despite good bowel prepa-

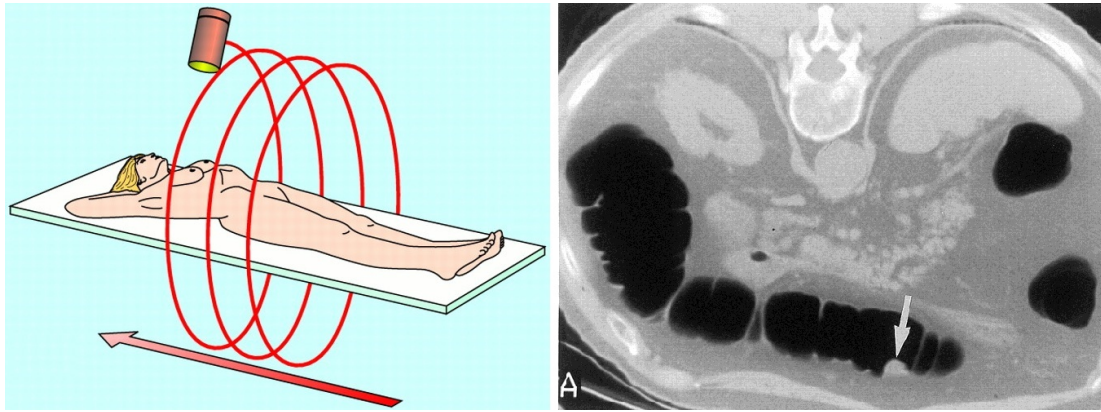


Figure 1.1: Spiral CT colonography of patient in supine position (left). The patient couch is moved while the x-ray tube rotates in the transaxial plane. A 10 mm polyp in the transverse colon (arrow) as visible in a CTC scan with the patient lying in prone position (right). The large intestine is inflated with air which enables a sharp contrast between the surrounding abdominal soft tissues and the colonic lumen. [Figures courtesy of Halligan and Fenlon (1999)]

ration and electronic cleansing, the shape of residual stool and fluid (or even normal anatomical variants) can sometimes appear like polyps. Furthermore, some regions of bowel may be insufficiently inflated and appear under-distended or might be even completely collapsed. This impairs image interpretation by radiologists. To counteract this, it is standard practice to image the patient in two positions – prone and supine<sup>2</sup> – which redistributes gas and residue within the colon (Taylor et al., 2007).

By comparing corresponding regions from prone and supine datasets, the radiologist can assess whether a potential abnormality perceived on one dataset is a real polyp (i.e. its position remains the same, indicating fixation to the bowel wall) or retained stool (i.e. it moves). However, the colon is a relatively long and flexible tubular structure (see Fig. 1.2) that is loosely attached to the abdominal wall via variable mesenteric attachments. The result is that the colon often undergoes considerable deformation during patient repositioning, mainly because of abdominal compression due to the patient's own weight and pelvic motion (Punwani et al., 2009), or even severe local under-distension which can lead to colonic collapse. This complicates the interpretation task - identifying corresponding locations on the endoluminal surface between prone and supine acquisitions is difficult, prolongs reporting time, and may lead to errors of interpretation.

<sup>1</sup>Fludeoxyglucose ( $^{18}\text{F}$ )

<sup>2</sup>In addition to prone and supine acquisitions, current CTC implementation guidelines sometimes recommend an additional series with the patient in decubitus position. Registration of decubitus datasets is the subject of future research.



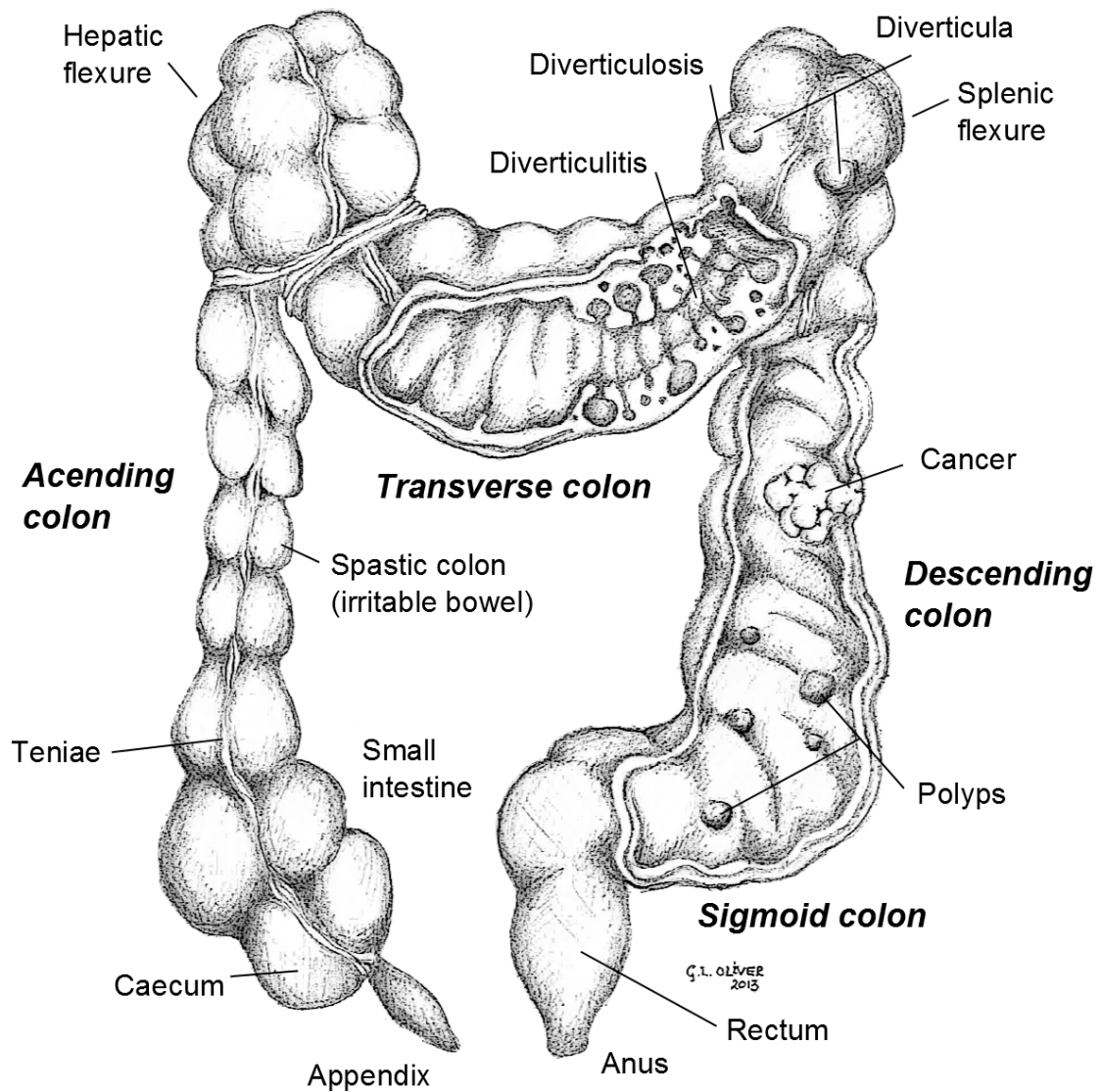


Figure 1.2: The *colon* or *large intestine* is a very flexible organ. It is about 1.5 metres long from the *caecum* (or *cecum*) to the *rectum* and *anus*. Starting from the *caecum*, where the *small intestine* fuses with the colon at the *ileo-caecal valve*, four parts can be differed: The *ascending*, the *transverse*, the *descending* and *sigmoid colon* which lead to the *rectum* (Gray, 1858). The above illustration further shows different stages of *colorectal diseases*: *polyps* in the *sigmoid colon* are likely to develop into *colorectal cancer* at a later stage (Cappell et al., 2005). Furthermore, several other diseases in the colon are illustrated, e.g. *irritable bowel syndrome* in the *ascending colon* and *diverticulitis* in the *transverse colon*. At the *hepatic*, *splenic flexures*, the colon remains more stable when the patient changes between prone and supine positions (Punwani et al., 2009). [Drawing courtesy of Georgina L. Oliver]

### 1.1.2 Current state of CTC in clinical practice

The implementation of CTC remains a cause of clinical controversy, in particular in the context of colorectal cancer (CRC) screening. Boone et al. (2011) propose that this controversy is likely to be due to conflicting recommendations by US studies such as (USPSTF, 2008) versus (Levin et al., 2008). Furthermore, concern has been raised about the cost-effectiveness of CTC in comparison to colonoscopy (Knudsen et al., 2010). CTC might raise healthcare costs by causing incidental extra-colonic findings, leading to unnecessary follow-up investigations if the findings ultimately prove to be unimportant (Pickhardt et al., 2010).

The question of who should perform the interpretation of CTC images is also for the subject of debate (Boone et al., 2011). The interpretation could be performed by radiologists, gastroenterologists, radiographic technicians, or automatically by computer algorithms. Recently, studies have even been performed using distributed (but non-expert) human intelligence via internet crowdsourcing Nguyen et al. (2012). Here, the “crowd” refers to a laypeople who are un-trained in CTC image analysis who interpreted CTC images and judged whether computer-aided-detection (CAdE) marks were true- or false-positive polyps. The results suggest that such untrained observers can achieve similar performance to CAdE algorithms for colonic polyp classification.

Diagnostic performance of CTC in an average-risk population has recently been compared to optical colonoscopy performed on the same day (Boone et al., 2011), e.g. in (Johnson et al., 2008), (Regge et al., 2009) and (Graser et al., 2009). In all these trials, colonoscopy was performed to validate the CTC findings. A comparison of the findings of these three trials is shown in Table 1.1. The results suggest good diagnostic performance for advanced adenomas in average-risk screening patients. However, the higher referral rates after CTC in comparison to after colonoscopy (31.4% vs. 7.2% respectively) raise challenging questions regarding cost-effectiveness of CTC and illustrate the importance of clearly defined criteria for follow-up referrals after CTC (Boone et al., 2011). A large European multi-centre

Table 1.1: Comparison of three clinical trials studying the diagnostic performance of CT colonography (CTC). CTC in all trials was validated with colonoscopy that was performed on the same day. [Table courtesy of Darren Boone]

	Johnson et al. (2008)	Regge et al. (2009)	Graser et al. (2009)
Number of patients in analysis	2531	937	307
risk of neoplasia	Predominantly average risk (89%)	All considered at increased risk (see text)	All considered average risk
Mean age (years)	58	60	61
Per patient sensitivity			
· Adenoma $\geq 6$ mm*	78%	85%	91%
· Adenoma $\geq 10$ mm*	90%	91%	92%
· Cancer	86%	95%	100%
Per patient specificity			
· Adenoma $\geq 6$ mm*	88%	88%	93%
· Adenoma $\geq 10$ mm*	86%	85%	98%

\*Graser et al. (2009) employed thresholds of  $> 5$  mm and  $> 9$  mm, respectively.

trial conducted on symptomatic patients – the *SIGGAR*<sup>3</sup> trial – compared the diagnostic performance of CTC with both barium enema and optical colonoscopy (Halligan et al., 2007, Taylor et al., 2010). The primary research interest of this study was the detection rates with CTC of polyps  $\geq 10$  mm or colorectal cancer in a symptomatic patient group with 5448 adults. They found that barium enema had a miss rate

<sup>3</sup>UK Special Interest Group in Gastrointestinal and Abdominal Radiology

twice as high with 14% as CTC with a miss rate of 7%. Furthermore, CTC lead to significantly more following colonic investigations of the colon than after barium enema: 23% vs. 18% (Halligan et al., 2007). This was mainly due to the higher polyp detection rates of CTC (Boone et al., 2011). As a result of the conclusions drawn from the SIGGAR trial, the Department of Health in the United Kingdom has recommended that CTC is the imaging method of choice for FOBT-based screening of colorectal cancer and removed barium enema from its national programme (Boone et al., 2011).

However, controversy remains about cost-effectiveness, the role of computer-aided detection, who should interpret CTC, and the impact of extra-colonic findings. However, Boone et al. Boone et al. (2011) concludes in his recent status update on CTC that the method has “excellent sensitivity compared to colonoscopy, and is significantly more accurate than barium enema, which should be abandoned for colorectal cancer screening purposes”. Furthermore, the three-dimensional images acquired during CTC offer opportunities for a wide range of new computer-based medical image computing methods, such as computer-aided detection and image registration, which are the topic of this thesis and have not been investigated previously in the clinical setting.

### 1.1.3 Registration of CT colonography images

Summers (2002) described prone-to-supine registration as a major challenge for CT colonography. A reliable method for correctly and automatically establishing spatial correspondence between the prone and supine CT colonography datasets has the potential to simultaneously improve diagnostic accuracy and reduce interpretation time. Furthermore, its result could be incorporated in computer-aided detection (CADE) algorithms in order to improve their robustness and accuracy. Establishing correspondence between points on the surface of the colon extracted from prone and supine CT scans will enable the clinician to view corresponding locations in the two CT scans (or virtual colonoscopy derived from these scans) when manually examining potential polyps. Registration allows rapid switching of views of corresponding locations in prone and supine CTC acquisitions. It will also enable data from the two scans to be fused into a single coherent dataset that could be used for improved automatic detection of potential polyps.

It was established during discussion at the scoping stage of this project that for guiding manual examinations and interpretation of CTC data, a relatively low accuracy (less than 100 mm) would provide significant clinical benefit. 100 mm corresponds to one mark on a standard colonoscope and this accuracy was seen to be useful in linking CTC findings to optical colonoscopy (Summers et al., 2009). Higher accuracy will be required to create a fused dataset that fully exploits the spatial resolution of the CT data (less than 1 mm<sup>3</sup> per voxel). However, clinically relevant polyps are typically 6-9 mm in size (see Chapter 5) and therefore the targeted registration accuracy should be at least 10 mm in order to accurately differentiate between significant polyps. I later show that even an accuracy of 36 mm is enough to significantly reduce false-positives in computer aided detection algorithms without loss of sensitivity (see Section 9.2.1). If achieved, accurate registration will have the potential to improve automatic detection and disease classification, and it will allow combination with other modalities such as colonoscopy and other optical methods (confocal micro-endoscopy etc.). Furthermore, it was established that correspondence is only required at the colonic wall for competent CTC interpretation. Therefore a full 3D transformation of the whole lower abdomen is not required nor is it likely to be useful during standard clinical practice using CTC for diagnosis. However, it is worth noting that the ability of CTC to image the entire anatomy surrounding the colon in the abdomen is of interest for radiologists. It provides the potential of early detection of important but unsuspected extracolonic diseases (Pickhardt et al., 2008).

## 1.2 Contributions of this thesis

Prone and supine registration has been researched by several groups for more than the last decade. The problem is challenging due to the complexity of the deformation when the patient changes position. A number of solutions have been proposed in the literature (see Chapter 2). The novel contribution of the work presented in this thesis is a cylindrical parametrisation that is used in order to align the endoluminal colon surface with non-rigid B-spline registrations. Unless stated otherwise, the following contributions described in more detail in the thesis are attributed to the Author:

- A method is proposed to extract the prone and supine surfaces from segmentations of the colonic lumen which corrects for topological errors and redundancy in the triangulated surface representations.
- A method is proposed in which cylindrical raster-images, generated by calculating a curvature-based shape index from the initial 3D surfaces, are used to drive prone-supine colon registration after a conformal mapping. This approach simplifies the challenging problem of aligning the prone and supine surfaces from 3D to a 2D task, but preserves the original 3D curvatures information in order to drive a subsequent non-rigid registration.
- An existing B-spline registration method has been modified to run in cylindrical space in order to account for the non-rigid deformations and torsion that occur between the prone and supine raster images. The hepatic and splenic flexures can be used as reliable anatomical landmarks to initialise this registration method (see Section 3.6), and the method has been adapted to work in traditionally difficult cases where several local colonic collapses or disconnected/incomplete colonic segmentations have occurred (see Section 3.7). The first implementation of this cylindrical B-spline registration method, based on the open-source *NiftyReg*<sup>4</sup> registration package (Modat et al., 2010), used in this thesis was completed by Jamie McClelland,.
- A landmark matching method for initialising registrations from a feature-based prone and supine registration algorithm developed by Thomas Hampshire. The inclusion of landmark matches further provides a piece-wise linear initialisation along the length of colon which improves registration accuracy (see Section 5.1.2).
- A thorough validation of the registration method with piecewise initialisation using independent external CT colonography data that were not used during the development of the algorithm (see Chapter 5). The clinical utility of the registration result was assessed by a radiologist (Dr. Darren Boone from University College Hospital). Further modifications to the registration algorithm include the incorporation of an improved non-rigid initialisation and the use of an alternative landmark matches, developed by Thomas Hampshire, which have been shown to further improve the robustness and accuracy of the method (Hampshire et al., 2011, 2012, 2013).
- Finally, the application of the method for the registration of temporally separated CT Colonography cases, which could be useful for the surveillance of polyps over time. The results, described in Chapter 7, show promise in terms of registration accuracy and robustness using the polyp locations provided by an expert radiologist (Dr. Emma Helbren from University College Hospital).

---

<sup>4</sup>[sourceforge.net/projects/niftyreg](https://sourceforge.net/projects/niftyreg)

### 1.3 Structure of this thesis

The remainder of this thesis is structured as follows:

**Chapter 2** reviews existing approaches for the registration of prone and supine CT images of the colon and discusses the drawbacks of these methods. It further introduces the proposed solution based on non-rigid registration of the colon surface in cylindrical space. **Chapter 3** presents the proposed registration method in detail. A detailed evaluation of registration accuracy on a limited number of cases is provided in **Chapter 4**.

In **Chapter 5** a piece-wise linear initialisation based on robust haustral fold matches is introduced. Initialisation is shown to improve the accuracy of the registration method. Robust initialisation allows the method to be evaluated using external cases that reflect standard CTC protocols used in current clinical practice. This external clinical evaluation is performed utilising a porcine phantom with accurate reference markers and using a large publicly available data set from external institutions.

**Chapter 6** discusses the inverse consistency error of the proposed registration method and shows how it can be reduced using an improved, non-rigid initialisation based on haustral fold feature matches. Additional performance gains are achieved by symmetric and inverse-consistent registration and these are described in the same chapter.

Robust and accurate non-rigid feature-based initialisation allows the registration of more challenging CT colonography cases, such as follow-up CT acquisitions that are temporally separated by several months or years. Here, anatomical correspondence is established in order to facilitate the clinical need to investigate polyp growth over time. Methods and results are described in **Chapter 7**.

**Chapter 8** presents a method that aims to compensate for differences in distension and bowel preparation by iteratively deforming the surface during the registration process.

**Chapter 9** discusses possible future work suitable for the proposed prone-to-supine registration method and how registration results could be used to improve CT colonography in general. Furthermore, it is discussed how prone-to-supine registration could be useful when aiming to match CTC with optical colonoscopy.

Finally, **Chapter 10** summarises each chapter individually and concludes this thesis.

## Chapter 2

# Literature review and proposed solution

## 2.1 Registration of prone and supine images

### 2.1.1 Centreline-based registration

The earliest attempt at prone-supine registration involves identifying similar distances along an extracted centreline of the segmented colon in both datasets (Acar et al., 2002, Nain et al., 2002, Li et al., 2004, de Vries et al., 2006, Wang et al., 2009). This line represents the virtual path through the centre of the virtual colonic lumen, from anus to caecum. A centreline extracted using Deschamp's method (Deschamps and Cohen, 2001) is shown in Fig. 2.1.

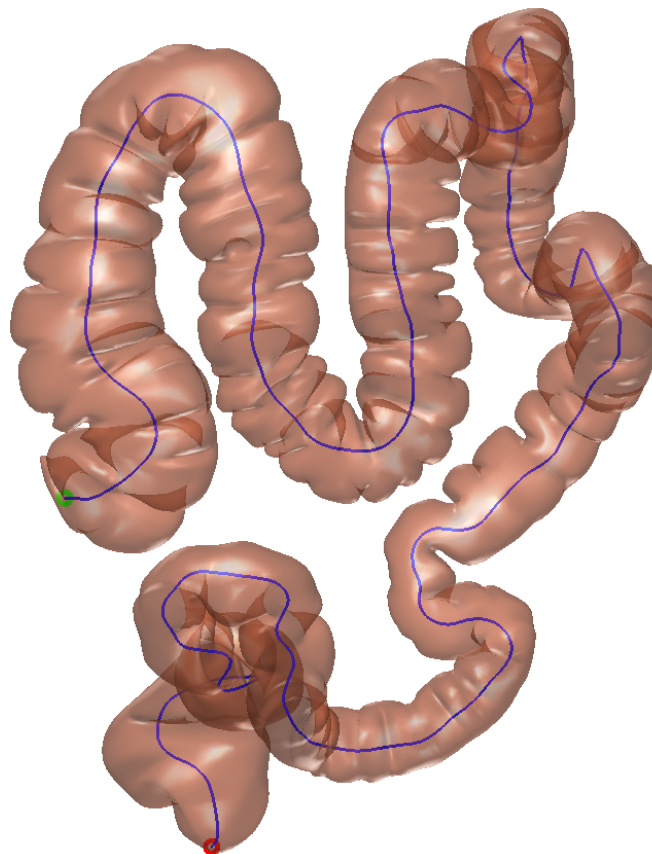


Figure 2.1: The colonic centreline (blue line), running virtually from the caecum (green circle) to the rectum (red circle) through the middle of the colonic lumen.

In order to account for changes of the colon's length between the prone and supine positions, meth-

ods have been proposed that express the current centreline position relative to the total centreline length (e.g. “normalised distance along the colon centreline” (NDACC) (Summers et al., 2009)). Furthermore, centreline matching methods can involve stretching and shrinkage of the extracted centerlines by matching relative path geometries (for example, local maxima on each centreline’s axial coordinate as feature points) as illustrated in Fig. 2.2. Some centreline-based methods can still be effective with colons exhibiting sections of colonic collapse where the segmented colon is disconnected, e. g. (Li et al., 2004, Wang et al., 2009).

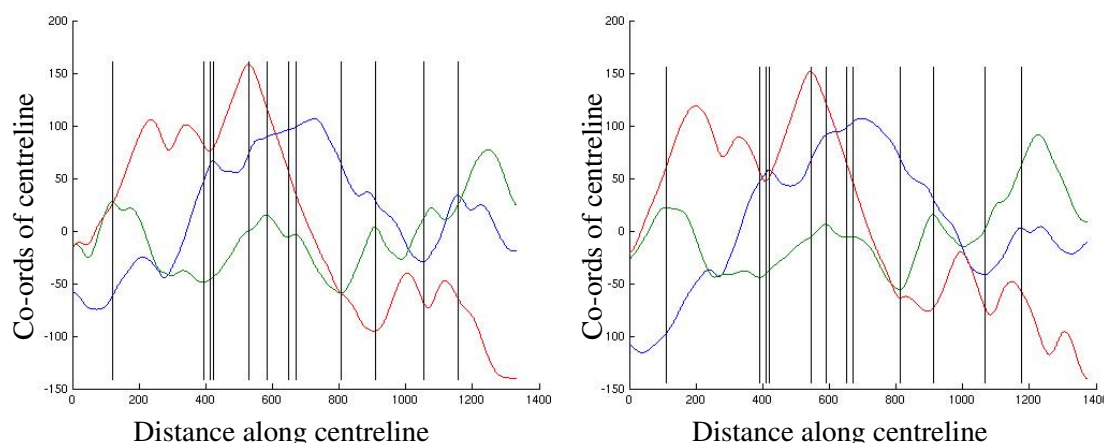


Figure 2.2: Plots of the x (blue), y (green), and z (red) co-ordinates of one of the centerlines against the distance along the centreline, from the prone (left) and supine (right) CT volumes. The black vertical lines indicate the corresponding points that have been detected by matching local maxima.

However, these methods provide only one degree of freedom relative to the colonic surface and so can only account for local stretching and shrinking along the length of the colon – they cannot account for torsion or other deformations ‘around’ the colon. Hence, they do not account for all the detailed deformations of the colon surface that are clinically interesting and that commonly occur between prone and supine positioning such as colonic torsions. Furthermore, aligning the centreline between the prone and supine images is restrained to establish the correspondence between the global shapes of the colon between both views. This shape can vary greatly when the patient changes positions and centreline-based methods might experience difficulties.

### 2.1.1.1 Extraction of the centreline

All the above described centreline-based registration methods are based on an extraction of an abstract centreline through the middle of both prone and supine colon images. The term centreline is classically defined (Blum et al., 1967) as “the locus of centres of maximal spheres contained in the shape”. Wan et al. (2002) also add the following attributes which a centreline and its detection algorithm should preferably possess:

1. Connectivity
2. Centricity
3. Singularity
4. Detectability
5. Robustness
6. Automation
7. Efficiency



The centreline extraction methods used in the publications described above are mostly based on topological thinning of the segmented colon, as proposed by (Iordanescu and Summers, 2003, Sadleir and Whelan, 2005). Disadvantages of these methods are that they can result in tree-like structures which have to be corrected afterwards with some minimal path extraction algorithm. Other extraction algorithms are based on level-set methods, such as *fast marching* (Adalsteinsson and Sethian, 1995), as proposed by Deschamps and Cohen (2001). They used this method to extract skeletons in several tubular structures such as the colon. Thereby, a first fast marching wave front is propagated through the colonic lumen, starting at the point of maximum Euclidean distance to the colonic wall. The point with maximum arrival time of the first wave front is then used as seed point for another fast marching producing a ‘time crossing map’ which shows the temporal progress of that second wave front in space. Using a backtracking method which follows the steepest gradient of this second time crossing map, the centreline can be extracted at subvoxel accuracy. Van Uitert et al. (2006) built on this method by incorporating a segmentation of the outer colonic wall in order to extract centrelines in the collapsed parts of the colon (Van Uitert and Summers, 2007).

### 2.1.2 Landmark-based registration

An alternative approach to prone-to-supine registration was proposed by Näppi et al. (2005). Several anatomical landmarks are defined in order to align the two datasets. Anatomical locations that are relatively resistant to deformation, such as the anus or colonic flexures, were identified. Other landmarks, including the caecum and recto-sigmoid junction, were then derived from the relative distance to the landmarks already defined. Despite robust matching of anatomical landmarks, the identification of a limited number of corresponding points is likely to be insufficient to describe the complex colonic deformations that occur when moving between prone and supine positions.

Other feature-based methods account for the rotation of the colonic surface by using the *teniae coli* as an additional feature. Teniae coli are three discrete smooth strands of muscles running longitudinally along the exterior colonic surface, namely the *teniae libera*, the *teniae mesocolica* and the *teniae omentalis* (Gray, 1858) (see Fig. 1.2). These methods often require user inputs in order to detect the teniae coli or they only work in some segments of the colon (see Section 2.1.4). The mostly disconnected parts of the extracted teniae coli must then be reconnected. Furthermore, teniae coli detection relies heavily on the correctness of the haustral fold detection (Lamy and Summers, 2007). This makes teniae coli difficult to extract robustly over the complete length of colonic surface.

Due to difficulties in automatic extraction of teniae coli, Huang et al. (2007) used manual selection of the teniae omentalis in order to correct for colonic torsion in prone-to-supine registration. However, they still report registration errors up to  $\pm 61$  mm with 95% confidence. As with centreline-based methods, teniae-coli-based methods aim to match the gross shape and bending of the colon and then interpolate to the surface in order to estimate finer deformations on the detailed surface structure.

Recently, Wang et al. (2012) used a *graph matching* approach to register prone and supine images based on *n-SIFT* features. Utilising mean field theory, they match features without the need of defining a colon centreline – their main advantage. However, a limited accuracy is achieved, with a mean registration error of 37.6 mm using a test set of 20 patients. A similar technique is deployed by Wei et al. (2012) but furthermore incorporates the detected teniae coli when building the graph, rather than building the graph over the full colon surface as proposed by Wang et al. (2012). They report an improvement in mean registration error to 25 mm, tested on 10 pairs of prone and supine CTC scans in comparison to the surface-based graph matching.

Fukano et al. (2010) aimed to establish correspondence between the detailed colon surface by matching haustral folds extracted from prone and supine data. Although haustral folds can be detected robustly, it is very challenging to establish their correct correspondence between both views as their results indicate. They report 65.1% of corresponding large haustral folds and 13.3% of small haustral

folds being matched correctly.

Hampshire et al. (2011) aimed to improve the matching accuracy of haustral folds using virtual surface renderings of the colonic lumen. The intensity difference between pairs of virtual images, along with additional information about the geometric neighbourhood of folds, is then used with a Markov Random Field (MRF) model to estimate matching haustral folds. The method achieved matching accuracies of 83.1% and 88.5% with and without local colonic collapse. Recent improvements to the method increased the matching accuracies to 96.0%, even in challenging cases exhibiting marked differences in distension (Hampshire et al., 2013).

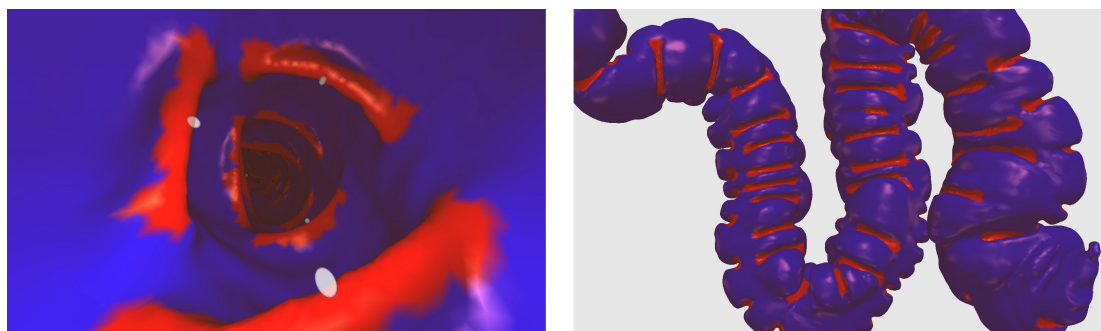


Figure 2.3: Internal (left) and external (right) view of segmented haustral folds with marked fold centres [Images courtesy of Thomas Hampshire].

Later in Chapter 6, I will show that landmark features (e.g. haustral folds), matched robustly between prone and supine acquisitions, can further improve registration accuracy by providing an initialisation for a non-rigid surface-based registration in cylindrical space (Hampshire et al., 2011, Roth et al., 2012, Hampshire et al., 2013).

### 2.1.3 Extraction of haustral folds

Several methods for detecting haustral folds have been proposed. One method of detecting folds is by using the extracted centreline (Oda et al., 2009). This algorithm proposes a difference filter which accounts for regions where voxels are the tissue of the colonic wall and where voxels tangential and anti-tangential to the centreline at particular distances are air.

Other methods make use of the local surface geometry (Lamy and Summers, 2007, Umemoto et al., 2008) in order to detect haustral folds. Measurements like principal curvature, Gaussian curvature, shape index and curvedness (Koenderink, 1990, Koenderink and van Doorn, 1992) are used to classify folds on the colonic wall. Hampshire et al. (2011) combines surface geometry with a graph cut method in order to segment folds more robustly. Furthermore, methods which use level set methods or diffusion-FCM (*fuzzy c-means*) have been proposed (Chowdhury et al., 2009).

### 2.1.4 Extraction of teniae coli

The teniae coli are three muscles which run alongside the colon between the locations where the haustral folds meet. Detection of teniae coli on the colonic surface is typically achieved by either clustering haustral fold extremities (Lamy and Summers, 2007) or joining up neighbouring fold centres in 2D unfolded views of the colonic surface (Umemoto et al., 2008, Wei et al., 2011, 2012).

Lamy and Summers (2007) cluster haustral fold extremities along the centreline to detect teniae coli segments. Single teniae coli segments need user input to be connected. On the other hand, Umemoto et al. (2008) compute continuous teniae coli, based on clustering the centres of gravity of each haustral folds in a virtually unfolded view of the colon (Oda et al., 2006). The teniae coli are then determined as those three lines which lie equally spaced between the three extracted lines extended through these

centres of gravity. However, this method is limited to the ascending and transverse colon as the number of haustral folds in the other parts of the colon is insufficient.

The method proposed by Wei et al. (2011, 2012) is similar to the one by Umemoto et al. (2008) such that it also utilises an unfolded representation of the colonic surface in order to extract teniae coli. However, Wei et al. (2011, 2012) also manage to extract teniae in the descending colon which is a more challenging colon segment due to it being typically less haustrated. However, they also report difficulties in extracting all three teniae over the full length of the colon robustly. It is unclear how the method would perform in cases of local endoluminal collapse.

Hence, all methods based on teniae coli detection to date suffer from the fact that all three teniae coli cannot be detected robustly and accurately along the full length of colon.

### 2.1.5 Voxel-based registration

A voxel-based approach has been developed by Suh and Wyatt (2009). Initially, their method involves rigid dataset alignment, based on the location of the anus and the flexures followed by generation of an initial deformation field using the centrelines. Level-set distance maps from the colonic surface to the centre of the lumen are then used to drive a non-rigid ‘demons’ registration (Thirion, 1998). They reported an mean (mean (std. dev.) error of 13.77 (6.20) mm for aligning polyps in 21 patients. Such voxel-based approaches might lack robustness: it is very difficult to adequately constrain the registration to prevent physically implausible deformations while still recovering the large and complex deformations that can occur. Furthermore, the measurement of overlap ratio used to validate the alignment of the registered colons does not directly indicate a correct alignment of corresponding regions.

They extended their method to handle cases with local colonic collapse where the segmentations are disconnected (Suh and Wyatt, 2008). Although this method shows promise in handling disconnected segmentations, the validation set was limited, with only four CTC cases, with only one collapse in one view and fully connected colon segmentation in the other. A reported average registration error of 30.1 mm for 4 polyps suggests limited accuracy. This may be due to their method of handling local collapses which allows the colon to change its topology during the registration using *Embedded Maps* (Wyatt and Laurienti, 2006). In theory, the source surface could be transformed completely into the targeted surface just by ‘adding to’ or ‘carving’ the source surface. This could cause different structures to appear similar to each other rather than correctly aligning the corresponding anatomical structures (e.g. a fold could be flattened rather than shifted).

### 2.1.6 Matching prone and supine polyps

Prone and supine registration methods can be used to match polyps between both acquisitions. However, alternative approaches, such as by Liu et al. (2011), have been proposed in order to match between polyps directly for the reduction of false-positives in CADe algorithms. They utilise a metric learning approach that utilises the CADe features of prone and supine polyps directly in order to establish correspondence. While such methods could be used to reduce false-positives in CADe, they lack the ability to match between the entire colonic surfaces – this is the basic challenge of the work described in this thesis.

## 2.2 Proposed solution

The difficulties described in the previous sections provide strong motivations for the development of a method that simplifies the task of establishing full spatial correspondence between prone and supine endoluminal colon surfaces. Unlike most image registration tasks, where the range of intensity values provides a great deal of information about the anatomy, in CTC the intensity information essentially only indicates whether a voxel lies inside or outside the colonic lumen. Therefore, there may be more information to help guide the registrations derived from the colon surface than from the image intensities. Hence, 3D surface-based non-rigid registration methods were investigated, incorporating measures such as the surface curvature into a similarity metric.

The colon is an extremely flexible structure. The 3D registration task requires a non-rigid transformation which preserves the topology of the colonic wall when transforming between prone and supine. The proposed method reduces complexity by using cylindrical 2D representations of the endoluminal surfaces derived from both prone and supine CTC datasets. This enables large deformations and twisting (that are inevitable between the two positions in 3D) to be accounted for by considering them as relatively simple deformations in the space of the cylinder.

Similar ideas of reducing of the complexity of the registration task by mapping 3D structures to 2D domains have been exploited for various applications. For example, the cortical brain surface can be mapped to a spherical domain in order to align several brain surfaces for neurological research (Fischl et al., 1999). Additionally, surfaces of the human face have been mapped to 2D disks in order to simplify a face matching process (Zeng et al., 2008). The idea of using the 'flattened' view for prone-to-supine registration was probably first proposed by Summers (2002) but without describing any details about how this could be realised.

The colon is essentially a tubular organ, topologically equal to an open-ended cylinder. Hence, any position within the colon can be mapped by two indices: length along the cylinder and angular position. Each 2D point  $p(x, y)$  on the cylindrical representation corresponds directly to a 3D point  $s(x, y, z)$  in the CTC data. Any measure acquired in 3D and on the surface can be assigned to a corresponding 2D point  $p$  which can be used to drive registration. This thesis proposes the use of conformal mapping of the endoluminal colonic surfaces from prone and supine CTC images to obtain 2D cylindrical representations of the colon. A metric value is assigned to each 2D point  $p$  in order to drive a non-rigid cylindrical registration in the parametrised cylindrical space. This simplifies the registration task compared to full 3D non-rigid volume registration. The registration result represents the transformation between two cylinders as deformation that includes non-linear stretches along the colon as well as local rotation and local torsion. This thesis also proposes a cylindrical implementation of the well-known B-spline registration method (Rueckert et al., 1999) in order to achieve this for fully connected colon and in the case of local colonic collapse.

A similar cylindrical B-spline transformation model was recently proposed by Huysmans et al. (2010) in order to produce active shape models of tubular structures (e.g. clavicles, tracheae, and thrombi). Although the transformation model is very similar to the one proposed in this thesis, their application is very different (they are trying to determine correspondence for a large population of shapes), and as such, their method of assessing correspondence (the minimum description length of the resulting shape model) and their overall framework for performing the registrations cannot be used for registering prone and supine colonic surfaces.

Novelty is claimed for the first use of a cylindrical non-rigid registration method to align image derived representations of the full colon endoluminal surface in order to establish a correspondence between colon surfaces extracted from prone and supine CTC images. The proposed method is motivated by the challenge of simplifying the radiologist's task of interpreting the two datasets for diagnostic purposes. In particular the assessment of possible polyps in the two views, to reduce the incidence

of false-positives, speed up interpretation and finally to provide correspondence in emerging computer assisted detection (CAdE) applications that merge prone and supine datasets in order to reduce false-positive detection rates.

## 2.3 Methods of unfolding

A number of groups have proposed methods for unfolding the colon to produce 2D images of the colon surface. These images are usually produced to enable better examination of the surface of the colon and to aid in detection of polyps. However, as described above, I aim to map the 3D colon surface onto a 2D coordinate system in order to establish correspondence between the colon surfaces in the cylindrical domain. This approach has the advantage of constraining the deformation to be between the colon surfaces (which is what is required) rather than being free to deform any point in 3D space to any other. So the registration will potentially be faster, more accurate and more robust (because better constrained) than a full 3D registration approach.

The reviewed methods for unfolding can be separated into two main classes: Methods based on *ray casting* and methods based on *conformal maps*.

### 2.3.1 Ray casting methods

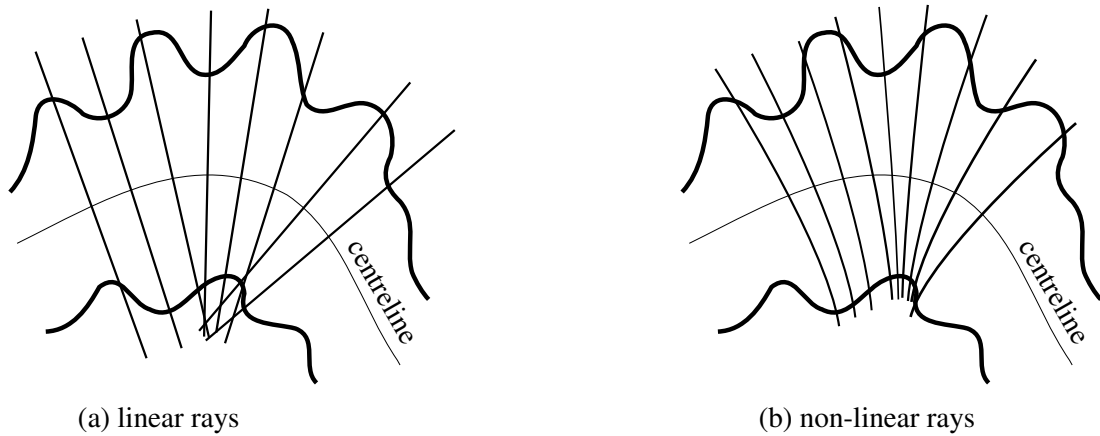


Figure 2.4: Ray casting using linear (a) and non-linear (b) rays in order to avoid self-intersections. [Figure based on Bartrolí et al. (2001)]

Several colon flattening approaches have been produced using ray casting methods. Here, rays are projected from a centreline inside the colonic lumen towards the colonic surface. Encoding each ray with information of its starting point, e. g. the length along the centreline and an angular value around the centreline can produce a two-dimensional map or image of the colonic surface, where each ray intersection can be assigned intensity based on distance to the centreline, local curvature, or values derived from volume rendering (Oda et al., 2005). Bartrolí et al. (2001) show how dividing the colon into a set of small cylinders with linear ray casting produces an unfolded image for each local camera position of the virtual colonoscopy.

However, just using linear rays, any ray perpendicular to the tangent direction of the centreline can result in a crossing of rays. Furthermore, surface areas could be missed out in regions where the colon is highly tortuous and therefore the centreline is strongly curved. To overcome this problem, several authors proposed the use of non-linear rays which can bend at areas of high curvature to hit all points on the surface with a coherent distribution over the full colon surface. Wang et al. (1998) simulate use of an electrical field model to apply electrical charges to each ray in order to bend it in the right direction. Bartrolí et al. (2001) use non-linear ray casting which follows the gradient of a pre-computed distance

map. Furthermore, they use a non-linear 2D scaling to correspond to the local circumference of the colon. Another method using bended rays was proposed by Passenger et al. (2008). It solves Laplace's equation of potential difference between the centreline and the colonic surface which results in a set of equipotential lines that can be used to establish the correct surface to centreline correspondence to parametrise the surface.

Sudarsky et al. (2008) use a different approach to overcome the intersection problem of linear rays. Rather than bending the rays, they straighten out the whole colon along its centreline using a *mesh skinning* technique. Correspondence between the centreline and points on the colonic surface is established by using a distance transform, based on region growing from the centreline. Subsequently, linear ray casting can be used to produce the unfolded view without large distortions. However, this method can still miss out areas of the colon, e. g. folds that cannot be hit by the linear rays, even in the straight colon. Yao et al. (2010) deploy a similar mesh skinning method, but improve upon (Sudarsky et al., 2008) by applying a topology-preserving correspondence search between the colon surface and the centreline. Furthermore, they use a more robust cylindrical projection method rather than linear ray casting.

A similar strategy to straighten the colon was deployed by Li et al. (2009) based on a gravity field model. Here, the colon is bio-mechanically modelled using a finite element method. The colon is fixed at one end and a gravitational force is then applied which causes the colon to straighten out.

Oda et al. (2006) proposed an unfolding method loosely based on bio-mechanical principles. It uses spring energies set between planes perpendicular to the centreline. Minimizing the lengths of all springs accordingly to their energies results in a reduction of intersecting rays.

## 2.3.2 Conformal mapping methods

Conformal maps are typically applied to surface mesh triangulations in order to find a simpler representation of the three-dimensional object. Such mappings have been applied in many different fields of engineering and science. The computational methods for computing these maps, however have mainly been developed for the purpose of texture mapping in order to enhance the appearance of digital objects in computer graphics (Floater and Hormann, 2005).

### 2.3.2.1 Conformal mapping background

Any one-to-one mapping that transforms a surface  $S$  to the space of another surface  $S^*$ , is said to be *conformal* if the following criterion holds: any two differentiable curves that intersect at a non-zero angle at a point in  $(u, v)$  on  $S$ , will be mapped to  $S^*$  such that the angle  $\vartheta$  at their intersection is preserved at the point at  $f(u, v)$  on  $S^*$  (Bieberbach et al., 1953). This is illustrated in Fig. 2.5. A conformal mapping also means that infinitesimal small circles will be mapped to infinitesimal small circles on the other surface (Jin et al., 2008). Classical examples of conformal maps are the *stereographic* and *Mercator* projections used in cartography; mapping a sphere (the earth) to the plane (Floater and Hormann, 2005). While conformal mappings preserve local angles, they do not necessarily preserve area (which would be an *equiareal mapping*). Mappings such as the unfolding of a cylinder to the plane are both conformal and equiareal; they are called *isometric mapping* (Floater and Hormann, 2005).

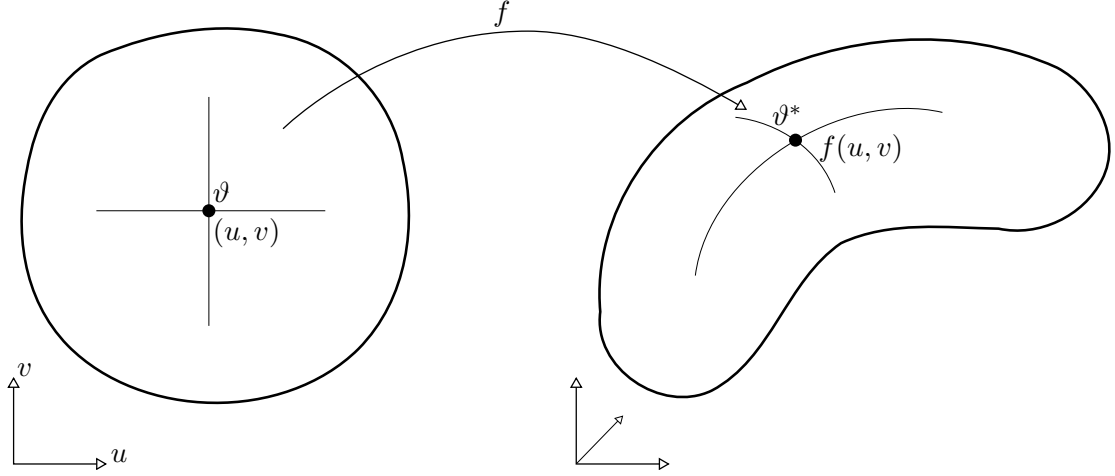


Figure 2.5: A one-to-one conformal mapping  $f$  that preserves the angle between any local intersection of curves:  $\vartheta^* = \vartheta$  [Figure based on Lévy et al. (2002)].

In contrast, Fig. 2.6 shows a one-to-one mapping that is not conformal.

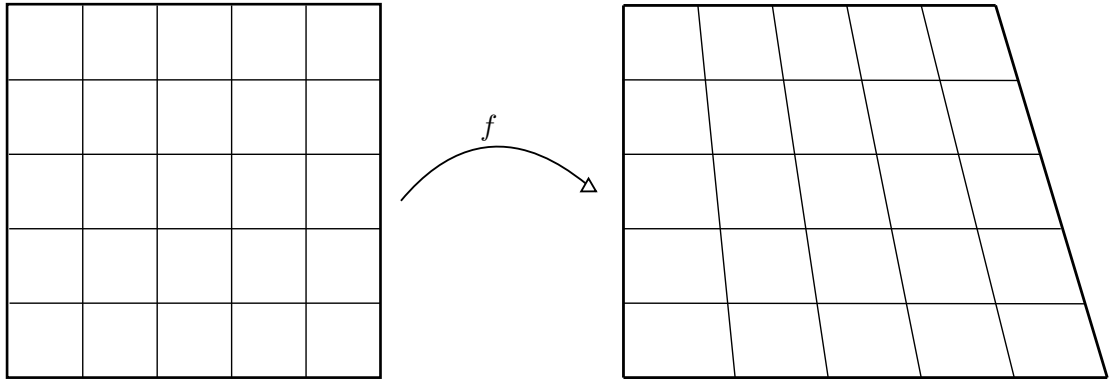


Figure 2.6: One-to-one mapping  $f$  that is not conformal [Figure based on Floater and Hormann (2005)].

### 2.3.2.2 Conformal mapping of the colon

Haker et al. (2000) and Hong et al. (2006) unfold the colon in a conformal manner. These flattening procedures are based on differential geometry and ensure conformal mapping of the entire surface while preserving appearance of local structures, e.g., polyps and haustral folds. This is due to the angle-preserving nature of conformal maps. Both methods minimise the global distortion. However, Hong's method can map the colonic surface into a rectangle rather than a parallelogram as in Haker's method (Hong et al., 2006).

Qiu et al. (2008) use the discrete surface Ricci flow (Jin et al., 2008) to do the flattening. Hereby, a desired curvature value is assigned to each vertex of the surface mesh. For the purpose of flattening, the desired curvature is zero at all vertices. Iteratively, the edge lengths and corner angles of each surface triangle are changed to comply with those curvature values. If the difference between desired and measured curvature is smaller than a threshold the Ricci Flow flattening is deemed to have converged and resulted in a planar image of the surface. I later show that Ricci flow can be used as a pre-processing step for prone and supine registration (see Chapter 3).

### 2.3.3 Unfolding for prone-to-supine registration

Recently, several groups developed prone-to-supine registration methods which utilises a mapping to an unfolded view of the colon in order to simplify the registration task, similar to the proposed solution. Their methods however differ in the computation of these mappings and how the correspondence between the two unfolded views is established as well as with the ability of dealing with sections of colonic collapse.

The method of Huang et al. (2005, 2007) was probably the first to use a 2D representation in order to provide improved alignment of the prone and supine CTC data sets. However, their parametrisation relied on manual selection of the teniae omentalis from the caecum to the descending colon in order to provide a boundary for the conformal mapping. After conformal mapping, the registration was confined to a linear scaling based on distance along the centreline and the linear angular displacement with respect to the previously defined teniae omentalis.

Zeng et al. (2010) presented a method based on conformal mapping combined with feature matching in order to establish correspondences between the prone and supine surfaces. They detect four flexures and one teniae coli in order to divide the colon surface into five segments and map each segment to a rectangle. Feature points on haustral folds are then detected in each segment using graph cut segmentation and morphological operations followed by principal component analysis. Correspondence between prone and supine surfaces is then established for each rectangular by matching feature points using a graph matching technique (Torresani et al., 2008) for each segment individually. Therefore the method relies on being able to accurately determine the exact same segments on the prone and supine surfaces, which can be difficult even for fully distended colons. This method may not be possible for cases with local colonic collapse. Furthermore, they established correspondence between the mapped segments using only a sparse point set of features extracted from some ‘prominent’ haustral folds, which are unlikely to provide an accurate alignment of the detailed colonic surface. Despite these drawbacks, they report promising results with an average 3D error of 5.65 mm using 20 validated pairs of polyps over 6 patients and an average 3D error of 7.51 mm using feature points.

An anatomically-based registration method in 2D space was proposed by Davis et al. (2011). Haustral folds, teniae coli and other anatomical landmarks are extracted from the segmented colon and the registration is performed on a 2D fillet representation of the surface using *simulated annealing* (Kirkpatrick et al., 1983). They claim robustness to differences in prone and supine landmarks, such as obscuration or apparent bifurcation of teniae coli. 57 manually selected features on 8 cases show a 3D registration mean error of 16.4 mm. Further validation on a latex phantom with 210 fiducial pairs results in a mean 3D error of 8.6 mm. It is unclear how the method would perform in cases with collapsed colons.

Principles from differential geometry are also used in the prone-to-supine registration method proposed by Lai et al. (2010). They compute the *Fiedler vector* based on the Laplace-Beltrami differential operator in order to find a one-dimensional embedding for each surface point which corresponds to a distance along the colon surface. Using an additional match between feature points at the anus, rectum and hepatic and splenic flexures enables a piece-wise linear registration between regions on the colon surface. Even though this provides an indexing for each surface point, non-rigid deformation such as twisting of the colon and non-linear stretch is not accounted for.



## Chapter 3

# Prone-to-supine registration in cylindrical space

The work presented in this Chapter was published in the journal *Medical Physics* (Roth et al., 2011).

### 3.1 Registration principle

Each surface point can be described by two indices  $x$  and  $y$  using a cylindrical representation of the endoluminal colon surface  $S$ . Here,  $x$  denotes a position along the length of the colon and  $y$  its angular orientation. Several groups have proposed methods to “unwrap” or “virtually dissect” the colon in order to produce flattened 2D images of the endoluminal surface. These methods were developed to facilitate more rapid interpretation by enabling inspection of a larger surface area at once (Johnson et al., 2006).

One technique for mapping the colon surface to a uniform cylinder is provided by conformal maps. Conformal maps are typically applied to surface mesh triangulations in order to find a simpler representation of the three-dimensional object in 2D space. They provide a one-to-one mapping of a 3D surface to 2D space while minimising the distortion of local angles in the triangles of the mesh (Floater and Hormann, 2005), see Section 2.3.2 in Chapter 2. These methods are based on differential geometry and ensure mapping of the entire surface while preserving appearance of local structures, e.g. polyps and haustral folds (Hong et al., 2006).

The proposed registration approach is based on the following principle: a prone endoluminal colon surface  $S_p$  in  $\mathbb{R}^3$  can be transformed using the one-to-one mapping  $f_p$  to a parametrisation  $P_p$  in  $\mathbb{R}^2$ . The supine surface  $S_s$  is mapped to  $P_s$  through  $f_s$ , respectively. Here, the subscripts  $p$  and  $s$  denote prone and supine, respectively. If the necessary transformation  $T_{cyl}$  between  $P_p$  and  $P_s$  can be determined, the transformation  $T_{ps}$  between the surfaces  $S_p$  and  $S_s$  follows as shown in Fig. 3.1, where the principle is illustrated with the endoluminal colon surfaces extracted from prone and supine CT colonography. The transformation  $T_{cyl}$  must be non-rigid in order to account for deformations such as local twists and stretches and other non-linear deformations, introduced by the patient changing positions and natural bowel movement.

### 3.2 Colon segmentation

In order to extract the endoluminal colonic surface  $S$  in both prone and supine CTC scans, the volume of the inflated lumen  $L$  is segmented using the method described by Slabaugh et al. (2010). This method was developed for segmenting intraluminal gas over the entire colonic length. All voxels representing *air*- or *gas*-filled regions are firstly segmented if their intensities are smaller than  $t_{air} = -750$  HU (Hounsfield units). Tagged residual fluids are detected by thresholding intensities larger than  $t_{fluids} = 300$  HU (see Fig. 3.2). Fluids- and air-filled regions then need to be combined in order to generate a complete segmentation of the inflated colonic lumen. However, partial volume effects cause the thresholded air and fluid segmentations to be separated by some voxels (Slabaugh et al., 2010). The

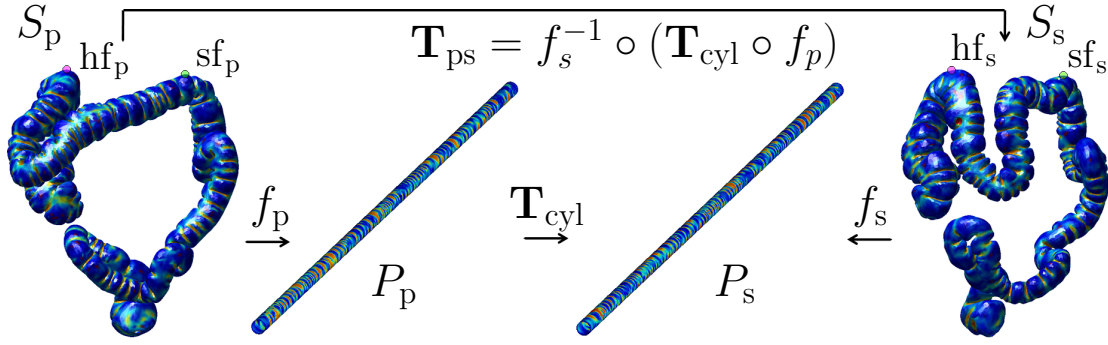


Figure 3.1: The principle of colon surface registration between prone ( $p$ ) and supine ( $s$ ) CTC using a cylindrical 2D parametrisation, where the colour scale indicates the shape index (see equation (3.25)) at each coordinate of the surface computed from the 3D endoluminal colon surfaces  $S$ . Both surfaces are parametrised in 2D on regular cylinders  $P$  between which a transformation  $\mathbf{T}_{\text{cyl}}$  can be estimated using non-rigid registration. Hence, the transformation  $\mathbf{T}_{\text{ps}}$  between the 3D surfaces  $S_p$  and  $S_s$  can be derived as shown in the figure. The hepatic and splenic flexures are marked as  $\text{hf}_{p/s}$  and  $\text{sf}_{p/s}$  respectively ( $_{p/s}$  denotes prone and supine, respectively); see Figure 1.2 in Chapter 1.

combination of these regions can be achieved by performing a morphological dilation of the fluids in direction opposing gravity. In this study, fluids were dilated between 2 to 4 voxels opposing gravity, with voxel sizes ranging from  $0.59\text{mm} \times 0.59\text{mm} \times 0.70\text{mm}$  to  $0.93\text{mm} \times 0.93\text{mm} \times 1.0\text{mm}$ . If the dilated fluids touch any air-filled regions, both segmentations are fused together, resulting in a segmentation of all gas-filled regions in the image including any tagged fluids as illustrated in Fig. 3.3.

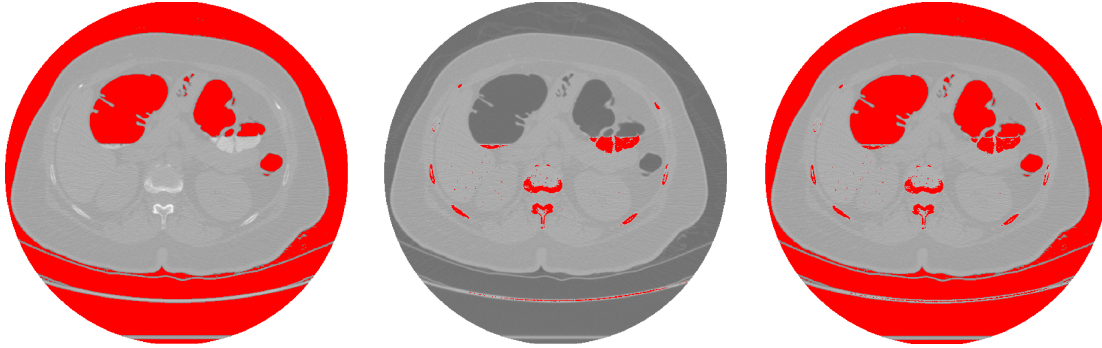


Figure 3.2: Segmentation of the colonic lumen by thresholding. The segmented voxels are overlaid in red above an original axial slice of a CTC image. Left: Any voxels representing air are found with an intensity smaller than  $t_{\text{air}} = -750$  HU (Hounsfield units). Middle: Any voxels representing fluids are found with an intensity greater than  $t_{\text{fluids}} = 300$  HU. Right: Both segmented air and fluids voxels are shown in red, illustrating the boundary between air and fluids caused by partial volume effects.

It is possible that these gas-filled regions of small intestine are segmented as either isolated structures or erroneously connected to the colonic segmentation. The main clinical interest lies in the endoluminal surface of the colon. Therefore all other objects are rejected by first eroding the segmentation with a spherical structure element of radius  $r$ . This enables the removing of erroneous connections if they are present in the segmentation  $L$ . Then the six-connected object with the largest volume is selected and subsequently dilated with a structure element of radius  $r$  in order to restore its original surface dimensions. Here, six-connected refers to an object in 3D voxel space which is only connected to direct neighbour-

ing voxels on its six sides. This has advantages for the later extraction of a surface triangulation using the marching cubes algorithm (Lorensen and Cline, 1987) as it reduces the chance of introducing non-manifold vertices as opposed to using 26-connected voxels (where the object can also connect over the corners of each voxel (Bertrand, 1994)). For this study, the radius  $r$  was adjusted interactively to produce the best segmentation by visual inspection of the colon surface. The parameter,  $r$ , ranged between 1 and 5 voxels, with voxel sizes ranging from  $0.59\text{mm} \times 0.59\text{mm} \times 0.70\text{mm}$  to  $0.93\text{mm} \times 0.93\text{mm} \times 1.0\text{mm}$  for all cases used in this chapter.



Figure 3.3: Rendering of all gas-filled regions and regions detected to include fluids. Each connected object is displayed in a different colour. Because the intensities of bones and fluids are similar, bones are also rendered. The large intestine is then manually selected when start and end points of each colonic segment are chosen (see Section 3.3 and 3.7).

The rectal insufflation catheter (used to introduce the colonic gas necessary for luminal distension) is often excluded from the segmentation and can therefore lead to errors when extracting the endoluminal surface of the colon. I use a combination of morphological operations on a rectal region of interest in order to segment this plastic tube and add it to the colon segmentation  $L$  if necessary.

The details of the proposed registration algorithm after segmentation of the colon lumina will be laid out in the flowing sections and an overview is provided by the flowchart in Fig. 3.4.

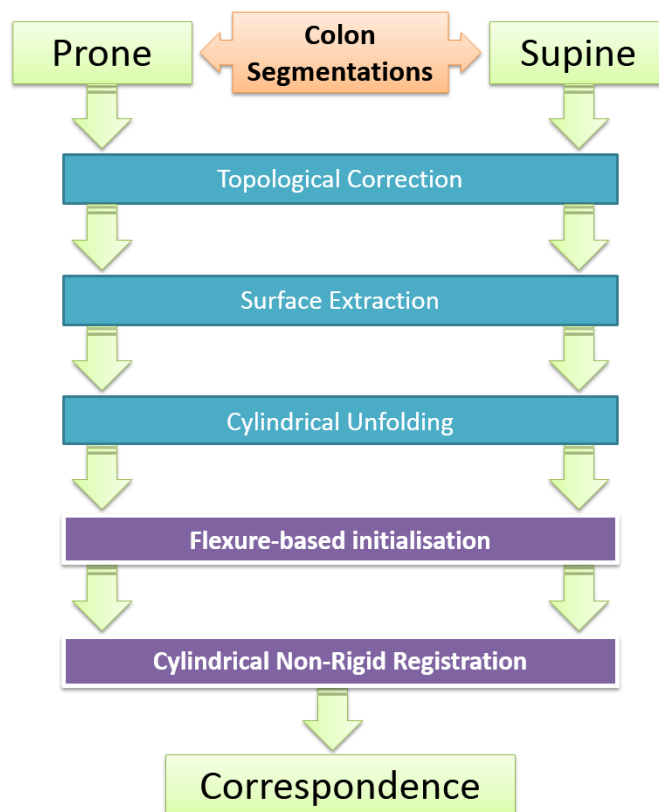


Figure 3.4: A flow chart of the proposed colon surface registration between prone and supine CTC: After the prone and supine colonic lumina have been segmented, topological correction is applied in order to allow the extraction of genus-zero surfaces. After using cylindrical 2D parametrisation (unfolding) and hepatic and splenic flexures for initialisation, a non-rigid intensity-based image registration performs aligns the surfaces in cylindrical space. The primary contributions of this thesis are highlighted (in purple) as the last two steps.

### 3.3 Topological correction

The colonic lumen  $L$  is now represented as a single six-connected object, ideally with a surface of genus zero which is topologically equivalent to a sphere. However, topological errors could be present in the segmentation due to noise, reconstruction artefacts or insufficiently tagged fluids in the CT colonography data. Potentially – although rare – colonic fistulas, sometimes caused by diverticular disease, could be present (Lavery, 1996). These occur particularly at adjacent folds or where the colon folds back against itself, resulting in erroneous connections in the surface, such as handles which span across haustral folds or are connecting different colonic segments (Hong et al., 2006). A schematic example of a small region of the colonic surface near a fold with a topological error (i.e. “handle”) is shown in Fig. 3.5 (left) and after correction using a cutting operation (right). Similarly “large” handles can occur if there is an erroneous connection between different segments of the colon. An example colonic surface region

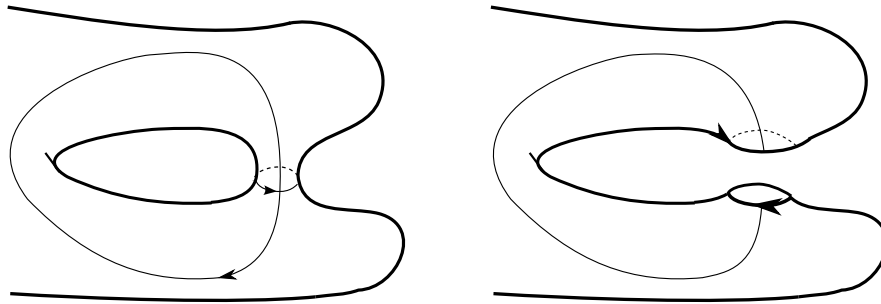


Figure 3.5: Left: Schematic view of a “handle” which erroneously connects two sides of a haustral fold, resulting in incorrect topology that would allow the creation of two separated “loops” along the surface and therefore a surface of higher genus than that shown on the right. Right: the same surface region after topological correction by cutting through the handle (and the loop) [Schematic after (Hong et al., 2006)].

with such handles is shown in Fig. 3.7 (left) based on real CTC data. A topology-preserving *region growing* algorithm is used to correct for any topological errors in the colonic lumen segmentation  $L$ . I used the implementation of Couprie et al. (2007)<sup>1</sup> which was developed for the extraction of *ultimate binary skeletons* that are guided by a priority images  $I_{\text{prior}}$ . The priority image  $I_{\text{prior}}$  in this case is the absolute of second derivative (Laplacian) of the lumen  $L$ , which causes high priority values at the object-boundary of  $L$ :

$$I_{\text{prior}}(x) = |\Delta L(x)|. \quad (3.1)$$

The correction algorithm then “grows” starting at the centreline (running at the virtual centre of the colonic lumen from caecum to rectum) and guided by the priority map. The centreline can be extracted with the method described by Deschamps and Cohen (2001) based on evolving a wave front through the colon using the fast marching method (Adalsteinsson and Sethian, 1995) for solving the Eikonal equation

$$F(x) |\nabla T(x)| = 1 \quad (3.2)$$

where  $F(x)$  is a speed function and  $T$  is time. Fig. 3.6 illustrates the extraction of the centreline on a 2D CT image slice of a porcine colon phantom<sup>2</sup>. The translation of this method to three-dimensional space is straightforward as described by Deschamps and Cohen (2001).

This method of centreline extraction requires a defined start- and end-point. If the insufflation tube has been detected, the most caudal point inside the tube is used, i.e. the most distal point at the

<sup>1</sup>[www.esiee.fr/~couprie/Pink/doc/html/](http://www.esiee.fr/~couprie/Pink/doc/html/)

<sup>2</sup>The CT data of the porcine phantom used here are from the study detailed in Chapter 5

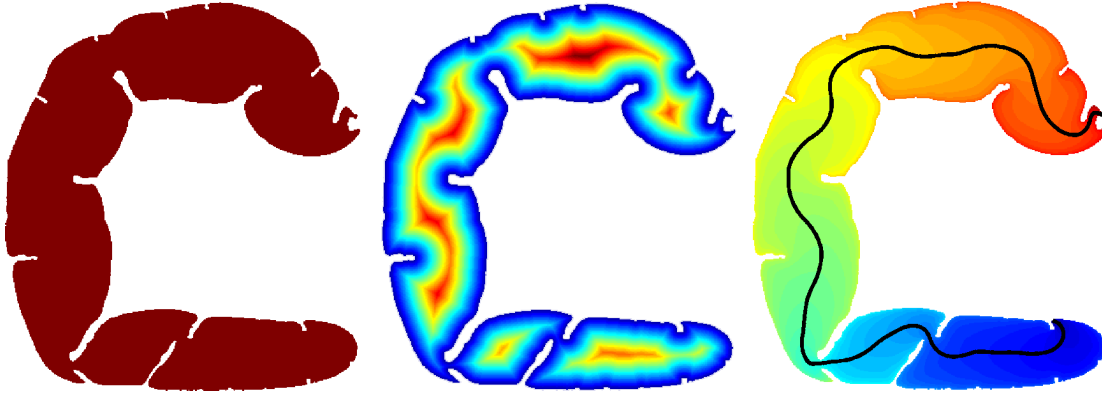


Figure 3.6: Centreline extraction using the fast marching method on a 2D CT image slice of a porcine colon phantom: the original segmentation of the colon lumen (left); a map of the distance to the endoluminal surface (middle) is used as a speed function  $F(x)$ . After wave propagation through the colon (right); the centreline path can be extracted by following the steepest gradient of the wave function (from blue to red colour coding).

anus. Otherwise the most caudal point in the colonic lumen  $L$  is used. This corresponds to the patient's anorectal junction in both projections. A point in the caecum is currently selected manually. Accurate correspondence for centreline start and end points is not essential for topological correction but improves similarity between the prone and supine rectal and caecal surface areas when conformally mapping to a cylindrical representation as described in section 3.5. Other centreline methods such as (Sadleir and Whelan, 2005) could be used as long as they guarantee the extraction of a topologically correct centreline, e. g. one that does not loop back onto itself and is therefore of genus zero.

The extracted centreline is used to generate an image  $C$  with each voxel on the centreline labelled as foreground. A topology preserving region growing algorithm is then applied to the foreground of  $C$  maintaining its topological characteristics. In this case, the centreline object is topologically equivalent to a sphere (genus zero). The region growing will thus fill  $L$  whilst leaving voxels untouched which would introduce a topological change (e.g. handles) as follows <sup>3</sup> (see Couprie et al. (2007)):

#### Topological correction procedure

Copy  $L_{\text{corr}} = L$

Repeat:

- Select a voxel  $x$  in  $C \setminus L$  such that  $I_{\text{prior}}(x)$  is minimal
- If  $x$  is “simple” for  $C$  then
  - remove  $x$  from  $C$
  - $L_{\text{corr}} = L_{\text{corr}} \cup x$

Until  $C == L_{\text{corr}}$

Result:  $L_{\text{corr}}$

Here, “simple” refers to voxels that are not essential for the the topology of the segmented object (Couprie et al., 2007), i.e. including them in the segmentation does not introduce any changes to the topology of the entire object (Bertrand, 1994).

This produces one-voxel-wide cuts through handles at the minimum distance position, resulting in a topologically correct genus-zero segmentation  $L_{\text{corr}}$  of the endoluminal colon lumen (see Fig. 3.7). Similar topology correction methods are often used for the extraction of topologically correct thickness measurements of spherical objects, such as the human brain (Cardoso et al., 2011).

<sup>3</sup>[www.esiee.fr/~talboth/ISBS/Morpho/pink/doc/skeleton\\_8c.html](http://www.esiee.fr/~talboth/ISBS/Morpho/pink/doc/skeleton_8c.html)



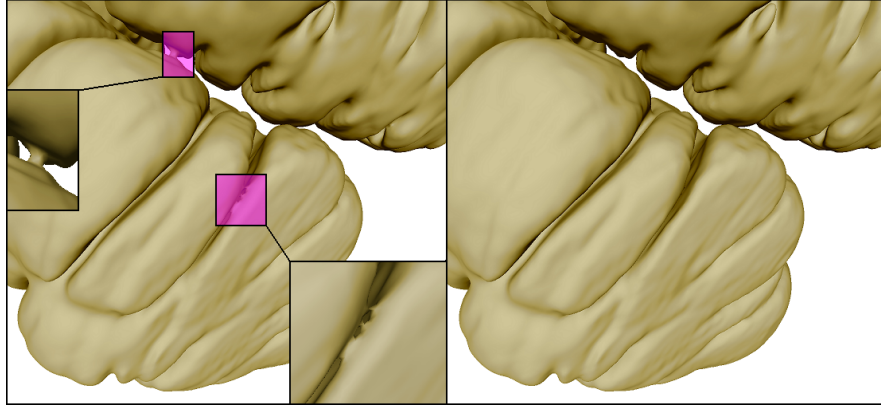


Figure 3.7: Left: Enlarged view of “handles” and an erroneous connection caused by limitation of the segmentation quality, resulting in incorrect topology. Right: the same surface region after topological correction. Comparison of the highlighted surface areas shows that the handles are now removed and the endoluminal surface is of genus zero.

### 3.4 Colonic surface extraction

The endoluminal colonic surfaces  $S$  are then modelled as triangulated meshes on the surfaces of  $L_{\text{corr}}$ , lying on the gas-tissue border in the CTC images. Those surfaces are now guaranteed to be topologically correct (i.e. of genus zero). In order to extract  $S$ , I use the marching cubes algorithm (Lorensen and Cline, 1987) on  $L_{\text{corr}}$  with a subsequent smoothing of the mesh using a standard low-pass filtering method with a *windowed sinc* function kernel (Taubin et al., 1996). This approximates a continuous surface which facilitates the convergence to a 2D parametrisation using the Ricci flow method in order to compute conformal mappings to cylinders (as described in section 3.5). Furthermore, the mesh is decimated using a quadric edge collapsing method (Hoppe, 1999) in order to reduce computation time of the subsequent conformal mapping. Loop’s subdivision method (Loop, 1987) is applied in order to achieve approximately uniformly sized and non-skewed faces over the entire surface  $S$ . However, the decimation method does not preserve the topology of the mesh and can result in a small number of topological incorrect faces. Any self-intersecting faces, complex edges and vertices are automatically detected using the utilities available in the open source software *Meshlab*<sup>4</sup> (Cignoni et al., 2008). Furthermore, any small components isolated from the colonic lumen are detected and removed. Finally, any incorrect faces are removed and the resulting holes are closed using the algorithm based on Liepa (2003), also provided by *Meshlab*.

This procedure is illustrated in Fig. 3.8 and results in a simply connected genus-zero surface  $S$  of the colonic lumen  $L_{\text{corr}}$ . For all cases used in this chapter, the surface meshes had typical edge lengths of mean (std. dev.) 3.3 (1.3) mm and about 60,000 triangles. This is typically sufficient to capture the relevant details of the colon surface (e.g. haustral folds and medium-sized polyps) without making the surface triangulation unnecessarily complex. This mesh simplification step preserves the colon surface in enough detail for smooth estimation of the surface curvatures (as described in Section 3.5.6.2) especially at the relevant features that drive the cylindrical registration accurately. Currently, these pre-processing steps do not implicitly guarantee a resulting genus-zero surface mesh. However, non genus-zero surfaces can be detected automatically using the following relationship for computing the genus  $g$ :

$$\mathcal{X} = 2 - 2g, \quad (3.3)$$

where  $\mathcal{X}$  is the *Euler characteristic* of the surface defined by the numbers of its vertices  $V$ , edges  $E$  and

<sup>4</sup>[meshlab.sourceforge.net/](http://meshlab.sourceforge.net/)

triangle faces  $F$  with:

$$\mathcal{X} = V - E + F. \quad (3.4)$$

After application of the previously described mesh correction steps, a genus-zero surface was achieved for all cases used in this thesis. Further research needs to be carried out in order to implement a surface extraction method that guarantees the generation of genus-zero representations of the endoluminal colon surface.

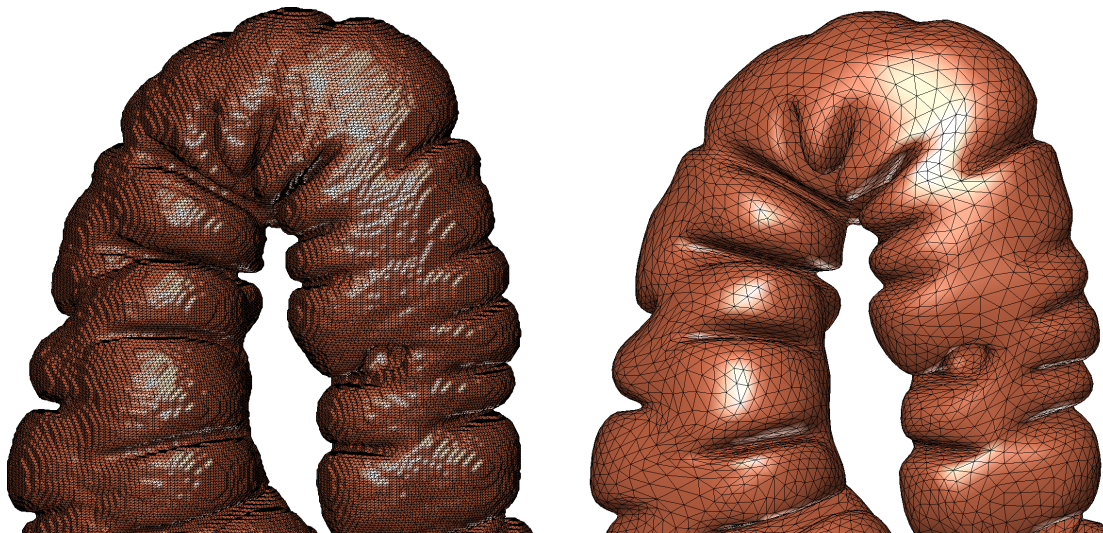


Figure 3.8: A colonic surface triangulation from the marching cubes algorithm (left). The smoothed and decimated triangulation  $S$  (right). The original marching cubes output can generate about one million triangles for a standard CTC image (left), while the mesh on the right consist of about 60,000 triangle faces. The decimation and smoothing parameters to generate the mesh on the right have been chosen such that details of the colonic surface (such as folds and polyps) are still clearly visible after simplification. However, redundant triangles in mesh representation of the colon surface have been removed.



### 3.5 Cylindrical representation of the endoluminal colonic surface

As described above, the endoluminal colon surfaces  $S$  can be modelled as piecewise-linear meshes composed of vertices  $v_i$  that are connected using triangular faces. Those surfaces  $S$  can be parametrised using a discrete conformal mapping method.

#### 3.5.1 Discrete Ricci flow

One method to parametrise arbitrary discrete surfaces was introduced by Hamilton (1982) for Riemannian geometry based on *Ricci flow*. Ricci flow deforms the surface proportionally to its local *Gaussian curvature* similar to a *heat diffusion* process until it converges towards a desired Gaussian curvature. It can be formulated for discrete surfaces such as piece-wise linear triangulated meshes (Jin et al., 2008). Rather than mapping the surface to a rectangle as with other methods (Zeng et al., 2010), the Ricci flow does not require a boundary. Many other conformal mapping methods require the definition of a boundary along the surface in order to enable a mapping of this boundary from 3D to 2D (Floater and Hormann, 2005). This typically requires selecting an arbitrary path (often the shortest path) where the surface can be sliced open. This path is then mapped onto the boundary of a rectangle in 2D which constrains how all other vertices are mapped to 2D. When computing parametrisations using Ricci flow, no requirement to define such a boundary is advantageous. Figure 3.9 illustrates this *geometry flow* on a 2-manifold of genus zero: a simply connected surface, topologically equal to a sphere, converges during the Ricci flow process to become eventually a spherical shape with constant Gaussian curvature everywhere (Jin et al., 2008). Qiu et al. (2008) were the first to apply Ricci flow to a colonic surface using volume rendering

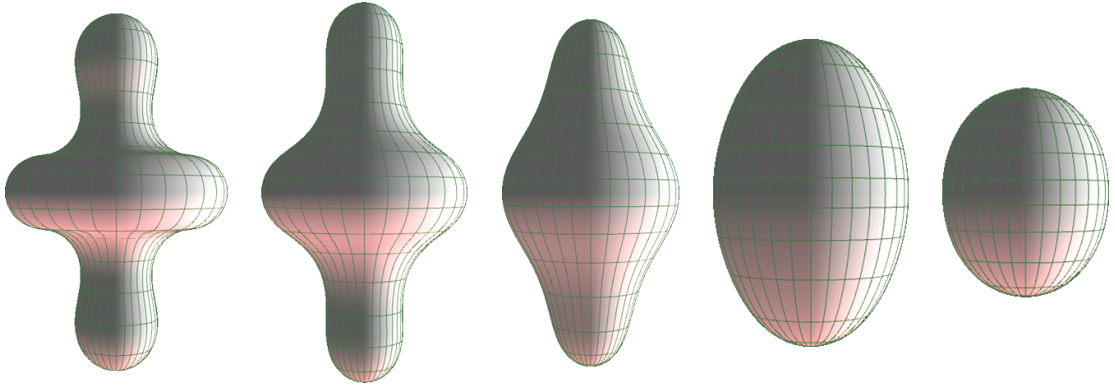


Figure 3.9: Ricci flow on a genus zero 2-manifold with topology equal to sphere, generated as a manifold of revolution. The figure shows several stages of Ricci flow at different time intervals of the *geometry flow*. All shapes are drawn at equal scale. [Generated using software provided by Rubinstein and Sinclair (2005)]

for the purpose of visualisation, and their approach is followed here with a small modification to the planar embedding (see below). Ricci flow is used to produce a conformal mapping onto a 2D plane. The discrete Ricci flow is defined in the following equation on a discrete surface mesh  $S$  with a discrete *circle packing* metric (Thurston and Milnor, 1979, Stephenson, 2005). Circle packing acts as a bridge between the continuous Riemannian setting and the discrete Ricci flow (Gu et al., 2005).

$$\frac{d\gamma_i(t)}{dt} = (\bar{K}_i - K_i)\gamma_i, \quad (3.5)$$

Here,  $\gamma_i$  is a radius, derived from the circle packing metric (see Fig. 3.10).  $K_i$  is the Gaussian curvature at vertex  $v_i$  and  $\bar{K}_i$  the desired Gaussian curvature, which can be chosen depending on the application of the Ricci flow computation. For the purpose of parametrisation of the colon surfaces  $S$  in two-

dimensional space, the target curvature  $K_i$  should be zero at all vertices  $v_i$ . For a given vertex  $v_i$  on the surface  $S$ , the discrete Gaussian curvature  $K_i$  can be computed from the angle deficit of its surrounding triangle faces  $f_{ijk}$  on a boundary-free surface  $S$ :

$$K_i = 2\pi - \sum_{f_{ijk} \in S} \theta_i^{jk} \quad (3.6)$$

Here,  $\theta_i^{jk}$  are the corner angles of the triangles  $f_{ijk}$  which include the vertex  $v_i$  as in Fig. 3.10 (right).

The background geometry of the surface has to be determined in order to compute the discrete Ricci flow. This could be Euclidean, spherical or hyperbolic. In case of the presented application, using triangulated meshes of the colonic surface, an Euclidean background geometry can be assumed.

The original genus-zero surface  $S$  also has to be converted to a surface  $SD$  of genus one for the purpose of cylindrical parametrisation of the colon surface. This means converting a sphere-like surface to a torus-like surface in order to achieve a closed surface of genus one. This step is necessary for mapping the surface onto the plane  $\mathbb{B}^2$  (Jin et al., 2008). Therefore, holes in the surface mesh are created by removing vertices and connected triangular faces closest to the previously selected caecal and rectal points. The remaining surface is doubled, inverted and glued with the original mesh onto the vertices and edges along the previously produced holes in a similar manner to the double covering technique described in Hong et al. (2006). The resulting surface  $SD$  serves then as input to the Ricci flow algorithm.

The first step of the algorithm is the approximation of an initial circle packing metric. Each vertex  $v_i$  gets a circle radius  $\gamma_i$  assigned to it. Each radius  $\gamma_i$  is defined as

$$\gamma_i = \frac{1}{m} \sum_{f_{ijk} \in F} \gamma_i^{jk}. \quad (3.7)$$

Here,  $m$  is the number of adjacent triangle faces  $F$  that share the vertex  $v_i$ .  $\gamma_i^{jk}$  is defined for each of the faces  $f_{ijk}$  of  $F$  with vertices  $i, j$  and  $k$  (see Fig. 3.10). The edge lengths  $l_{ij}$ ,  $l_{jk}$  and  $l_{ki}$  of each triangle  $f_{ijk}$  allow the computation of

$$\gamma_i^{jk} = \frac{l_{ki} + l_{ij} - l_{jk}}{2}. \quad (3.8)$$

The resulting circle packing metric for a triangulated mesh after Ricci flow convergence and embedded 2D space is shown in Fig. 3.10 (left). From the circle packing metric an initial weight factor  $\phi_{ij}$  for each edge  $e_{ij}$ , connecting  $v_i$  with  $v_j$ , can be determined using the cosine law (see Fig. 3.10 (right)):

$$l_{ij}^2 = \gamma_i^2 + \gamma_j^2 + 2\gamma_i\gamma_j \cos \phi_{ij}. \quad (3.9)$$

### 3.5.2 Gradient descent method

It can be shown that the Ricci Flow is essentially the gradient flow of a function which can be minimised using the gradient descent method (Jin et al., 2008). Convergence is guaranteed for Euclidean Ricci flow as its energies are convex and therefore have a unique minimum. Using a measure  $u_i$ , that is proportional to  $\gamma_i$  leads to the discrete Ricci flow formulation as in equation 3.10. The relationship between  $u_i$  and the circle packing radii  $\gamma_i$  is  $u_i = \log \gamma_i$  for Euclidean background geometry (Jin et al., 2008).

$$\frac{du_i(t)}{dt} = (\bar{K}_i - K_i). \quad (3.10)$$

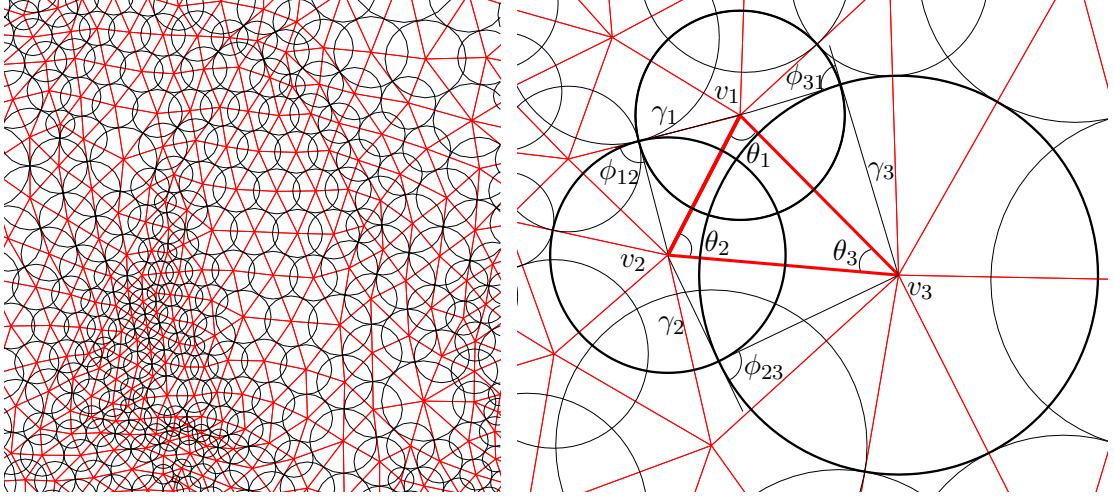


Figure 3.10: Circle packing metric on a mesh in two-dimensional space after Ricci flow convergence (left) and on an individual triangle (right). Each vertex  $v_i$  is circumscribed by a circle of radius  $\gamma_i$ , defined by the geometry of the surface mesh  $S$ . The angles  $\theta_i$  are the inside corner angles of the triangle.

This can be solved using the gradient descent method with a step factor  $\epsilon$  as in equation 3.11. Here,  $K_i$  is the current curvature at vertex  $v_i$  and  $\bar{K}_i$  is the desired curvature (zero everywhere in this case).

$$\dot{u}_i = u_i + \epsilon (\bar{K}_i - K_i), \quad (3.11)$$

The double covered surface  $SD$  can be parametrised using Ricci flow while minimising the global maximum difference error between all current  $K_i$  and  $\bar{K}_i$ ,  $E_{\max}$ . The minimisation is computed until  $E_{\max}$  converges below a pre-set value, resulting in a mesh  $P$  in  $\mathbb{R}^2$  providing two-dimensional parametrisation of each surface location on  $S$ . For all patients used in this chapter, the Ricci flow was minimised to below an error of  $E_{\max} = 1e^{-6}$ , using a step size  $\epsilon = 0.1$  in the gradient descent algorithm.

### 3.5.3 Newton's method

Faster convergence of the Ricci flow can be achieved using Newton's method (Jin et al., 2008). Using equation 3.6 and the cosine law on the circle packing metric (equ. 3.9), it can be shown that

$$K_i = 2\pi - \sum_{f_{ijk} \in S} \cos^{-1} (\gamma_i^2 + \gamma_i \gamma_j \cos \phi_{ij} + \gamma_k \gamma_i \cos \phi_{ki} - \gamma_j \gamma_k \cos \phi_{jk}). \quad (3.12)$$

Differentiation of this equation leads to  $\partial K_i / \partial u_i$  and  $\partial K_i / \partial u_j$  as follows

$$\begin{aligned} \frac{\partial K_i}{\partial u_i} &= \frac{\partial \gamma_i}{\partial u_i} \frac{\partial K_i}{\partial \gamma_i} = \gamma_i \sum_{f_{ijk} \in S} \frac{AD - BC}{A\sqrt{A^2 - B^2}} \\ \frac{\partial K_i}{\partial u_j} &= \frac{\partial \gamma_j}{\partial u_j} \frac{\partial K_i}{\partial \gamma_j} = \gamma_j \sum_{f_{ijk} \in S} \frac{AF - BE}{A\sqrt{A^2 - B^2}} \end{aligned} \quad (3.13)$$

where,

$$A = 2l_{ij}l_{ki} \quad (3.14)$$

$$B = l_{ij}^2 + l_{ki}^2 - l_{jk}^2 \quad (3.15)$$

$$C = 2(\gamma_i + \gamma_j \cos \phi_{ij}) \frac{l_{ki}}{l_{ij}} + 2(\gamma_i + \gamma_k \cos \phi_{ki}) \frac{l_{ij}}{l_{ki}} \quad (3.16)$$

$$D = 2(2\gamma_i + \gamma_j \cos \phi_{ij} + \gamma_k \cos \phi_{ki}) \quad (3.17)$$

$$E = 2(\gamma_j + \gamma_i \cos \phi_{ij}) \frac{l_{ki}}{l_{ij}} \quad (3.18)$$

$$F = 2(\gamma_i \cos \phi_{ij} - \gamma_k \cos \phi_{jk}) \quad (3.19)$$

The derivatives in equations 3.13 enable the computation of the Hessian matrix with its elements  $\partial K_i / \partial u_i$  and  $\partial K_i / \partial u_j$  in order to solve the discrete Ricci flow using Newton's method (Jin et al., 2008). A performance comparison of convergence speed using the gradient descent and Newton's method<sup>5</sup> is shown in Fig. 3.11. It can be seen that Newton's method performs faster by several orders of magnitude.

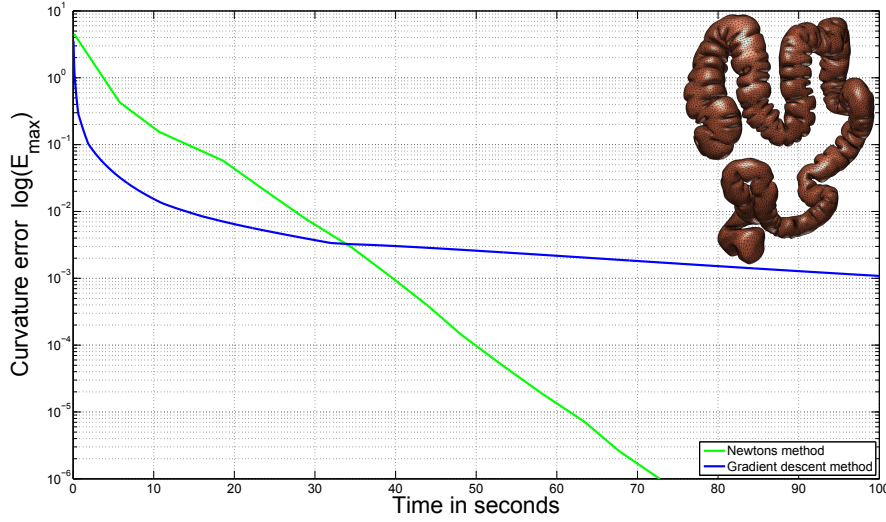


Figure 3.11: Comparison of convergence speed of Ricci flow using gradient descent (blue) and Newton's method (green) for optimisation. The curvature error is plotted in logarithmic scale. Computations were executed using a C++ implementation on a CPU with 2.13 GHz and 12.0 GB RAM. For both optimisation methods, Ricci flow was minimised until the error criterion,  $E_{\max} \leq 1e^{-6}$ , was fulfilled. In this case, the gradient descent minimisation converged after 10.5 hours computation time (off the horizontal graph limits).

### 3.5.4 Embedding into two-dimensional space

The resulting surface mesh has its local Gaussian curvatures  $K_i$  tending to zero everywhere. These curvatures are sufficient for embedding this mesh into two-dimensional space  $\mathbb{R}^2$ , using the resulting edge lengths of each triangle. Starting from an arbitrary seed face  $f_{012}$  whose coordinates are computed as

$$P(v_o) = |(0, 0), P(v_1) = (l_{01}, 0) \text{ and } P(v_2) = (l_{02} \cos \theta_0^{12}, l_{02} \sin \theta_0^{12}), \quad (3.20)$$

the remaining faces are iteratively added. This iterative addition is done in a similar manner to the planar embedding described by Jin et al. (2008), utilising the neighbourhood faces on the surface and

<sup>5</sup>I hereby acknowledge Topraj Gurung from Medicsight PLC who provided the C++ implementation of Newton's method for Ricci flow optimisation.

by computing the position of each triangle vertex, based on the intersection of two circles which have radii equal to the corresponding edge lengths. However, as  $K_i$  is not exactly zero at every vertex  $v_i$ , the resulting accumulated 2D mesh can have cracks and overlapping faces. These errors in computing the planar embedding  $P$  can be reduced if the Ricci flow converges towards smaller values of  $E_{\max}$ , but needs to be balanced against the computation time required for the Ricci flow. Segments of 2D surfaces, generated from the same endoluminal colon surface after convergence to different error levels  $E_{\max}$ , are shown in Fig. 3.12 (left, middle). However, if the errors in the planar embedding are small enough, the Ricci flow can be stopped and corresponding vertices of neighbouring triangles can be joined together by averaging their two-dimensional positions. This results in a closed 2D mesh  $P$  without discontinuities as in Fig. 3.12 (right).

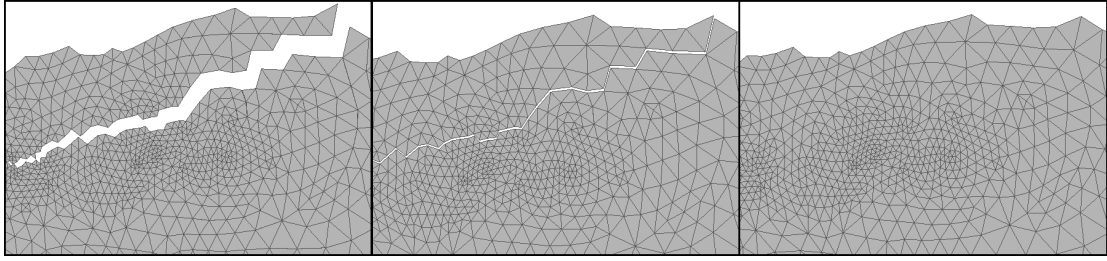


Figure 3.12: Computed planar embeddings  $P$  of the endoluminal colonic surface  $S$  with convergence errors  $E_{\max} = 1e^{-4}$  (left),  $E_{\max} = 1e^{-6}$  (middle) and the averaged planar embedding (right) with  $E_{\max} = 1e^{-6}$ .

### 3.5.5 Conformality

The conformality of the Ricci flow mapping can be seen in Fig. 3.13, showing a histogram of the ratio between original corner angles on the 3D triangles and the angles mapped to 2D. A chequerboard with right angles is mapped onto the colonic surface in order to illustrate the angle-preserving nature of the mappings. The right angles of the squares are still preserved in 3D, while the areas of the squares changes (see 2).

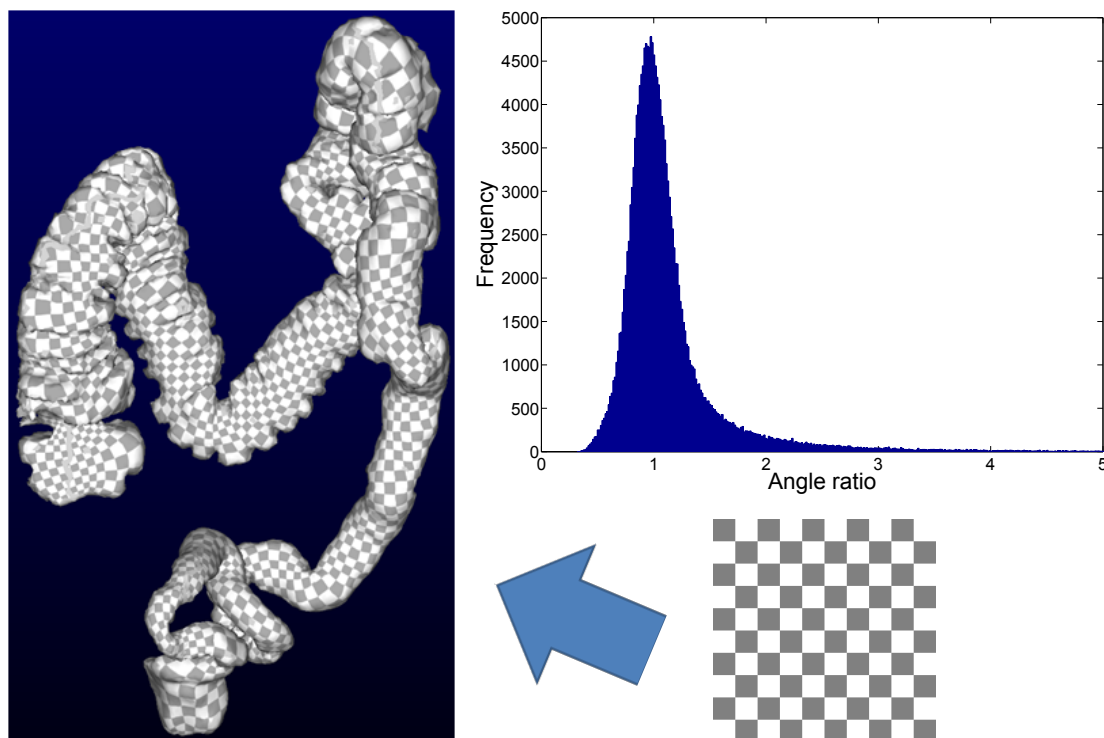


Figure 3.13: Conformality of parametrisation illustrated by mapping a chequerboard onto the colonic surface (renderings with *Alice Graphite*<sup>7</sup>). Right angles of the 2D squares are preserved in 3D. The histogram of angle ratios is concentrated around one.

<sup>7</sup>[alice.loria.fr](http://alice.loria.fr)

### 3.5.6 Generating cylindrical images

The 2D mesh  $P$  represents a regular cylinder and can be re-sampled between 0 and  $360^\circ$  to generate rectangular raster images for use in an intensity-based cylindrical registration (as illustrated in Fig. 3.14). Here, the horizontal dimension  $x$  corresponds to a distance along the colon from caecum to rectum and the vertical dimension  $y$  to the angular position around the circumference of the colon.

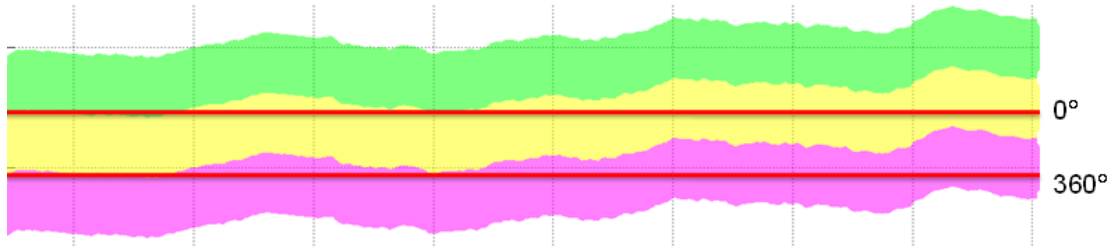


Figure 3.14: Sampling the unfolded mesh to generate rectangular raster-images  $I$  suitable for image registration. Each band represents a shifted copy of the planar embedded meshes  $P$  which are sampled between the horizontal lines to cover a full  $360^\circ$  of endoluminal colon surfaces  $S$ .

#### 3.5.6.1 Sampling the parametrisation

Sampling curvature information onto the parametrisation  $P$  results in raster-images  $I$  for supine and prone endoluminal colon surfaces as shown in Fig. 3.15 (top, middle). The top and bottom edges of the images  $I$  correspond to the same line along the endoluminal surfaces  $S$ , running from caecum to rectum. Thus, these images  $I$  represent the endoluminal colonic surface as cylinders. The chosen resolution ratio of 16 between  $n_x = 4096$  and  $n_y = 256$  corresponds approximately to the ratio between the length of the centreline and the average circumference around the colon. For all un-collapsed cases used in this chapter, the average length was 1.7 m and the average circumference was 108 mm, giving a ratio of 15.7.

For this resolution  $n_x \times n_y$ , any two neighbouring pixels correspond to 3D points which are 0.27 (standard deviation 0.29) mm apart on average, with 99% of neighbouring pixels being less than 1.2 mm apart. This suggests that, even though the circumference of the colon changes along its length, the distortion introduced by mapping  $S$  onto a cylindrical image  $I$  with constant width is sufficiently small enough over most of the endoluminal colon surface. This allows a fine alignment of the prone and supine surfaces within the targeted registration accuracy ( $\ll 10$  mm see Chapter 1). Any 3D surface location on  $S$  can be computed with even higher accuracy using bi-linear interpolation between neighbouring pixel values of the cylindrical images. Furthermore, my experiments show that the distortion introduced by this conformal mapping step can be successfully recovered by the cylindrical non-rigid registration (as described in section 3.6).

#### 3.5.6.2 Curvature estimation

Each pixel of  $I$  has an intensity value assigned to it in order to drive a non-rigid registration in cylindrical space. These values are estimated from local curvature measures estimated on each vertex  $v_i$  of the three-dimensional surface mesh, representing  $S$ . Curvature computation theoretically requires surfaces that are twice differentiable. However, the colon surface  $S$  is represented with a piecewise linear mesh, consisting of vertices and triangles (faces). Many curvature computation approaches fit a local surface patch around each vertex in order to allow the computation of two local derivations. However, this study follows the approach of Batchelor et al. (2002) in the proposed method and extract the curvature measures directly from the geometric data contained in the triangulated mesh  $S$  in  $\mathbb{R}^3$ . This curvature computation in this study used the C++ implementation of VTK<sup>8</sup> (Schroeder et al., 2001).

<sup>8</sup>[www.vtk.org](http://www.vtk.org)



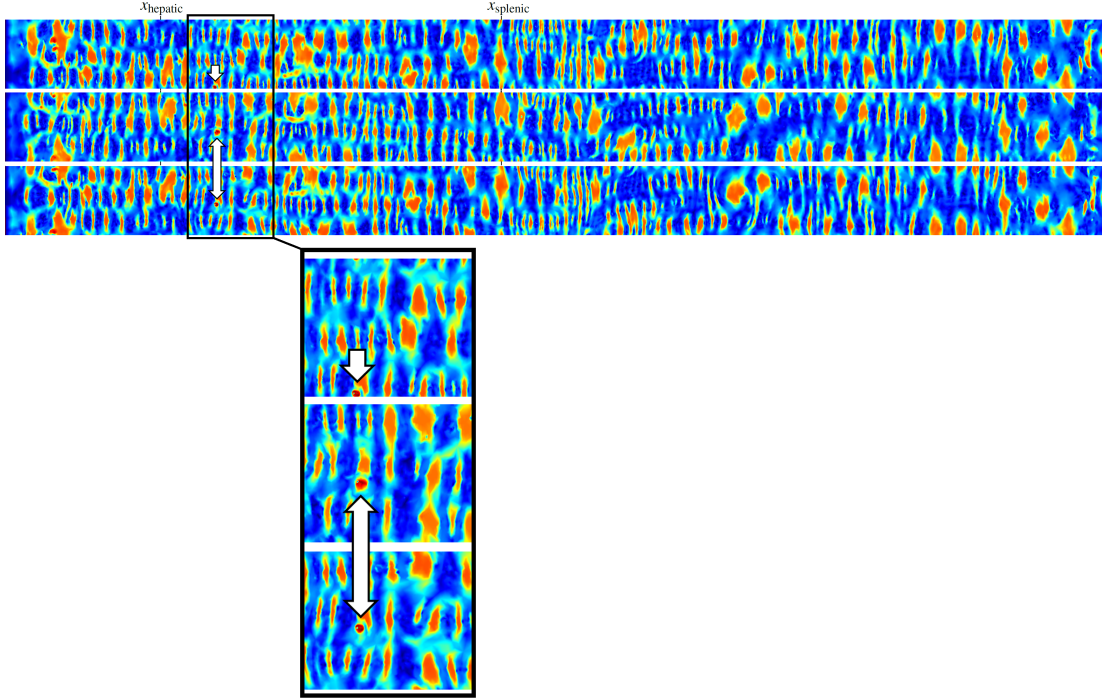


Figure 3.15: Supine (top), prone (middle) and deformed supine deformed to match prone (bottom) raster images of patient 7 where each pixel has the value of the corresponding shape index ( $SI$ , see Equation 3.25) computed on the endoluminal colonic surface. The  $x$ -axis is the position along the colon, while the  $y$ -axis is its circumferential location. The  $x$ -positions for the detected hepatic and splenic flexures are marked as  $x_{\text{hepatic}}$  and  $x_{\text{splenic}}$ . The location of a polyp is marked before (top) and after registration (middle, bottom) and in a zoom-in section. Corresponding 3D renderings are illustrated in Fig. 3.1.

Any point on the continuous surface can be intersected by an infinite number of geodesic lines along that surface. Each line has a particular curvature value at this local intersection point. Intuitively, there will be two intersecting lines with minimum and maximum curvatures. These are called the *principal curvatures*  $\kappa_{\min}$  and  $\kappa_{\max}$  (see Fig. 3.16 for illustration). If  $\kappa_{\min} = \kappa_{\max} \neq 0$ , the surface is locally a sphere; and if both are zero, the point lies on the plane. The principal curvatures can be used to derive higher order curvature measures such as mean curvature  $H$  and Gaussian curvature  $K$ . The classical definitions of  $H$  and  $K$  are:

$$\begin{aligned} H &= \frac{\kappa_{\max} + \kappa_{\min}}{2} \\ K &= \kappa_{\max} \kappa_{\min}. \end{aligned} \quad (3.21)$$

Having computed both measures, the maximum and minimum principal curvatures can be derived as:

$$\begin{aligned} \kappa_{\min} &= \frac{-H - \sqrt{H^2 - K}}{2} \\ \kappa_{\max} &= \frac{-H + \sqrt{H^2 - K}}{2}. \end{aligned} \quad (3.22)$$

As introduced in Equation 3.6, the Gaussian curvature for a given vertex  $v_i$  can be computed from the angle deficit in the discrete setting:

$$K_i = 2\pi - \sum_{f_{ijk} \in S} \theta_i^{jk} \quad (3.23)$$



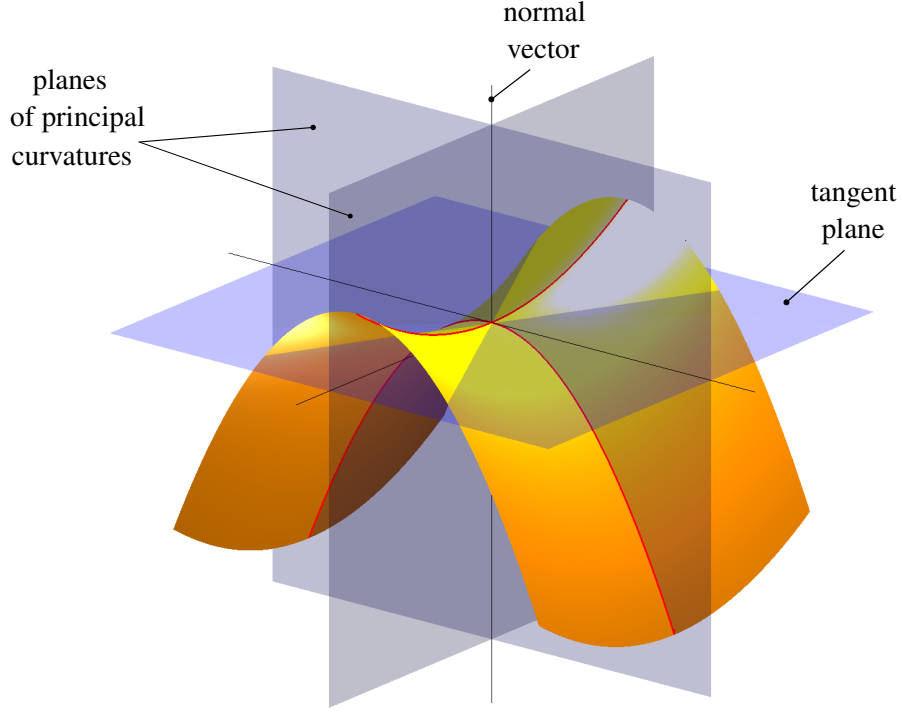


Figure 3.16: Normal planes, defining the principal curvatures on a saddle surface.

In the discrete setting, the mean curvature can be computed for each edge  $e$  as given by (Castellano, 1999):

$$H(e) = \frac{l_{ij} \times \alpha_{ij}}{A}. \quad (3.24)$$

Here,  $l_{ij}$  is the length of the edge  $e_{ij}$  with the dihedral angle  $\alpha_{ij}$  at this edge being the angle between the normals of the two faces adjacent to  $e_{ij}$ .  $A$  is  $1/3$  of the area of the two faces sharing  $e_{ij}$ , see Fig. 3.17 for an example. This measure describes the angular change of surface normal orientations when the particular edge is crossed and would be zero if both faces lie on the plane  $\mathbb{E}^2$ . The mean curvature  $H$  at a vertex  $v_i$  is then just the average of  $H(e)$  at each edge containing that vertex. More detailed descriptions of the derivative of curvatures at the vertices can be found in Banchoff (1967) and Brehm and Kühnel (1981).

From the local surface curvature measures, the shape index ( $SI$ ) can be computed. The shape index  $SI$  is a normalised shape descriptor based on local curvature (see Fig. 3.18) and defined as

$$SI \equiv \frac{1}{2} - \frac{1}{\pi} \arctan \left( \frac{\kappa_{\max} + \kappa_{\min}}{\kappa_{\max} - \kappa_{\min}} \right), \quad (3.25)$$

where the principal curvatures  $\kappa_{\max}$  and  $\kappa_{\min}$  are the maximum and minimum curvatures computed on the surface  $S$  (Koenderink, 1990).

The shape index represents the local topological shape of the surface  $S$  (as illustrated in Fig. 3.18). It is a good scalar measure for describing the local structures on colonic surfaces, such as haustra, folds and polyps. It also has been used successfully for automated detection of colonic polyps (Yoshida and Nappi, 2002).

The advantage of using shape index as a measure to describe the prone and supine colonic surfaces is illustrated in Fig. 3.19 on a local set of simulated corresponding folds.

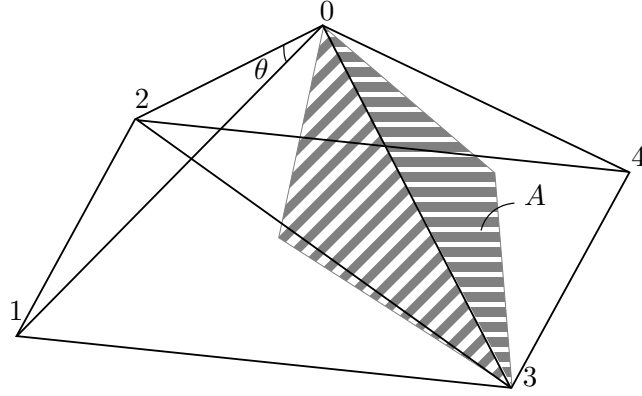


Figure 3.17: Computation of surface curvature: the base  $\{1, 2, 3, 4\}$  is a square with side length of 1. The vertex 0 is centred above the square at a height of 0.5. Therefore, the area of each side triangle is  $\sqrt{2}/4$  and the angle  $\alpha$  is  $2 \arctan \sqrt{2}/2$  at each face adjacent to  $v_0$ . Hence,  $K_0 = 2\pi - 4\theta \approx 1.3593$ . The area  $A$  is used for computation of the mean curvature  $H(e)$  (see equation 3.24.  $A$  is  $1/3$  of the area of the two faces sharing  $e_{ij}$ . [Figure and text based on Batchelor et al. (2002) and Castellano (1999)].

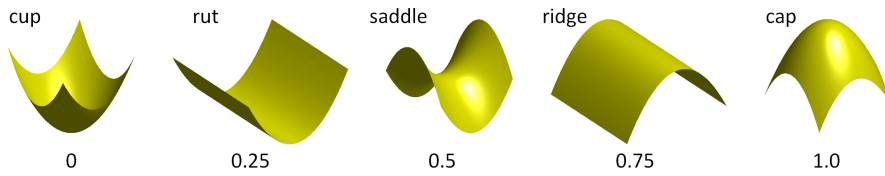


Figure 3.18: The shape index  $SI$  is a normalised shape measurement to describe local surface structures [Figure based on (Yoshida and Nappi, 2002)].

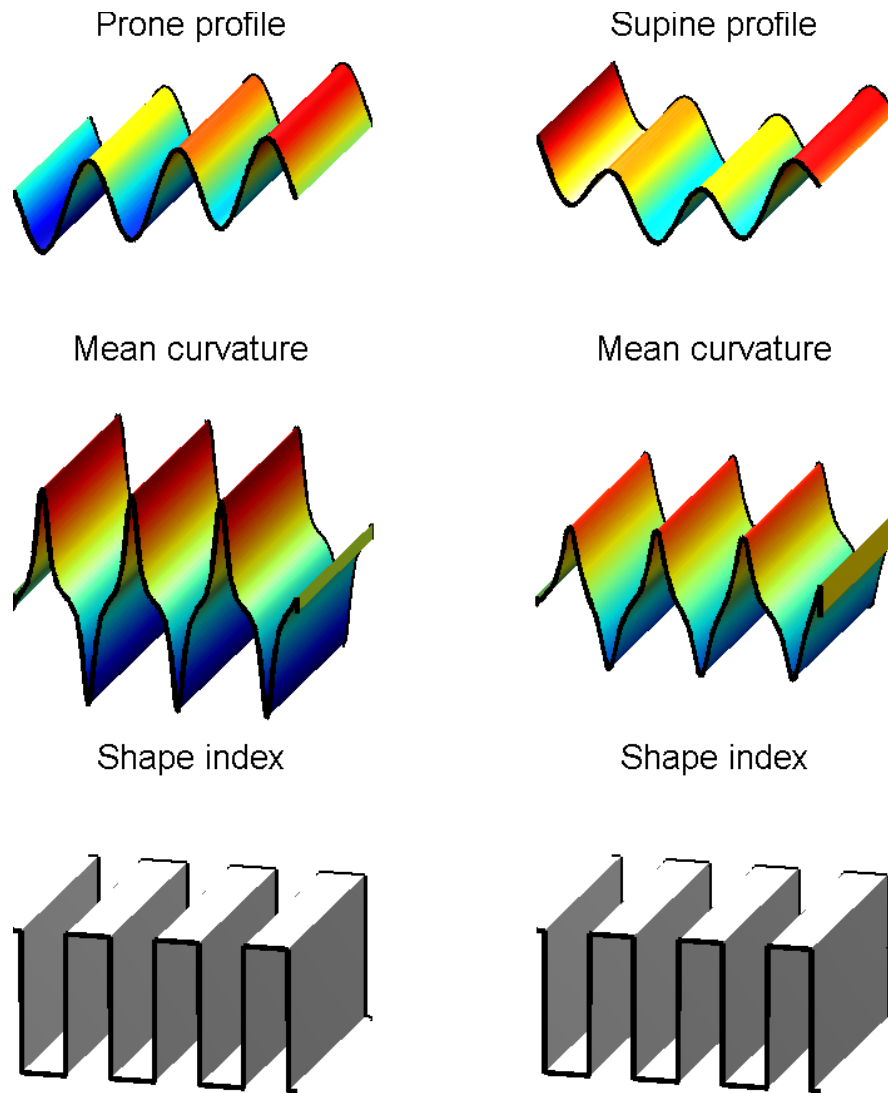


Figure 3.19: A simulated profile of three anatomically corresponding haustral folds of the prone and the supine colonic surface. The folds move markedly between both views. While the mean curvature varies markedly between prone and supine, the shape index profile is virtually identical and therefore invariant to these changes. In this example, I assume the profiles to be ‘perfect ridges’. Therefore, the shape index instantly steps between 0.25 (*rut*) and 0.75 (*ridge*) as one of the principal curvatures will always be zero.

### 3.5.6.3 Interpolation of pixel values

Now, the pixel values of the cylindrical raster images  $I$  are estimated using interpolation between the curvature values that were computed at the each vertex positions in  $\mathbb{R}^3$ . Each 3D vertex maps to a 2D location on the parametrisation  $P$  in  $\mathbb{R}^2$  using the conformal mapping described before. A third value is assigned to each vertex in  $\mathbb{R}^2$  that is equal to the local curvature, measured at that vertex. This allows the computation of the curvature values (and  $SI$ ) at each 2D pixel location of the cylindrical images using linear interpolation. In order to determine within which 2D triangle a pixel lies, a spatial search is performed using a *uniform-level Octree subdivision* of the mesh<sup>9</sup>. This interpolation method is illustrated in Fig. 3.20.

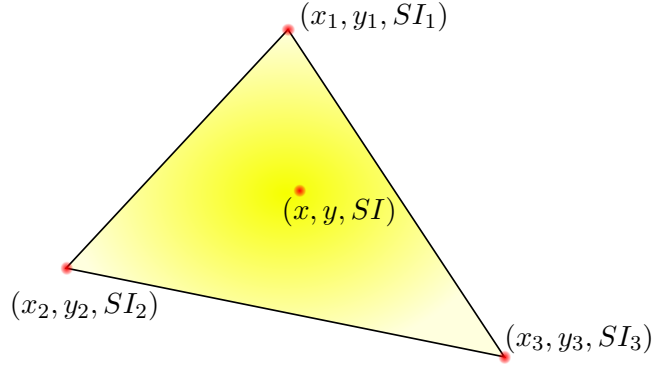


Figure 3.20: Interpolation of pixel values on a 2D triangle. The value  $SI$  at a pixel position  $(x, y)$  can be derived from the  $SI_1$ ,  $SI_2$  and  $SI_3$  (computed at the 3D vertices) as  $SI = Ax + By + C$ . It is known that  $SI_1 = Ax_1 + By_1 + C$ ,  $SI_2 = Ax_2 + By_2 + C$  and  $SI_3 = Ax_3 + By_3 + C$ . Hence,  $A$ ,  $B$  and  $C$  can be computed by solving a system of three equations and hence computing  $SI$ .

After interpolating the intensity value at each pixel location, corresponding features, like haustral folds (see 1) or the teniae coli (three “lines” running horizontally between haustral folds) are clearly visible in both images of Fig. 3.15 (top, middle). The following flow chart in Fig. 3.21 summarises the process of generating cylindrical raster images that represent the entire colonic surface as described in this Chapter. These images are now non-rigidly aligned using a cylindrical intensity-based registration method which will establish the full spatial correspondence between the prone and supine endoluminal colon surfaces  $S_p$  and  $S_s$ .

---

<sup>9</sup>My implementation uses *vtkCellLocator* from the *VTk* library ([www.vtk.org](http://www.vtk.org))

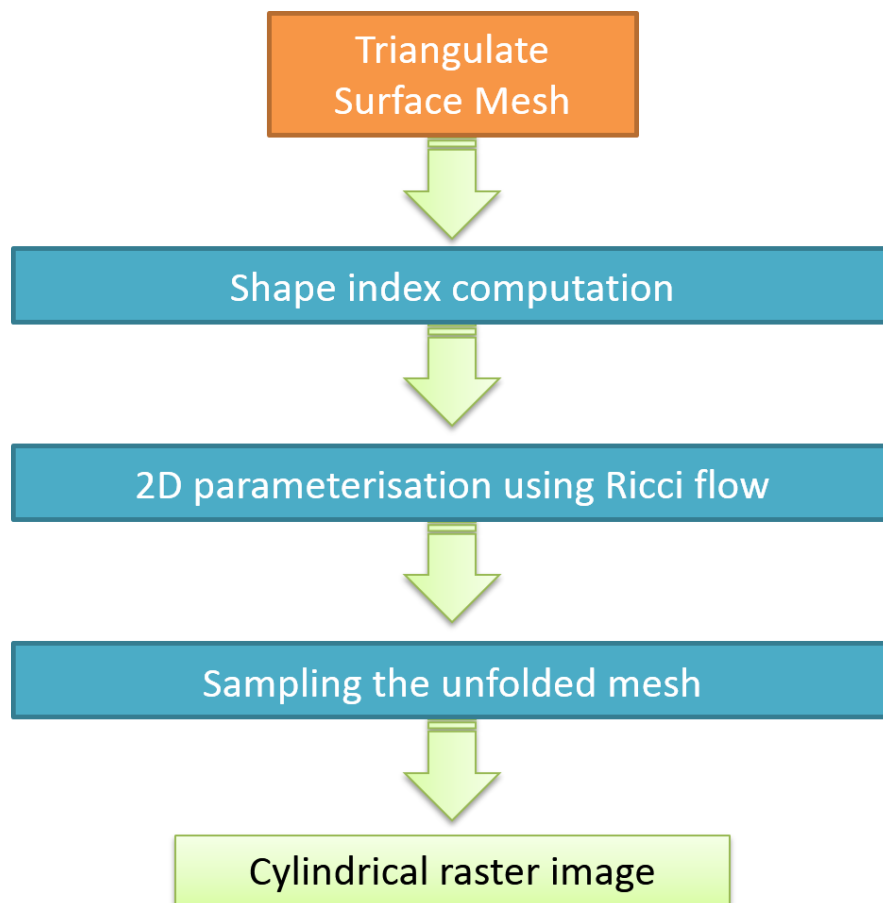


Figure 3.21: Flow chart illustrating the process of generating cylindrical raster images that represent the entire colonic surface: after extracting the triangulated surface mesh representing the colonic surface, the shape indices are computed on the 3D surface based on local discrete curvatures (see Sec. 3.5.6.2). In a next step, the mesh is parametrised in 2D using Ricci flow (see Sec. 3.5.1). Then, the 2D parametrisation is sampled on a regular pixel raster covering the entire cylindrical space (see Sec. 3.5.6). The shape index value at each pixel location is interpolated using linear interpolation (see Sec. 3.5.6.3).

### 3.6 Establishing spatial correspondence between prone and supine datasets

The two cylindrical representations of the prone and supine cylindrical surfaces are now in the same 2D domain, however, local anatomical structures are still misaligned. Non-rigid image registration can be used to align those local anatomical structures accurately. In order to provide good initialisation for the registration algorithm, the corresponding surface points at the hepatic flexure ( $hf_{p/s}$ ) and splenic flexure ( $sf_{p/s}$ ) are used for initialisation. The 2D parametrisations are linearly scaled between both flexures  $x_{\text{hepatic}}$  and  $x_{\text{splenic}}$  along the  $x$ -axis. The flexures are detected based on local maxima of the  $z$ -coordinate of the centreline. The hepatic flexure can be detected as the first local maximum, coming from the caecum, to be above  $t_{\text{hepatic}}$  of the maximum centreline  $z$ -coordinate. The splenic flexure is detected as the local maximum which is the first to lie above  $t_{\text{splenic}}$  of the maximum centreline  $z$ -coordinate, relative to the rectum. The landmark matches at the hepatic and splenic flexures in prone and supine are illustrated in Figure 3.22. In order to provide robustness against wrongly detected flexure correspondences, any flexures are discarded if their centreline distances vary by greater than  $t_{\text{var}}$  between prone and supine datasets. Based on empirical experiments, good parameters were found to be  $t_{\text{hepatic}} = 60\%$ ,  $t_{\text{splenic}} = 95\%$  and  $t_{\text{var}} = 5\%$ . These values were used for all cases in this chapter. The corresponding  $x$ -positions for the hepatic and splenic flexures are marked as  $x_{\text{hepatic}}$  and  $x_{\text{splenic}}$  in Fig. 3.15 after linear scaling along the  $x$ -direction. The detection and scaling process is illustrated in the two following Figures 3.22 and 3.23.

#### 3.6.1 Cylindrical B-spline registration

The cylindrical representations are used to generate shape index images  $I_p$  and  $I_s$ , where each pixel corresponds to a position on the colon surface in 3D. The alignment between  $I_p$  and  $I_s$  is established using a cylindrical non-rigid B-spline registration method. This method is developed from the 3D free form deformation based registration of Rueckert et al. (1999) with the fast implementation provided by Modat et al. (2010) in the open-source package *NiftyReg*<sup>10</sup>.

A standard (non-cylindrical) 2D cubic B-Splines deformation model uses a lattice of control points  $\{\vec{\phi}\}$ . The spacing between each control point is uniform and noted as  $\delta_x$  and  $\delta_y$  along the  $x$ - and  $y$ -axis respectively. For each pixel  $\vec{x}$  in the domain  $\Omega$  of the target image, the deformation  $\mathbf{T}_{2D}(\vec{x})$  can be computed as:

$$\mathbf{T}_{2D}(\vec{x}) = \sum_{i,j} \beta^3 \left( \frac{x}{\delta_x} - i \right) \times \beta^3 \left( \frac{y}{\delta_y} - j \right) \times \vec{\phi}_{ij}, \quad (3.26)$$

where,  $\{x, y\}$  indexes each pixel and  $\{i, j\}$  are the indices of a control point in  $\{\vec{\phi}\}$ . The cubic B-Spline function  $\beta^3$  is defined in one dimension as:

$$\beta^3(x) = \begin{cases} \frac{2}{3} - |x|^2 + \frac{1}{2}|x|^3, & |x| < 1 \\ -\frac{1}{6}(|x| - 2)^3, & 1 \leq |x| < 2 \\ 0, & |x| \geq 2 \end{cases} \quad (3.27)$$

In order to account for the cylindrical nature of the registration problem, the transformation model can be modified in a similar fashion to Huysmans et al. (2010), who use cylindrical B-splines to find correspondences for generating active shape models of tubular surfaces or similar to Metz et al. (2011) who use them for motion estimation in respiratory cycles. For standard B-spline registrations the control point grid must extend outside the image by at least one control point spacing in each direction so that the deformation is defined over the whole image. For the cylindrical registrations, the control point grid

<sup>10</sup> [sourceforge.net/projects/niftyreg/](https://sourceforge.net/projects/niftyreg/), I hereby acknowledge the first implementation of this cylindrical B-spline registration by Jamie McClelland based on the *NiftyReg* registration package.

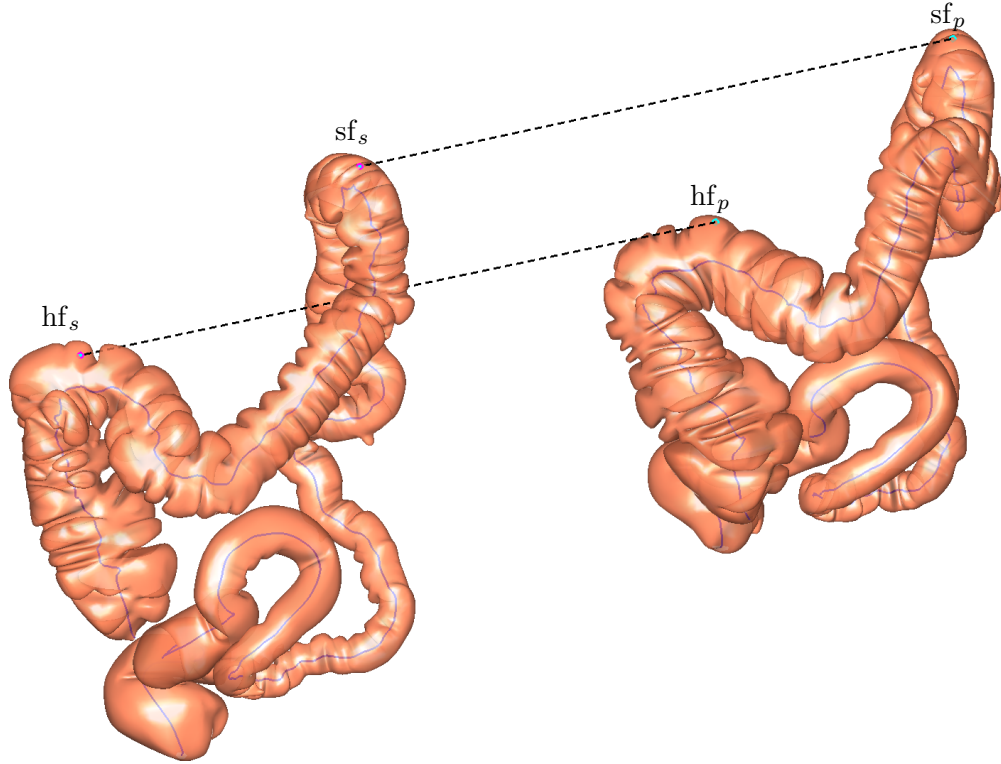


Figure 3.22: The hepatic flexure is detected as the first local maximum, coming from the caecum, to be above  $t_{\text{hepatic}}$  of the maximum centreline z-coordinate. The splenic flexure is detected as the local maximum which is the first to lie above  $t_{\text{splenic}}$  of the maximum centreline z-coordinate, relative to the rectum. Both pairs of landmark matches can be used to initialise the registration by linear scaling the cylindrical images between the landmark matches as illustrated in Fig.3.23. The hepatic and splenic flexures are marked as  $hf_{p/s}$  and  $sf_{p/s}$  respectively ( $p/s$  denotes prone and supine, respectively)

does not extend outside the images in the  $y$ -direction (around the cylinder). Instead, when an extended control point is required, the corresponding value is taken from the opposite side of the grid. Therefore the equation for the cylindrical deformation is:

$$\mathbf{T}_{\text{cyl}}(\vec{x}) = \sum_{i,j} \beta^3 \left( \frac{x}{\delta_x} - i \right) \times \beta^3 \left( \frac{y}{\delta_y} - j \right) \times \vec{\phi}_{ik}, \quad (3.28)$$

where the control point is indexed by  $k$  instead of  $j$ , and  $k$  is defined as:

$$k = \begin{cases} j + N_{\delta_y} & \text{if } j < 0 \\ j & \text{if } 0 \leq j < N_{\delta_y} \\ j - N_{\delta_y} & \text{if } j \geq N_{\delta_y} \end{cases} \quad (3.29)$$

Here,  $N_{\delta_y}$  is the number of control points in the  $y$ -direction. This definition is equal to  $k = j \pmod{N_{\delta_y}}$ . The concept behind making the control point grid cylindrical is illustrated in Fig. 3.24. In addition any displacement in the  $x$ -direction (along the colon) at each end of the image is prevented by fixing the  $x$ -displacement of the first and last three control points to be zero. This ensures that the ends of the images are aligned with each other, while still allowing for twists around the colon.

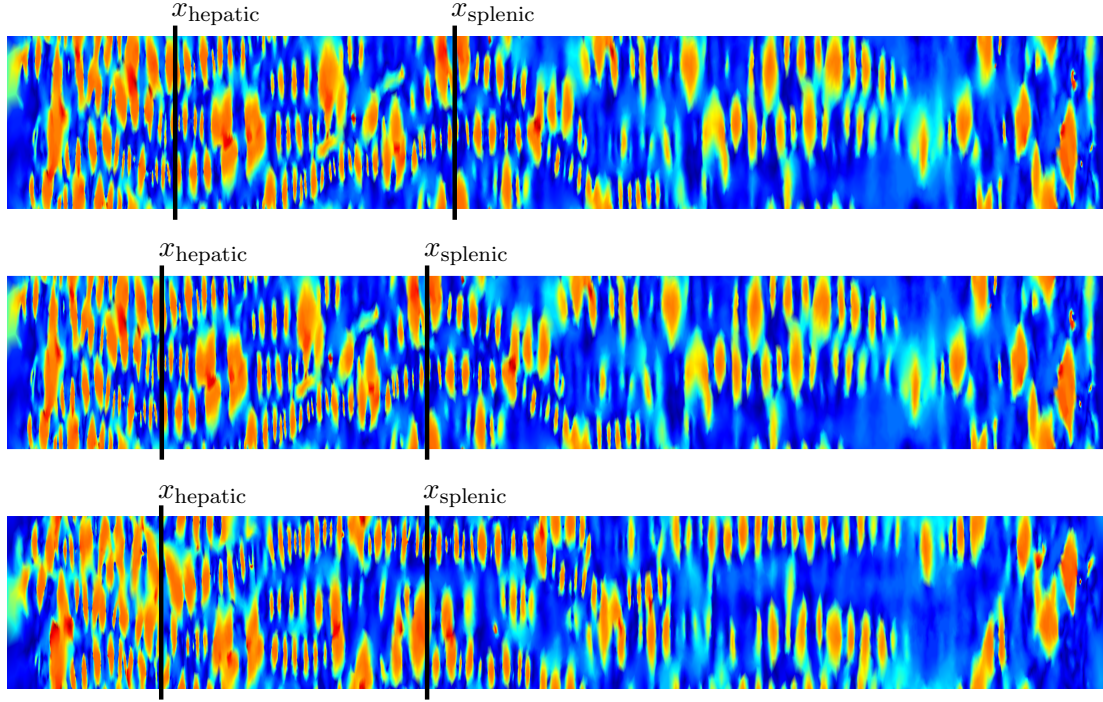


Figure 3.23: Both pairs of prone and supine landmark matches are used to initialise the registration by linear scaling along the  $x$ -direction of the cylindrical images between the landmark matches. The corresponding  $x$ -positions for the hepatic and splenic flexures are marked as  $x_{\text{hepatic}}$  and  $x_{\text{splenic}}$  in the figure before (top) and after linear scaling (middle) of the source image; the target cylindrical image is shown at the bottom.

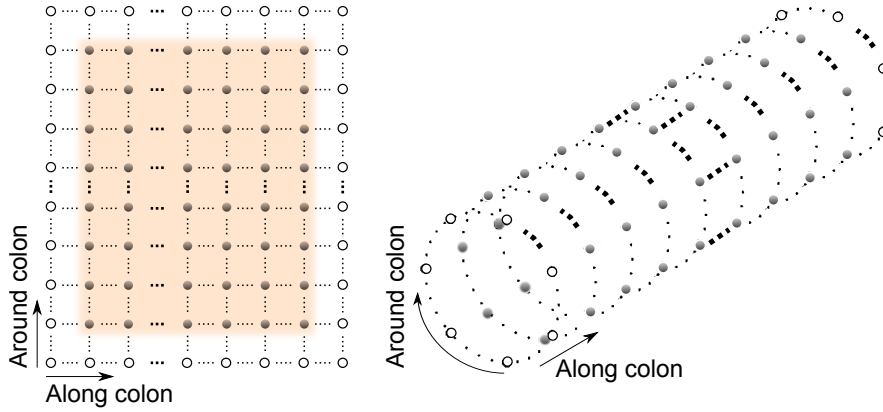


Figure 3.24: Standard lattice of control points  $\{\vec{\phi}\}$  for a 2D cubic B-Splines deformation model (left): the control point grid extends outside the image by one control point spacing in each direction. The cylindrical control points only extend in the ‘Along colon’ direction ( $x$ ) and loop around in  $y$  direction. The deformation is therefore cylindrical.

### 3.6.2 Objective function

The two cylindrical shape index images  $I_p$  and  $I_s$  are aligned by finding the non-rigid transformation which maximises the objective function:

$$\mathcal{O}(I_p, I_s(\mathbf{T}_{\text{cyl}}); \{\vec{\phi}\}) = (1 - \lambda - \mu) C_{\text{similarity}}(I_p, I_s(\mathbf{T}_{\text{cyl}})) - \lambda C_{\text{smooth}}(\mathbf{T}_{\text{cyl}}) - \mu C_{\text{areapres}}(\mathbf{T}_{\text{cyl}}) \quad (3.30)$$



which combines a similarity measure,  $C_{\text{similarity}}$ , and two penalty terms,  $C_{\text{smooth}}$  and  $C_{\text{areapres}}$ , weighted against each other by the user-specified weights  $\lambda$  and  $\mu$ . The similarity measure used was the mean squared differences (*MSD*)

$$C_{\text{similarity}} = -\text{MSD} = -\frac{1}{N} \sum_{\vec{x} \in \Omega} [I_p(\vec{x}) - I_s(\mathbf{T}_{\text{cyl}}(\vec{x}))]^2, \quad (3.31)$$

where  $N = n_x \times n_y$  is the number of pixels in the cylindrical images.

Two constraint terms were used to try and prevent unrealistic deformations while registering both images. The bending energy describes the smoothness of the deformation and is defined as:

$$C_{\text{smooth}} = \frac{1}{N} \sum_{\vec{x} \in \Omega} \left( \left| \frac{\partial^2 \mathbf{T}_{\text{cyl}}(\vec{x})}{\partial x^2} \right|^2 + \left| \frac{\partial^2 \mathbf{T}_{\text{cyl}}(\vec{x})}{\partial y^2} \right|^2 + 2 \left| \frac{\partial^2 \mathbf{T}_{\text{cyl}}(\vec{x})}{\partial xy} \right|^2 \right), \quad (3.32)$$

This bending energy formulation is the analogy of the energy needed to bend a thin metal plate and acts as a regulariser of the transformation. The bending energy will be zero for any affine transformations. Therefore this penalty term only affects non-affine transformations (Rueckert et al., 1999).

The area-preserving penalty term discourages large expansions/contractions, and is defined as:

$$C_{\text{areapres}} = \frac{1}{N} \sum_{\vec{x} \in \Omega} [\log(\det(\text{Jac}(\mathbf{T}_{\text{cyl}}(\vec{x}))) )]^2 \quad (3.33)$$

Here, the area change of one pixel is computed using the determinant of the Jacobian matrix:

$$\det(\text{Jac}(\mathbf{T}_{\text{cyl}}(\vec{x}))) = |\text{Jac}(\mathbf{T}_{\text{cyl}}(\vec{x}))| = \begin{vmatrix} \frac{\partial \mathbf{T}_{\text{cyl}_x}(\vec{x})}{\partial x} & \frac{\partial \mathbf{T}_{\text{cyl}_x}(\vec{x})}{\partial y} \\ \frac{\partial \mathbf{T}_{\text{cyl}_y}(\vec{x})}{\partial x} & \frac{\partial \mathbf{T}_{\text{cyl}_y}(\vec{x})}{\partial y} \end{vmatrix} \quad (3.34)$$

In addition, folding is prevented from occurring by introducing a folding correction scheme performed concurrently with the registration process (Modat et al., 2010). For each voxel that corresponds to a negative Jacobian determinant, its influence on its neighbouring control points is computed. The folding correction scheme then changes the control point positions until the Jacobian determinant value is positive.

Both, the smoothness term  $C_{\text{smooth}}$  and  $C_{\text{areapres}}$  term need to be traded against the similarity term  $C_{\text{similarity}}$ , using the user-specified weights  $\lambda$  and  $\mu$ . Weights that are too large might prevent the cylindrical registration from capturing complex deformations. On the other hand, weights that are specified too small might allow for too many unrealistic deformations in order to optimise the similarity metric. (Rueckert et al., 1999) In order to find optimal parameters for the B-spline registration, a sub-set of the available cases was used for tuning the registration algorithm parameters. The following reported optimal parameters were found empirically by visual examination of the alignment of anatomical structures such as haustral folds and by quantitative assessment of the alignment of polyps after registration.

A coarse-to-fine approach was used in order to capture first the largest deformations and then the smaller differences between both input images. This is achieved with a seven-level multi-resolution approach using  $I_p$  as target and  $I_s$  as source. Both the image and B-spline control point grid resolutions are doubled with increasing resolution levels. The final resolution level uses images with  $4096 \times 256$  ( $n_x \times n_y$ ) pixels. The control point spacing  $\delta$  is 16 pixels in both directions at each resolution level. The gradient of the cost function is smoothed after each iteration, using a Gaussian kernel with a standard deviation of 3 pixels. Gaussian smoothing of the 2D images is applied at each resolution level with a standard deviation of two pixels. The objective function weights are set to  $\lambda = 1e^{-4}$  and  $\mu = 1e^{-4}$ . These parameters were found to recover the majority of the deformation between the two images for the data used for tuning, while preventing unrealistic deformations from occurring, e. g. the stretching of

one haustral folds over several folds in the other cylindrical image.

The cylindrical B-spline registration results in a continuous transformation around the entire endoluminal colon surface and allows the mapping  $\mathbf{T}_{cyl}(\vec{x})$  between  $P_p$  and  $P_s$  in cylindrical space. From this mapping it is straightforward to determine the full 3D mapping  $\mathbf{T}_{ps}$  between  $S_p$  and  $S_s$  using  $f_p$  and  $f_s$  as shown in Fig. 3.1. Figure 3.25 illustrates the registration result for a section of the colon, applying the deformation field at the final control point spacing level, which has been used to deform a regular grid.

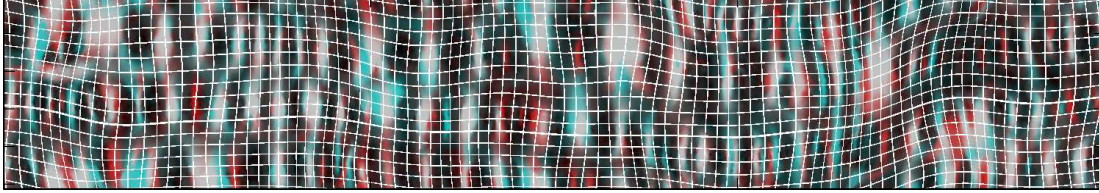


Figure 3.25: Deformation field on a section of the colon at the final control point spacing level. The deformation field has been used to deform a regular grid and been overlaid on top of the deformed supine  $T_{cyl}(I_s)$  (red) and target  $I_p$  (cyan) cylindrical images. Red and cyan pixels of the same intensity are displayed in grey after registration.

### 3.7 Dealing with collapsed colons

Despite adequate colonic insufflation, short segments of colonic collapse commonly occur, particularly when the patient changes position from supine-to-prone. Furthermore, residual colonic fluid due to sub-optimal bowel preparation can occlude the colonic lumen, resulting in more than one colonic segment for 3D reconstruction of the endoluminal surfaces. If the colon is locally severely under-distended, the segmentation method described in section 3.2 can lead to disconnected colon segments. Most 3D workstations allow the radiologist to manually choose the order in which the centreline connects these disconnected colonic segmentations. Fig. 3.26 shows a patient's colon with a collapse in the descending colon (DC) in the supine position. While some centreline-based methods can handle local colonic collapse, they only provide a 1D correspondence along the centreline. To the best of my knowledge, only Suh and Wyatt (2008) have attempted a 3D registration of images where the colon is collapsed in only one view but report limited accuracy.

If the collapsed segment is relatively straight, its length can be estimated as the Euclidean distance between the centrelines of the well-distended segments. The length of each well-distended segment is estimated based on the length of its centreline. More accurate estimations of the length of a collapsed segment could be achieved utilising segmentations of the colonic wall (Van Uitert et al., 2006, Lu et al., 2012, Näppi and Yoshida, 2007) in order to extract the centrelines of the collapsed regions of the colon as achieved in (Van Uitert and Summers, 2007). The beginning and end points, as well as the correct order of each segment, were selected manually in this study. The angular alignment between each segment was determined as the shift around the  $y$ -axis which minimises the 3D distance between points with the same angular orientation on either side of the collapse. The cylindrical images  $I$  of such a case (patient 17) are shown in Fig. 3.27. It can be seen that despite the missing data in the collapsed section of the descending colon, both supine colon segments are registered with the fully distended prone endoluminal colon surface. The accuracy of polyp alignment (marked by arrow) is unaffected by the collapse as it is sufficiently far away from the collapsed region. However, the registration might be less accurate in the un-collapsed region near the collapse, due the effect of missing information. Still, registration is accurate over (most of) the rest of the un-collapsed colonic surface.

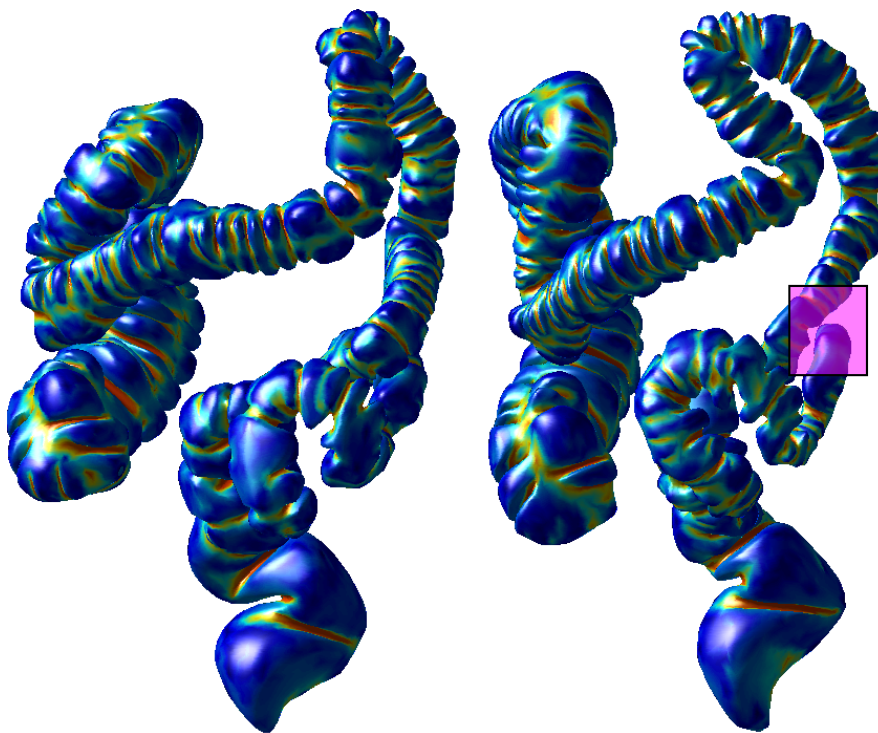


Figure 3.26: A case where the descending colon is collapsed in the supine position (marked, right image) but fully distended in the prone (left).

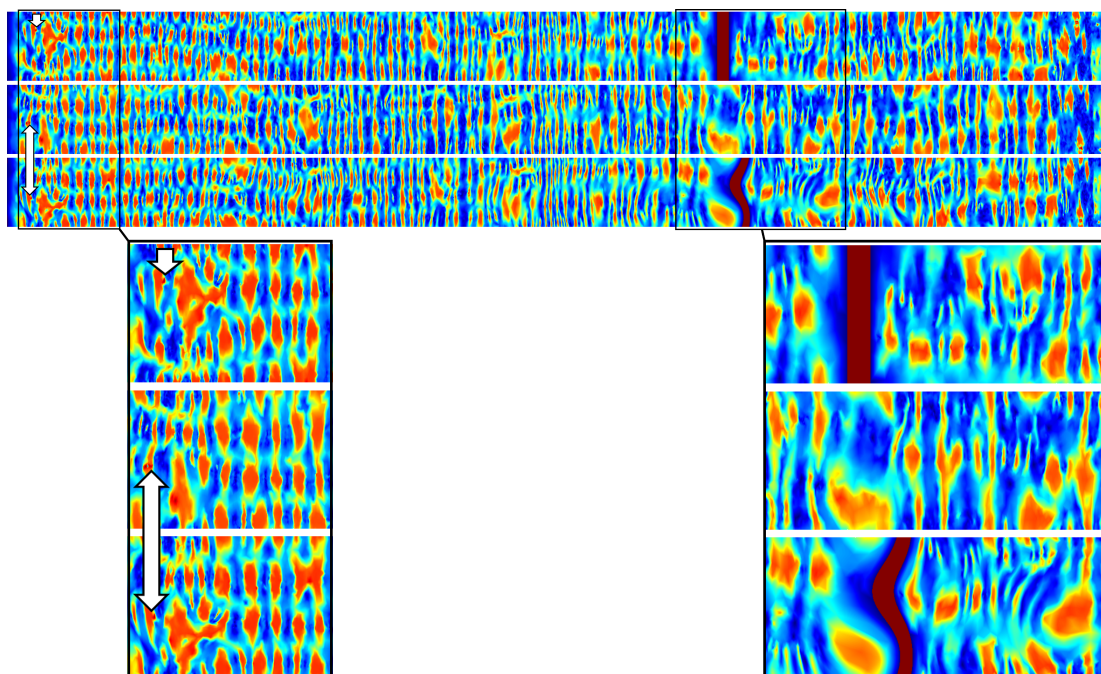


Figure 3.27: Cylindrical representation as raster images of the collapsed supine (top), prone (middle) and deformed supine (bottom) endoluminal colon surface of patient 17. The location of a polyp is marked before (top) and after registration (middle, bottom) with an arrow. Note, the polyp is not visible in Fig. 3.26

## Chapter 4

# Evaluation of registration accuracy

Ethical permission was obtained to utilise anonymised CT colonography data acquired as part of normal day-to-day clinical practice at University College Hospital, London. CT colonography had been performed in accordance with current recommendations for good clinical practice (Taylor et al., 2007) and any detected polyps subsequently validated via optical colonoscopy. For the purpose of establishing spatial correspondence across complete endoluminal surfaces, I selected 24 patients where the colon was not under-distended in both the prone or supine positions and who had either fluid ‘tagging’ (the increased radio-density allows ‘digital cleansing’ of residual fluid) or little remaining fluid. This allowed a continuous segmentation over the full length of the colon using the methods described in section 3.2.

The datasets were randomly allocated into development and validation sets (using random permutation), with 12 cases each. During the course of the development, I discovered that it is difficult to identify corresponding features by eye in the cylindrical image representations for some cases. Closer examination revealed that this was due to either large difference in distension of the colon in the prone and supine views or to insufficient fluid tagging, causing artefacts in the segmentation of the endoluminal surfaces. Large differences in distension can lead to considerable local dissimilarity of surface features (such as haustral folds) which also influences the conformal mapping of these folds differently. Figure 4.1 and 4.2 show such a case with marked differences in cylindrical representations  $I_p$  and  $I_s$  (Fig. 4.1, top and bottom), resulting from very different distensions (Fig. 4.2). These can occur only partially or over the full extent of the colon. Furthermore, differences in the colon surface can occur due to insufficient fluid tagging for accurate digital cleansing. This also leads to artefacts in the segmentation. I identified 4 development datasets with marked differences in local distension, which therefore had different surface features and these were excluded from the study, leaving 8 development cases (patients 1 to 8). The development set was used to tune the registration algorithm parameters (as described in section 3.6).

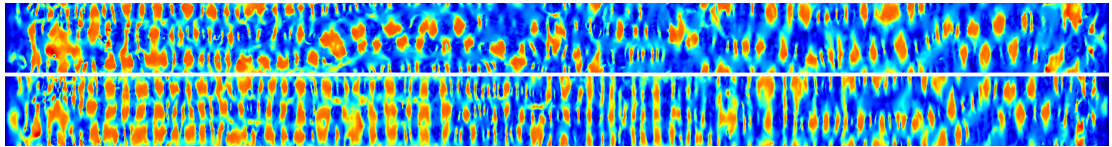


Figure 4.1: Widely different distension changes the shape index of the cylindrical representations in supine (top) and prone (bottom). 3D renderings are shown in Fig. 4.2

Furthermore, this observation led to the exclusion of another 4 cases of the validation set which showed large differences in the cylindrical images. Of those, 2 showed marked differences in distension, 1 case showed insufficient fluid tagging and 1 case showed both problems. This resulted in a total of 8 data sets with fully connected colon segmentations in both views for validation (patients 9 to 16).

Recognising the problems introduced by cases with marked differences in distension, I selected another 5 cases for validation of the method on cases with local colonic collapse (patients 17 to 21).

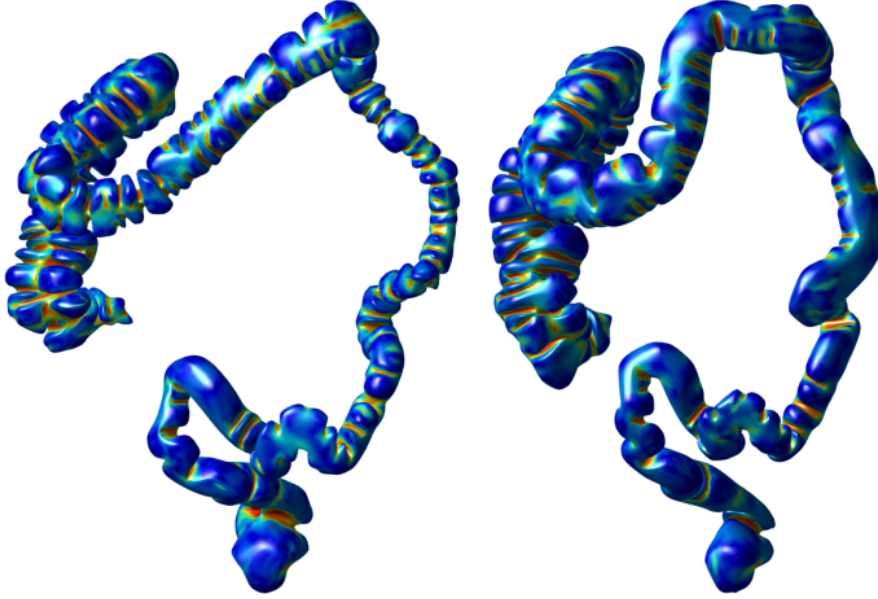


Figure 4.2: Different amounts of distension in prone and supine view cause differences of local features in the cylindrical images.

Here, the distension and surface features of the 3D endoluminal surfaces  $S$  were judged by eye to be sufficiently similar in the well-distended segments before execution of the registration algorithm. This selection process results in a total of 13 cases used for validation, as described in the following sections: 8 fully connected sets and 5 with local colonic collapse. In order to assess the spatial accuracy of the proposed registration method, I used clinically validated polyps and haustral folds to measure the registration error.

## 4.1 Validation using polyps

Experienced radiologists identified polyps in both prone and supine CT colonography scans using 2D multi-planar reformats and endoscopy data for guidance. The polyps' endoluminal extent was labelled to provide reference coordinates for validation. Polyp labels were checked and corrected if necessary and then matched by eye between the prone and supine view by an experienced colonography radiologist (Darren J. Boone).

The cases were selected to present a widespread distribution of polyps throughout the colonic length so that registration accuracy could be investigated over the entire endoluminal surface. Crucially however, any polyps were masked in the 2D cylindrical images  $I$  such that those pixels lying on or close to the polyp were ignored during registration when computing the similarity measure  $C_{\text{similarity}}$ . This means that the similarity cost function is only normalised over the pixels which are not ignored. Thus, it was impossible for the polyps used for validation to bias the registration results and gives an estimation of how accurate the algorithm can perform on any point of the colonic surface. Figure 4.3 illustrates the masking of polyps. In order to determine registration error, the radiologists identified a pair of reference points for each manually matched polyp in the prone and supine views. The reference points were defined as the points at the centre of the intersecting surface between the extracted endoluminal colon surfaces  $S$  and the segmented polyps. Therefore, these points lie on the surfaces  $S_p$  and  $S_s$  respectively. The centre point  $c(x, y)$  is computed as the centre of mass of the intersecting pixels in the 2D images  $I$ , as indicated in Fig. 4.3 (right). Each 2D reference point  $c(x, y)$  corresponds to a 3D point  $c'_i(x, y, z)$  on the surfaces  $S$  which lies inside the polyp's volume. I then determined the registration error in mm by transforming each reference point  $c'_s$  on  $S_s$  using the 3D mapping  $T_{ps}$  to find  $T_{ps}(c'_s)$ , which lies on



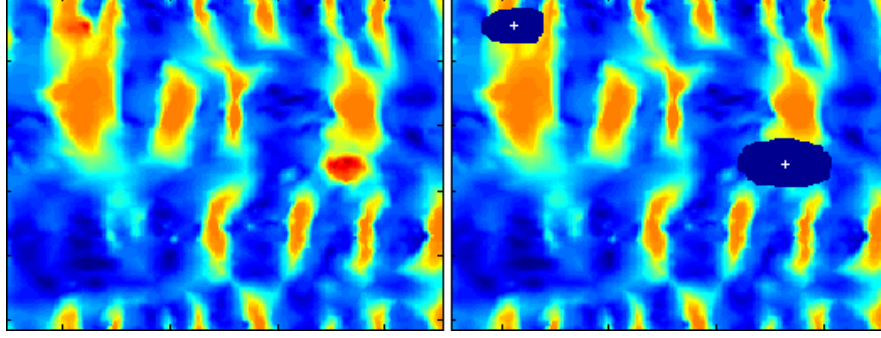


Figure 4.3: Masking of polyps to ensure they do not influence subsequent registration: polyps in unfolded view (left). Masked polyps (right) to be ignored in registration. The centre of mass  $c$  which is used as a reference point is marked with a cross.

surface  $S_p$ , and computing the 3D Euclidean distance to  $c'_p$ , which also lies on surface  $S_p$ .

All 8 datasets used to fine-tune the algorithm had clearly corresponding features in both prone and supine 2D representations, such as patient 7 in Fig. 3.15 (top, middle). It can be seen that after cylindrical B-spline registration, the corresponding features are well aligned (Fig. 3.15, bottom). The corresponding 3D renderings are illustrated in Fig. 3.1. Polyps of the same case and corresponding virtual endoscopic views after their prone and supine views were aligned using the registration result are shown in Fig. 4.4 and Fig. 4.5. I used the same registration parameters as optimised using the

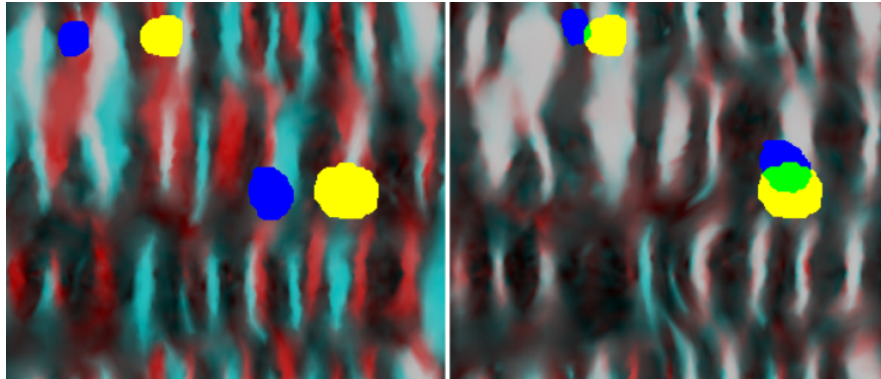


Figure 4.4: Overlay of masked out polyps before (left) and after (right) establishing spatial correspondence. The prone image is coloured red with a yellow polyp mask, and the supine is coloured cyan with a blue polyp mask. After establishing spatial correspondence, aligned features display grey and the overlapping region of polyp masks in green.

development set (patient 1 to 8) on the validation set (patients 9 to 21). Table 4.1 shows the results of assessing the registrations using the polyps of the 13 validation sets. The error after the cylindrical parametrisation but before the B-spline registration is denoted Polyp Parametrisation Error ( $PPE$ ) and the error after the B-spline registration is denoted Polyp Registration Error ( $PRE$ ). Before calculating  $PPE$  the images are translated in the  $y$ -direction (around the colon) to minimise the  $SSD$  between the images, as the 0 degrees position is arbitrarily assigned by the cylindrical parametrisation. This step gives a rough initialisation in  $y$ -direction.

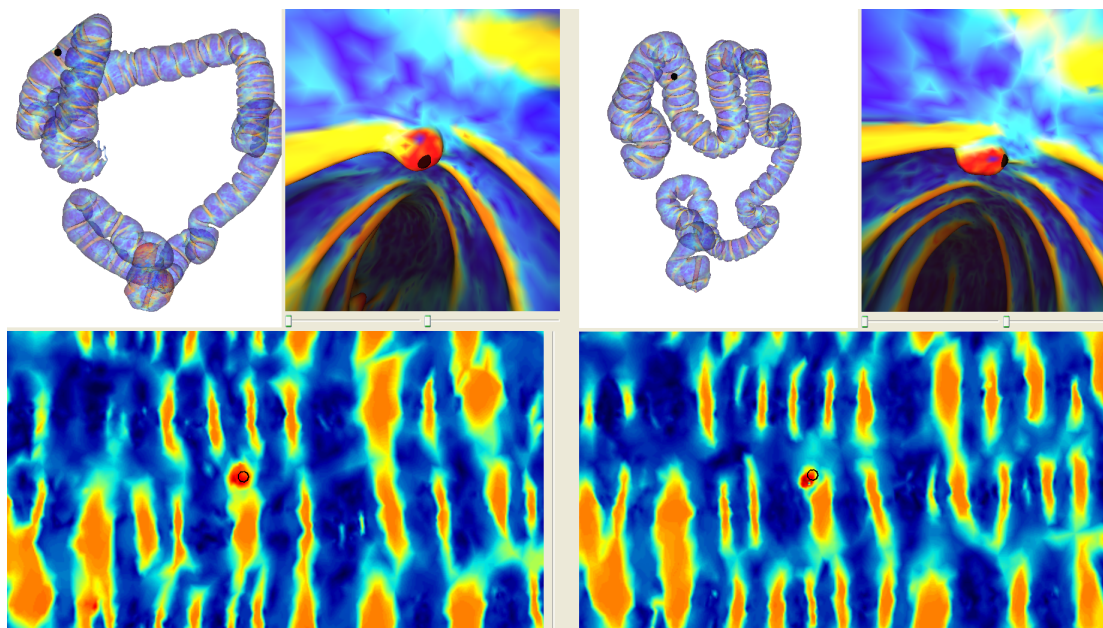


Figure 4.5: Polyp localisation for patient 7 after registration using the prone (left) and supine (right) virtual endoscopic views. The black dot shows the resulting correspondence in the 2D (bottom) and 3D (top) renderings.



Table 4.1: Registration error in mm for 13 polyps in the 13 patients used for validation of the registration method. These included 8 fully connected cases (patients 9 to 16) and 5 cases with local colonic collapse (patients 17 to 19). The Polyp Parametrisation Error ( $PPE$ ) gives the error in aligning the polyps after cylindrical parametrisation but before registration, the Polyp Registration Error ( $PRE$ ) gives the error after cylindrical registration.

Patient #	Polyp location	Collapsed location in prone	Collapsed location in supine	$PPE$ [mm]	$PRE$ [mm]
9	AC	none	none	32.4	3.0
10	Caecum	none	none	13.7	6.0
11	Caecum	none	none	30.2	3.1
12	Caecum	none	none	41.9	2.4
13	DC	none	none	15.7	6.8
14	AC	none	none	11.8	4.6
15	DC	none	none	23.9	3.6
16	AC	none	none	18.5	11.1
17	Caecum	none	1 x DC	24.8	9.4
18	AC	none	1 x SC	62.6	3.9
19	Rectum	1 x DC	1 x DC	55.9	6.0
20	Caecum	3 x (DC, SC)	none	13.3	12.4
21	AC	1 x DC	1 x DC	39.0	1.5
Mean [mm]				29.5	5.7
Std. dev. [mm]				16.4	3.4

The  $PRE$  had a mean (std. dev.) of 5.7 (3.4) mm for 13 validation patients with a single polyp each, and all 13 polyps were well aligned. The  $PPE$  results (mean (std. dev.) was 29.5 (16.4) mm) show that cylindrical parametrisation on its own is not enough to align the datasets accurately – the cylindrical non-rigid B-spline registration is required for accurate alignment. This result is sufficiently accurate to direct the radiologist to an area of the endoluminal surface, which is close to the suspected lesion in both views, even in the case of local colonic collapse (patients 17 to 21). This improvement of registration error is statistically significant with  $p = 0.001^1$ .

The hepatic flexure were not used to initialise the registration for patient 12 and patients 18-20, as the distances along the centreline between prone and supine varied more than  $t_{\text{var}}$  (here, 5%). However, the cylindrical registration was still able to align features well.

The resulting error for 9 polyps in the 8 development cases was a mean (std. dev.) of 6.6 (4.2) mm after non-rigid registration ( $PRE$ ) and therefore slightly higher than  $PRE$  of the validation set. The polyps for development of the registration method occurred in the ascending colon (AC), transverse colon (TC), descending colon (DC) and sigmoid colon (SC).

## 4.2 Validation of spatial correspondence along the entire length of the colon

Polyps can give definite points of correspondence on the colon surface and give a good estimate of the registration performance. However, their number is limited to only one polyp per case in the validation set. In order to assess the registration quality over the entire endoluminal colon surface, corresponding haustral folds were chosen from the prone and supine datasets. Reference point coordinates were provided to lie centrally on the fold in both views; the haustral fold centres were automatically calculated by first segmenting each fold on the colon surfaces  $S$  using a graph-cut method (Boykov et al., 2002)

<sup>1</sup>Related-Samples Wilcoxon Signed Rank Test, 5% significance level.

based on the principal curvatures  $\kappa_1$  and  $\kappa_2$ . Then, the centre of each fold was computed as the vertex which has the lowest maximum distance to any vertex on the border of the segmented fold.

Using the cylindrical representations to establish regions of likely correspondence and virtual colonoscopic views for assurance, a radiologist (Darren Boone, with experience in over 500 validated colonography studies) then manually identified corresponding folds from the prone and supine views. Any folds where the radiologist could not be certain of correspondence were not used for validation, but this still provided an average of 90 pairs of corresponding folds per patient, with a total of 1175 pairs over all 13 validation cases (patients 9 to 21). The centre points of the corresponding folds were then used as corresponding reference points for assessing the registration.

Fig. 4.6 shows the normalised distributions of reference points versus a normalised position along the centreline from caecum (0.0) to rectum (1.0) for 8 un-collapsed and 5 cases exhibiting local colonic collapse. The decline in number of reference points is due to the fact that there are naturally fewer folds in the left hemi-colon. I assessed the Fold Registration Error ( $FRE$ ) in the same way as described

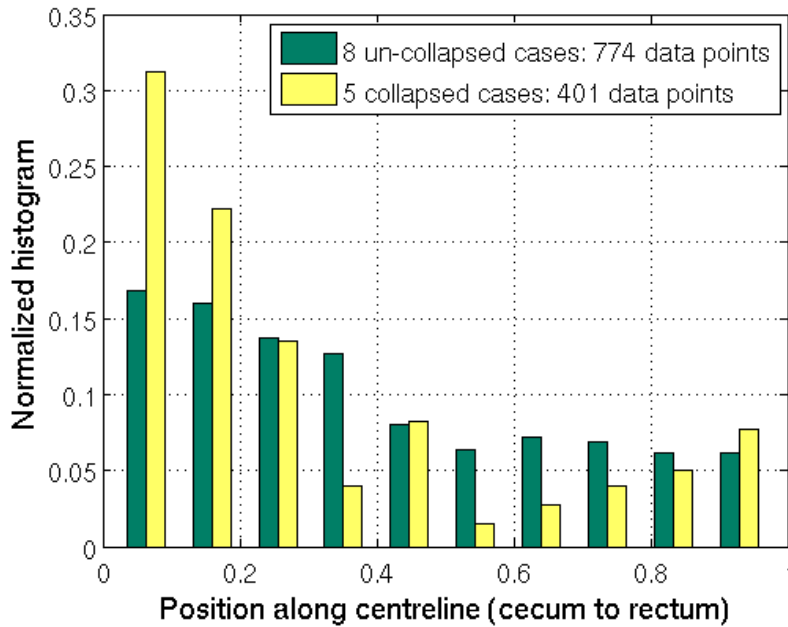


Figure 4.6: Normalised distributions of reference points normalised along the centreline from caecum to rectum for un-collapsed and collapsed cases.

in section 4.1 but using the haustral fold centres as reference points. Using this large set of reference points, the  $FRE$  had a mean (std. dev.) of 7.7 (7.4) mm for a total of 1175 points distributed over all 13 validation patients. In comparison, just using the cylindrical parametrisation on its own (before B-spline registration) a Fold Parametrisation Error ( $FPE$ ) results in an error of 23.4 (12.3) mm. This improvement in registration error after non-rigid cylindrical registration is significant with  $p < 0.0001^2$ . A histogram of the registration error ( $FRE$ ) is shown in Fig. 4.7. Here, the normalised distributions of  $FRE$  for un-collapsed and collapsed cases are coloured differently and displayed next to each other for comparison. It can be seen that the majority of points (95%) lie below an error of 22.8 mm, with a maximum error of 44.1 mm. However, the  $FRE$  is slightly higher for the 5 collapsed cases with 9.7 (8.7) mm as opposed to the 8 un-collapsed cases with  $FRE$  of 6.6 (6.3) mm. This difference between un-collapsed and collapsed cases is significant ( $p < 0.0001^3$ ) and highlights the importance of good

<sup>2</sup>Related-Samples Wilcoxon Signed Rank Test, 5% significance level.

<sup>3</sup>Independent-Samples Kruskal-Wallis Test, 5% significance level.

bowel distension for accurate automatic registration.

Using the proposed method haustral folds are almost always aligned with another haustral fold in the other image, but this is not always the correct corresponding fold. Using the segmented haustral folds I could analyse how many of the folds were aligned with the correct corresponding fold, and how many were misaligned by one or more fold. 82% of all 1175 reference points were assigned to the correct corresponding fold. 15% of reference points were misaligned by just one fold and 3% misaligned between two and three folds. This assumes that the radiologist correctly labelled corresponding haustral folds. I had no way to assess this but it is likely that at least some of the apparently misregistered data is due to this observer error. Nevertheless the identification of corresponding haustral folds is high.

In agreement with the *FRE* results, 71 % of haustral folds were correctly matched in the 5 cases with local colonic collapse. Whereas 88% of haustral folds in the 8 un-collapsed cases were assigned to the correct corresponding fold. The slight decline in registration quality of cases exhibiting local colonic collapse is due to the fact that, typically, the colon distension varies in the areas close to the collapse, e. g. the surface area of the descending colon in Fig. 3.26. Again, this introduces marked difference in the local surface features which degrades the registration accuracy in these areas.

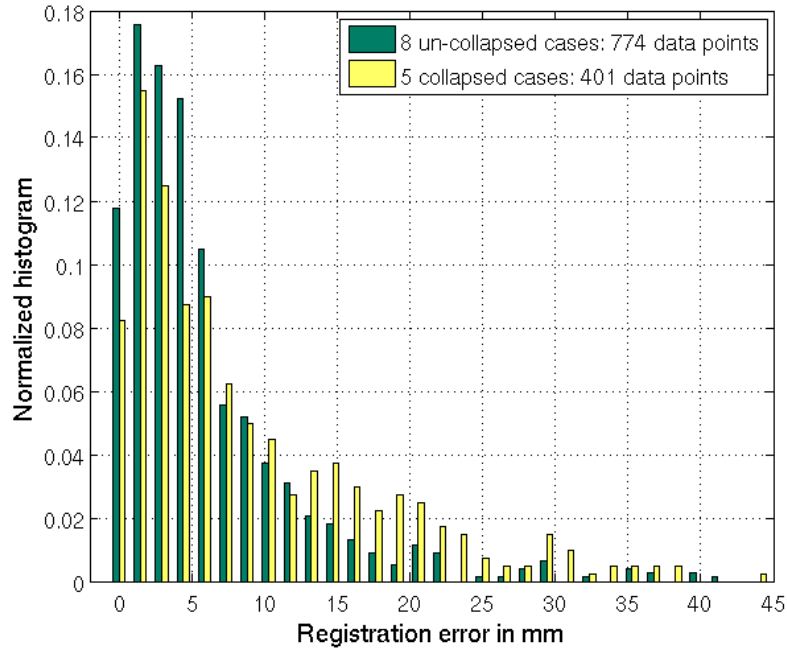


Figure 4.7: Normalised histograms of the Fold Registration Error (*FRE*) distributions in mm using reference points spread over the endoluminal colon surface for un-collapsed and collapsed cases.

### 4.3 Influence of segmentation quality on the registration result

Intuitively, any artefacts in the extracted endoluminal colon surface will influence the proposed registration method negatively. In order to assess the potential impact of the quality of segmentation to the registration result quantitatively, the following experiment was performed. Two pairs of prone and supine colonic segmentations of the colonic lumen were generated: one including the tagged fluids  $L_{\text{tagged}}$ , the other not including any tagged fluids  $L_{\text{untagged}}$  – therefore simulating how the registration would perform if the residual fluids were insufficiently tagged for *electronic cleansing*. Fig. 4.8 shows the supine surfaces  $S$  extracted from both segmentations; one including residual fluids  $S_{\text{tagged}}$  and one excluding residual fluids  $S_{\text{untagged}}$ . The two pairs of cylindrical  $SI$  images for either case are presented in Fig.

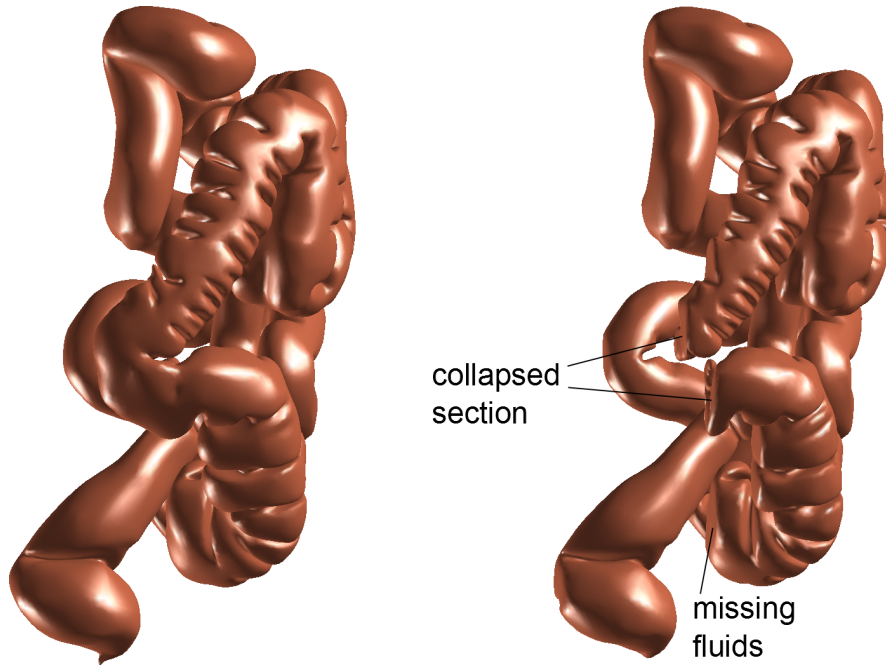


Figure 4.8: A supine endoluminal surface extracted from a segmentation that included residual fluids (left); and a supine surface that excluding residual fluids, simulating insufficient fluid tagging for accurate colonic surface extraction (right). Note that not including the fluids in the right image caused a short section of collapse in the ascending colon and several ‘flat’ areas that are artefacts caused by the surface boundaries of the residual fluids (right).

4.9. The short section of collapse in the ascending colon can be seen in the supine image without fluid tagging (2nd from bottom in Fig. 4.9). Furthermore, it can be seen that some folds present in the two top images are now obscured by the non-tagged residual fluids in different areas. Some regions where these differences are more obvious are framed for highlighting. Despite these differences, it can also be seen that the majority of both images pairs still look similar, illustrating the advantage of using  $SI$  as the intensity metric in the cylindrical images. After each pair of cylindrical  $SI$  images, the respective registration result is overlaid over the target image. It can be observed that the case of excluded residual fluids in the bottom row image leads to a less accurate registration result.

#### 4.3.1 Results and conclusion

The mean (std. dev.) fold registration error increased by 92.2% from 11.2 (10.4) mm to 22.1 (18.9) mm. This is significant with  $p = 0.007^4$ . This is not surprising as many of the fold features that are needed in the cylindrical images in order to align both endoluminal surface correctly, are now are obscured

<sup>4</sup>Related-Samples Wilcoxon Signed Rank Test, 5% significance level.

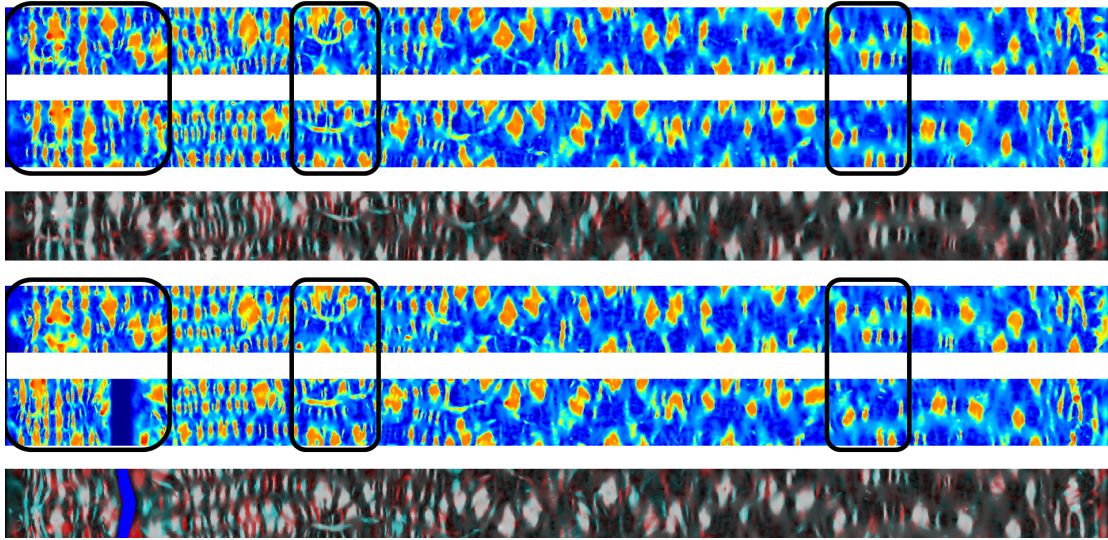


Figure 4.9: Cylindrical representations of prone (top) and supine (2nd from top) endoluminal surfaces extracted from a segmentation that included residual fluids. The cylindrical representations of the prone (3rd from bottom) and supine (2nd from bottom) surfaces that excluded residual fluids, simulating insufficient fluid tagging for accurate colonic surface extraction. After each pair of cylindrical images, the respective registration result is overlaid over the target image. The target image is coloured in red and the floating image in cyan. Pixels of the same intensity after registration are displayed in grey. The less accurate registration result in the case of excluded residual fluids can be observed in the bottom row image.

by the un-tagged fluids. When the patient changes between prone and supine positions, the un-tagged fluids move as well and therefore obscure the surface features at different anatomical locations which influences the registration result very negatively.

The lower accuracy of the registration is also reflected in the mean of squared differences ( $MSD$ ) between the pixel intensities of both cylindrical images after registration. In the case of tagged and digitally cleansed residual fluids, the  $MSD$  is reduced to 0.017; while in the case of excluded residual fluids, the  $MSD$  could only be reduced to a value of 0.024 (this is a 42% higher value in comparison to the registration result of the well-cleansed colon, see top three images in Fig. 4.9).

It can be seen that sufficient fluid tagging and electronic cleansing is beneficial for the successful and accurate alignment of the endoluminal colonic surfaces.

## 4.4 Discussion

I have presented a novel method for establishing spatial correspondence between endoluminal colonic surfaces extracted from prone and supine CT colonography data. The proposed method simplifies the problem of aligning the prone and supine surfaces from a 3D to a 2D task. This is achieved by mapping the full endoluminal surface to a cylindrical parametrisation using a conformal mapping. The novel contribution of this work is that a cylindrical parametrisation is used in order to align the endoluminal colon surface using non-rigid B-spline registration. Cylindrical raster-images with shape index values derived from the initial 3D surfaces are used to drive the registration. This process can establish accurate correspondence between the 2D cylindrical parametrisations, and hence give correspondence over the full 3D colonic surfaces which is able to recover the large colonic deformations and torsion that occurs between the two acquisition positions.

The proposed registration approach is motivated by the assumption that the overall shape of the colon can undergo large deformations when the patient changes position, but that the local shape of surface structures, such as haustral folds, remains similar enough between scans to align the surfaces with the desired accuracy. During the development of the method it was discovered that for 8 of the 24 un-collapsed cases had large regions where the surfaces structures appeared markedly different between the two scans. These were due to large differences in the distension of the colon or insufficient fluid tagging. These cases were excluded from this chapter as the current method was expected to fail for such cases. However, I strongly suspect that most other methods presented in the literature that aim to generate accurate correspondence over the colonic surface (i.e. the feature-based methods (Zeng et al., 2010) and the voxel based methods (Suh and Wyatt, 2009, 2008)) will also experience difficulties with cases where the surface features appear differently in the two scans. The number of such cases observed in this study indicates that these cases are not infrequent, and methods that can address these cases must be developed to achieve maximum clinical benefit.

Another common occurrence is for there to be some regions of local colon collapse in one or both scans. Validation of the proposed registration method on 5 cases where there was a collapse in at least one view showed promising performance. It shows that the method is able to handle cases with multiple collapses in both views. Some of the centreline based approaches can handle regions of local collapse, but these only give approximate correspondence based on the shape of the centreline, and do not attempt to provide accurate correspondence over the colon surface. To the best of my knowledge there has only been one other method proposed to date that attempts to provide accurate correspondence over the colon surface (as opposed to just at the centreline) and to handle regions of local colon collapse (Suh and Wyatt, 2008). However, this method has not yet been validated on cases with multiple collapses in both views as used in this study. Furthermore, their results show limited accuracy.

The method presented here relies on extracted colon surfaces of good quality (see Section 4.3). Therefore, pre-processing steps of segmentation (which involved manual interaction) and automated topological correction were necessary to extract topologically correct surfaces for the patient data used here. It is clear that obtaining good quality segmentations of the intraluminal colon surface reliably and robustly is a significant impediment to the clinical adoption of the proposed method.

The current method requires some manual interaction. These are: 1) choosing the structure element sizes interactively in order to correct the colon segmentations and include the rectal insufflation catheter while visually inspecting the segmentation quality. 2) The start and end-point as well as the correct order of each well-distended colon segment were selected manually. Standard commercial 3D workstations already require the radiologist to manually choose the order of each colon segment. These steps are relatively quick to perform and require minimal manual input. Therefore, I did not consider these few manual interactions to be a major impediment to the proposed method. However, future work should investigate how individual colon segments can be arranged automatically in the case of colonic collapse.

This will also incorporate methods of detecting two corresponding points at each segment which defined the start and end of each parametrised cylinder.

Automatic identification of caecum and rectum has been proposed in the literature but was not performed for any case included in the present study so as not to affect the estimation of registration accuracy of the cylindrical registration method. To date, automatic identification of landmarks in the colon (such as caecum and rectum) is still a topic of active research in the literature (Lu et al., 2009). Moreover, it cannot be said that a robust detection of corresponding start and end points in both prone and supine CTC images is readily available using existing methods. For example, in only 44% of cases, the caecum could be established automatically as a landmark for the registration method of Näppi et al. (2005).

Given topologically correct surface meshes of the size used in this study, a single processor implementation of the Ricci flow conformal mapping (using the steepest gradient descent minimization) would take several hours to achieve sufficient convergence. However, faster solvers (such as the Newton method (Jin et al., 2008)) have been implemented to improve convergence time to within a few minutes (see Section 3.5.3). Alternatively, GPU-based implementations of Ricci flow (Qiu et al., 2008) could further speed up the computation time. Alternatively, other conformal mapping methods could be used, e.g. (Haker et al., 2000) which require less computation time. It should be made clear that obtaining the cylindrical parametrisation was not the focus of this study. There have been a number of parametrisation methods presented in the literature, some based on conformal mappings (Floater and Hormann, 2005, Haker et al., 2000, Hong et al., 2006) and some on other techniques (Wang et al., 2002), and I simply chose one that would generate an appropriate mapping for to use for a cylindrical registration. Future work could investigate fast implementations of the Ricci flow optimisation as well as alternative techniques for generating the cylindrical parametrisations in order to produce a registration result in a clinically feasible time frame.

The cylindrical B-spline registration can provide a result within a few minutes, which is fast enough to be clinically useful. A multi-resolution-level registration approach was used in order to help the registration optimization avoid getting stuck in local minima and to reduce the computation time. However, the presented validation shows that some haustral folds were misaligned by one or more folds indicating that the registrations were occasionally still getting trapped in local minima. In the Chapter 6, I will investigate how better initialisation of the cylindrical registration and/or a better choice of registration parameters could solve this problem.

In conclusion, I have presented a framework for the alignment of information from prone and supine CT colonography; a very challenging registration problem. The method comprises conformal mapping of CT derived features onto a cylindrical surface, followed by a cylindrical registration of these features. This establishes an estimate of a dense correspondence throughout the derived colon surface. The results show promise, not only for polyp detection but also for establishing correspondence between corresponding haustral folds on a limited set of colonography datasets. A registration-based filtering algorithm was shown to reduce FP findings in CADe without reduction in sensitivity associated with the filtering process. This has the potential to further enhance computer-aided CTC interpretation.

## **Chapter 5**

# **Clinical application of prone-to-supine registration**

This chapter aims to provide an estimate of how the proposed method for prone-to-supine registration would perform in clinical practice. Firstly, a phantom study utilising a porcine colon was performed in order to accurately measure the registration accuracy achievable by the method. The physical experiments were led by Darren Boone. A reference standard was generated by using metallic fiducial markers attached to the colon's surface.

Secondly, an external clinical validation was performed with collaborators at University College Hospital (UCH), London, (Darren Boone and Steve Halligan). The validation reported in this chapter is based on a large publicly available CTC data set: the ACRIN CTC trial (Johnson et al., 2008). A total of 66 polyps in 49 patients were used in order to judge the algorithm's performance on data generalisable to clinical practice. Furthermore, the method was compared to using a simpler, centreline-based method, i.e. "normalised distance along the centreline" in order to estimate the clinical benefit of using the proposed method.



## 5.1 Estimation of registration accuracy using a porcine phantom

Manually establishing an accurate reference standard for validation of the prone-to-supine registration method on real patient data is very challenging, even for experienced observers using visualisation aids like virtual fly-through renderings. Therefore, reliable fiducial markers, which allow to measure the registration error more reliably, are desirable. Polyps can give an accurate gold standard as they are fixed to the colonic wall (Laks et al., 2004). However, polyps are typically rare in occurrence and can vary in size and shape severely. Pedunculated polyps can even “flap” around when they are growing from long stalks. This makes the definition of an accurate reference point on the polyp surface, which matches between acquisitions, very challenging. Previous studies showed that validation, using manually matched reference points on the colonic surface with a combination of polyps, colonic diverticula and folds, is technically challenging. A blinded repetition of the manual matching (following an interval of seven days) revealed an intra-observer error of 8.2 mm (std. dev. 12.5 mm) (Roth et al., 2010). Errors in the reference standard are likely to underestimate the performance accuracy of the registration method.

### 5.1.1 Methods and Materials

In this section, a phantom study using a porcine colon is described in order to establish an accurate reference standard. The porcine phantom was labelled with radiopaque markers along its length and was imaged in a variety of orientations in order to simulate in-vivo colonic deformation. Especially deformation that takes place during the prone-to-supine repositioning of the patient. The porcine colon had to be constrained such that the pattern of haustral folds remained consistent between scans. The haustral fold pattern is an important feature for driving the proposed registration algorithm.

While a human colon specimen would be preferable, panproctocolectomy (removing the entire colon, rectum and anal canal) is usually only carried out for severe colitis, cancer or multiple polyposis syndromes – all of which render the specimen potentially unsuitable for the purpose of validating a registration algorithm aimed for performing under normal clinical CTC practise. Another route is post mortem human colon - but due to rapid deterioration of the GI tract at death this is, practically speaking, a very demanding process and was ruled out by the clinical collaborators of this study. Porcine colons on the other hand are readily available and the morphology is similar to the human colon. However, the porcine colon is typically less haustrated, but ethical issues involving human specimens are avoided. For this very reason it is used extensively in CT colonography research (Slater et al., 2006, Lee et al., 2009) and optical colonoscopy training (Von Renteln et al., 2010).

Specifically for this porcine phantom experiment, the specimen had to be constrained in such a way that the haustral fold pattern was not disrupted. Distension during insufflation of the colon reduces mural thickness (which is on the order of 1-4 mm). Therefore, in order to provide suitable CT contrast resolution, the specimen was immersed in fluid of similar attenuation value to abdominal tissue. Ideally, the porcine colonic phantom should conform naturally with minimal extrinsic deformation induced by the experimental set-up. However, submerging it in water imposes a challenge to this study as the insufflated colon is buoyant. Previous phantom studies have overcome this by submerging the specimen under bags of normal saline (Slater et al., 2006). However, this inevitably deforms and distorts colonic morphology and haustral fold pattern.

The porcine bowel was obtained from a pig previously slaughtered for human consumption (*Humphrie's Slaughterhouse*, Brentwood, Essex, UK). The colon was removed from the pig's abdomen and separated from its gastrointestinal tract (see Fig. 5.1), washed and trimmed by Darren Boone. This left a porcine colon of about 80 cm length which was closed at either end and connected to a rectal insufflation catheter (*Trimline DC*; E-Z-Em, Westbury, NY, USA) such that the pig's colon could be filled with air. In order to image the colon with high contrast, it was submerged into a 500 × 300 × 300 mm sealable plastic crate filled with 20 litres of 0.9% saline solution during CT scanning. In order to achieve attenuation similar to that of human abdominal tissue (Dachman et al., 1997), 60 ml of diatrizoate meglu-

mine containing 370 mg of iodine per millilitre (*Gastrografin*; Schering Health Care, Burgess Hill, West Sussex, UK) were added to the solution. This resulted in approximately 40 HU in the reconstructed CT images outside the air-filled porcine colon.

The air inside the colon induced a strong buoyancy effect which caused the colon to float above water level. This was overcome by inserting the entire colon phantom into an elastic stocking (acrylic, 60 denier) that was fixed to the bottom of the water container. This ensured that the colon was fully submerged under water during CT scanning as shown in Fig. 5.2 (right).



Figure 5.1: Unprepared porcine colonic specimen with gastrointestinal tract. The animal was slaughtered for human consumption. At this stage, the colonic specimen remains distended due to retained residue. Note the haustral fold pattern is not dissimilar to the human colon [Image courtesy of Darren Boone].

The reference standard was established using 5-mm metal markers, i.e. wound closure clips (*3M<sup>TM</sup> Precise<sup>TM</sup>*), attached to the tissue of the outside surface of the colon wall. These markers are easily visible in the CT images due to their higher attenuation and can be segmented in an automated fashion. I used the centre of each clip intersection with the colon surface as the reference point to measure the registration error. Five scans were performed with the phantom fully inflated and submerged under water. Different mechanical forces were induced to the external surface of the colon manually in order to model different deformations of the colon in each scan (as if the patient was changing body positions). This provided ten combinations of pairs of CT scans between which can be registered in order to evaluate registration accuracy. Figure 5.3 shows the segmented colon in such a CT scan with orthogonal cross-sectional views. Figure 5.4 illustrates the different amounts of deformations induced to the porcine phantom on five occasions using 3D renderings of the colonic surfaces extracted from the colon segmentations. 12 corresponding metal markers can be seen in each scan on the inflated endoluminal surface tissue. The centroid positions of each marker were then used for evaluation of the accuracy of the proposed registration method (see Fig. 5.7).



Figure 5.2: Pig phantom filled with water for cleaning purposes (left). One of twelve 5 mm metal clips is marked by an arrow. Phantom submerged under water using stockings (right) in front of CT scanner.

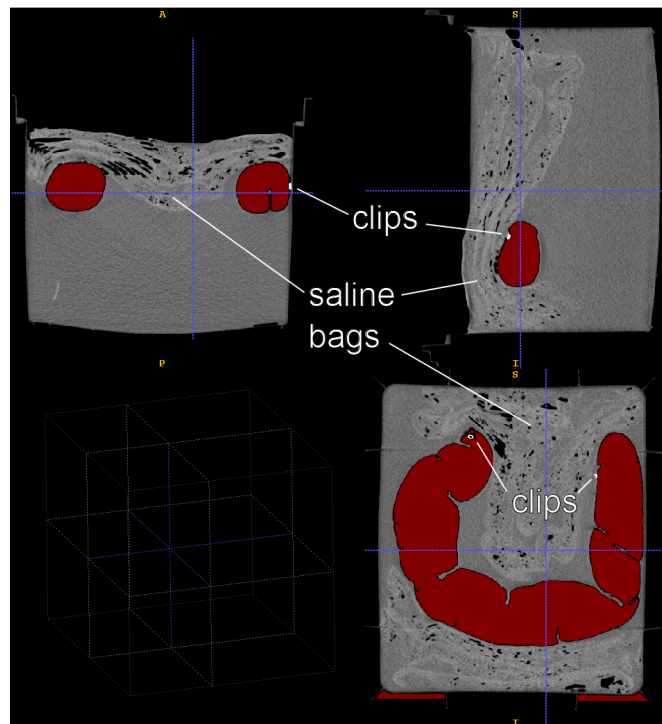


Figure 5.3: Cross-sections of a CT scan acquired of the segmented porcine colon submerged under water. Deformations were induced by applying weights to different external areas of the colon and by relocation of the air inside. Some of the metal markers (clips) and bags of saline are marked.

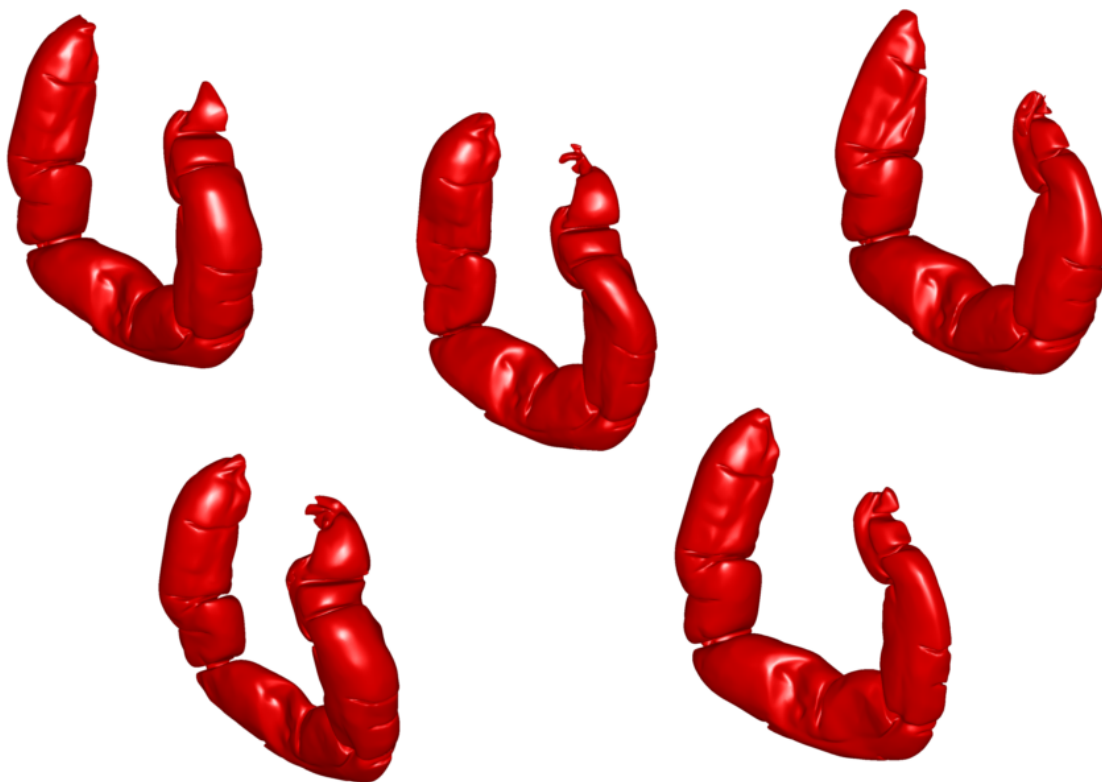


Figure 5.4: Pig phantom segmentations of 5 CT scans. This results in 10 combinations for registration between any two of the scans.

### 5.1.2 Piece-wise linear initialisation

The registration accuracy can be improved by using robust fold matches between both views in order to initialise the cylindrical registration. Hampshire et al. (2013) proposed the automatic detection and matching of haustral folds between two colonic surfaces based on graph-cut segmentation of folds. Pairs of haustral folds are matched robustly using a Markov Random Field (MRF) model. The method of Hampshire et al. (2013) matches haustral folds using virtual surface renderings of the colonic lumen. The intensity difference between pairs of virtual images, along with additional information about the geometric neighbourhood of folds, is then used in the MRF in order to estimate matching haustral folds. This allows the matching of very prominent features between the two surfaces which can be used for initialisation of the cylindrical intensity-based registration.

In order to provide a simple and robust initialisation, the fold positions are mapped onto conformally mapped cylindrical images. Prior to the B-spline registration where full surface correspondence is established, a piece-wise linear scaling between pairs of haustral folds along the length of the colon is performed<sup>1</sup>. This initialisation step is illustrated in Fig. 5.5 and Fig. 5.6.

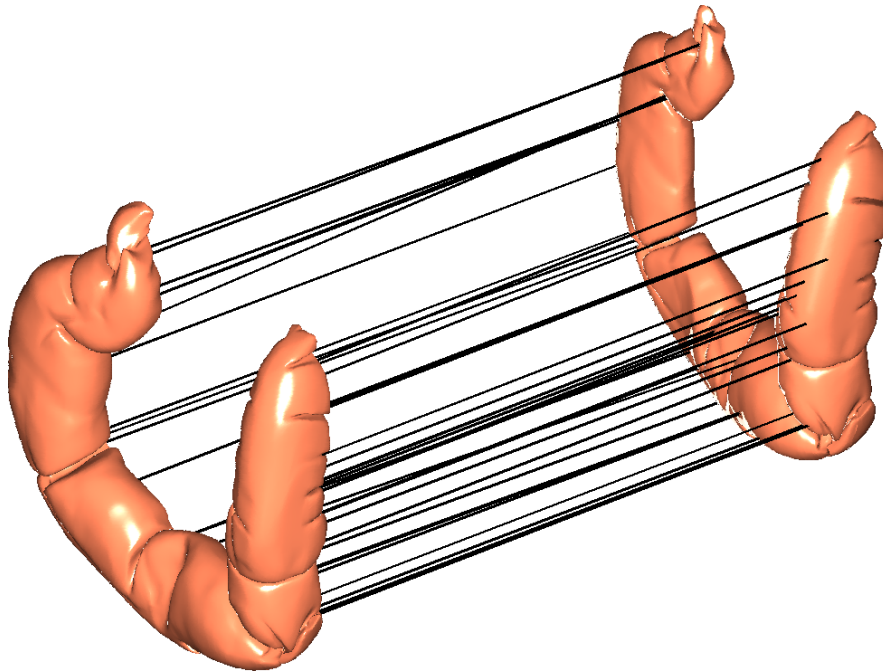


Figure 5.5: Haustral fold matches between two surface representations of the porcine phantom (a matched pair of folds is indicated by a connecting line between both surfaces). These matches can be used to provide a simple piece-wise linear initialisation along the length of the colon (shown in Fig. 5.6). The shown feature matches correspond to the combination of scans 1 and 5.

---

<sup>1</sup>Later, in chapter 6, an improved non-rigid initialisation method will be introduced.



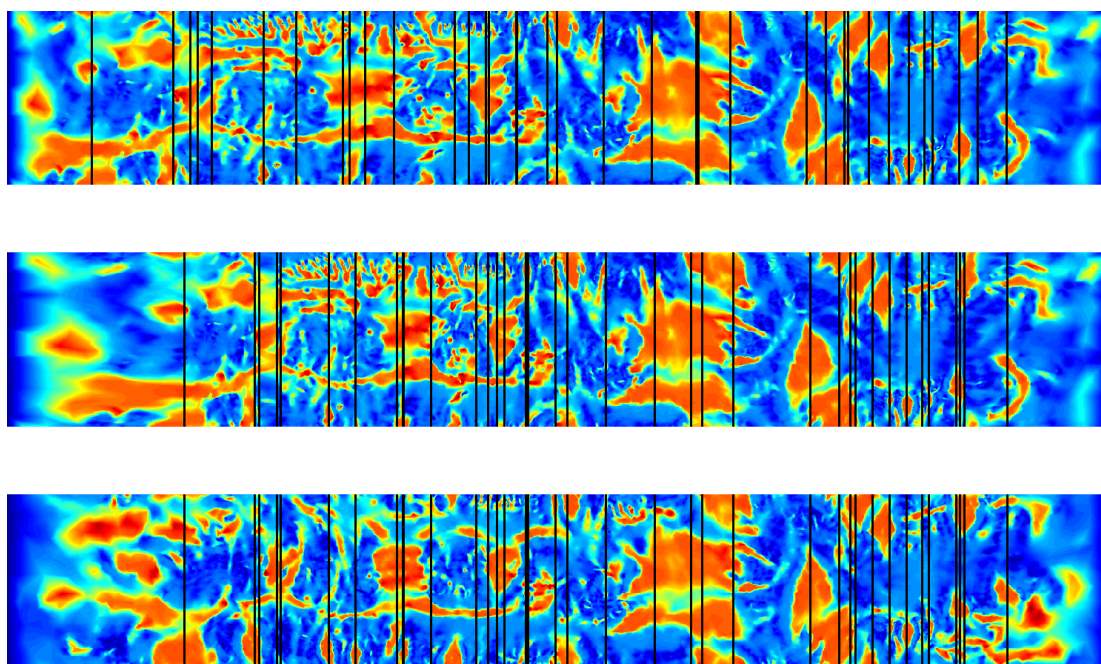


Figure 5.6: Piece-wise linear initialisation along the the length of the colon. A 3D feature is mapped to its corresponding location along the length of the cylinders (vertical lines). The top and bottom images correspond to the original cylindrical image. The middle image is the top image, after applying a piece-wise linear scaling in order to initialise it with the bottom image, prior to non-rigid cylindrical registration. Note that the vertical lines are now aligned between the middle and bottom images. The shown feature matches correspond to the combination of scans 1 and 5.

The registration was performed with and without feature-based initialisation, using Hampshire's fold matches (Hampshire et al., 2013). The metal markers were masked from the similarity measure computation when driving the registration, in order to not influence the accuracy of the registration. The 3D position of every metal marker is transformed into the space of the target scan by using the deformation field resulting from the cylindrical registration. 3D registration errors are then measured as the Euclidean distance between transformed and targeted marker positions. Figure 5.7 illustrates the computation of 3D registration errors measured at the transformed points and reference points of the 12 metal markers between scan 1 and 5.

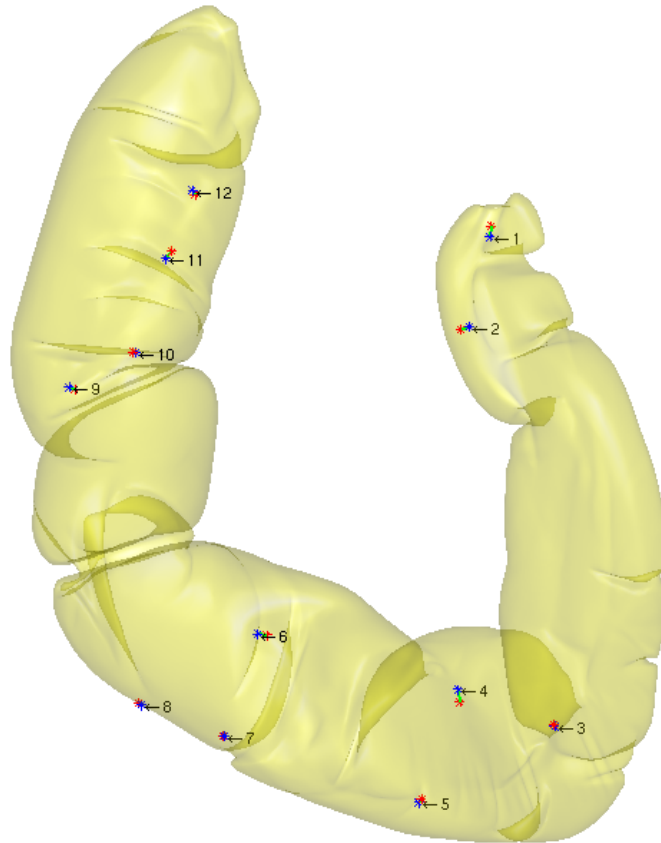


Figure 5.7: 3D rendering of the porcine surface. The registration errors after feature-based Clip Registration Error ( $CRE_2$ ) are plotted as green lines between the transformed points (blue) and reference points at the 12 metal marker positions (red) in the space of the endoluminal surface. The shown errors correspond to the combination of scans 1 and 5.

### 5.1.3 Results

The resulting registration errors are shown in Table 5.1 before (1) and after (2) using feature-based initialisation. A comparison of registration errors is illustrated in Fig. 5.8. The mean (std. dev.) 3D registration error is significantly reduced - from 24.7 (22.9) mm to 4.9 (1.5) mm - when using the feature-based approach ( $p = 0.024^2$ ) when using the feature-based approach (from a mean (std. dev.) of 24.7 (22.9) mm to 4.9 (1.5) mm). This registration accuracy is comparable to the results after feature initialisation achieved in the human colon cases (see Chapter 3). It clearly illustrates the importance of accurate initialisation between the cylindrical images in order to achieve accurate registration results.

---

<sup>2</sup>Related-Samples Wilcoxon Signed Rank Test, 5% significance level.

Table 5.1: This table summarises the mean Clip Registration Error  $\overline{CRE}_1$  using only the cylindrical B-spline registration (see Chapter 3) and after  $\overline{CRE}_2$  feature-based initialisation with subsequent intensity-based B-spline registration for the 10 possible combinations of pig colon scans using the 12 metal clips as reference points; leading to 120 pairs of reference points to test the algorithm.

Combination	Using Scans	$\overline{CRE}_1$ [mm]	$\overline{CRE}_2$ [mm]
1	1 and 2	56.0	4.6
2	1 and 3	4.6	5.0
3	1 and 4	9.4	4.6
4	1 and 5	8.8	2.7
5	2 and 3	17.5	4.0
6	2 and 4	56.7	4.6
7	2 and 5	59.1	4.3
8	3 and 4	16.2	8.2
9	3 and 5	14.4	6.6
10	4 and 5	4.1	4.5
Mean [mm]		24.7	4.9
Std. dev. [mm]		22.9	1.5

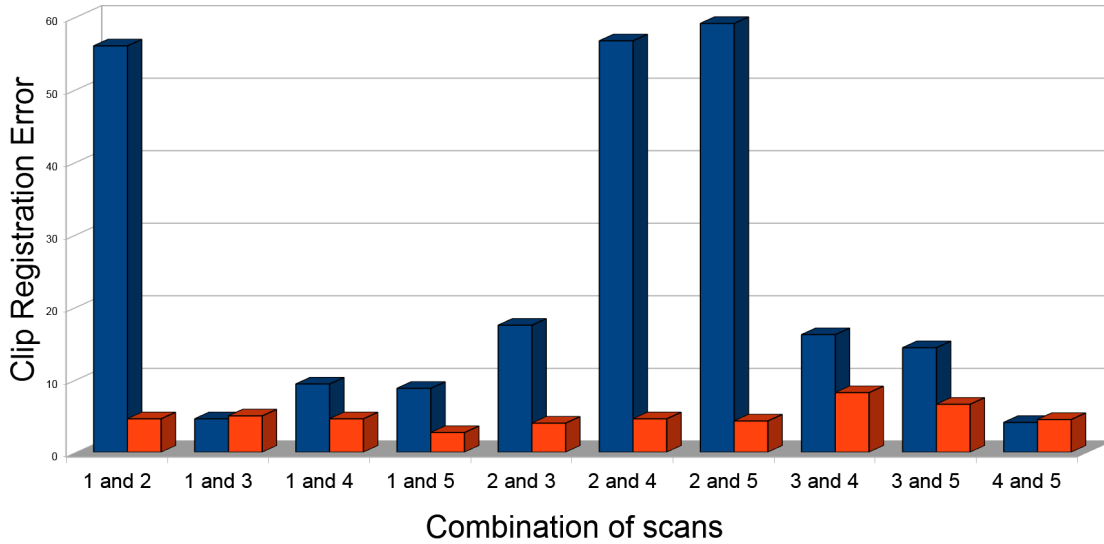


Figure 5.8: Comparison of clip registration errors before (blue) and after (red) feature-based initialisation for the 10 possible combinations of pig colon scans, using the 12 metal clips as reference points; leading to 120 pairs of reference to test the algorithm. A marked increase in registration error can be observed when registering with surface number 2 is likely, due to an ‘unrealistic’ artefact introduced by the bags of saline during deformation of porcine phantom. However, feature-based initialisation (red) compensates for this artefact and reduces the error significantly.



#### 5.1.4 Conclusion

Porcine phantom experiments have a long history in CT colonography research. Even the technical acquisition parameters used in current clinical practice have been optimised by performing early phantom studies (Dachman et al., 1997). Nevertheless, this study posed unique challenges and is not without limitations. The requirement to maintain submersion of the insufflated colonic specimen while minimising extrinsic haustral distortion was especially challenging and caused buoyancy effects that would not occur in humans in-vivo.

There are differences between the human and the porcine colon: the porcine colon is typically less haustrated and the phantom was, with circa 80 cm, roughly shorter by half than the average human colon (Gray, 1858). The porcine colon segment had less prominent features that could have driven the cylindrical registration and achieved detailed alignment of the surface. Furthermore, the experimental set-up might have introduced some unrealistic deformations, even though the introduced deformations were likely not as marked as those happening during the patient changing between prone and supine positions. Forcing the phantom to stay under water using the above-mentioned stockings caused dissimilar features between some views. Furthermore, handling the strong buoyancy effects meant that the specimen had to be constrained such that colonic torsion was minimised. However, attempts to introduce larger deformations of the porcine colon in order to ‘challenge’ the registration algorithm caused unrealistic distortion of haustral fold patterns. An alternative solution to this problem could be filling the specimen colon with tagged water and surrounded by room air for CT scanning – which would enable easy segmentations of the colonic surface. This would inevitably cause some flattening of the colon surface but might enable more realistic deformations, including more torsion and true prone, supine and decubitus positions.

The reference markers were masked out from the similarity measure before driving the registration in order to not influence the accuracy of the registration. It can be seen that the initialisation improves the registration results drastically (see Fig. 5.8). This is because a lack of initialisation causes big differences in the cylindrical representations, likely caused by the conformal mapping.

The experiments show that it is possible to construct a phantom suitable for assessing prone-supine registration accuracy. While the registration without initialisation is less likely to produce clinically useful accuracy in insufficiently well prepared cases, using the feature-based initialisation improves the registration result, especially in cases where the colon surfaces are dissimilar. Differences in distension can cause marked differences in the initial conformal mapping results, causing the cylindrical images to appear differently. The amount of stretching introduced to different local areas when mapping from 3D to cylindrical space can differ drastically and can also depend on how differently the same anatomical endoluminal surface area was stretched in 3D. These differences in stretching can result in the registration converging towards incorrect local minima. However, a feature-based initialisation in cylindrical space can correct for these coarse differences in stretching. A rough initial alignment utilising the features along the x-axis cylinder (length of the colon) can provide enough alignment to guide the non-rigid registration into converging towards the correct local solution.

Considering the reduction in registration error, it is clear that using a robust initialisation improves the overall performance of the prone-to-supine registration method (comparable to the results in Chapter 6). Even just a rough alignment of folds improves the chances that the automated cylindrical registration will align things more correctly and reliably.

## 5.2 External clinical validation of prone and supine CT colonography registration

This section provides an external validation of a prone-supine registration algorithm for CT colonography (CTC), introduced in the previous chapters (Roth et al., 2011, Hampshire et al., 2013). A validation sample of 49 patient cases with 66 polyps (6 to 30 mm) was selected from a publicly available, anonymised CTC archive. To enhance generalisability, no case was excluded due to poor preparation or inadequate distension. Corresponding prone and supine polyp coordinates were recorded and the endoluminal surfaces registered using the proposed method. The polyp registration error was determined and a subjective assessment of registration made for 2D slice-based and 3D endoluminal data display using a scoring system, pre-specified by experts. Results were compared to using “normalised distance along the colon centreline” (NDACC) which approximates the method currently deployed to match colonic positions using proprietary CT colonography interpretation software.

Image data used in this research were obtained from *The Cancer Imaging Archive*<sup>3</sup> sponsored by the *Cancer Imaging Program, DCTD/NCI/NIH*. The results of this section have been presented at *Computational and Clinical Applications in Abdominal Imaging at MICCAI 2012* (Roth et al., 2012) and have recently been accepted for publication in the journal *Radiology*.

### 5.2.1 Introduction

As described in previous chapters, CT colonography interpretation is difficult and time consuming. Faecal residue can simulate or obscure polyps, leading to both false-positive and false-negative diagnoses. To compensate for this, it is normal practice to obtain CT data with the patient both prone and supine to redistribute faecal residue and colonic gas; faecal residue tends to move, while fixed mural pathology does not. Matching corresponding endoluminal locations between prone and supine acquisitions is the cornerstone of competent interpretation (Yee et al., 2003). Unfortunately, the colon often undergoes significant deformation during repositioning (Punwani et al., 2009) which complicates the interpretative task and can induce reader error.

Software algorithms have attempted to facilitate matching of corresponding locations between prone and supine acquisitions: matching of distances along centrelines enables navigation to approximate endoluminal locations in both datasets (Acar et al., 2001, Li et al., 2004, Wang et al., 2009, Näppi et al., 2005, de Vries et al., 2006). The most straight-forward method (and the only technique available in commercial workstations at present) is the “normalised distance along the colon centreline” (NDACC) (Summers et al., 2009). While centreline matching studies have shown promising results (Acar et al., 2001, Li et al., 2004, Wang et al., 2009, Näppi et al., 2005, de Vries et al., 2006), they tend to report registration error in only one dimension. However, it can be argued that centreline-based methods are inherently limited because the interpretation task requires readers to find a specific point on the endoluminal surface rather than along the centreline. Moreover, many readers favour using multiplanar reformats rather than endoluminal 3D displays, further limiting the utility of centreline methods in routine daily practice.

Alternative methods that aim to register the full colonic surfaces have been proposed (Suh and Wyatt, 2008, 2009, Huang et al., 2007, Zeng et al., 2010). However, such studies often report the selection criteria incompletely (Acar et al., 2001, Li et al., 2004, Wang et al., 2009, Fukano et al., 2010, Zeng et al., 2010, Suh and Wyatt, 2009) such that the actual transferability of results into clinical practice remains uncertain. For example, studies routinely use optimally prepared CT colonography datasets, yet in reality, approximately 50% of cases are “poorly prepared” (Hara et al., 2011). Likewise, validation should use data from centres that have not contributed to algorithm development (external validation) (Halligan et al., 2006), to ensure previous exposure to the test data does not bias the result.

---

<sup>3</sup>cancerimagingarchive.net/

The developed registration method establishes full spatial correspondence between the prone and supine endoluminal surfaces. This section describes an external validation of this registration algorithm using CT colonography data generalisable to clinical practice and compares the results to those obtained using NDACC. This external validation was performed together with collaborators at University College Hospital, London (Darren Boone and Steve Halligan).

### 5.2.2 Prone-to-supine registration

The registration method has been described in detail in the previous chapters. Initialisation is provided by robust matches of haustral folds between both views. The haustral folds are segmented on the colon surface, using a graph-cut method applied to a surface curvature-based metric. Using a Markov Random Field based on similarity of folds and additional neighbourhood information, fold matches are then estimated between both views. Only inverse-consistent matches were used, i.e. the same match is obtained supine-to-prone and prone-to-supine (Hampshire et al., 2013). Secondly, the entire endoluminal surface is mapped to a cylinder, utilising a conformal mapping based on Ricci flow (Jin et al., 2008). The original surface curvature information is preserved during this step. Surface correspondence is then achieved using a non-rigid, cylindrical version of the well-known B-spline registration (Modat et al., 2010). Registration is driven by local shape measurements, i.e. shape index ( $SI$ ) computed on the colon surface. This measure has also shown to be useful in computer-aided detection (CADE) for CT colonography (Yoshida and Nappi, 2002). The sum-of-squared differences (SSD) of these  $SI$  measures are used to drive the cylindrical registration. In case of insufficient colonic distension, any locally collapsed region can be ignored during this cylindrical registration when computing the similarity measure. This is important as collapse can commonly occur in clinical practice. After convergence of the algorithm, any point on the endoluminal surface can be mapped between both corresponding acquisitions in either direction (prone-to-supine and supine-to-prone) by inverting the result (Roth et al., 2011, Hampshire et al., 2011).

### 5.2.3 Methods and materials

The external validation is based on publicly available CTC data (Johnson et al., 2008): the ACRIN CTC trial<sup>4</sup> investigators have made 103 anonymised cases, from 15 US centres, with polyps (including reference standard) available on the National Cancer Institutes National Biomedical Imaging Archive (NBIA)<sup>5</sup>. These cases include 69 medium (6-9 mm) and 32 large ( $\geq 10$  mm) polyps. These data represent cases that are generalisable to daily practice and which were not involved with the development of the registration method. No attempt has been performed to select ‘perfect’ cases – cases were examined and excluded if:

- no independent CTC reference data were available (41)
- the polyp was not visible in both datasets (7)
- the dataset was incomplete/corrupted (3) or the cancer/polyp was  $> 30mm$  (3).

This leaves 49 cases with 66 polyps (38 large, 28 medium) used for validation. Each present polyp was identified by an experienced observer [D. Boone] using the independent reference data and prone and supine 3D polyp volumes were labelled manually using *ITK-snap*<sup>6</sup>. The segmental distribution of polyps in the validation sample ( $n=66$ ) was compared to polyps  $\geq 6$  mm ( $n=547$ ) from the entire ACRIN CTC study (21) (with 2525 patients) to investigate the likely generalisability of the results. The segmental distribution of the used subset is comparable to the overall ACRIN CTC dataset as shown in Table 5.2. There is no significant difference when comparing the segmental distribution percentages between the

<sup>4</sup>[www.acrin.org/TabID/151/Default.aspx](http://www.acrin.org/TabID/151/Default.aspx)

<sup>5</sup>[imaging.nci.nih.gov/ncia/](http://imaging.nci.nih.gov/ncia/)

<sup>6</sup>[www.itksnap.org](http://www.itksnap.org)

two datasets with  $p = 0.85^7$ . By adopting the criteria proposed by Hara et al. (2011), 55% of validation cases ( $n=27$ ) had excess residual fluid compared to 52% (1313) of the total CT colonography studies from the same trial. 47% (23) had at least one region of complete luminal collapse, similar to the 48% (50) observed in the total, 103, positive cases in the publicly available database.

Table 5.2: Segmental distribution of polyps in the validation set and the total ACRIN CTC study.

<b>Colonic segment</b>	<b>Total Polyps in ACRIN study n (%)</b>	<b>Polyps included in this validation sample n (%)</b>
Rectum	90 (16)	14 (21)
Sigmoid	147 (27)	15 (23)
Descending	58 (11)	11 (17)
Transverse	95 (17)	7 (11)
Ascending	97 (18)	12 (18)
Caecum	60 (11)	7 (11)
Total	547	66

#### 5.2.4 Assessment of clinical utility

Currently, standard clinical workstations for CT colonography interpretation allow the rendering of a *virtual endoscopic* or *virtual fly-through* views in order to replicate the view during colonoscopy. The usefulness of the proposed registration algorithm in clinical practice can be judged using these three-dimensional renderings. To score the registration results, a polyp conspicuity grading was developed by two experienced radiologists (Darren Boone and Steve Halligan): after successfully establishing the prone-to-supine correspondence over the full colon surface, the user is automatically guided to the corresponding view in the opposing data set when clicking on a potential polyp (see Fig. 5.9). The endoluminal display is generated using a standard 120° field-of-view camera model and centring the camera origin at the corresponding centreline position, pointing towards the surface registration result. The clinical usefulness is then judged by using the following objective polyp conspicuity score. The score is proportional to the amount of 'mouse-driven navigation' necessary to bring the target polyp into view after registration:

- **5 'Successful'**: Polyp directly marked by registration prompt (Fig. 5.9)
- **4 'Successful'**: Polyp within same field of view (Fig. 5.10)
- **3 'Partially successful'**: Polyp becomes visible after  $\pm 90^\circ$  pan
- **2 'Partially successful'**: Polyp becomes visible after  $360^\circ$  pan
- **1 'Unsuccessful'**: Polyp only comes into view after navigation along centreline

---

<sup>7</sup>Related-Samples Wilcoxon Signed Rank Test, 5% significance level.

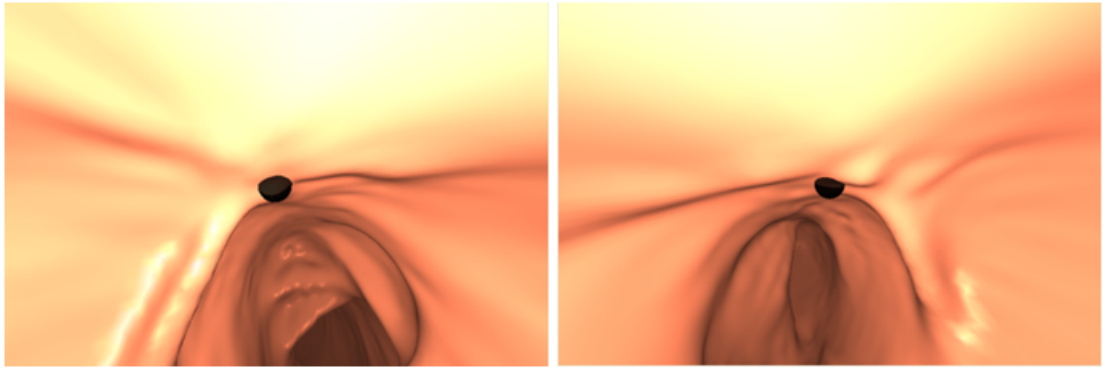


Figure 5.9: Example of polyp conspicuity score of 5 ('direct hit'). The registration prompt (black dot) marks the polyp indicated by the observer in the supine dataset (left). Following registration, the algorithm centres the prone view to point towards the endoluminal coordinates calculated by the algorithm (right). [Images courtesy of Darren Boone]

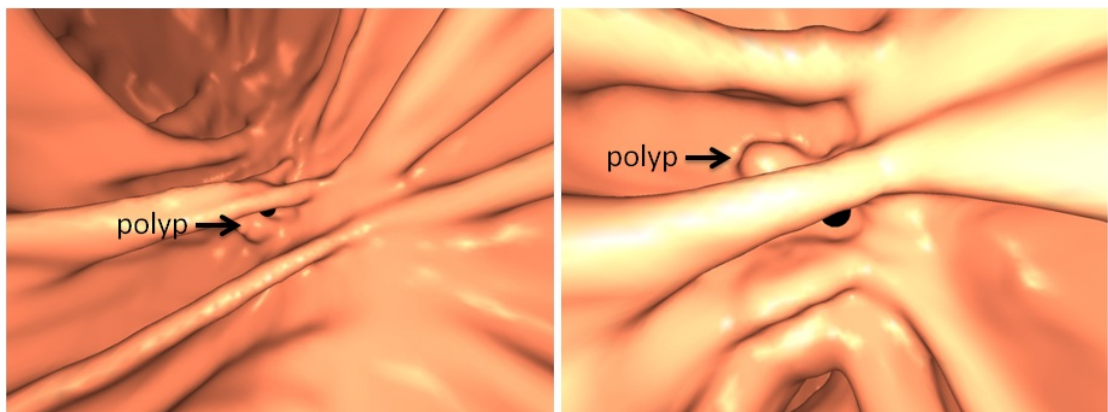


Figure 5.10: Example of polyp conspicuity score of 4 ('near miss'). The registration prompt (black dot) marks the polyp indicated by the observer in the prone dataset (left). Following registration, the algorithm centres the supine 3D field of view to point towards the coordinates calculated by the algorithm (right). The algorithm fails to indicate the polyp (arrow) correctly but the polyp is clearly visible in the same field of view. [Images courtesy of Darren Boone]

Similarly, a 3D conspicuity assessment is performed in order to compare to NDACC. Here, the scores of category 4 and 5 are combined as NDACC will not provide a registration prompt on the colon surface. It will only synchronise the virtual endoscopic views, looking straight along the centreline.

Furthermore, a conspicuity score was developed for aligning polyps using a standard multiplanar slice viewer which reflects the increasing necessity of mouse-driven navigation in all three orthogonal directions (axial, sagittal, coronal):

- **5 'Successful':** Polyp directly marked by registration prompt.
- **4 'Successful':** Polyp visible after  $\pm 15$  mm mouse-navigation
- **3 'Partially successful':** Polyp visible after  $\pm 20$  mm mouse-navigation
- **2 'Partially successful':** Polyp visible within  $\pm 30$  mm mouse-navigation
- **1 'Unsuccessful':** Polyp not within  $\pm 30$  mm of registration prompt

The polyp's apex was computed using the manual segmentations and was used to compute the 3D registration error and 2D slice displacement (measured in all 3 orthogonal directions). Both errors are

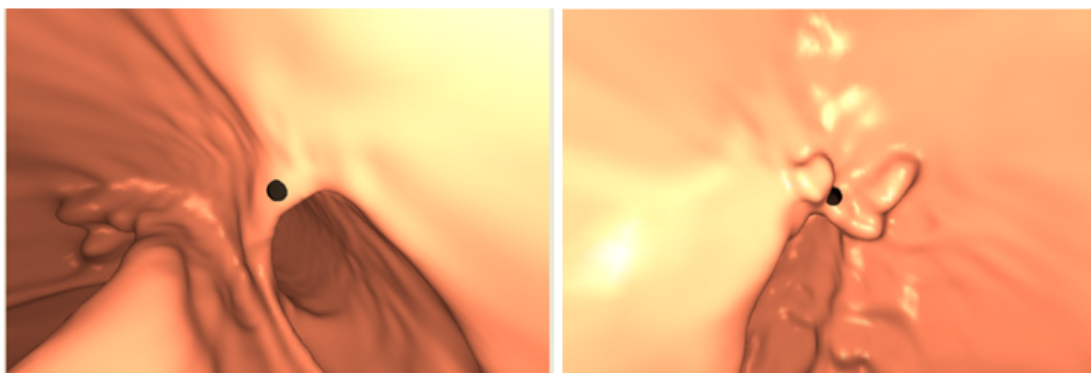


Figure 5.11: Example of polyp conspicuity score of 2 or 3 ('partially successful'). The polyp is only visible after rotation around the camera centre, but without navigation along the centreline when using virtual fly-through visualisation. [Images courtesy of Darren Boone]

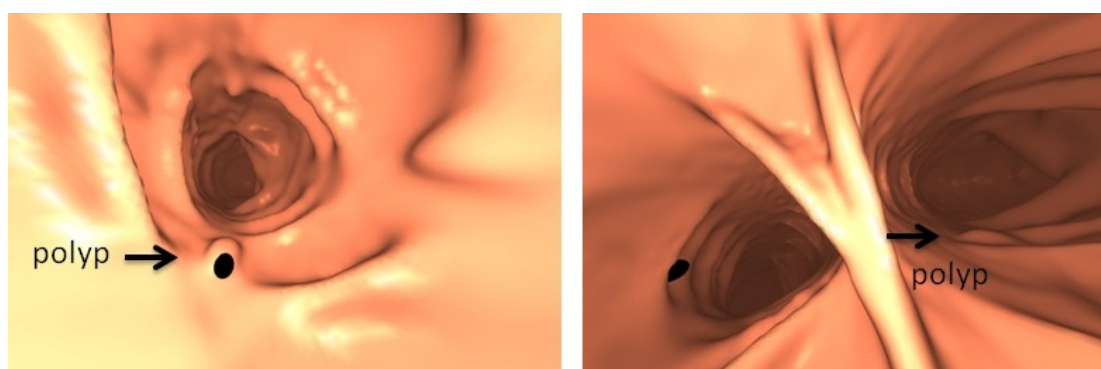


Figure 5.12: Example of polyp conspicuity score of 1 ('registration failure'). The polyp comes only visible after navigation along the colonic centreline. The algorithm places the registration prompt to a neighbouring fold close to the polyp (only 11 mm away). However, the fold is obstructing the view of the polyp and navigation along the centreline was required. This illustrates that the Euclidean distance alone is not enough when assessing the clinical usefulness of the registration method. [Images courtesy of Darren Boone]

reported in millimetres (mm). Polyps could be in the field of view or not, depending on the particular local configuration of the endoluminal colon shape and centreline. In order to reduce any bias towards the direction of transformation, all polyps were transformed in prone-to-supine as well as in supine-to-prone directions. This resulted in a total of 132 point transformations of 66 polyps for the following analysis. A 5% significance level was applied to all following cases when computing statistical significance. Despite the data reflecting clinical practice and depicting many areas of local colonic collapse, the registration was successfully computed in all of the cases (100%).

## 5.2.5 Results

### 5.2.5.1 3D registration error

The mean (std. dev.) 3D registration error, calculated for the whole data set (66 polyps in 49 cases), was 19.9 (20.6) mm. This error measures the distance between the target polyp's apex and the point indicated on the colon surface by the proposed method. A median error of 11.9 mm was achieved and the 3D registration error ranged between 1.0 mm and 85.8 mm. This maximum 3D error (85.8 mm) can be regarded as an outlier due to incomplete segmentation of the colonic lumen because of insufficient bowel distension. The prone segmentation had a large section of a 'loopy' sigmoid colon missing, in contrast

to a fully connected segmentation in supine. This resulted in a wrong estimation of the length of missing segment when using Euclidean distance between the un-collapsed segments, causing a suboptimal initial alignment of prone and supine cylindrical images, even after feature-based initialisation. This case can be considered a registration failure at the polyp location.

The 3D registration error did not vary significantly when comparing the polyp's location in different colonic segments ( $p = 0.65^8$ ). Furthermore, there was no significant increase in registration error within data cases exhibiting at least one local luminal collapse ( $p = 0.075^8$ ) using a Kruskal-Wallis test.

In order to provide a comparison to how a NDACC method would be used in clinical practice, the polyp's position along the centreline is found as the minimum distance between the polyps position on the colonic wall and at all points along the centreline, following the approach by Wang et al. (2009). In comparison, using NDACC leads to a mean (std. dev.) 3D error of 27.7 (15.2) mm between apex of the polyp and the point indicated along the centreline. Here, the measured error is significantly smaller ( $p = 0.001^9$ ).

#### 5.2.5.2 1D registration error

Finding the polyp's position along the centreline further allows to measure the registration error as a 1D distance along the centreline, summarised in Table 5.3. Using a non-parametric paired analysis (Wilcoxon Signed-Rank Test), the proposed method gives no significant advantage over using NDACC when using all 66 polyps: mean (std. dev.) of 17.6 (24.0) mm compared to 20.8 (18.5) mm using NDACC. However, when comparing registration by colonic segment, the method shows significant improvement over NDACC in the transverse, descending and sigmoid colon (see Table 5.3). A mean (std. dev.) of 19.3 (26.5) mm is achieved for these colonic segments in comparison to 26.9 (22.1) mm (NDACC). This is a significant improvement with  $p = 0.047^9$ . The largest improvement occurred in the transverse colon with a 15.3 mm reduction in mean registration error. This was anticipated as this segment was reported as being most mobile during positional change of the patient (Punwani et al., 2009).

Table 5.3: 1D registration error, measured as displacement along centreline [mm].

Colonic segment	Number of polyps		1D error proposed method	1D error NDACC
Rectum	14		13.1	14.7
Sigmoid	15		20.9	23.6
Descending	11		18.1	27.5
Transverse	7		17.9	33.2
Ascending	12		22.7	17.2
Caecum	7		9.9	10.5
Total	66	Mean	17.6	20.8
		Std. dev.	24.0	18.5

#### 5.2.5.3 Polyp conspicuity score in 3D

The registration achieved a direct alignment of the registration prompt in both opposing data sets in 89 (67.4%) of cases using virtual fly-throughs (conspicuity score of 5; see Fig. 5.9). Of 132 point transformations, 20 (15.2%) were transformed within the same field of view, leading to a score of 4 (see Fig. 5.10). Using the conspicuity grading, this leads to 82.7% 'successful' registrations. Nine (6.8%) polyp transformations required up to 90 degrees mouse-driven rotation around the camera centre in order to bring the polyp into view. In three cases (2.3%), a full 360 degrees of rotation were required

<sup>8</sup>Independent-Samples Kruskal-Wallis Test, 5% significance level.

<sup>9</sup>Related-Samples Wilcoxon Signed Rank Test, 5% significance level.

to achieve the same. Therefore, a total of 9.1% were rated being aligned 'partially successful' for clinical relevance. A total of eleven (8.4%) point transformations failed as further navigation along the centreline was necessary in order to bring the polyp into view. This compares favourably to using NDACC where a 'successful' (score 4) was only achieved in 37.1% of point transformations.

Figure 5.13 illustrates the conspicuity score in comparison to 3D registration error. This scatter plot shows the average conspicuity score from prone-to-supine and supine-to-prone directions versus the 3D registration error. An inverse relationship can be clearly observed as one would expect.

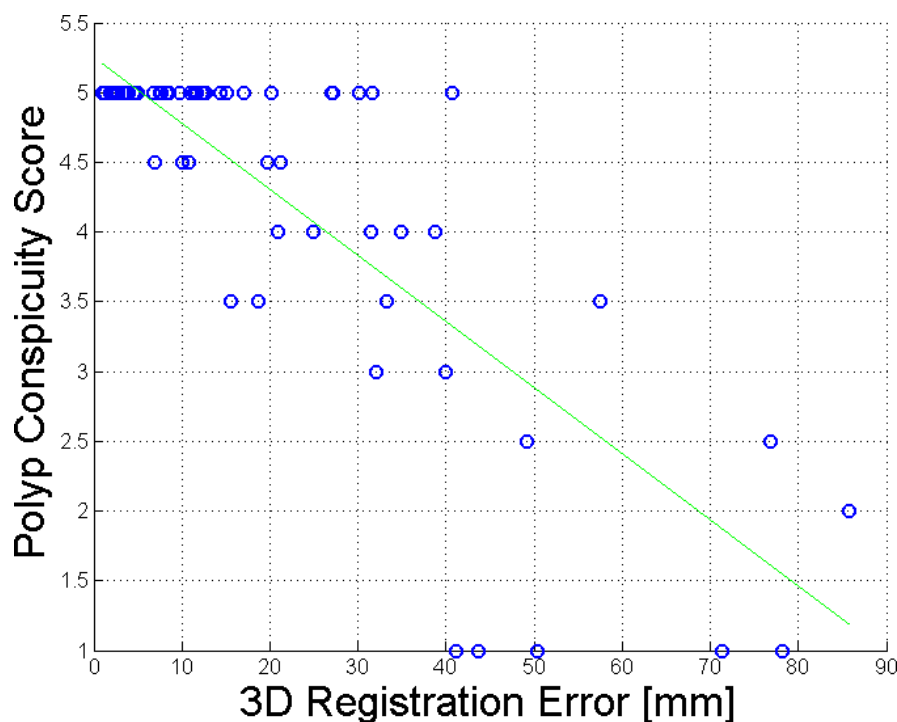


Figure 5.13: Scatter plot of the observer's conspicuity scores versus the 3D registration errors of the proposed method. An inverse relationship can clearly be seen and is illustrated by the line fitted in the least squares sense.

#### 5.2.5.4 Polyp conspicuity score in 2D

Using a purely multiplanar 2D slice visualisation, the registration error was assessed by judging clinical utility. This was expressed in necessary mouse-driven navigation in order to align the polyp apices in all three orthogonal directions. The algorithm correctly aligned the slices of 82 (62.1%) pairs of prone and supine polyps within  $\pm 15$  mm of displacement and were therefore being judged 'successful' for 2D navigation. 28 (21.3%) of cases were 'partially successful' registered, meaning that they were aligned within  $\pm 30$  mm. A total of 22 registrations (16.7%) failed as more than  $\pm 30$  mm of navigation was necessary to bring them into view. In comparison, NDACC achieved only 30 (22.7%) 'successful' alignments within  $\pm 15$  mm of displacement. 78 (59.1%) were judged 'partially successful' and 24 (18.2%) failed and was not visible within  $\pm 30$  mm of navigation.

### 5.2.6 Conclusion

In current clinical practice, prior to virtual colonoscopy, the interpreting clinician must check the validity of the workstation's proposed colonic segmentation to ensure correct navigation along the colonic lumen, primarily to ensure the computed centreline takes the correct path. Likewise, the proposed registration algorithm currently relies on the user accepting the colon segmentation and the correct order of colonic segments, defining start and end points. Thereafter, the algorithm for establishing correspondence over



the whole colonic surface is automated.

The assessment of registration accuracy used data from several hospitals unrelated to the development of the algorithm. This enables a generalisable assessment of the algorithm's performance which could be applied to normal clinical practice. The used study sample closely parallels the ACRIN data in quality of the bowel preparation and distension. The proposed algorithm compares favourably with previous methods which use optimally prepared cases or exclude cases exhibiting local collapses for validation. It provides a full surface registration of the colonographic data that enables the indication of a specific location on the endoluminal surface. Full surface registration would provide the observer with considerably more information, compared to a centreline position from where further navigation is necessary in order to find the target location. This is reflected in the choice of pre-specified criteria for polyp conspicuity, using 3D endoscopic fly-through visualisation following registration. Measuring the amount of navigation necessary in order to align prone and supine polyps after registration allows a direct comparison to centreline-based matching using NDACC. While it is intuitive that an accurate prone-to-supine registration would be beneficial for shortening interpretation time, further studies of clinical utility in everyday practice are necessary. For example, the effect on sensitivity and specificity when finding polyps needs to be evaluated.

This study is not without limitations: Some studies from the ACRIN validation archive were necessarily excluded due to the inability of the radiologists to confirm the presence of a polyp in both the prone and supine acquisitions. It is therefore possible that some inadequately distended cases were excluded from the analysis due to the lack of a reasonable reference standard.

In addition, while the processing of the endoluminal centreline occurs rapidly and is available to the reporting radiologist at the time of reporting, the method, at present, requires considerable processing time. This is for surface extraction, feature matching and non-rigid registration. However, once this step has been completed, transferring between matched prone and supine locations is practically instantaneous. This is reminiscent of another, well-established adjunct to CT colonographic interpretation – computer-aided detection (CADe) which, although now integrated into many vendor platforms, initially required several hours of processing time. I anticipate that with the implementation of the algorithms described in this thesis on multi-threaded and/or GPU architectures<sup>10</sup> the computation time can be reduced such that integration into a routine clinical workflow is feasible.

---

<sup>10</sup>Both conformal mapping using Ricci flow (Qiu et al., 2008) and B-spline registration (Modat et al., 2010) are parallelisable for the GPU.

### 5.3 Summary

In summary, computer-assisted prone-to-supine registration of the entire endoluminal surface can successfully be applied. An estimation of the achievable registration accuracies was performed using a porcine phantom with a reliable reference standard. Furthermore, publicly available CT colonography data, subset of a larger multi-centre trial, was used for external clinical validation. It compared favourably to using “normalised distance along the centreline”.

In all cases, the registration results show promise of the ability to rapidly and automatically switch between prone and supine positions after registration. This will further facilitate the interpretation of CT colonography data.

## Chapter 6

# Inverse consistency in the registration of prone and supine CTC

The work of this chapter is based on work presented at the *2011 MICCAI Workshop on Computational and Clinical Applications in Abdominal Imaging* (Roth et al., 2012). Section 6.4 was presented at *SPIE Medical Imaging 2013*.

### 6.1 Introduction

Robust registration between prone and supine data acquisitions for CT colonography is pivotal for medical interpretation but a challenging problem. In Chapter 3, a method for establishing spatial correspondence between prone and supine colonic surfaces derived from computed tomographic (CT) colonography (CTC) data was presented. The registration method involves the conformal mapping of both endoluminal surfaces derived from colon segmentations to cylindrical 2D domains in order to simplify this challenging 3D registration problem. This simplification is followed by a non-rigid cylindrical registration based on the well-accepted B-spline registration method (Rueckert et al., 1999, Modat et al., 2010). The similarity metric used to drive the cylindrical registration is the sum-of-squared differences ( $SSD$ ) of the shape index ( $SI$ ). The shape index (Koenderink, 1990, Koenderink and van Doorn, 1992) has also been used for detection of colonic polyps by computer-aided detection (CADe) methods, also applied to CT colonography data (Yoshida and Nappi, 2002). The  $SI$  values are computed on the original surface meshes which describe the endoluminal colon surface with the patient in the prone and supine position. Regions of possible local colonic collapse can be ignored during computation of the similarity measure when performing this cylindrical registration, this is important since luminal collapse is commonly encountered during clinical interpretation.

The registration method promises good accuracy in regions where the colon is well-distended in both orientations and when no segmentation errors are present. The reported mean (std. dev.) registration error of 13 polyps was 5.7 (3.4) mm when tested in 13 validation cases. However, the method might be less accurate if marked differences in distension or segmentation between prone and supine acquisitions are encountered, since this can precipitate marked dissimilarities in derived surface features. Similar feature patterns for driving the registration are required to align both surfaces accurately.

One measure when evaluating non-rigid registration algorithms over the whole of the deformation field is the inverse consistency error. This suggests improved registration quality when the inverse deformation is consistent with the forward deformation. This chapter aims to further investigate the effect of feature-based initialisation on the registration via evaluation of the inverse consistency error ( $ICE$ ). Furthermore, I aim to improve the registration result by constraining the optimisation process to be symmetric and inversely consistent.

## 6.2 Inverse consistency error

The *ICE* was proposed as an important criterion for evaluation of non-rigid registration methods by Christensen et al. (2006). The registration between CTC images can be computed in two directions: prone-to-supine and supine-to-prone. I arbitrarily denote the prone-to-supine direction as the forward transformation  $T_{ps}$ , e.g. with prone as source and supine as target image. The supine image as source and prone image as target is denoted as the inverse (supine-to-prone) transformation  $T_{sp}$ . The standard B-spline registration method is not inverse consistent, with the result that registration can converge to different solutions depending on the transformation direction; i.e. prone-to-supine or supine-to-prone. The inverse consistency error *ICE* measures this inconsistency as follows (Christensen and Johnson, 2001): any point  $p$  on the prone surface  $S_p$  can be transformed to the supine surface  $S_s$ , using the forward transformation  $T_{ps}$ . The inverse transformation  $T_{sp}$  is then applied to map the transformed point back to  $p'$  on  $S_p$ . The Euclidean distance  $\|\cdot\|$  between point  $p$  and  $p'$  in 3D space gives the value of *ICE* for any point  $p$ . This principle is illustrated in Fig. 6.1 for a point  $p$  in the transverse colon and can be formulated as

$$ICE = \|p' - p\| = \|T_{sp}(T_{ps}(p)) - p\|. \quad (6.1)$$

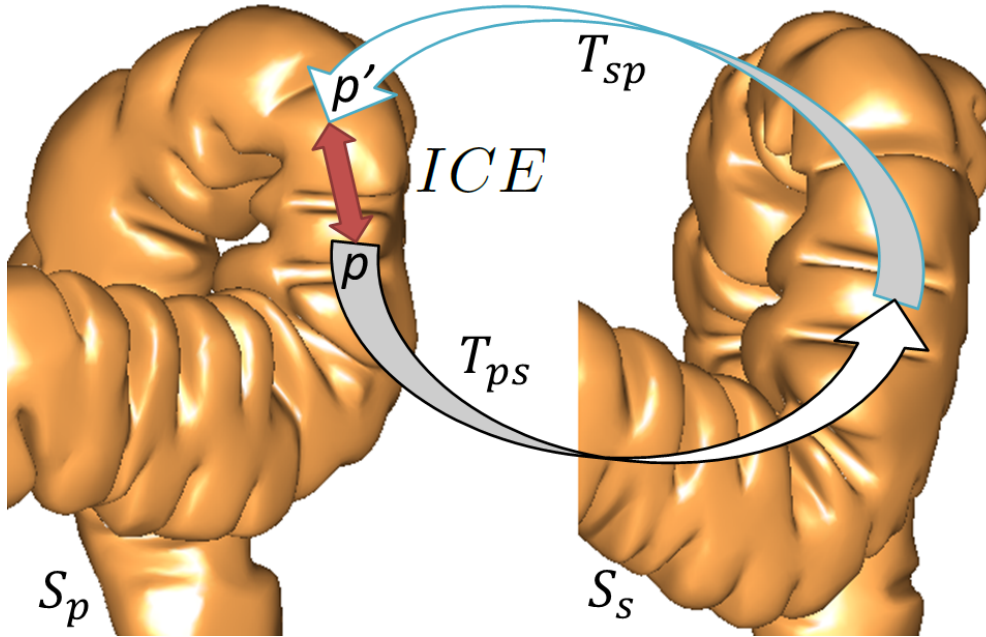


Figure 6.1: Computing the inverse consistency error (*ICE*). The prone-to-supine direction is denoted as the forward transformation  $T_{ps}$ , e.g. with prone as source and supine as target image. The supine image as source and prone image as target is denoted as the inverse (supine-to-prone) transformation  $T_{sp}$  between the colon surfaces  $S_s$  and  $S_p$ . Any point  $p$  is transformed in both directions such that the Euclidean distance  $\|\cdot\|$  between point  $p$  and  $p'$  in 3D space gives the value of *ICE*.

## 6.3 Evaluation of inverse consistency

For the following experiments, I used anonymised CTC data, acquired during normal clinical practice and following generally accepted recommendations for CTC data acquisition (Taylor et al., 2007). These data consist of a total of 17 validation cases<sup>1</sup>, of which 5 exhibited local luminal collapse in at least one

<sup>1</sup>These are the same patient data sets as were used for validation in Chapter 4; plus four cases which were previously excluded due to vast differences in distension. This reference standard has been produced for the study

of the patient's positions. Two experienced radiologists (E. Helbren and A. Plumb) and a computer scientist (T. Hampshire) manually identified haustral folds of confident correspondence, with all three readers in consensus. This was achieved using cylindrical image representations and virtual 3D fly-through renderings for navigation through the prone and supine acquisitions. This procedure resulted in a total of 1743 pairs of corresponding landmarks with an average of 103 pairs of haustral folds per case (see (Hampshire et al., 2013) for more detail).

### 6.3.1 Inverse consistency without feature initialisation

Accuracy of registration can only be evaluated where corresponding features have been identified. This is only feasible when there are easily identifiable corresponding features (e.g. polyps) in both acquisitions (i.e. where the registration is more likely to give a good result). In contrast, the *ICE* can be calculated anywhere on the cylindrical representations and does not require manually identified landmarks, simultaneously eliminating any error due to landmark mismatching.

The *ICE* values can vary for different regions of the images. Large *ICE* values often occur where the surface features in the two acquisitions appear very different since the registration algorithm is unable to align the different features successfully. Figure 6.2 illustrates the *ICE* computed for each pixel of the cylindrical images and mapped back to the endoluminal colon surface in Fig. 6.3. The total mean (std. dev.) *ICE* for all 17 validation patients is 5.7 (4.5) mm. The mean and std. dev. of *ICE* is higher in the 5 collapsed cases and in 4 cases with varying amounts of distension excluded from previous studies; 8.4 (3.6) mm and 7.9 (5.3) mm as opposed to a mean *ICE* for the 8 well insufflated cases of 2.9 (3.0) mm (see Table 6.2). Areas of high *ICE* might indicate more uncertainty in both images regarding which features need to be aligned with which. Therefore, registration does not necessarily converge towards the same solution in forward and inverse directions. However, a registration result with low *ICE* does not necessarily suggest good correspondence between two images (Christensen et al., 2006); further evaluation of registration accuracy is necessary. Manually selected fold correspondences can be used to establish a fold registration error (*FRE*), which measures misalignment of reference points in 3D after cylindrical non-rigid registration as an index of accuracy (as in chapter 3).

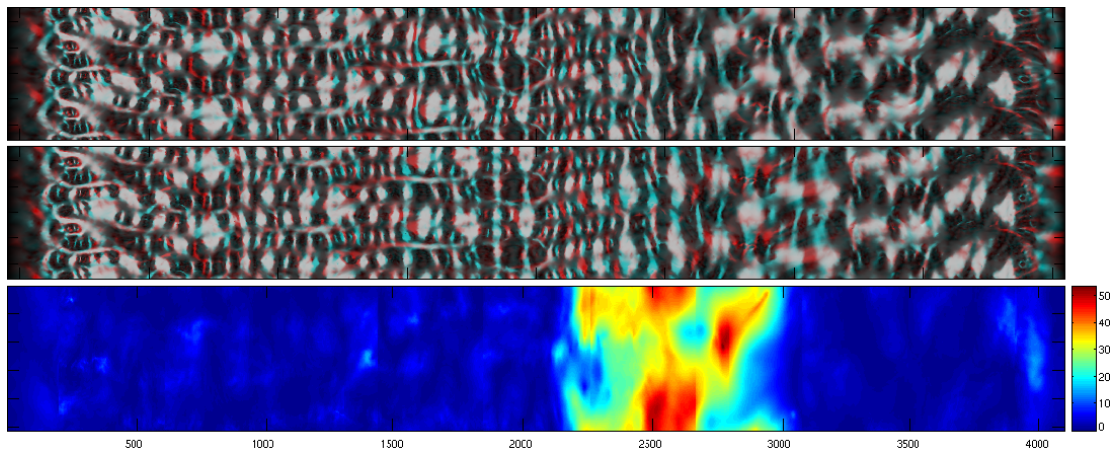


Figure 6.2: Difference between forward (top) and inverse (middle) registrations. The registration results are shown using a colour scheme which displays source features as blue and target features as red. After non-rigid alignment, overlapping features are displayed in grey. The forward (top) and inverse (middle) registrations show areas of inconsistency, especially around 2500 pixels in  $x$ -direction (along the colon). This is reflected in larger *ICE* values in these areas (bottom). The colour scale is in mm.

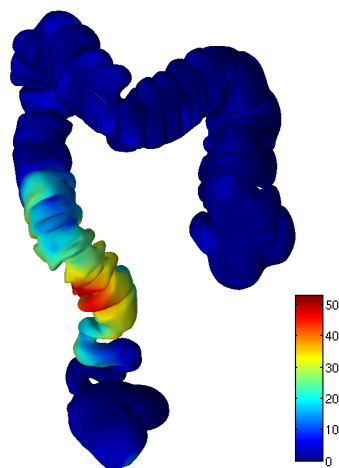


Figure 6.3: *ICE* values mapped onto the colon surface. The colour scale is in mm.

### 6.3.2 Initialisation using B-Spline approximation

Hampshire et al. (2011, 2013) show that an initialisation of the registration method using robustly matched features (e.g. haustral folds) can improve the registration accuracy. Only inverse-consistent matches are used, i.e. the same match being obtained supine-to-prone and prone-to-supine, which provides more robust matchings (Hampshire et al., 2013). Using a good initialisation can roughly align the correct folds of the cylindrical images leading to convergence to the correct solution in the subsequent cylindrical B-spline registration. The following Table (6.1) shows the number of fold matches generated by Hampshire et al. (2013)’s method for each validation case which will be used to provide a feature-based initialisation. It can be observed that well-prepared and similarly distended cases (1-8) lead to more feature matches (120.3 on average) in comparison to cases exhibiting local collapses (9-13 with 79.0 on average) or with marked differences in distension (14-17 with 81.5 on average).

Table 6.1: Number of inverse-consistent haustral fold matches that can be used for a feature-based initialisation. The segmental locations of local colonic collapse are indicated with DC (descending colon) and SC (sigmoid colon).

Patient #	Collapse in prone	Collapse in supine	# Fold matches
1	none	none	93
2	none	none	136
3	none	none	140
4	none	none	78
5	none	none	94
6	none	none	152
7	none	none	175
8	none	none	94
<b>Mean</b>			<b>120.3</b>
<b>Std. dev.</b>			<b>34.9</b>
9	1×DC	1×DC	82
10	1×DC	1×DC	18
11	none	1×SC	68
12	3×(DC, SC)	none	104
13	none	1×DC	123
<b>Mean</b>			<b>79.0</b>
<b>Std. dev.</b>			<b>40.0</b>
	Previously	excluded	
14	none	none	61
15	none	none	69
16	none	none	151
17	none	none	45
<b>Mean</b>			<b>81.5</b>
<b>Std. dev.</b>			<b>47.4</b>
	<b>Total</b>		
<b>Mean</b>			<b>99.0</b>
<b>Std. dev.</b>			<b>42.2</b>

Initialisation is achieved by approximating a smooth function  $f$  which relates 2D positions of feature matches in one cylindrical image (e.g. prone  $\{(x, y)\}$ ) to their corresponding position in the other image (e.g. supine  $\{(x', y')\}$ ). The following approximation of  $f$  used for initialisation is based on a *scattered data interpolation algorithm* presented by Lee et al. (1997), but modified to perform in cylindrical space by Hampshire et al. (2012). The domain of the cylindrical images is  $\Omega$  with  $0 \leq x \leq N_x$  and  $0 \leq y \leq N_y$ . Here,  $N_x$  and  $N_y$  denote the size of the cylindrical images. The approximations  $x' = f_x(x, y)$  and  $y' = f_y(x, y)$  which map between both images in  $x$ - and  $y$ -directions are independent and can be derived simultaneously. The overall mapping between both images that approximates the displacement for any point over the continuous domain  $\Omega$  is therefore  $(x', y') = f(x, y)$ . A set of sparse feature points in prone  $P = \{(x_c, y_c, v_c)\}$  with the known  $x, y$ -displacement vector  $v_c$  is approximated by using a bicubic B-spline defined by a uniform control point lattice  $\Phi$  over the entire domain  $\Omega$  (Lee et al., 1997). The control point lattice is of size  $(m + 3) \times (n + 3)$  with its values  $\phi_{ij}$  indexed by  $i = -1, 0, \dots, m + 1$  and  $j = -1, 0, \dots, n + 1$  and spanning an integer grid in  $\Omega$ . For example, the approximated function  $f_x$  is defined by:

$$f_x(x, y) = \sum_{k=0}^3 \sum_{l=0}^3 B_k(s) B_l(t) \phi_{(i+k)(j+l)}. \quad (6.2)$$

Here  $i = \lfloor x \rfloor - 1$ ,  $j = \lfloor y \rfloor - 1$ ,  $s = x - \lfloor x \rfloor$  and  $t = y - \lfloor y \rfloor$ . The approximation for  $f_y(x, y)$  is defined in the same way.  $B_k$  and  $B_l$  represent the cubic B-Spline basis functions consisting of the following terms:

$$\begin{aligned} B_0(t) &= (1 - t)^3 / 6 \\ B_1(t) &= (3t^3 - 6t^2 + 4) / 6 \\ B_2(t) &= (-3t^3 + 3t^2 + 3t + 4) / 6 \\ B_3(t) &= t^3 / 6 \end{aligned} \quad (6.3)$$

with  $t$  being in the range  $0 \leq t < 1$ . For every feature location  $(x_c, y_c)$  in the continuous space of  $\Omega$ , a different value  $\phi_c$  of a control point  $\phi_{ij}$  is computed by:

$$\phi_c = \frac{w_c v_c}{\sum_{a=0}^3 \sum_{b=0}^3 w_{ab}^2} \quad (6.4)$$

with  $w_c = w_{kl} = B_k(s) B_l(t)$ ,  $k = (i + 1) - \lfloor x_c \rfloor$ ,  $l = (j + 1) - \lfloor y_c \rfloor$ ,  $s = x_c - \lfloor x_c \rfloor$  and  $t = y_c - \lfloor y_c \rfloor$ . The subscripts of  $w$  describe the indexing of a basis function in 6.3 The use of basis functions means that only the  $4 \times 4$  neighbourhood of each control point needs to be taken into account in order to compute the value of any control point  $\phi_{ij}$  (Lee et al., 1997). Any  $4 \times 4$  neighbourhood is defined as

$$P_{ij} = \{(x_c, y_c, v_c) \in P \mid i - 2 \leq x_c < i + 2, j - 2 \leq y_c < j + 2\}. \quad (6.5)$$

In order to compromise between all different values of  $\phi_c$  at control point  $\phi_{ij}$ , the value of  $\phi_{ij}$  is chosen such that the following error function is minimised:

$$e(\phi_{ij}) = \sum_c (w_c \phi_{ij} - w_c \phi_c)^2. \quad (6.6)$$

The analytical solution uses the differential of  $e(\phi_{ij})$  with respect to  $\phi_{ij}$ , resulting in (Lee et al., 1997):

$$\phi_{ij} = \frac{\sum_c w_c^2 \phi_c}{\sum_c w_c^2} \quad (6.7)$$



In case  $P_{ij}$  contains several feature points, equation 6.7 results in a least-squared solution of  $\phi_{ij}$  that minimises a local approximation error. If only one feature point is present in  $P_{ij}$ , equation 6.7 can be simplified to 6.4. In case no feature point is present in the local neighbourhood  $P_{ij}$ ,  $f(x_c, y_c)$  remains unaffected by the control point  $\phi_{ij}$  (Lee et al., 1997).

### 6.3.2.1 Hierarchical B-Spline approximation

In order to establish a smooth functional over the entire colonic surface domain  $\Omega$ , Hampshire et al. (2013) follow the approach of Lee et al. (1997). A multilevel B-spline with coarse to fine control point lattices is used to generate a final transformation  $f(x, y)^2$ . This allows larger global deformations in the coarser levels and more accurate local deformations in the finer levels of the approximation scheme. Multilevel control point lattices are generated by using a refinement process which combines the above functions into one B-spline function. Each finer level of control point lattice  $\Psi'_k$  is derived from the previous coarser level  $\Psi_k$  such that  $F(\Psi'_{k-1}) = F(\Psi_k - 1)$ , with  $F(\Psi'_0) = f_0(x_c, y_c)$ . If  $\Psi_k$  is an  $(m + 3) \times (n + 3)$  control point grid, then the next grid level  $\Psi_{k+1}$  is refined to be of size  $(2m + 3) \times (2n + 3)$  (Lee et al., 1997). The refinement process starts at level  $\Psi_0$  and the control point at position  $ij$  in level  $\Psi_k$  is equal to that of the control point at position  $(2i, 2j)$  in level  $\Psi'_{k-1}$ . A function  $f_{k+1}$  is derived using the control point lattice  $\Phi_{k+1}$  which approximates the data  $P_k = \{(x_c, y_c, \Delta_k v_c)\}$  in order to remove the *residual error* in the current level. The approximated data in  $P_{k+1}$  is defined as

$$\Delta_k v_c = v_c - \sum_{i=0}^{k-1} f_i(x_c, y_c) = \Delta_{k-1} v_c - f_{k-1}(x_c, y_c) \quad (6.8)$$

In the coarsest level,  $\Delta_0 v_c = v_c$ . At each subsequent level the function minimises the residual errors from the previous coarser control point lattice level  $\Psi'_{k-1}$ . This approach is defined by a progressive control point lattice  $\Psi_k = \Psi'_{k-1} + \Phi_k$  which continues from the coarsest to the finest levels.

### 6.3.2.2 Application to cylindrical images

The above described hierarchical B-spline approximation technique is now applied to the cylindrical representations of the colonic surface. The sparse set of haustral fold correspondences in the prone and supine 3D space are mapped to the common 2D domain of the cylindrical images, generated by conformal mapping (see Ricci flow in Chapter 3). Knowledge of the correspondence between the horizontal and vertical positions  $\{(x_c, y_c)\}$  in each 2D image allows the computation of 2D displacement vectors  $v_c$  between these sparse points which will be used to approximate the B-spline deformation over the full cylindrical images.

In order to account for the cylindrical nature of the 2D images, both images and point correspondences are tripled in  $y$ -direction. However, this cylindricity causes ambiguity to whether a vertical displacement should be pointing up or down. Hampshire et al. (2013) account for this by forcing all displacements in  $y$ -direction to be smooth over the domain  $\Omega$ . An iterative scheme is applied at each level of B-spline approximation which aims to minimise the *residual error*  $e_y$ . This error measures the maximum displacement between the approximated and the true  $y$ -position of all corresponding point locations:

$$e_y = |F(x_c, y_c) - v_c|_y. \quad (6.9)$$

At each iteration, the point displacements in  $y$  are adjusted such that

$$v'_c = v_c + \text{sign}(F(x_c, y_c) - v_c) \cdot N_y. \quad (6.10)$$

Here,  $N_y$  again denotes the size of the original cylindrical image in  $y$ -direction. After this process, the entire image is shifted in the  $y$ -direction such that the  $y$ -components of  $v_c$  are minimised. Finally, the

---

<sup>2</sup>In this study 6 levels were used.

full hierarchical B-spline approximation is repeated a second time with the sorted and shifted 2D point correspondences in order to estimate the final function  $F(\Phi)$ . Figures 6.4 and 6.5 illustrate the B-spline approximation process. Either end of the cylindrical images should stay fixed in  $x$ -dimension. Therefore, at each refinement level of the hierarchical B-spline approximation, the  $x$ -component of the transformation data is set to  $x' = 0$  at the control points  $\{\phi_{ij} | i = -1, 0, m, m+1; j = -1, 0, \dots, n+1\}$ . The

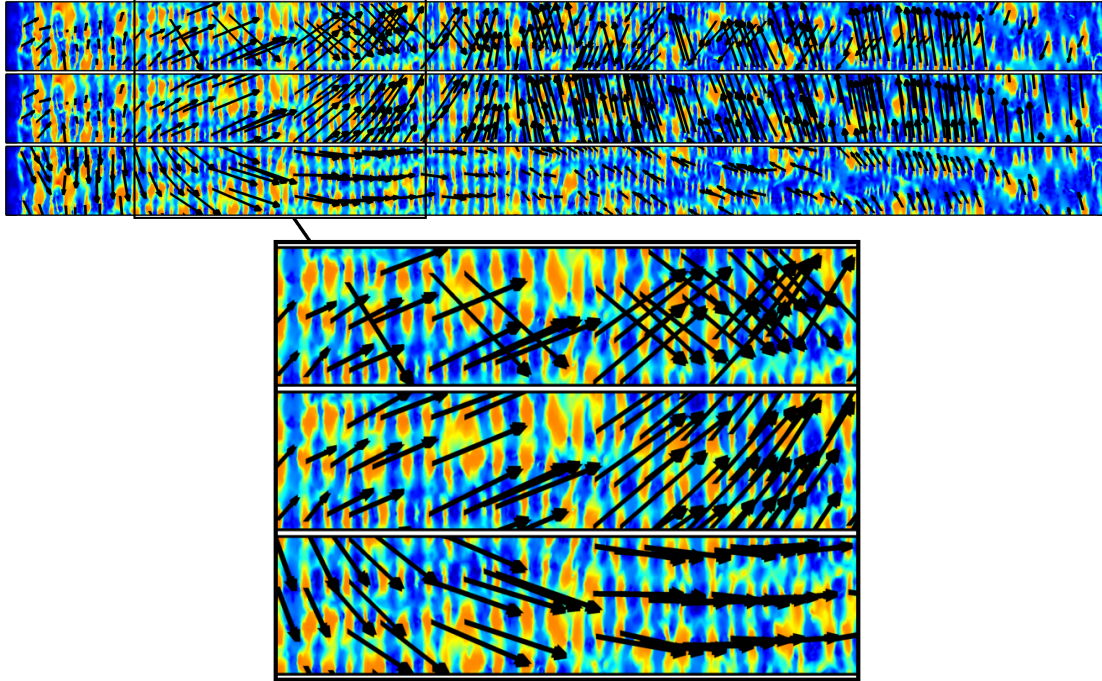


Figure 6.4: A cylindrical image with arrows depicting the displacements  $v_c$  computed from the prone and supine fold correspondences. The top image illustrates the ambiguity of these displacements in  $y$ . The middle image illustrates the sorted displacements after minimising the error  $e_y$  and the bottom image shows the image shifted in  $y$  in order to minimise the total displacement in  $y$ -direction. [Images courtesy of Thomas Hampshire]

final B-spline approximation  $F$  allows the transformation of any point  $\{(x, y)\} \in \Omega$  in one of the cylindrical images into the space of the other. The transformation  $F$  could be used on its own to establish correspondence between the entire prone and supine cylindrical images and therefore in the original 3D surface domain of the CTC images. However, the transformation  $F$  can furthermore be used as a robust initialisation to the registration method presented in Chapter 3: the entire cylindrical source image is deformed and re-sampled, based on the approximation  $F$  and used as input image for a subsequent intensity-based B-spline registration (as introduced in Chapter 3). This intensity-based B-spline registration will allow an even finer alignment of surface features and therefore improve the registration result upon the B-spline approximation.

This assumption is confirmed by the measurements of registration accuracy summarised in Table 6.2. Hampshire et al. (2013) report a significant improvement in registration accuracy from a mean (std. dev.) of 11.9 (11.1) mm to 6.0 (1.9) mm for the total of cases ( $p < 0.001$ ). Large improvements in accuracy were especially achieved in cases where the dissimilarity of features is inherently higher (e.g. the five cases exhibiting local colonic collapses) and cases which were excluded from previous studies due to vast differences in local distension (i.e. patients 14-17, see Chapter 3).

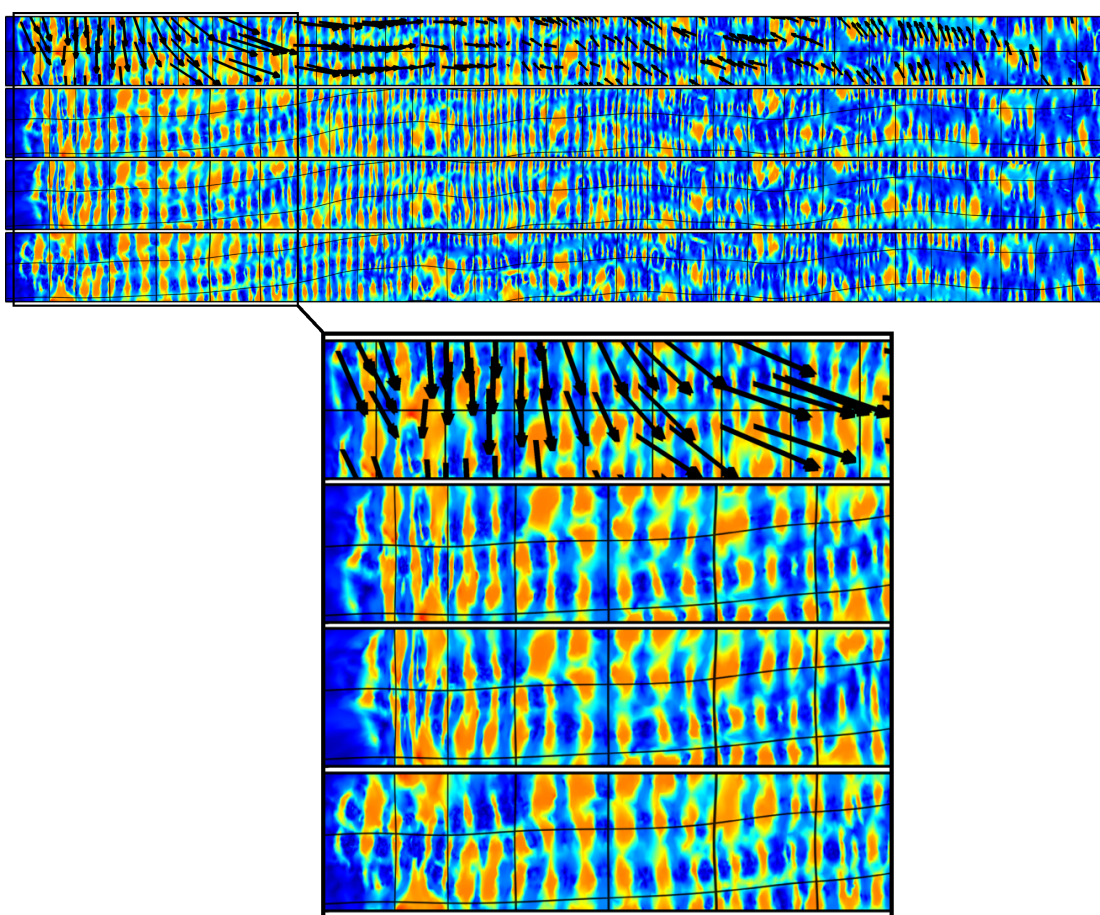


Figure 6.5: B-spline approximation of the deformation field used for initialisation. The top image shows the sorted displacements and the initial uniform control point lattice (indicated by the grid lines). After approximation, the entire cylindrical image is deformed using the final control point lattice (2nd from top). This provides good initialisation for a subsequent intensity-based B-spline registration in cylindrical domain which provides further alignment (3rd from top). The target image (supine) is shown in the bottom row. [Images courtesy of Thomas Hampshire]

Table 6.2: The mean fold registration error ( $\overline{FRE}$ ) and mean inverse consistency error ( $\overline{ICE}$ ) in mm just using the B-spline registration as in Chapter 3 ( $_1$ ), after just using the feature-based initialisation as registration ( $_2$ ) and after initialisation followed by a subsequent intensity-based B-spline registration ( $_3$ ).  $\overline{ICE}$  is only computed after intensity-based registration without ( $_1$ ) and with ( $_3$ ) feature-based initialisation. The locations of where the colon is collapsed are given (DC: descending colon, SC: sigmoid colon). Cases which were previously excluded due to vast differences in distension are now included.

Patient	Collapse in prone	Collapse in supine	$\overline{FRE}_1$ [mm]	$\overline{FRE}_2$ [mm]	$\overline{FRE}_3$ [mm]	$\overline{ICE}_1$ [mm]	$\overline{ICE}_3$ [mm]
1	none	none	6.9	7.1	6.4	2.4	2.2
2	none	none	6.9	7.4	5.4	2.8	1.7
3	none	none	4.6	5.4	4.5	1.3	1.0
4	none	none	9.2	4.3	4.3	10.1	1.4
5	none	none	5.0	4.4	5.1	1.4	1.3
6	none	none	3.5	4.6	3.6	1.2	1.1
7	none	none	5.0	5.5	5.0	1.3	1.1
8	none	none	5.2	6.0	4.9	2.3	1.2
9	1×DC	1×DC	27.5	14.9	11.7	12.9	2.9
10	1×DC	1×DC	4.8	12.2	5.7	9.0	2.9
11	none	1×SC	5.1	9.5	5.0	6.4	11.0
12	3×(DC, SC)	none	17.4	8.1	5.9	10.0	2.4
13	none	1×DC	6.2	6.7	5.4	3.5	2.3
Previously excluded							
14	none	none	48.1	18.8	9.1	10.2	4.6
15	none	none	12.9	9.0	7.8	4.4	6.2
16	none	none	19.7	9.9	5.8	2.7	7.6
17	none	none	14.2	9.9	6.8	14.3	5.7
Mean			<b>11.9</b>	<b>8.5</b>	<b>6.0</b>	<b>5.7</b>	<b>3.3</b>
Std. dev.			<b>11.1</b>	<b>3.8</b>	<b>1.9</b>	<b>4.5</b>	<b>2.8</b>

### 6.3.3 Inverse consistency after feature initialisation

This improvement in registration accuracy suggests the method is more robust when initialisation is good. Increased robustness is also reflected in a reduction of inverse consistency error  $ICE$  as shown in Table 6.2. Figure 6.6 shows the reduction of an area of high  $ICE$  after initialisation. Another example is shown in Fig. 6.7 and confirms this assumption for another patient in which a short section of colon is collapsed. The total mean  $ICE$  for all 17 validation patients is reduced from a mean (std. dev.) of 5.7 (4.5) mm to 3.3 (2.8) mm. Table 6.2 lists the mean  $FRE$  and mean  $ICE$  before and after using a feature-based initialisation for each patient. In all but three cases (patients 11, 15 and 16) a reduction of mean  $ICE$  can be observed after feature-based initialisation. However, registration accuracy ( $FRE$ ) is improved in those three cases. In fact, only three cases (patients 5, 6 and 10) show a slight increase in registration error of  $\leq 0.8$  mm which is likely to be negligible, due to inaccuracies of the reference standard in defining exactly corresponding points at the centre of prone and supine haustral folds.

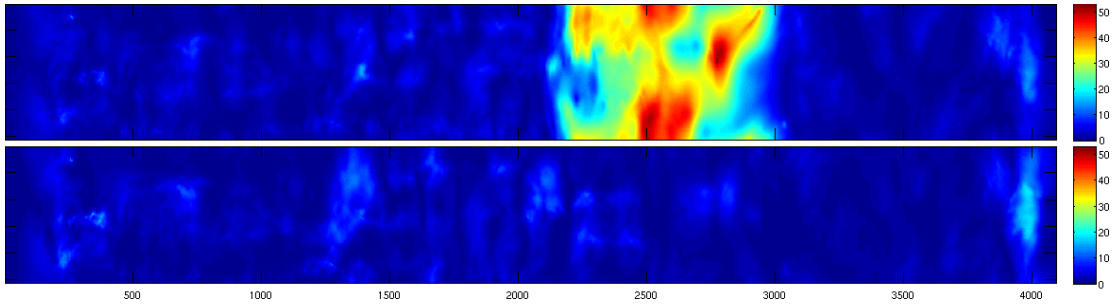


Figure 6.6: The inverse difference metric ( $ICE$ ) before (top) and after (bottom) initialisation using feature correspondences for a fully connected case.

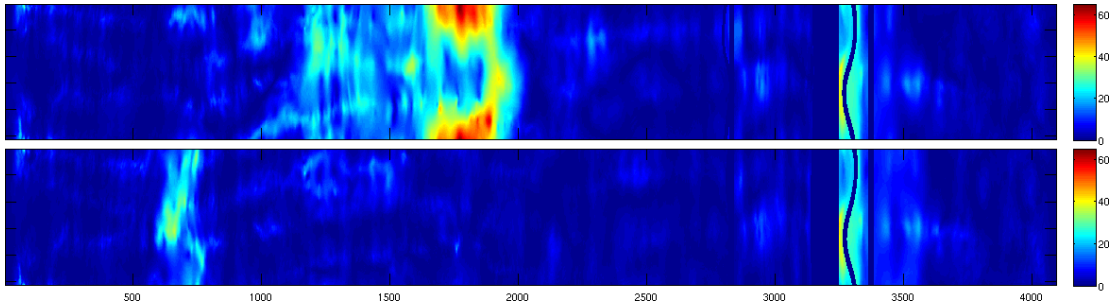


Figure 6.7: The inverse difference metric ( $ICE$ ) before (top) and after (bottom) initialisation using feature correspondences for a collapsed case.

## 6.4 Inverse-consistent symmetric registration

The results in the previous section show that a robust initialisation can improve the inverse consistency of the cylindrical B-spline registration method. While improved inverse consistency alone does not guarantee good correspondence, a concomitant improvement in registration accuracy suggests that registration is more robust when using a feature-based initialisation.

Further improvement might be achieved by implementing a non-rigid registration method that is inverse-consistent. This might help optimise registration in cases where false local minima in the similarity function that is being optimised are present. Information from both forward and inverse direction may encourage convergence towards the correct solution. Investigation of such a registration method is the topic of the following section.

### 6.4.1 Motivation

I hope that robust and accurate registration of prone and supine colonic surfaces acquired during CT colonography might lead to faster and more precise detection of colorectal cancer and polyps. Any directional bias when registering the colonic surfaces could lead to incorrect anatomical correspondence resulting in diagnostic errors. Despite this, non-rigid registration methods are often implemented asymmetrically, which could influence the registration result negatively. The aim is to reduce directional bias and so increase robustness by adapting a cylindrical registration algorithm to be both symmetric and inverse-consistent.

The problem of establishing spatial correspondence between the full colonic surface extracted from prone and supine CT colonography acquisitions is a challenging one. Several algorithms have been proposed to align both surfaces (e.g. (Huang et al., 2007, Suh and Wyatt, 2009, Zeng et al., 2010, Roth et al., 2011)). All these methods assume that registration is being performed with one image (e.g. the prone) as the transformed or “floating” image and the other image (e.g. the supine) as the “reference” image. Image registration then finds spatial correspondences between the reference and floating image. However, computing these correspondences in just one direction might bias the registration result: i.e. such computation might result in different spatial correspondences depending on the order of input images. Assuming there is a unique anatomical correspondence between the prone and supine surface, this is undesirable. With perfect inverse consistency, the result of registering the prone to the supine colonic surface should be identical to the inverse of registering the supine to the prone colonic surface. Therefore, inverse-consistent symmetry in the registration transformation, which is independent of the order of input images, is preferable.

The amount of difference depending on the direction of registration can be measured by the inverse consistency error (*ICE*) (as introduced earlier). A prone-to-supine registration method which aims to minimise *ICE* could lead to improved registration accuracy and robustness by providing inversely consistent anatomical correspondence. By constraining inverse-consistency in the registration, false local minima in the objective function might be reduced. In such cases the registration might achieve better alignment using an inverse-consistent symmetric approach. Using both forward (prone-to-supine) and backward (supine-to-prone) directions for registration may encourage convergence towards the correct result. Symmetric image registration has been shown to reduce local minima in the objective function and generally improves registration quality (Avants et al., 2008, Vercauteren et al., 2008).

It can be assumed that there is only one ‘true’ anatomical correspondence between images of the same patient. If the registration result differs depending on the direction of registration, at least one of the results has to be incorrect. Therefore, the registration result might be implausible. Reducing the amount of inconsistency in the registration can be a useful method of improving the registration accuracy and might result in a more valid deformation.



### 6.4.2 Related work

Recent work that aims to remove directional bias in non-rigid image registration algorithms includes Symmetric Normalization (SyN) (Avants et al., 2008) from the Advance Normalization Tools (ANTs<sup>3</sup>) package and the approach proposed by Vercauteren et al. (2008), using demons-based registration. Bias introduced by the direction of registration was recently shown to cause overoptimistic estimation of statistical power when quantifying longitudinal atrophy in structural MRI images (Thompson et al., 2011).

It was shown in the previous sections of this Chapter (Roth et al., 2012) that using robustly matched features to initialise the well-known non-rigid B-spline registration method (Rueckert et al., 1999) can reduce the inverse consistency error. This generally increases the quality of the registration result. However, the standard B-spline registration algorithm is not inverse-consistent and could therefore still bias the result negatively towards direction of registration. In order to overcome this limitation, Christensen and Johnson (2001) proposed an inverse-consistent image registration method using a 3-D Fourier series representation for parametrisation of the forward and backward transformations (Amit, 1994). Feng et al. (2009) modified the B-spline registration to minimise the inverse consistency error by optimising forward and backward transformations concurrently. However, their implementation does not ensure one-to-one correspondence. Preservation of one-to-one correspondence was incorporated by Modat et al. (2012) using a Jacobian-based constraint. I follow this approach based on B-spline registration but modify the deformation to occur in cylindrical space, taking advantage of the anatomical topology specific to the colon. The prone-to-supine and supine-to-prone transformations are concurrently optimised to be inverse consistent and symmetric. Furthermore, both transformations are penalised against folding and therefore encourage one-to-one mappings.

Assessment of the implementation is performed using a set of fully distended cases as well as cases exhibiting local colonic collapse.

### 6.4.3 Symmetric prone-to-supine transformation model

I implemented a symmetric formulation of the same non-rigid B-spline image registration method in cylindrical space in order to align the cylindrical representations of the prone and supine endoluminal surfaces (see Chapter 3). My cylindrical implementation is based on the open-source<sup>4</sup> software developed by Modat et al. (2012). A symmetric similarity cost function measures the mean-of-squared-differences ( $MSD$ ) between the prone and supine cylindrical images  $P$  and  $S$ , using both the prone-to-supine transformation  $\mathbf{T}_{ps}$  and the supine-to-prone transformation  $\mathbf{T}_{sp}$  simultaneously. This principle is illustrated in Fig. 6.8, where the colour indicates local  $SI$  values. Inverse consistency of the transformation is encouraged by adding an appropriately weighted penalty term to the optimisation function. A symmetric similarity cost function measures the mean-of-squared differences ( $MSD$ ) between the prone and supine cylindrical images  $P$  and  $S$ , using both the prone-to-supine transformation  $\mathbf{T}_{ps}$  and the supine-to-prone transformation  $\mathbf{T}_{sp}$  simultaneously:

$$MSD_{Sym} = -\frac{1}{N_S} \sum_{\vec{x} \in S} [S(\vec{x}) - P(\mathbf{T}_{ps}(\vec{x}))]^2 - \frac{1}{N_P} \sum_{\vec{x} \in P} [P(\vec{x}) - S(\mathbf{T}_{sp}(\vec{x}))]^2 \quad (6.11)$$

Both transformations are implemented in cylindrical space. In an ideal case, these transformations are the inverse of each other, e.g.  $\mathbf{T}_{ps} = \mathbf{T}_{sp}^{-1}$  and  $\mathbf{T}_{sp} = \mathbf{T}_{ps}^{-1}$ . However, this symmetric similarity measure alone does not ensure that the registration is inverse-consistent. Additionally, one needs to modify the optimisation function to include a penalty term that encourages inverse consistency of both transformations. The proposed method follows the approach of Feng et al. (2009) using compositions of

<sup>3</sup>[picsl.upenn.edu/ANTS](http://picsl.upenn.edu/ANTS)

<sup>4</sup>[sourceforge.net/projects/niftyreg](http://sourceforge.net/projects/niftyreg)

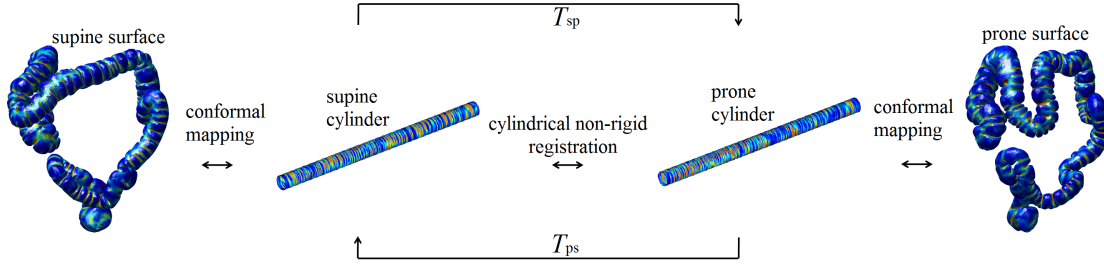


Figure 6.8: Symmetric prone-to-supine transformation model. The colour indicates the local shape indices. The prone-to-supine direction is denoted as the forward transformation  $\mathbf{T}_{ps}$ , e.g. with prone as source and supine as target image. The supine image as source and prone image as target is denoted as the inverse (supine-to-prone) transformation  $\mathbf{T}_{sp}$  between the colon surfaces  $S_s$  and  $S_p$ .

$\mathbf{T}_{ps}$  and  $\mathbf{T}_{sp}$  and add

$$\mathcal{P}_{IC} = \sum_{\vec{x} \in S} \|\mathbf{T}_{sp}(\mathbf{T}_{ps}(\vec{x}))\|^2 + \sum_{\vec{x} \in P} \|\mathbf{T}_{ps}(\mathbf{T}_{sp}(\vec{x}))\|^2 \quad (6.12)$$

to the objective function being optimised. Furthermore, two more symmetric penalty terms  $\mathcal{P}_{BE}$  and  $\mathcal{P}_{Jac}$  are included in order to promote realistic deformations. The first term  $\mathcal{P}_{BE}$  causes a smooth transformation based on bending energy:

$$\begin{aligned} \mathcal{P}_{BE} = & \frac{1}{N} \sum_{\vec{x} \in S} \left( \left| \frac{\partial^2 \mathbf{T}_{sp}(\vec{x})}{\partial x^2} \right|^2 + \left| \frac{\partial^2 \mathbf{T}_{sp}(\vec{x})}{\partial y^2} \right|^2 + 2 \left| \frac{\partial^2 \mathbf{T}_{sp}(\vec{x})}{\partial xy} \right|^2 \right) \\ & + \frac{1}{N} \sum_{\vec{x} \in P} \left( \left| \frac{\partial^2 \mathbf{T}_{ps}(\vec{x})}{\partial x^2} \right|^2 + \left| \frac{\partial^2 \mathbf{T}_{ps}(\vec{x})}{\partial y^2} \right|^2 + 2 \left| \frac{\partial^2 \mathbf{T}_{ps}(\vec{x})}{\partial xy} \right|^2 \right). \end{aligned} \quad (6.13)$$

The inverse-consistency penalty term  $\mathcal{P}_{IC}$  alone does not guarantee folding-free transformations as the inverse-consistency error is constrained but will not be zero. Hence, a second Jacobian-based penalty term  $\mathcal{P}_{Jac}$  is also added in order to encourage one-to-one mapping by preventing folding as in (Modat et al., 2012):

$$\mathcal{P}_{Jac} = \frac{1}{N} \sum_{\vec{x} \in S} [\log(\det(\text{Jac}(\mathbf{T}_{sp})))^2] + \frac{1}{N} \sum_{\vec{x} \in P} [\log(\det(\text{Jac}(\mathbf{T}_{ps})))^2] \quad (6.14)$$

Therefore, the function being optimised in the inverse-consistent symmetric registration scheme is:

$$\mathcal{O}(P, S; \mu_{ps}, \mu_{sp}) = (1 - \alpha - \beta - \gamma) \times MSD_{\text{Sym}} + \alpha \times \mathcal{P}_{BE} + \beta \times \mathcal{P}_{Jac} + \gamma \times \mathcal{P}_{IC} \quad (6.15)$$

where  $\mu_{ps}$  and  $\mu_{sp}$  are the control point positions defining the transformations  $\mathbf{T}_{ps}$  and  $\mathbf{T}_{sp}$ .  $\alpha + \beta + \gamma$  need to be less than 1.

#### 6.4.4 Optimisation

A conjugate gradient ascent optimisation is used in order to maximise the objective function in equation 6.15. For optimisation, the gradients of  $\mathcal{O}$  with respect to the control points  $\mu_{ps}$  and  $\mu_{sp}$  are required:

$$\frac{\partial \mathcal{O}(P, S; \mu_{ps}, \mu_{sp})}{\partial \mu_{ps}} \text{ and } \frac{\partial \mathcal{O}(P, S; \mu_{ps}, \mu_{sp})}{\partial \mu_{sp}} \quad (6.16)$$



The analytical derivatives of the *MSD* similarity measure, bending energy  $\mathcal{P}_{BE}$  and the Jacobian-based penalty term  $\mathcal{P}_{Jac}$  have been defined in the literature (Modat et al., 2010). The derivative of the inverse-consistency error penalty term  $\mathcal{P}_{IC}$  can be computed using a two step approach as in (Modat et al., 2012). Firstly, the *ICE* derivatives are computed at each voxel position and then the derivatives are estimated at the control point positions of  $\mu_{ps}$  and  $\mu_{sp}$ . This is implemented by computing four displacement fields using composition:

$$\begin{aligned} -D1_P(x) &= x - \mathbf{T}_{ps}(\mathbf{T}_{sp}(x)) \quad \text{where } x \in P \\ -D2_P(x) &= x - \mathbf{T}_{sp}(\mathbf{T}_{ps}(x)) \quad \text{where } x \in P \\ -D1_S(x) &= x - \mathbf{T}_{ps}(\mathbf{T}_{sp}(x)) \quad \text{where } x \in S \\ -D2_S(x) &= x - \mathbf{T}_{sp}(\mathbf{T}_{ps}(x)) \quad \text{where } x \in S \end{aligned} \tag{6.17}$$

A cubic B-spline kernel is then convolved with the computed displacements fields  $D1_P$  and  $D2_P$  in order to produce a cubic B-spline parametrisation of the transformation  $\mathbf{T}_{ps}$ . The same is computed for  $\mathbf{T}_{sp}$  using the displacements fields  $D1_S$  and  $D2_S$ . The gradient information at each control point position  $\mu_{ps}$  and  $\mu_{sp}$  can then be estimated using linear interpolation as in (Modat et al., 2012).

### 6.4.5 Inverse-consistent results

Registration parameters were tuned empirically on 8 prone/supine CTC cases<sup>5</sup>, based on visual assessment and assessment of registration error. This resulted in a 73% reduction in mean *ICE*, whilst keeping similar registration accuracy compared to a standard asymmetric registration. Tuning resulted in the registration weights  $\alpha(\mathcal{P}_{BE})$ ,  $\beta(\mathcal{P}_{Jac})$  and  $\gamma(\mathcal{P}_{IC})$  in the objective function (6.15) being set to  $1e^{-5}$ ,  $1e^{-5}$  and  $1e^{-3}$ , respectively. I found that these values for  $\beta$  and  $\gamma$  performed better in combination with the inverse-consistency penalty ( $\mathcal{P}_{IC}$ ) (using visual assessment) than the previously used weights of  $1e^{-4}$  and  $1e^{-4}$  for  $\alpha$  and  $\beta$  respectively (see Chapter 3).

Table (6.3) shows the mean inverse consistency errors ( $\overline{ICE}$ ) before (3) and after (4) penalising for inverse consistency error using the symmetric registration approach in 17 prone/supine CTC sets (not used for tuning)<sup>6</sup>, of which five were exhibiting local colonic collapses. Furthermore, registration accuracy is measured using 1743 pairs of reference points. These reference points were manually selected between corresponding haustral folds by experts, leading to 103 references points per case on average (Hampshire et al., 2013). These reference points enable the computation of a *fold registration error FRE* as in Chapter 3.

In the validation set, the mean inverse-consistency error ( $\overline{ICE}$ ) was reduced by 86% from a mean (std. dev.) of 3.3 (2.8) mm to 0.45 (0.16) mm using the proposed symmetric formulation. This reduction of  $\overline{ICE}$  is statistically significant ( $p < 0.001^7$ ).

The total mean *FRE* stayed at a similar value with a mean (std. dev.) of 6.6 (3.0) mm, when compared to the previous value of 6.0 (1.9) mm. This change in registration accuracy was not significant for the 17 validation data sets ( $p = 0.78^7$ ). However, the registration error was improved significantly in the set of eight well-distended cases from 4.9 (0.8) mm to 4.4 (0.7) mm ( $p = 0.017^7$ ). Nevertheless, the total registration error is slightly worse because of increased registration errors in the cases exhibiting a collapse or large differences in distension.

The advantage of using an inverse-consistent symmetric formulation however is illustrated in Fig. 6.9 via a small section of the endoluminal colonic surface of one patient where no reference standard

<sup>5</sup>The used tuning cases were the same as in Chapter 3.

<sup>6</sup>These are the same patient data sets as were used for validation in Chapter 4; plus four cases which were previously excluded due to vast differences in distension. This reference standard has been produced for the study by Hampshire et al. (2013)

<sup>7</sup> Related-Samples Wilcoxon Signed Rank Test, 5% significance level.

was selected. The local squared-differences ( $SD$ ) between the floating and the reference image pixels intensities is displayed before (left) and after (right) penalizing for inverse-consistency. The vertical dimension of both images goes around the circumference of the colon, while the horizontal dimension goes along the length of the colon. The  $MSD$  was reduced in each of the 17 validation sets, with a total 43% reduction from a mean (std. dev.) of 0.023 (0.005) to 0.013 (0.004). This is a significant reduction in  $MSD$  ( $p < 0.001$ ).

Table 6.3: Mean inverse consistency errors ( $\overline{ICE}$ ), registration accuracy ( $\overline{FRE}$ ) and mean-of-squared-differences ( $MSD$ ) without ( $_3$ ) and with ( $_4$ ) using the symmetric approach for the validation set of 17 CTC cases. The locations of where the colon is collapsed are given (DC: descending colon, SC: sigmoid colon).

Patient #	Collapse in prone	Collapse in supine	$\overline{ICE}_3$ [mm]	$\overline{ICE}_4$ [mm]	$\overline{FRE}_3$ [mm]	$\overline{FRE}_4$ [mm]	$MSD_3$ [ $\times 1e^{-2}$ ]	$MSD_4$ [ $\times 1e^{-2}$ ]
1	none	none	2.2	0.39	6.4	5.6	1.8	0.9
2	none	none	1.7	0.34	5.4	4.8	2.0	0.9
3	none	none	1.0	0.30	4.5	4.1	1.8	0.8
4	none	none	1.4	0.30	4.3	3.9	2.1	1.0
5	none	none	1.3	0.30	5.1	5.1	1.7	0.9
6	none	none	1.1	0.30	3.6	3.1	2.2	1.1
7	none	none	1.1	0.32	5.0	4.4	1.9	0.9
8	none	none	1.2	0.32	4.9	4.5	1.7	1.0
<b>Mean</b>			<b>1.4</b>	<b>0.3</b>	<b>4.9</b>	<b>4.4</b>	<b>1.9</b>	<b>0.9</b>
<b>Std. dev.</b>			<b>0.4</b>	<b>0.0</b>	<b>0.8</b>	<b>0.7</b>	<b>0.2</b>	<b>0.1</b>
9	1 $\times$ DC	1 $\times$ DC	2.9	0.62	11.7	12.6	2.5	1.5
10	1 $\times$ DC	1 $\times$ DC	2.9	0.35	5.7	9.3	2.4	1.3
11	none	1 $\times$ SC	11.0	0.68	5.0	7.3	2.5	2.1
12	3 $\times$ (DC, SC)	none	2.4	0.54	5.9	5.6	3.0	1.4
13	none	1 $\times$ DC	2.3	0.45	5.4	5.0	2.9	1.7
<b>Mean</b>			<b>4.3</b>	<b>0.5</b>	<b>6.7</b>	<b>7.9</b>	<b>2.7</b>	<b>1.6</b>
<b>Std. dev.</b>			<b>3.7</b>	<b>0.1</b>	<b>2.8</b>	<b>3.1</b>	<b>0.3</b>	<b>0.3</b>
	Previously excluded							
14	none	none	4.6	0.85	9.1	13.6	2.9	1.7
15	none	none	6.2	0.58	7.8	7.3	3.0	1.6
16	none	none	7.6	0.46	5.8	8.7	2.2	1.3
17	none	none	5.7	0.55	6.8	6.8	2.5	1.3
<b>Mean</b>			<b>6.0</b>	<b>0.6</b>	<b>7.4</b>	<b>9.1</b>	<b>2.7</b>	<b>1.5</b>
<b>Std. dev.</b>			<b>1.2</b>	<b>0.2</b>	<b>1.4</b>	<b>3.1</b>	<b>0.4</b>	<b>0.2</b>
	<b>Total</b>							
<b>Mean</b>			<b>3.3</b>	<b>0.45</b>	<b>6.0</b>	<b>6.6</b>	<b>2.3</b>	<b>1.3</b>
<b>Std. dev.</b>			<b>2.8</b>	<b>0.16</b>	<b>1.9</b>	<b>3.0</b>	<b>0.5</b>	<b>0.4</b>

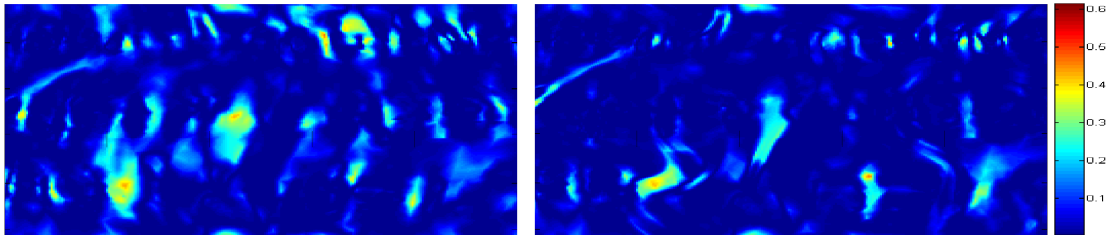


Figure 6.9: Local squared-differences ( $SD$ ) of registration result where no reference standard was provided. The  $SD$  is measured between the floating and the reference image using the non-symmetric (left) and the inverse-consistent symmetric approach (right). Reduction in  $SD$  indicates an improved registration (right).

## 6.5 Conclusions

I have shown that a robust initialisation can improve inverse consistency of the cylindrical B-spline registration method. While improved inverse consistency alone does not guarantee good correspondence, concomitant improvement in registration accuracy suggests that registration is more robust when using a feature-based initialisation.

Further improvement of inverse-consistency was achieved by implementing an inverse-consistent non-rigid registration method. An extension to the previous work of Feng et al. (2009), Modat et al. (2012) and Roth et al. (2011) is presented which enables inverse-consistent symmetric registration of prone and supine colonic endoluminal surfaces in cylindrical space. The transformations (both prone-to-supine and supine-to-prone) are parametrised, using a uniform cubic B-spline. *MSD* is used as a symmetric similarity measure. The inverse-consistent symmetric formulation reduces bias resulting from the direction of registration and improves robustness and quality of the registration result.

I showed a large reduction in directional bias by implementing a symmetric non-rigid registration in cylindrical space that penalises inverse-consistency error. The proposed registration method generates an improved visual alignment between the prone and supine colonic surfaces, as indicated by a highly significant reduction of *MSD* between the prone and supine colon surfaces after registration. However, the registration error measured at a sparse set of manually selected reference points remained similar to the non-symmetric method.

Due to feasibility issues, the registration error can currently only be assessed with this sparse set of reference points as it is very challenging and time-consuming for radiologists to find corresponding locations between prone and supine positions manually. Therefore, only a limited region of the colon surface can be assessed with the reference standard available. This is due to difficulties in finding accurate reference points when the appearance of the colon is largely different (e.g. differing distension or segmentation errors). This means that reference points are often not present in regions where the registration result has nevertheless improved visually (as indicated by a reduction in *MSD*, as shown for example in Fig. 6.9).

On the other hand, the fact that only well-distended cases show an improvement in registration error might indicate that a symmetric inverse-consistent registration is more dependent on good initialisation. Cases with collapsed regions or cases that exhibit large differences in distension typically have less feature matches that can then be used for the initialisation based on B-splines (see Table 6.1 in Section 6.3.2). In the validation set used, cases with collapse or vast differences in distension had an average 80 feature matches compared with an average 120 matches in the well-distended cases. If the initial alignment of the cylindrical intensity images is inadequate, a symmetric registration might ‘pull’ in different directions depending on the direction of registration. This will be penalised by the inverse-consistency term and can cause the registration to align features poorly in these regions.

This indicates that the inverse consistency weight  $\gamma(\mathcal{P}_{IC})$  was probably chosen too high for the cases exhibiting local endoluminal collapse or marked differences in distension – this is likely to be due to over-fitting to the well-distended cases that were used for tuning the registration parameters, these being the only ones available. Although the total registration error is slightly worse, the difference is in fact negligible when compared to the uncertainty in identifying the landmark points.

In conclusion, the highly significant improvement of inverse-consistency that has been demonstrated, together with the accompanying stability of registration accuracy, provides a more robust and reliable registration method – at least in well-distended CTC cases. Information from both prone-to-supine and supine-to-prone directions helps to enforce convergence towards a more accurate solution if a good initialisation is provided. More robust and accurate inverse-consistent symmetric registration in cylindrical space will likely facilitate improved interpretation of CT colonography and has the potential to enhance existing computer-aided detection methods in the future.

## Chapter 7

# Temporally separated CT Colonography cases

The registrations method's ability to align temporally separated CTC cases, acquired several months apart, was investigated with collaborators from UCH, (Emma Helbren and Steve Halligan). Establishing of correspondence between these follow-up studies is challenging but important to the radiologists in order to monitor the growth of polyps. A total of 29 follow-up cases were investigated and registration was measured by using the polyp locations in all available scans.

### 7.1 Introduction

The following section describes the performance of the proposed prone-to-supine registration method to establish correspondence between CTC data sets acquired on temporally separated occasions, i.e. follow-up CTC data. Follow-up CT colonography (CTC) scans are necessary when a polyp detected on initial CTC is relatively small and so left in situ. This is because the risk of resection during subsequent optical colonoscopy (OC) outweighs the risk of leaving the polyp in situ and monitoring its growth. Polyp growth, if any, is monitored by sequential CTC, taken months or years later Pickhardt et al. (2008). Clearly, it is essential that the radiologist can identify the polyp under surveillance in both the initial prone/supine and the follow-up prone/supine data sets. Manual matching of polyps across longitudinal CTCs can be (even more) challenging and time-consuming than manual matching between prone and supine scans taken on the same day.

This study investigates the ability of a registrations method ability to align temporally separated CTC cases, acquired several months apart. To my knowledge, no other study has investigated registration accuracy for methods that establish full surface correspondence between follow-up CTC examinations.

A polyp observed over several months is shown in Fig. 7.1 using virtual fly-through renderings of the endoluminal surfaces. 7.1.

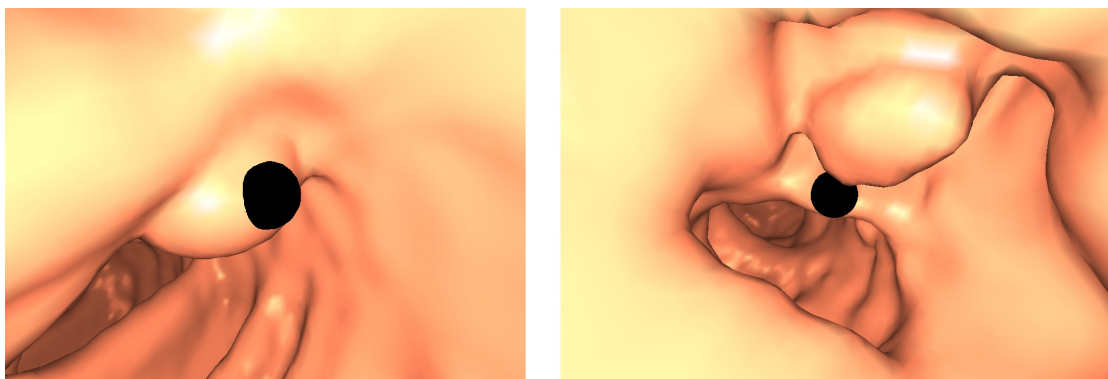


Figure 7.1: Virtual fly-through renderings of a polyp in prone position (left) and prone position scanned 43 months later (right), now grown to about 11 mm in size.

## 7.2 Methods

Required ethics and patient consent were obtained. All cases were selected from patients with two or more CTC investigations undertaken for the identification and subsequent follow-up of colonic polyps. No attempt was made to select ‘perfect cases’ or exclude cases with poor distension from the study. These data had not previously been used for the development of the registration method. I provided the software and registration results for the following experiments, while Emma Helbren provided radiological assessment.

The following schematic in Fig. 7.2 illustrates how correspondence between all data sets can be achieved. The follow-up prone ( $P$ ) and supine ( $S$ ) data sets acquired on the first or second occasion are superscripted with <sub>1</sub> or <sub>2</sub> respectively. One could transform between all data sets by only computing

$$\begin{array}{ccc} P_1 & \rightarrow & P_2 \\ \downarrow & & \downarrow \\ S_1 & \rightarrow & S_2 \end{array}$$

Figure 7.2: Establishing correspondence between the follow-up prone ( $P$ ) and supine ( $S$ ) data sets acquired on the first or second occasion is superscripted with <sub>1</sub> or <sub>2</sub> respectively.

three registrations:  $P_1 \rightarrow P_2$ ,  $S_1 \rightarrow P_1$  and  $P_2 \rightarrow S_2$ . Therefore,

$$S_1 \rightarrow S_2 = S_1 \rightarrow P_1 \circ P_1 \rightarrow P_2 \circ P_2 \rightarrow S_2. \quad (7.1)$$

However, I also compute  $S_1 \rightarrow S_2$  in order to reduce any accumulated error that would occur when composing three transformations as in equation 7.1. Furthermore, the computation of  $S_1 \rightarrow S_2$  allows the generation of a “temporal consistency measure” over the whole colonic surface. This would measure how similar the registration results are (e.g. resulting in the same anatomical correspondence) when transforming one point around the full transformation ‘loop’ ( $S_1 \rightarrow S_2 \rightarrow P_2 \rightarrow P_1 \rightarrow S_1$ ). This might be a good indicator for judging the successfulness of the registration without referring to a reference standard at the polyps positions (‘loop consistency’). Computation of the diagonal directions (e.g.  $P_1 \rightarrow S_2$  or  $S_1 \rightarrow P_2$ ) were not seen to be of clinical importance as the radiologist is more used to tracking the polyp over time in the same body orientation of the patient.

## 7.3 Results

### 7.3.1 Initial feasibility study

Three patients with known polyps on initial and subsequent surveillance (follow-up) CTC were identified from patients recruited and consented at University College Hospital. The polyp locations were specified by an experienced radiologist (Emma Helbren) on the initial supine study. For all three patients the mean (std. dev.) registration error was 23.0 (9.7) mm (ranging 5.0 to 34.0 mm). Using the same 3D polyp conspicuity score as in Section 5.2, 60% (6 of 9) registration tasks were deemed to be at least ‘partially successful’. The polyp shown in Fig. 7.1 is an example for a ‘successful’ registration (black dot) over time. Table 7.1 lists number of days separating each colonography study together with *longitudinal registration errors*.

Table 7.1: Registrations of follow-up studies in an initial feasibility study. The number of days separating each colonography study are listed together with *longitudinal registration errors* (averaged over the number of polyps per case).

Patient #	Days	# Polyps*	Longitudinal Error [mm]
1	168	1	25.2
2	1299	1	16.6
3	550	1	27.6
<b>Mean</b>	<b>23</b>	<b>1</b>	<b>23.1</b>
<b>Std. dev.</b>	<b>6</b>	<b>1</b>	<b>5.8</b>
<b>Minimum</b>	<b>17</b>	<b>1</b>	<b>16.6</b>
<b>Maximum</b>	<b>28</b>	<b>1</b>	<b>27.6</b>

\*The total number of polyps as 3

### 7.3.2 Results on external CTC data

Professor Perry Pickhardt kindly provided external CTC follow-up cases from his hospital<sup>1</sup> for the evaluation of the registration accuracy over time. The evaluation sample consisted of 26 patients. From this group the radiologist (Emma Helbren) was able to identify 35 polyps in all acquisitions of the initial and subsequent studies. This group was then used with myself being blinded to the true polyp locations before applying the registration algorithm.

Registration was successful in all 26 patients, and polyp locations in all subsequent acquisitions were estimated using the registration result. Table 7.2 lists the number of days separating each colonography study together with *longitudinal* and *consistency registration errors*. Using direct *longitudinal* transformations over time ( $P_1 \rightarrow P_2$  and  $S_1 \rightarrow S_2$ ), a mean (std. dev.) Euclidean registration error of 17.4 (12.1) mm (range 1.7 to 49.7 mm) was achieved.

Measuring the ‘consistency’ around the loop (predicting polyp location through all acquisitions from the specified location on the initial supine scan alone) a mean (std. dev.) Euclidean registration error of 26.9 (20.8) mm (range 0.9 to 84.5 mm) was achieved.

Both the *longitudinal errors* and *consistency errors* are not correlated to the number of days between the two CTC studies with  $p = 0.105$  and  $p = 0.055$  respectively<sup>2</sup>.

<sup>1</sup>University of Wisconsin Hospital and Clinics

<sup>2</sup>Two-tailed Pearson Correlation, 1% significance level.

Table 7.2: Registrations of follow-up studies on external CTC data. The number of days separating each colonography study are listed together with *longitudinal* and *consistency registration errors* (averaged over the number of polyps per case).

Patient #	Days	# Polyps*	Longitudinal Error [mm]	Consistency Error [mm]
1	1500	3	23.6	42.7
2	734	1	12.9	56.4
3	741	1	34.5	44.1
4	779	1	1.7	2.9
5	730	1	5.2	7.7
6	1524	2	30.1	30.0
7	779	1	49.7	84.5
8	1905	1	17.5	28.8
9	742	1	18.1	8.7
10	755	1	5.4	10.1
11	1886	1	9.3	11.5
12	865	1	8.5	9.5
13	757	1	15.3	29.0
14	369	2	13.3	28.2
15	1842	2	4.3	3.3
16	1498	1	8.0	31.0
17	747	2	21.4	15.3
18	371	3	33.7	33.7
19	755	2	8.9	18.6
20	375	1	6.3	0.9
21	405	1	17.1	27.8
22	753	1	29.0	53.3
23	749	1	38.2	49.0
24	266	1	14.5	18.9
25	777	1	16.7	51.0
26	735	1	9.1	2.6
<b>Mean</b>	<b>898</b>	<b>1.3</b>	<b>17.4</b>	<b>26.9</b>
<b>Std. dev.</b>	<b>480</b>	<b>0.6</b>	<b>12.1</b>	<b>20.8</b>
<b>Minimum</b>	<b>266</b>	<b>1.0</b>	<b>1.7</b>	<b>0.9</b>
<b>Maximum</b>	<b>1905</b>	<b>3.0</b>	<b>49.7</b>	<b>84.5</b>

\*The total number of polyps is 35.



## 7.4 Discussion

The challenge of automatically registering endoluminal colonic surface acquired with CTC several month or years apart is harder than the registration between scans taken during the same CTC session. In order to compensate for this increased challenge, a more robust and accurate initialisation was required in order to produce accurate results (see Chapter 6), as opposed to using the more simple piece-wise linear scaling introduced in Chapter 5.

The achieved accuracies show this to be an efficient and accurate method of lesion matching over time. Therefore, automatic registration could be a useful adjunct for those performing CTC for the follow-up surveillance of colonic polyps. Registration is likely to be especially helpful in the follow-up of small polyps. These are likely harder to locate and to identify manually. It was previously demonstrated that the proposed registration algorithm can be used to accurately match prone and supine datasets. In this study I have further demonstrated one of the algorithms wider applications – in the follow-up of polyps on interval CTC. There is a increased chance of dissimilarity between bowel preparation and overall quality of CTC quality when comparing temporally separated data sets, which makes automatic registration between these data sets more difficult. Despite this challenge, the level of accuracy achieved by the registration algorithm is similar to the ACRIN data set used in Section 5.2. The fact, that there is no dependency of *longitudinal errors* and *consistency errors* on the length of time between the initial and follow-up CTC studies highlights that registration errors are more likely caused by differences in distension and bowel-preparation than by any anatomical changes that could occur over the months and years between studies.

Further applications of follow-up registration could include automatic detection of structural abnormalities on the endoluminal surface. One could use the similarity measure of the registration cost-function not only to achieve alignment between colonic surfaces but also to automatically identify areas of dissimilarity that might be caused by colorectal cancer arising between follow-up scans. Furthermore, the deformation fields resulting from the registration could be used to estimate the growth or change of anatomical structures such as polyps.

## Chapter 8

# Registration of cases with different distensions

### 8.1 Introduction

Currently, the proposed prone-to-supine registration performs an alignment of shape index images in cylindrical space. The shape index in both prone and supine is computed on the original smoothed colon surfaces, while cylindrical registration only aims to align shape index features spatially. This method performs well if the colon is similarly distended, well-prepared for scanning in both positions, and the CT-quality of the images is sufficient for an accurate segmentation of the colonic lumen.

Good-quality scans enable accurate extraction of endoluminal surfaces from segmentations of the colon. This subsequently enables computation of the local shape indices on the surface that are sufficiently similar in both cylindrical representations in order to align surface features accurately. However, if the colon varies in distension between the two views or artefacts in the segmentation are present, a purely spatial alignment of features in the cylindrical images proves to be more challenging. As features appear markedly different, this results in an inferior automated alignment based on the intensity differences of the images.

In order to overcome the limitation of this registration method, a new method is proposed that deforms the source colon surface in an iterative manner in 3D in order to increase the similarity between both surfaces. This allows re-computation of surface curvatures and therefore the shape index values on the deformed surface. The deformed surface aims to represent the target surface more closely. Therefore, the similarity of the cylindrical representations increases with each optimisation step. This subsequently can improve the spatial alignment of surface features using a non-rigid image registration in cylindrical space which aligns surface features spatially at each iteration level. Figure 8.1 illustrates this principle. A multi-resolution-approach is used in order to deform one 3D surface towards the other.

### 8.2 Methods

#### 8.2.1 Extraction of good quality point correspondences

In order to deform one surface, a thin plate spline (TPS) is fitted using a set of local point correspondences acquired from the initial cylindrical registration result. At each iteration level, the majority of point correspondences are extracted from surface areas where the registration found good local correspondence. The quality of local correspondence is measured using a local similarity measure  $S$  computed with a certain window-sized area of the colon surface (as illustrated in Figure 8.2). In this experiment I used a multi-resolution approach with local windows of different sizes and using sum of squared difference (SSD) as the local similarity measure. Surface areas with  $S \geq t_s$  are then used to extract a dense set of local correspondences, allowing for increased bending of TPS transformation. While surface areas with an  $S < t_s$  are used to extract a sparser set of point correspondences, allowing for less bending. This is specified by specifically weighing the influence of each corresponding point. Here,  $t_s$  is a certain threshold which separates good quality areas of the registration from inferior quality regions. Figure 8.3

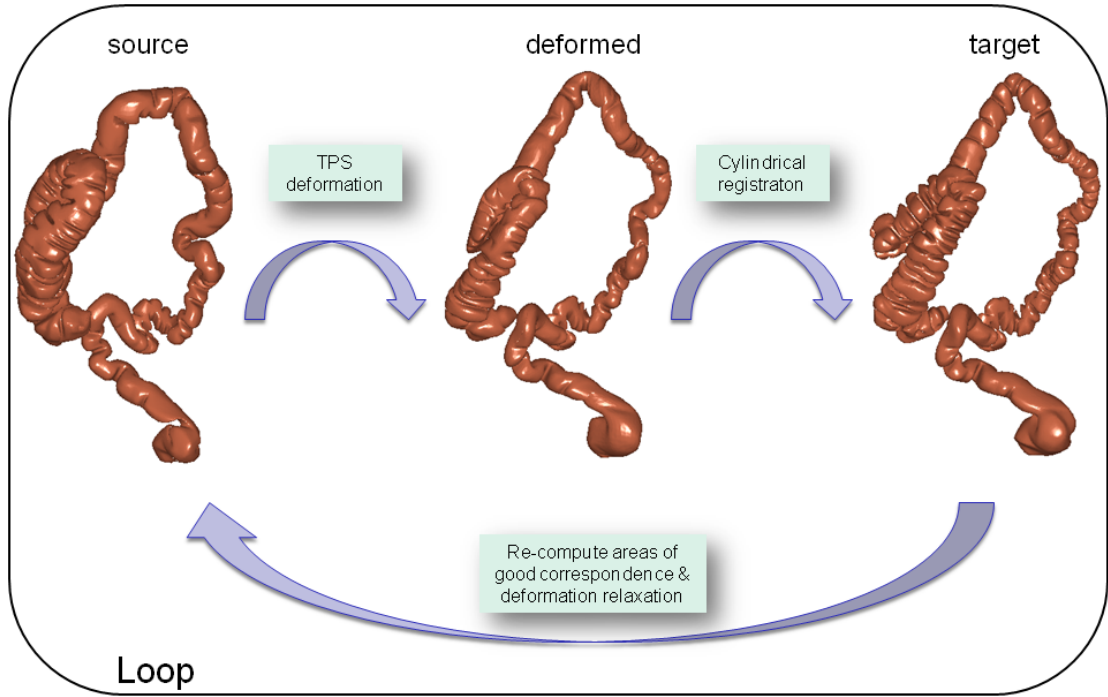


Figure 8.1: Principle of the proposed iterative thin plate spline deformation process

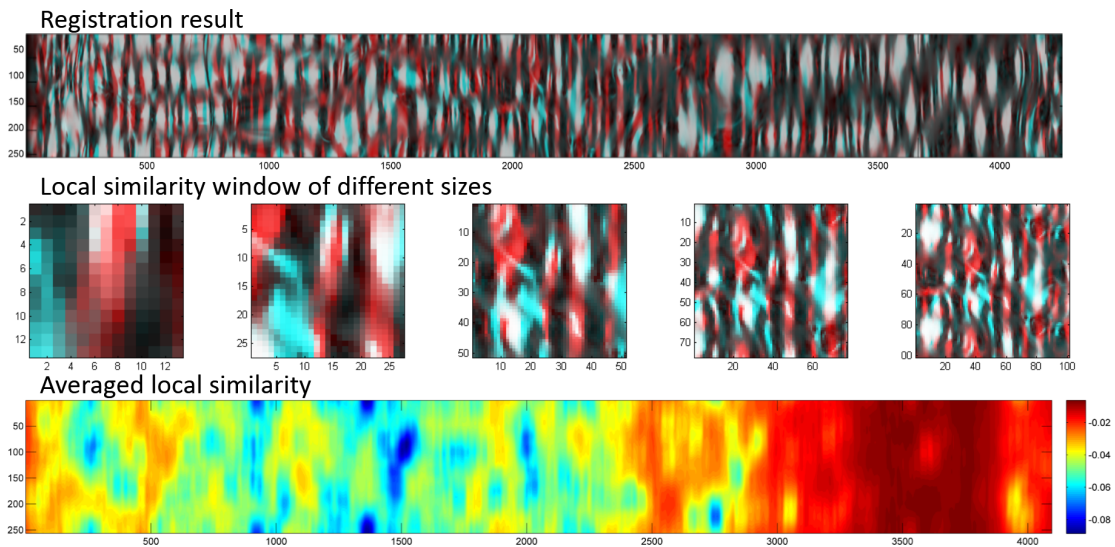


Figure 8.2: Determining areas of good registration quality using a multi-resolution approach of local SSD computation

shows the extraction of corresponding point locations between the source and target colon surface which are used to fit the TPS at each iteration level.

### 8.2.2 Surface deformation using thin plate splines

TPS allows the non-linear transformation of the whole image space of the source surface towards the space of the target surface. The transformation is based on modelling the physical deformation of bending a sheet of metal. This enables the selection of different local bending properties of TPS in order to allow different degrees of local deformations. TPS can be fully fitted based on a set of point correspondences between the source and target 3D space and the bending properties as TPS can be estimated in

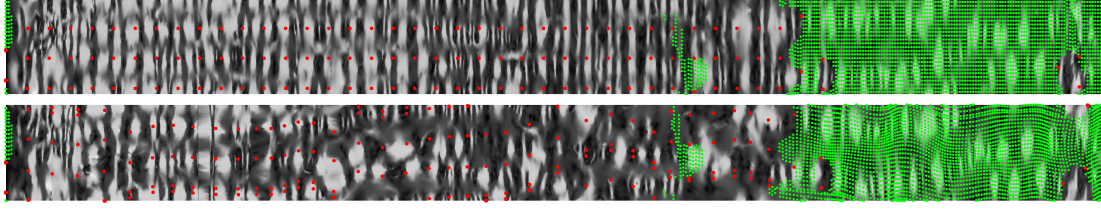


Figure 8.3: Extraction of point correspondences (white dots). Right hand side shows better local correspondences and therefore a much higher concentration as in the middle section (magenta dots)

a closed-form solution (Wahba, 1990). TPS can be estimated using a radial basic function  $\varphi(r)$  which defines the transformation of any point  $x$  in the source space to  $f(x)$  in the target space, given a set of correspondences functioning as control points of the TPS  $\{w_i; i = 1, 2, \dots, K\}$ .

$$f(x) = \sum_i^K c_i \varphi(\|x - w_i\|) \quad (8.1)$$

For TPS the radial basis function is defined as  $\varphi(r) = r^2 \log r$  in 2D and can be simplified to  $\varphi(r) = -r$  in 3D (Holden, 2008, Fornefett et al., 2001).  $\{c_i\}$  denotes a set of transformation coefficients. Additionally, a smoothness term is minimised in order to allow a smooth TPS fitting:

$$E = \iiint \left[ \left( \frac{\partial^2 f}{\partial x} \right)^2 + \left( \frac{\partial^2 f}{\partial y} \right)^2 + \left( \frac{\partial^2 f}{\partial z} \right)^2 + 2 \times \left[ \left( \frac{\partial^2 f}{\partial xy} \right)^2 + \left( \frac{\partial^2 f}{\partial yz} \right)^2 + \left( \frac{\partial^2 f}{\partial xz} \right)^2 \right] \right] dx dy dz \quad (8.2)$$

After applying the TPS deformation the source surface aims to match the target surface more closely. This deformation is illustrated in Fig. 8.4. As the source surface is being deformed using TPS and mapped into the 3D space of the target image, a good overlap can be seen in the colonic segments where previously a good spatial correspondence was detected using the local similarity measure  $S$  (rectum towards halfway along the descending colon in Fig. 8.4, right).

The shape index values can now be re-computed on the deformed surface and mapped onto the cylindrical source space using the original conformal mapping. This leads to more similarity between both cylindrical images. A subsequent registration in cylindrical space driven by these shape index values is then more likely to align features correctly in the areas neighbouring the good areas ( $S \geq t_s$ ).

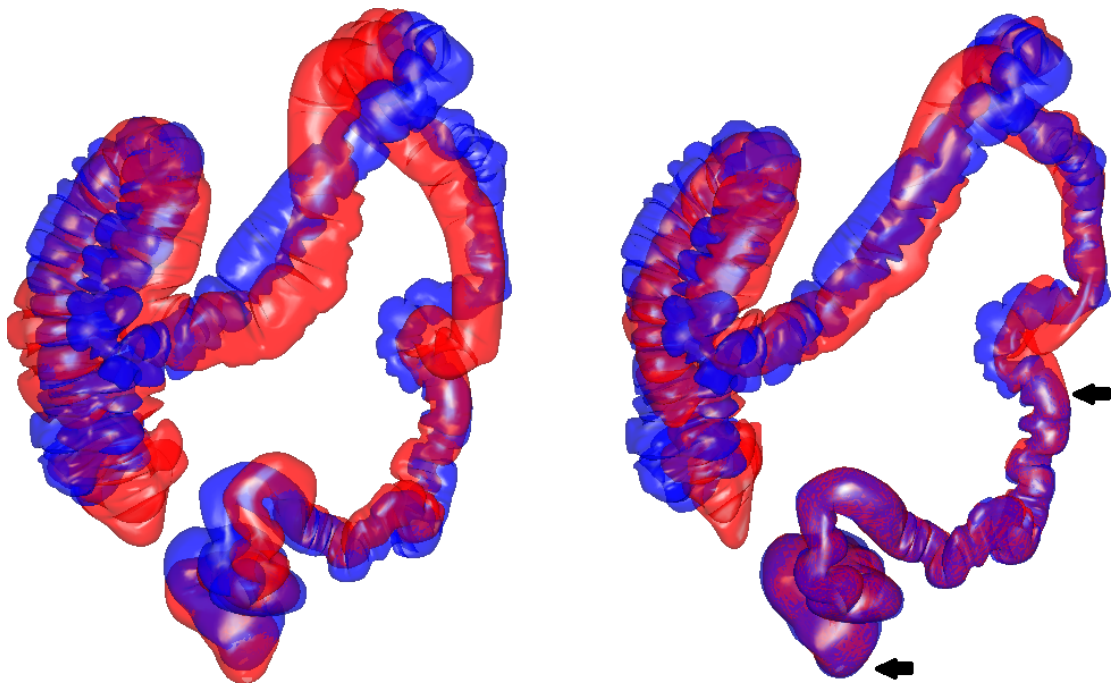


Figure 8.4: Colon surface deformation using thin plate splines. Left: source (red) and target (blue) surfaces. Right: deformed source (red) and target (blue) surfaces. Overlaid with the target surface on the right, a good match can be seen in the sigmoid and descending colon segments which were previously detected as areas of successful registration, resulting in good spatial correspondence (between the arrows).

### 8.2.3 Re-establishing correspondence in cylindrical space using a deformation relaxation approach

I then re-compute the cylindrical non-rigid registration in order to account for the rotational twist and individual fold deformations in cylindrical space. However, in order to correct for misaligned areas in cylindrical space caused by the dissimilar features from previous registration levels, the B-spline deformation grid is 'relaxed' in areas where the registration was badly aligned, judging by the previous local similarity measure ( $S < t_s$ ). This 'relaxation' of the cylindrical deformation field is achieved by utilising the bending energy  $C_{smooth}$  in the optimisation function of the cylindrical B-spline registration formulation:

All bad areas ( $S < t_s$ ) of the registration are ignored when computing the similarity measure in this formulation. Therefore, in these areas, the registration algorithm is purely minimising the bending energy of the deformation field. Whereas, features in good areas ( $S \geq t_s$ ) are aligned by optimisation of a similarity measure  $C_{similarity}$ , namely the SSD measure in the optimisation of the cylindrical B-spline registration. This modified registration provides a 'relaxed deformation field' which can be used as the initialisation to the 'normal' cylindrical registration scheme over the full colonic surface, after TPS deformation of the source surface and using the updated shape index information in order to drive the registration.

This deformation relaxation is computed at the final resolution level of an image pyramid as the initial cylindrical registration has already accounted for the large deformations. The interest really only lies in capturing the features in the vicinity of the good regions ( $S \geq t_s$ ) in order to improve the overall registration result. Figure 8.5 illustrates this relaxation of the deformation field in the bad areas of the cylindrical images. The result of this cylindrical registration is then used to initialise the next iteration

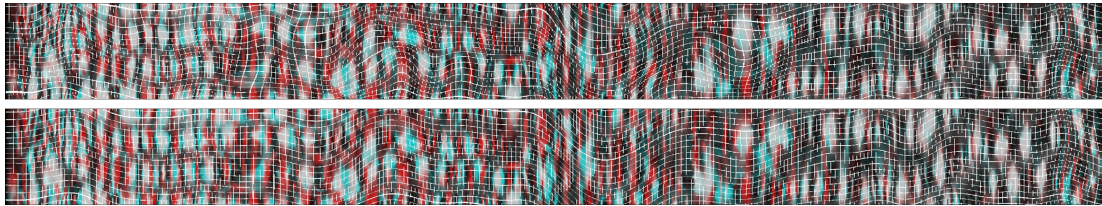


Figure 8.5: Top: Deformation field in beginning. Bottom: deformation after relaxation. This step keeps the good parts of the deformation but “relaxes” the control points where the registration is bad. This relaxing can be achieved by minimising the bending energy in the bad regions in order to provide a re-initialisation for a subsequent cylindrical registration.

of the proposed algorithm. The flow chart in Fig. 8.6 illustrates this iterative process. The process is continued until the TPS is fitted using points over the whole of the cylindrical deformation field.

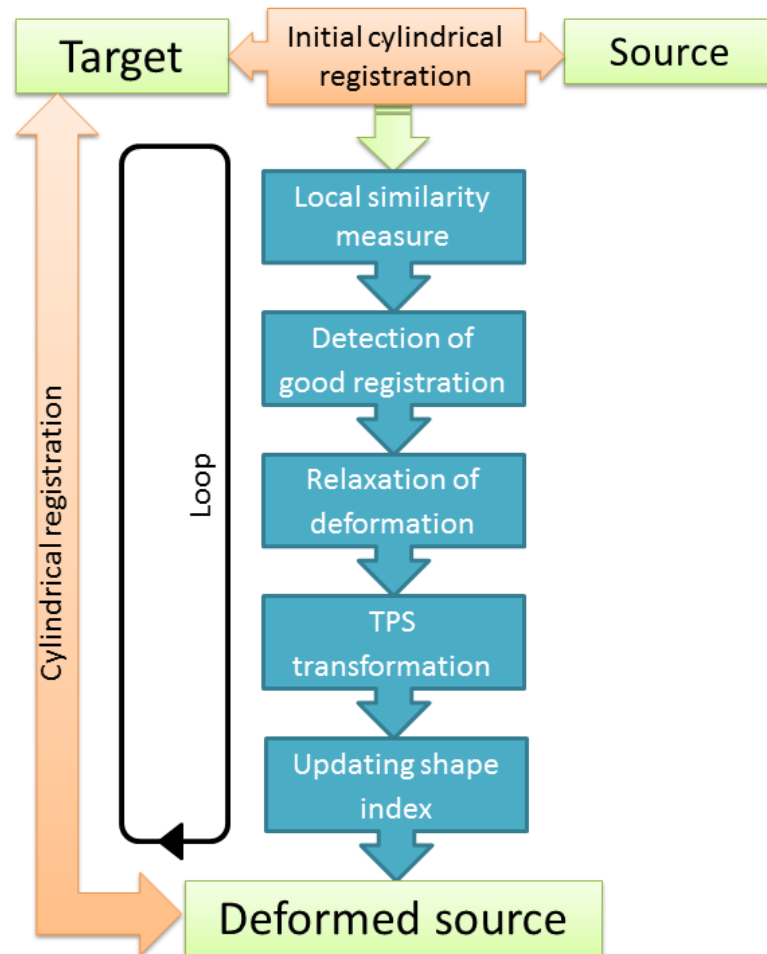


Figure 8.6: Flow chart of the proposed iterative thin plate spline deformation process.



### 8.3 Results

The proposed algorithm was applied to four patient cases where the cylindrical non-rigid registration alone could not provide sufficient registration accuracy, e.g. average registration errors of over 10 mm. Figure 8.7 shows the mean registration error for each case with increasing iterations of the proposed algorithm. Decreased registration error is observed in three cases (A, B and C) when previously mis-aligned features that neighbour good regions are ‘captured’ by the algorithm and then aligned correctly. The average registration error of all four cases improved from 14.5 mm to 13.2 (-9 %) mm; with the largest improvement in case C with 2.8 mm (-16.4 %) decrease in registration error. One case (D) did not improve but the initial error was already relatively small.

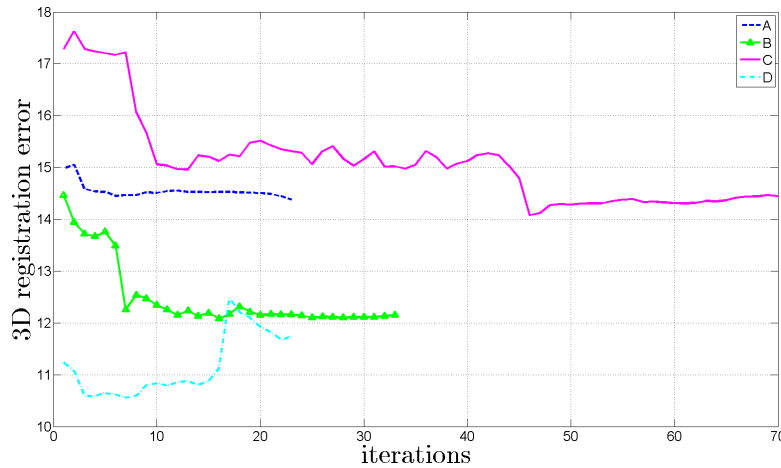


Figure 8.7: Evolution of registration error in mm over several iterations of the proposed optimisation method.

### 8.4 Discussion

This Chapter introduced an approach that aims to overcome the difficulties posed for the proposed registration method caused by marked differences in distension. Differences in distension can cause the surface features in the prone and supine cylindrical images to appear very differently. Using TPS can transform one surface to resemble the other surface more closely.

Areas that show high local similarity (based on a local multi-resolution *SSD* measurement) are used to fit a TPS transformation between the two colon surfaces. However, local *SSD* might not be the ideal measurement to establish whether the registration achieved a correct result or not. It only describes the ‘visual’ similarity of both surfaces in cylindrical space. Alternative measures such as correlation-based measures have shown promise in non-rigid image registration and might be less effected by differences in the shape index images. Measures such as normalised cross-correlation (*NCC*) might account better for intensity changes between prone and supine shape index images. *NCC* could also be computed locally in order to better measure the local feature patterns of the cylindrical images.

Current stability issues can occur when re-sampling the transformed surface meshes in order to regenerate the cylindrical images. For example, case C shows an improvement in mean registration error for over 15 iterations in comparison to the starting value. However, the registration misaligned one large haustral fold in the caecum end of the image in the 16th iteration, causing an increasing step of mean registration error by 1.2 mm (11 %).

An alternative to TPS when modelling of the 3D transformations between prone and supine cases of different distension could be the use of B-splines. However, B-splines might more difficult to constrain because of the need to define control points over the entire three-dimensional space that embeds the



colon surfaces. As the colon does not cover all that 3D space, a multi-resolution approach would be necessary. A useful fitting could be achieved using an extension to 3D of the B-spline approximation presented by Hampshire et al. (2013) as a 2D initialisation (see Chapter 6 for more details). Furthermore, the application of *Non-Uniform Rational B-splines* (NURBS) (Piegl and Tiller, 1997) could be helpful to constrain the deformations of the colon more easily.

A second alternative would be the exploitation of bio-mechanical models in order to model the deformation between cases with differences in distension more realistically. This will be further discussed in the next Chapter.

## Chapter 9

# Future work

### 9.1 Improving prone-to-supine surface registration

During development of the described prone-to-supine registration method it was discovered that a third (four out of twelve) of the un-collapsed validation cases used in Chapter 4 had large regions with a markedly different appearance of local surface structures between the prone and supine cylindrical images (Roth et al., 2011). It was demonstrated that using robust feature matches can improve the registration accuracy in these previously excluded cases (see Chapter 6). However, the proposed registration method still depends on good initial similarity between the surface features from prone and supine in order to align both surfaces accurately. Therefore, any marked differences in the surface structures will negatively influence registration and limit accuracy of the result. There are three main reasons for differences between the two scans which result in *challenges* for future work:

1. Differences in local and global distension (majority of the problematic cases<sup>1</sup>)
2. Different surface features introduced by tight bends of the colon (few cases)
3. Inaccurate inclusion of fluids caused by insufficient fluid tagging (frequently occurring cases)

#### 9.1.1 Bio-mechanical modelling of colonic inflation

An alternative to the *thin plate spline* deformation approach, presented in Chapter 8, could exploit bio-mechanical modelling in order to handle cases with different distension. Bio-mechanical modelling of the colon surface could be investigated in order to make surface features more similar before the execution of registration. Bio-mechanical models could be used to virtually inflate the less-inflated parts of the colon in order to make the surface more similar to the more distended colon in the other scan.

A *hyperelastic* surface model could be utilised to simulate inflation of the colon. During inflation, the colon can undergo large deformations with non-linear stress behaviour of the colon material. These deformations could be modelled using Neo-Hookean mechanics (Ogden, 1998), which can predict the deformation of materials undergoing non-linear stresses. Bio-mechanical approaches for medical image registration show promise for modelling organ and tissue deformations (e.g. for breast imaging (Carter et al., 2005, Mertzaniidou et al., 2012)) or for simulating tissue deformations during surgery (Cotin et al., 1999). While bio-mechanical concepts have been applied to the simulation of colonic behaviour for *colonoscopy simulators* (Ahn et al., 2005, Ikuta et al., 2000) using *virtual reality*, suitable bio-mechanical models for simulating the inflation of colonic segments still need to be established. It is likely that this will involve different material properties for different sections of the surface, e.g. haustra, folds and teniae coli. From experience with prone and supine CTC scans and optical colonoscopy, it can be assumed that haustral folds are more elastic, e.g. more 'stretchable' than the haustrated areas of the

---

<sup>1</sup>47% had at least one region of complete luminal collapse and 55% of the validation cases had excess residual fluid (see Section 5.2)

colon. Furthermore, the intersection of the colon surface with itself (especially at haustral folds) during virtual inflation needs to be averted. This might involve further constraints including collision detection methods (Moore and Wilhelms, 1988). One might also consider the modelling of colon inflation as a solid object with the lumen of the colon hollowed out in its centre. This would enable the use of tetrahedral elements (which are often used in the literature), rather than shell elements. The result of a preliminary experiment using a shell-based bio-mechanical model of the colon surface is illustrated in Fig. 9.1. Regions of different distension could be detected based on a local measure of the distance

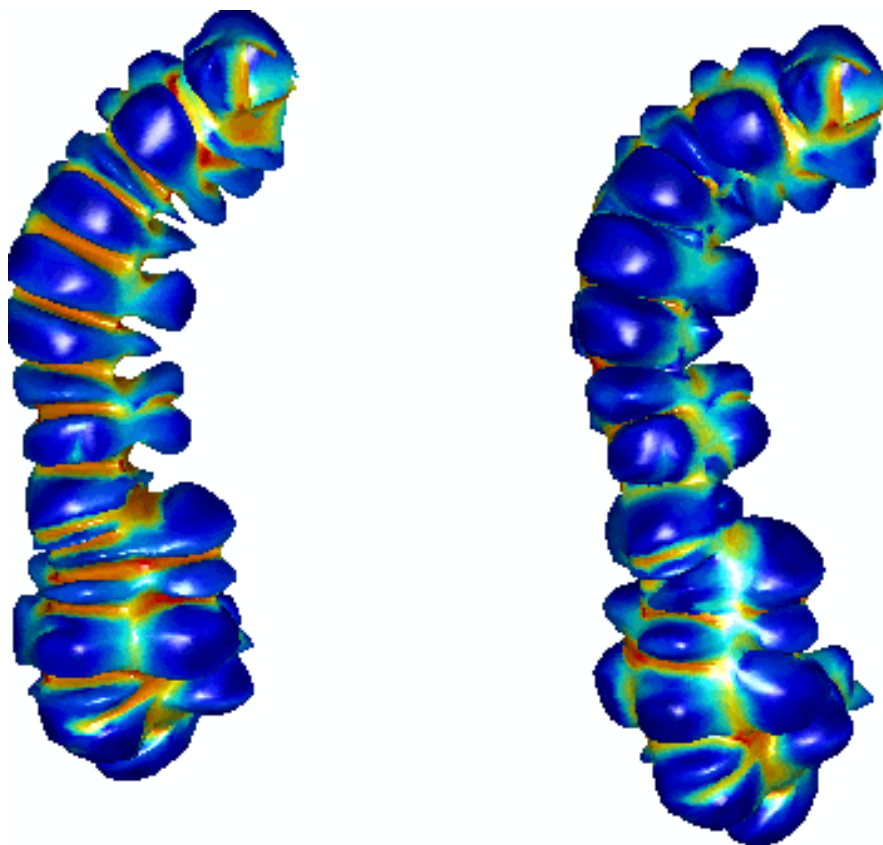


Figure 9.1: Virtual inflation of the colon using a bio-mechanical model of the ascending colon surface. Before inflation (left surface) and after applying a constant internal pressure to the inside of the colon (right surface). It can be observed how the shape index values change with the more inflated surface on the right.

between the surface and centreline, which corresponds to the local volume or degree of insufflation. Virtual inflation could be used until a similar amount of distension is achieved in both scans. This would then enable the re-computation of surface measurements (such as the shape index) and can then drive the non-rigid registration in cylindrical space, as in Chapter 3. Similar technology as used for virtual colon inflation could also be used to simulate the inflation of the colon at the tip of the endoscope during colonoscopy. This could be useful for methods which aim to align the current position of a colonoscope with CT colonography data of the same patient.

### 9.1.2 Reduction of different features introduced by tight bends

Challenge 2 introduces different surface features when the colon has a tight bend in one image but not the other. This occurs when folding in the colonic surface near the bend is visible in one view but not the other view. Information from the extracted centreline could be utilised to detect tight bends of the colon and its surface. These surface regions could then be ignored during non-rigid registration. Furthermore,

it could be worth investigating how effective ‘straightening’ the colon centreline and therefore the endoluminal surface around tight bends would be. Colon straightening can be achieved by using techniques as proposed by Sudarsky et al. (2008) and by Yao et al. (2010). Re-computation of the 3D surface curvatures (and shape indices) after the straightening procedure would remove features introduced by tight bends in the cylindrical images. The non-rigid cylindrical registration should be less effected by such dissimilarities between prone and supine.

Straightening the colon surface could also be advantageous for modelling the virtual inflation as possible self-intersections of individual colonic segments would be less likely, allowing for simpler biomechanical constraints.

### 9.1.3 Improving colon segmentation

The registration methods developed in this thesis use curvature measurements derived from colon segmentations in order to align both colonic surfaces. Therefore, they rely on extracted colon surfaces of good quality. Insufficient tagging and a bad image quality of CT colonography will cause errors in the segmentations and extracted surfaces, thus degrading the registration results.

Robust segmentation of the lumen inside the colon, which enables accurate extraction of the inner colon surface is still an active research topic (Ismail et al., 2012, Chang et al., 2011, Yigitsoy et al., 2012, Lu et al., 2011, Chowdhury and Whelan, 2011, Lu and Zhao, 2011, Peterson et al., 2011, Taimouri et al., 2011, Kilic, 2012). Colon segmentation was not a major focus of this thesis and therefore only a relatively simple threshold-based segmentation, combined with morphological operations (see Section 3.2), was used in order to extract the inner surfaces of the colonic lumen. In the case of insufficient fluid tagging (challenge 3), more specialised segmentation methods could be investigated. Methods that analyse shape rather than intensities show promise for improving segmentation results (Cai et al., 2008, 2010).

Dual energy approaches in CT imaging have shown promise for an improved separation between the colon and surrounding tissues (Cai et al., 2012). Despite controversy about the true influence of radiation exposure caused by CTC scanning and potential additional cancer risks for the patient (Laghi et al., 2010) and the fact that the benefits from CTC screening seem to outweigh the radiation risks (de González et al., 2011), there is a current trend in CTC towards lower radiation doses (van Gelder et al., 2002). Lower radiation doses reduce the potential cancer risks related to radiation but provide new challenges to computer-based algorithms aimed at CTC imaging (Näppi et al., 2012), as the image quality will inevitably be reduced.

Furthermore, less “aggressive” and more “acceptable” bowel preparation (i.e. without full cathartic preparation (Callstrom et al., 2001, Zalis et al., 2012)) are being investigated that might introduce further challenges for accurate colon segmentation. Furthermore, in cases where the colon is insufficiently insufflated (collapsed) or untagged fluid residuals are present, extracting an accurate segmentation of the colon becomes more challenging. Here, labelling of just the remaining air inside the colon will result in disconnected segments of the colon. Improved segmentations that can better estimate the anatomical extent of the colon when collapsed could be used to improve the cylindrical representations for these cases. Even if the surface features of collapsed regions cannot be used for driving the cylindrical registrations, a correct estimate of the length of the collapsed region will still be useful. An accurate length estimation of the collapsed segment could provide better initial cylindrical representations in comparison to just using the Euclidean distance between un-collapsed segmentations (as used in the previous chapters). A potential method to overcome this limitation could use a segmentation of the outer colonic wall which would allow a better estimation of the extent of collapsed regions (Van Uitert et al., 2006, Lu et al., 2012, Näppi and Yoshida, 2007). Furthermore, the automated detection of start and end point of each colonic segment would be feasible by implementing a colon segmentation scheme such as proposed by Lu et al. (2009). Alternatively, start and end points could be detected on the extracted surface mesh

triangulations of each segment, for example by using *Fiedler vectors* as in (Lai et al., 2010) in order to find a one-dimensional embedding which corresponds to a distance along the colon surface. This could further reduce the workload and interpretation time for the radiologist.

#### 9.1.4 Increasing the surface detail to allow finer alignment

Faster optimisation methods (e.g. *Newton's method*) can drastically improve the speed of conformally mapping the colon to a cylinder using Ricci flow. Further speed reductions could be achieved by parallel computing, utilising GPU-technology for Ricci flow (Qiu et al., 2008). A reduction of computation time from hours using gradient-descent to within a few minutes with Newton's method was achieved using an implementation by *Medicsight PLC* (see Section 3.5.3). This improvement in speed makes it feasible to investigate how more detailed surface triangulations of the colon would influence the registration results. Currently, meshes with circa 60,000 faces have been used to model the inner colon surface for computation of the local curvature measures and shape indices of the 3D surface. Increasing the number of faces could allow a more detailed representation of the inner colon surfaces and might improve registration results by allowing a finer local alignment of the prone and supine surfaces.

Secondly, dissimilarities between the prone and supine cylindrical images occur when the same folds in 3D are mapped to very different sized areas in 2D. This means there are differences in how the colon is stretched in order to map the 3D surface to a 2D cylinder. This might be caused by the fact that differently distended haustral folds are modelled with a markedly different number of triangles after mesh decimation. To some degree, this negative effect introduced by the conformal mapping can be compensated by utilising robust feature matches between the cylindrical images for non-rigid initialisation, as described in Chapter 6. However, further improvement could be achieved by increasing the number of faces in the triangulations used to model the colonic surfaces. This could allow to represent the colonic surfaces, using more regularly triangulated meshes. Increasing the number of faces might result in more similar conformal mappings to the cylindrical domain of the prone and supine surfaces.

Furthermore, analysing the stretch introduced by the conformal mapping (Sander et al., 2001) and how much it differs between the prone and supine mappings could be helpful in order to gain additional information about how much stretch/deformation is necessary to align both cylindrical images, using non-rigid image registration. Incorporated into the registration algorithm, this could mean a further improvement of the method. Additional advantages could be achieved by incorporating area-preserving transformation methods when mapping from a 3D surface to a cylindrical space (Zou et al., 2011).

#### 9.1.5 Alternative and multiple similarity measures

When driving the cylindrical intensity-based registration, presented in Chapter 3, I currently use only one intensity measure, based on the local 3D curvatures on the surface, namely the shape indices (*SI*). The shape index is a normalised shape descriptor based on local curvatures and it represents the local shape of the surface. As shown in the previous chapters, it is a good scalar measure for describing the local structures on colonic surfaces, such as haustra, folds and polyps; especially in well-prepared and well-distended cases. Using shape indices is advantageous for many cases: a haustral fold might be more or less prominent in either the prone or supine image. However, it will most likely retain its ridge-like shape; this will result in very similar shape index values for the same fold in both prone and supine cylindrical images.

However, *SI* might be suboptimal in certain regions where the distension and surface shapes are markedly different for the majority of the colon. For example, a very slight cap-like shape with low local curvatures will have the same *SI* as a polyp with high local curvatures at its apex. Furthermore, a clear separation between 'rings' of haustral folds (divided by the teniae coli) might be less visible if the colon is under-distended using *SI*. Any intensity-based registration will rely on the images which it tries to align to have a good enough degree of similar features between them. If the same anatomical structures

appears very different, it will present a challenge for the registration to find the correct correspondences automatically. Finding a similarity measure that is less affected by vast differences in global and local shape or distension than by shape index will improve registration accuracy and robustness.

Alternatives to the *shape index* adopted in this work could include curvature-derived measures, such as *mean curvature*, *Gaussian curvature*, or *curvedness* (See section 3.5.6.2). However, it is possible that an optimal measure of similarity might be the combination of several of the measures derived from the CTC images. Other measures derived directly from the CTC images could include the CT intensities or anatomical measures such as the colon wall thickness (Van Uitert et al., 2006). It needs yet to be established how similar such additional measures remain during the patient's changing between prone and supine positions. Multiple similarity measures could easily be integrated into the objective function of the registration as additional weighted penalty terms.

In the field of non-rigid image registration, a number of alternatives to using the sum-of-squared-differences *SSD* have been proposed in order to improve the robustness of the algorithms. *SSD* was used in this thesis as it is the intuitive measure of similarity due to the cylindrical images being of the same modality, i.e. prone and supine images with *SI* values as intensities. This assumes a one-to-one relationship between both images. However, alternatively proposed measures, such as correlation-based measures, have shown promise in non-rigid image registration and might be less affected by differences in the shape index images. Measures such as normalised cross-correlation (*NCC*) might account better for intensity changes between prone and supine shape index images. *NCC* could be computed globally or locally in order to adapt to the local feature patterns of the cylindrical images.

### 9.1.6 Integration of features in the registration optimisation

I demonstrated that using robust feature matches increases the accuracy of the proposed registration method when used as an initialisation to the non-rigid cylindrical registration (see Chapter 6). The features are currently purely used to transform the source image as an initialisation step and, thereafter, the registration is driven by the intensities of the cylindrical images (see Chapter 3). Further improvements to accuracy and robustness could be achieved by incorporating said feature matches into the optimisation process itself, when running the cylindrical registration. Registration approaches such as the one proposed by West et al. (2005) include an additional penalty term to the objective function of the registration algorithm. It penalises the transformation from misaligning pairs of features, using the distance between these corresponding points:

$$\mathcal{P}_{\text{Features}} = \frac{1}{N_{p,s}} \sum_{p,s=0}^{N_{p,s}} (x_p - \mathbf{T}_{\text{cyl}}(x_s))^2. \quad (9.1)$$

Here,  $N_{p,s}$  is the number of matching pairs of feature points  $(x_p, x_s)$  between the prone and supine cylindrical images. This penalty term can easily be integrated to the objective function of the registration by adding a weighted factor and it is differentiable with respect to the spline control points (West et al., 2005). Furthermore, it would be straightforward to integrate such a penalty term into the symmetric inverse-consistent registration case presented in Section 6.4.

### 9.1.7 Patient-specific registration

So far, all pre-specified parameters of the proposed registration method have been optimised by experimentation to work with a wide range of patient data and configurations (collapsed cases, follow-up cases, etc.). For example, the simplified meshes used for Ricci flow and computation of surface curvatures (shape index) consist of about 60,000 triangle faces. The decimation and smoothing parameters for generating these meshes have been chosen such that details of the colonic surface (such as folds and larger polyps) are still clearly visible after simplification. The resulting meshes proved sufficient for estimating the surface curvatures to drive the registration accurately in cylindrical space. However,

redundant triangles in the mesh representation of the colon surface have been removed. I used exactly the same parameters for extracting the colon surfaces from the segmentation of all colon lumina used in this study. A constant triangle face number for each patient however might be suboptimal as the number of haustral folds and colon distension can vary from patient to patient.

The resolution of the cylindrical images has also been kept constant despite the fact that the length of the colon can vary significantly between different patients, especially if parts of the large intestine have been removed by surgery. The same is true for the parameters of the B-spline registration algorithm. For example, the spacing between control points and multi-resolution levels have been kept constant between patients. However, setting an optimal control point spacing can be essential for successful image registration to generate physically meaningful results (Crum et al., 2004). In my experience, the number of haustral folds and the spacing between them can vary markedly in the cylindrical images, sometimes causing very different configurations of the feature patterns that drive the non-rigid registration. A registration method that automatically accounts for the colonic length differences between patients and finds optimal control-point spacings by automatically analysing the feature patterns of the image could be advantageous. Approaches such as proposed by Wang and Jiang (2007) that use *Non-Uniform Rational B-splines* (NURBS) (Piegl and Tiller, 1997) could adjust the registration parameters depending on patient-specific haustral fold configurations and potentially improve the registration results and robustness.

## 9.2 Using the registration result

The registration result itself can already be very useful for the clinician during diagnostic interpretation in order to allow rapid switching between the same anatomical position in the prone and supine images. However, the registration results could be useful in several ways in order to improve interpretation.

### 9.2.1 False-positive reduction in computer-aided-detection

Together with collaborators at *Medicsight PLC*, London, (Xujiong Ye and Greg Slabaugh et al.), a short feasibility study was performed in order to assess the possibility of using the prone-to-supine registration results for the reduction of false-positive (FP) detections in computer-aided-detection (CADE) algorithms for CT colonography. The proposed filtering method was developed by X. Ye et al. and I provided the prone and supine registration results as input. The results of this study were presented at *RSNA 2011*.

After I had provided automated prone-to-supine surface correspondence in 27 patients, using the proposed method (see Chapter 3), each finding of the *Medicsight's* CADE classifier (Slabaugh et al., 2010) was weighted, using a confidence measure based on the classifier's posterior probability. CADE findings were judged as false-positives and removed in two cases: 1) if the confidence weighting was below a certain pre-defined threshold ( $C$ ) in either the prone or supine view or 2), based on the registration result: the automatically established anatomical correspondence between both prone and supine endoluminal surfaces was used to filter CADE findings. The principle is based on the assumption that when the patient changes between prone and supine position, faecal residue (which might cause false-positives in CADE) tends to move, while fixed mural pathology (i.e. true polyps) does not. If the location of a CADE finding was outside a spherical region with pre-defined radius ( $R$ ) to a CADE finding in the opposing scan, the CADE mark was considered a FP and removed. This principle is illustrated in Fig. 9.2.

#### 9.2.1.1 Preliminary results

Initially, the CADE algorithm had a per-lesion sensitivity of 92.6% (25/27 lesions detected, median diameter 7 mm) and an average of 3.9 FPs per CTC volume. After prone-to-supine registration and application of the proposed registration-based FP filter with  $R=36$  mm and  $C=0.76$ , FP detections were reduced to 2.9 FP per volume. This is a 25.6% reduction without any loss of sensitivity.

To conclude, registration-based filtering algorithm reduces FP findings in CADE without any reduction in sensitivity, associated with the filtering process. The proposed registration-based FP filtering

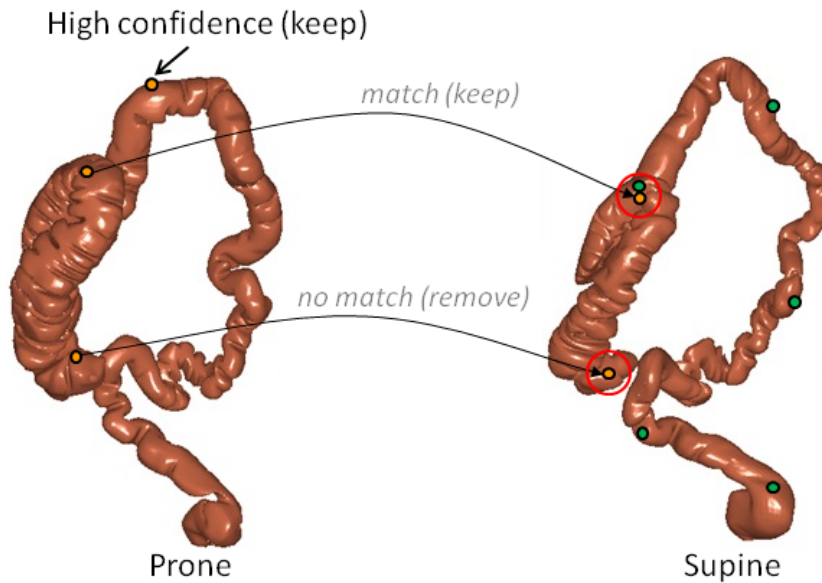


Figure 9.2: False-positive reduction in computer-aided-detection [After Xujiong Ye].

method has the potential to reduce FP findings in clinical colon CADe systems, e.g. (Slabaugh et al., 2010). These CADe systems have been designed to assist radiologists in the identification of colorectal lesions in CT colonography image data. Any reduction of FP findings will further facilitate CTC interpretation.

This work utilised the fact that a polyp will be at the same anatomical location in both patient positions, whereas false-positives (caused by remaining stool or folds mimicking the appearance of polyps) are likely to move or only be present in one scan. Any improvement in robustness and accuracy of the registration method would further increase the effectiveness of this false-positive reduction approach.

## 9.2.2 Registration of follow-up studies

Chapter 7 showed the promise of the ability of the proposed method to register follow-up CT colonography scans of the same patient over time. This has the potential to not just guide the radiologist to the same anatomical location in all temporally separated images rapidly, but also to assist in the understanding of how anatomical structures of the colon change over time. More than two scans of the same patient would allow a more accurate estimation of the flexibility of the colon and therefore allow more accurate parameter estimation for the above-mentioned bio-mechanical modelling (see Section 9.1.1). The amount of polyp growth could be estimated directly from the deformation field generated by the registration algorithm. Furthermore, changes to surface features of the colon over time (e.g. diverticula growth and haustration) could be more easily investigated.

For improving the registration accuracy of follow-up studies, one might consider the integration of group-wise registration approaches (Geng et al., 2009). This would mean that all cylindrical images from a follow-up study would be registered to the same ‘common’ reference space, rather than computing pairwise registrations as in Chapter 7. This could be realised by minimising one ‘larger’ objective function that includes the information from all directions of transformation at once.

## 9.2.3 Providing more information to the colonoscopist

After a true-positive polyp is established during CT colonography, it might be removed surgically in a subsequent colonoscopy procedure. Hence, the endoscopist would like to know the best patient position for reaching the polyp via the colonoscope in the optimal way for *polypectomy* (removal of the polyp). Information gathered from the polyp’s location in prone and supine positions could be used to estimate



the polyp's location during colonoscopy, taking gravitational forces into account. Furthermore, the endoscopist could be provided with the information of how far the polyp is located along the length of the colon as proposed by Summers et al. (2009) and after how many haustral folds. When haustral folds cannot be detected due to local colonic collapse in one of the views, information from the fused model could be used to fill the missing segment.

Potentially, the combination of the registration result with other modalities such as PET and MRI could improve sensitivity of the diagnosis. For example, PET allows an increase in diagnostic specificity by showing an increased uptake of  $^{18}\text{F}$ -FDG by colonic neoplasia (Taylor et al., 2010). MRI could be beneficial due to its better soft tissue differentiation in comparison to CTC (Sun et al., 2008).

### 9.2.4 Data fusion for optical colonoscopy guidance

Data from both prone and supine acquisitions could be fused after registration in order to maximise the amount of information that can be gained from the two images. Especially in the case of local colonic collapses in one view, the other view could provide information about the shape of the collapsed segment – if sufficiently insufflated in the opposing position. This means that anatomical information like haustral folds, polyps and teniae coli could be matched between prone and supine acquisitions in order to generate a fused representation of the colon. This will be especially useful if both prone and supine acquisitions are collapsed in different segments.

Data fusion could be especially important for methods that aim to establish correspondence between optical colonoscopy (OC) and CT colonography for improved image-based guidance for the colonoscopist. The fused data from prone-to-supine CTC colonography images could be used to build a patient-specific model of the colon's surface. This model could potentially be updated using real-time electromagnetic tracking data of the colonoscope's 3D shape during the colonoscopy (as provided by modern colonoscopes, for example by the *Olympus ScopeGuide*<sup>2</sup>).

Image-based guidance could be very helpful for the colonoscopic procedure that follows positive CTC interpretation. The detection of potentially precancerous polyps and cancer by CT colonography (CTC) is only the first step of patient treatment. Once a polyp has been detected with CTC, the patient must undergo subsequent optical colonoscopy (OC) to enable polypectomy. A computer-assisted guidance system would help the colonoscopist to navigate the anatomical location of suspicious regions, as identified by CTC. If accurate guidance is provided, a distinction between CTC false-positives and true abnormalities can be made more safely and efficiently by the colonoscopist. Potentially, any abnormalities perceived during optical colonoscopy could be automatically matched with the findings reported on the prior CTC. Computer-assisted guidance during colonoscopy would inevitably accelerate the procedure. Furthermore, it would have the potential to reduce adverse effects for the patient.

---

<sup>2</sup>[www.olympusamerica.com/msg\\_section/msg\\_scopeguide.asp](http://www.olympusamerica.com/msg_section/msg_scopeguide.asp)

## **Chapter 10**

# **Summary, discussion and conclusion**

## **10.1 Summary**

The following sections summarise all previous chapters individually.

### **10.1.1 Chapter 1: Introduction**

Robust and accurate automated registration between prone and supine CT colonography (CTC) acquisitions is pivotal for medical interpretation, but a challenging problem. The first chapter of this thesis gives an introduction and motivation to CT colonography and explains why automatic registration of prone and supine images is desirable for improving the diagnostic interpretation capabilities of CTC.

### **10.1.2 Chapter 2: Literature review and proposed solution**

The second chapter reviews existing approaches for the registration of prone and supine CT images. Methods that are based on matching of colon centrelines, anatomical landmarks such as flexures, haustral folds and/or teniae coli are described. Furthermore, I discuss voxel-based registration methods and polyp matching approaches. The drawbacks of these methods are explained and the proposed solution, based on a non-rigid registration of the colon surface in cylindrical space is introduced.

### **10.1.3 Chapter 3: Prone-to-supine registration in cylindrical space**

The chapter introduces the proposed registration method in detail. The described method represents the prone and supine surfaces, using triangulated meshes extracted from image segmentations of the colonic lumen. The complexity of the registration task is reduced by mapping both surfaces to the cylindrical domain using a conformal mapping based on Ricci flow. While mapping, the 3D curvatures of the surfaces are preserved, which allows these to drive a subsequent non-rigid registration. Automated alignment of the surfaces is achieved by using a modified version of B-spline registration that runs in the cylindrical domain. Using measurements of local shape index to drive the registration, the method is applicable even when cases exhibit local luminal collapses by estimating the length of collapsed regions and ignoring them during the registration process. This establishes a dense correspondence throughout the derived colon surface. Using a development set, suitable parameters were found to constrain the cylindrical registration method.

### **10.1.4 Chapter 4: Evaluation of registration accuracy**

The chapter provides a detailed evaluation of registration accuracy on a limited number of well-prepared of cases. All polyps present were well aligned, with a mean (std. dev.) registration error of 5.7 (3.4) mm. An additional set of 1175 reference points on haustral folds spread over the full endoluminal colon surfaces resulted in an error of 7.7 (7.4) mm. Here, 82% of folds were aligned correctly after registration with a further 15% misregistered by only one fold. The results show promise, not only for polyp detection but also for establishing dense correspondence between haustral folds and the full colonic surface.

### 10.1.5 Chapter 5: Clinical application of prone-to-supine registration

This chapter aims to provide an estimate of how the proposed method for prone-to-supine registration would perform in clinical practice. For increased robustness, a piece-wise linear initialisation based on robust haustral fold matches is introduced. It is validated with a phantom study utilising a porcine colon. Initialisation is shown to improve the accuracy of the registration method. The phantom study was performed in order to accurately measure registration accuracy achievable by the proposed method. An accurate reference standard was generated by using metallic fiducial markers attached to the colon's surface. Registration accuracy is improved from a mean (std. dev.) of 24.7 (22.9) mm to 4.9 (1.5) mm error using the proposed initialisation.

Secondly, an external clinical validation was performed with collaborators at University College Hospital (UCH), London (Darren Boone and Steve Halligan). The validation is based on a large publicly available CTC data set: the *ACRIN CTC trial* (Johnson et al., 2008). A total of 66 polyps in 49 patients were used in order to judge the algorithm's performance on data generalisable to clinical practice. Furthermore, the method was compared to a simpler, centreline-based method, i.e. "normalised distance along the centreline" in order to estimate the clinical benefit of the proposed method. Overall mean 3D polyp registration error was significantly smaller with mean (std. dev.) of 19.9 (20.6) mm in comparison to 27.7 (15.2) mm using NDACC ( $p = 0.001^1$ ). 82.7% of polyp matches were defined as "successful" in comparison to 37.1% using NDACC, according to the pre-specified criteria. Similarly, using 2D visualisation, 62.1% registrations were deemed "successful" compared to only 22.7% successful registrations using NDACC. The proposed method compares favourably to using NDACC.

### 10.1.6 Chapter 6: Inverse consistency in the registration of prone and supine CTC

It is furthermore shown in Chapter 6 that landmark matches for initialisation improve the registration's accuracy and robustness. The spatial registration errors and inverse consistency error are both significantly reduced by deploying an improved non-rigid initialisation scheme using robust haustral fold matches (Hampshire et al., 2013). Using 17 validation cases, registration accuracy is improved from a mean (std. dev.) of 11.9 (11.1) mm to 6.0 (1.9) mm and inverse consistency error is reduced from 5.7 (4.5) mm to 3.3 (2.8) mm. While improved inverse-consistency alone does not guarantee good correspondence, concomitant improvement in registration accuracy suggests that registration is more robust when using a non-rigid feature-based initialisation.

Additional performance improvements are achieved by symmetric and inverse-consistent registration. This helps to optimise registration in cases where false local minima are present in the similarity function that is being optimised. Information from both forward and inverse direction encourages convergence towards the correct solution in well prepared cases. The mean (std. dev.) inverse-consistency error was reduced significantly by 86%, from 3.3 (2.8) mm to 0.45 (0.45) mm. Furthermore, I showed improved visual alignment of the prone and supine colonic surfaces, evidenced by a reduction in the mean-of-squared-differences by 43% overall. Mean registration error, measured at a sparse set of manually selected reference points, remained at the same level as the non-symmetric method (no significant differences). The results suggest that the inverse-consistent symmetric algorithm performs more robustly than non-symmetric implementation of B-spline registration – at least in well-prepared CTC cases.

### 10.1.7 Chapter 7: Temporally separated CT Colonography cases

Robust and accurate non-rigid feature-based initialisation allows the registration of more challenging CT colonography cases, such as follow-up CT acquisitions. The method's ability to register temporally separated CTC cases, acquired several months or years apart, was investigated with collaborators from

---

<sup>1</sup>Related-Samples Wilcoxon Signed Rank Test, 5% significance level.

UCH, (Emma Helbren and Steve Halligan). Establishing correspondence between these follow-up studies is challenging, but important to the radiologists in order to monitor the growth of polyps. 26 external follow-up cases were investigated and registration was measured using the polyp's locations in all scans. A mean (std. dev.) registration error of 17.4 (12.1) mm (range 1.7 to 49.7 mm) was achieved when transforming polyp locations over time. The level of accuracy achieved by the registration algorithm is similar to the ACRIN data set used in Section 5.2 and therefore indicates a clinically useful result.

#### **10.1.8 Chapter 8: Registration of cases with different distensions**

This chapter describes a method that iteratively deforms the surface in order to compensate for differences in distension and bowel preparation. In order to overcome limitations of this registration method, I presented a new method that deforms the source colon surface in an iterative manner in 3D in order to increase similarity between the surfaces. Iterative deformation allows the re-computation of surface curvatures and, therefore, the shape index values on the deformed surface. The deformed surface aims to represent the target surface more closely. Therefore, the similarity of the cylindrical representations increases with each optimisation step. I showed that this can subsequently improve the spatial alignment of surface features in a limited number of challenging cases. Results are preliminary and the method has the potential to be improved by incorporating better 3D transformation models or bio-mechanical constraints.

#### **10.1.9 Chapter 9: Future work**

This chapter elaborates on possible future work which could improve the proposed registration method. The method presented relies on extracted colon surfaces of good quality. Obtaining good quality segmentations of the endoluminal colon surface reliably and accurately is a significant impediment to the clinical adoption of the proposed method.

Additionally, the chapter discusses how the similarity between the cylindrical images can be improved prior to non-rigid registration using bio-mechanical modelling, straightening of the colon surface and general improvement of the colon segmentations. Furthermore, the integration of additional or alternative similarity measures for driving the optimisation process are discussed; and a patient-specific registration parameter set is proposed.

Furthermore, it is discussed how the correspondences of the registration result and method could be used to improve the diagnostic process. Correspondence could further improve computer-aided detection algorithms (CADE). For example, a registration-based filtering algorithm was presented that was shown to reduce false-positive findings in CADE without any reduction in sensitivity associated with the filtering process. This has the potential to further enhance computer-aided CTC interpretation.

Finally, a future outlook is provided as to how a fused representation of a prone and supine CTC data set could be useful when establishing correspondence to optical colonoscopy. Prone and supine data fusion might be beneficial for improved colonoscopy planning when aiming to resect polyps reported at the prior CTC stage.

## 10.2 Discussion

I have presented a method that simplifies the problem of aligning the prone and supine surfaces from a 3D to a 2D task. Simplification is achieved by mapping the full endoluminal surface to a cylindrical parametrisation which reflects the colon's specific anatomy, using a conformal mapping technique. The novel contribution of my work is that cylindrical parametrisation is used in order to align the endoluminal colon surface using non-rigid B-spline registrations in the parametrised space – rather than performing a registration in full 3D space. This approach was motivated by the assumption that, while the overall shape of the colon can undergo large deformations when the patient changes position, the local shape of surface structures, such as haustral folds, and their relative local configuration remains similar enough between CTC scans to align the surfaces. Cylindrical registration enables the recovering of large non-linear deformations and torsions of the colon that occur between CTC acquisitions.

The reported registration results show promise of the ability to rapidly and automatically switch between prone and supine positions after registration. While it is intuitive that an accurate prone-to-supine registration would be beneficial for shortening interpretation time, further studies of clinical utility in everyday practice are necessary. For example, the effect on sensitivity and specificity when finding polyps needs to be evaluated.

A common occurrence in CT colonography is that of local collapse of the colon in one or both scans. Indeed, nearly half of the data (47%) used in Section 5.2 had at least one region of complete luminal collapse. I showed that the method is able to handle such cases – even with multiple collapses in both views. The current trend towards less bowel preparation for CTC (i.e. without full cathartic preparation (Callstrom et al., 2001, Zalis et al., 2012)) will introduce challenges for accurate colon segmentation and is likely to cause more segmentation errors. How exactly reduced bowel preparation would affect registration accuracy would need to be investigated in the future.

In current clinical practice, prior to virtual colonoscopy, the interpreting clinician must check the validity of the workstation's proposed colonic segmentation to make sure correct navigation along the colonic lumen, primarily to ensure the computed centreline takes the correct path. Likewise, the current method requires some manual interaction. These are: 1) choosing the structure element sizes interactively in order to correct the colon segmentations and include the rectal insufflation catheter while visually inspecting the segmentation quality. 2) selecting the start and end-point as well as the correct order of each well-distended colon segment. Thereafter, the algorithm for establishing correspondence over the whole colonic surface is automated. Future work should aim to improve automation of the pre-processing steps as described in Chapter 9.

The presented method relies on extracted colon surfaces of good quality, i.e. a surface that has few artefacts that would introduce wrong haustral folds and/or polyps, and/or would cause the extracted surface representation to be incorrectly aligned with the true inner colon surface. Clearly, the quality of surface representations depends on the quality, noise and resolution of the CTC scans as these parameters will affect the quality of the colon segmentation, and in turn the features that drive the cylindrical registrations. Pre-processing steps of surface smoothing and topological correction can correct for some errors and noise in the segmentations but have their own limitations. Obtaining good quality segmentations of the intraluminal colon surface reliably and robustly is an important requirement for the clinical adoption of the proposed method.

In addition, while the processing of the endoluminal centreline occurs rapidly and is available to the reporting radiologist at the time of reporting, the proposed registration method, at present, requires considerable processing time. This is for surface extraction, feature matching and non-rigid registration. However, once this step has been completed, transferring between matched prone and supine locations is practically instantaneous. This is reminiscent of another, well-established adjunct to CT colonographic interpretation – computer-aided detection (CADE) which, although now integrated into many vendor

platforms, initially required several hours of processing time. Similarly, the current implementation of the feature matching takes several hours to complete. Work by T. Hampshire is currently underway to drastically improve this computation time. On the other hand, the current implementations of surface extraction, conformal mapping based on Ricci flow (using Newton's method for optimisation), and non-rigid registration run in the order of minutes on the CPU. I anticipate that with the integration of multi-threading and/or GPU-technology the computation time required can be reduced, such that integration into routine work-flow could be possible.

### **10.3 Conclusion**

In conclusion, I have presented an innovative method for establishing spatial correspondence between endoluminal colonic surfaces extracted from CTC acquisitions. The registration provides a dense correspondence between the extracted colon surfaces. This will further facilitate the interpretation of CTC data and has the potential for integration into subsequent computer-based algorithms for the analysis and the clinical work-flow for colonographic interpretation.

# Bibliography

**The page(s) on which each reference is cited in this thesis is(are) indicated at the end of each reference.**

- Acar, B., S. Napel, D. Paik, P. Li, J. Yee, C. Beaulieu, and R. Jeffrey (2001). Registration of supine and prone ct colonography data: Method and evaluation. *Radiology* 221(332), 332. [p. 84]
- Acar, B., S. Napel, D. Paik, P. Li, J. Yee, R. Jeffrey Jr, and C. Beaulieu (2002). Medial axis registration of supine and prone CT colonography data. *Engineering in Medicine and Biology Society, 2001. Proc. 23rd Annual International Conference of the IEEE* 3, 2433–2436. [p. 25]
- Adalsteinsson, D. and J. Sethian (1995). A fast level set method for propagating interfaces. *J. Comput. Phys.* 118(2), 269–277. [p. 27], [p. 39]
- Ahn, W., H. Woo, J. Kwon, J. Joo, D. Lee, and S. Yi (2005). Model of frictional contact with soft tissue for colonoscopy simulator. In *Systems, Man and Cybernetics, 2005 IEEE International Conference on*, Volume 3, pp. 2714–2719. IEEE. [p. 124]
- Amit, Y. (1994). A nonlinear variational problem for image matching. *SIAM Journal on Scientific Computing* 15(1), 207–224. [p. 105]
- Atkin, W., R. Edwards, I. Kralj-Hans, K. Wooldrage, A. Hart, J. Northover, D. Parkin, J. Wardle, S. Duffy, and J. Cuzick (2010). Once-only flexible sigmoidoscopy screening in prevention of colorectal cancer: A multicentre randomised controlled trial. *The Lancet* 375(9726), 1624–1633. [p. 17]
- Avants, B., C. Epstein, M. Grossman, and J. Gee (2008). Symmetric diffeomorphic image registration with cross-correlation: Evaluating automated labeling of elderly and neurodegenerative brain. *Medical image analysis* 12(1), 26–41. [p. 104], [p. 105]
- Banchoff, T. (1967). Critical points and curvature for embedded polyhedra. *J. Diff. Geom* 1(245-256), 34. [p. 51]
- Bartolí, A., R. Wegenkittl, A. König, and E. Gröller (2001). Nonlinear virtual colon unfolding. In *Proceedings of the conference on Visualization'01*, pp. 411–420. IEEE Computer Society. [p. 10], [p. 31]
- Bartolí, A., R. Wegenkittl, A. König, E. Gröller, E. Sorantin, and T. Medgraph (2001). Virtual colon flattening. *VisSym Joint Eurographics - IEEE TCVG Symposium on Visualization*, 127–136. [p. 31]
- Batchelor, P., A. Castellano Smith, D. Hill, D. Hawkes, T. Cox, and A. Dean (2002). Measures of folding applied to the development of the human fetal brain. *Medical Imaging, IEEE Transactions on* 21(8), 953–965. [p. 12], [p. 49], [p. 52]



- Bertrand, G. (1994). Simple points, topological numbers and geodesic neighborhoods in cubic grids. *Pattern recognition letters* 15(10), 1003–1011. [p. 37], [p. 40]
- Bieberbach, L., F. Steinhardt, and P. Morse (1953). *Conformal mapping*. Chelsea Publishing Company, Translation of the 4th ed of Einführung in die Konforme Abbildung, Berlin, 1949. [p. 32]
- Blum, H. et al. (1967). A transformation for extracting new descriptors of shape. *Models for the perception of speech and visual form* 19(5), 362–380. [p. 26]
- Boone, D., S. Halligan, and S. Taylor (2011). Evidence review and status update on computed tomography colonography. *Current gastroenterology reports* 13(5), 486–494. [p. 18], [p. 20], [p. 21]
- Boykov, Y., O. Veksler, and R. Zabih (2002). Fast approximate energy minimization via graph cuts. *IEEE Trans. Pattern Anal. Mach. Intell.* 23(11), 1222–1239. [p. 67]
- Brehm, U. and W. Kühnel (1981). Smooth approximation of polyhedral surfaces with respect to curvature measures. *Global Differential Geometry and Global Analysis*, 64–68. [p. 51]
- Burling, D., S. Halligan, A. Slater, M. Noakes, and S. Taylor (2006). Potentially serious adverse events at CT colonography in symptomatic patients: National survey of the United Kingdom. *Radiology* 239(2), 464–471. [p. 17]
- Cai, W., J.-G. Lee, S. Kim, and H. Yoshida (2012). Dual-energy electronic cleansing for artifact-free visualization of the colon in fecal-tagging ct colonography. In H. Yoshida, G. Sakas, and M. Linguraru (Eds.), *Abdominal Imaging. Computational and Clinical Applications*, Volume 7029 of *Lecture Notes in Computer Science*, pp. 8–17. Springer Berlin / Heidelberg. [p. 126]
- Cai, W., H. Yoshida, M. Zalis, J. Näppi, and G. Harris (2010). Informatics in radiology: Electronic cleansing for noncathartic ct colonography: A structure-analysis scheme. *Radiographics* 30(3), 585–602. [p. 126]
- Cai, W., M. E. Zalis, J. Näppi, G. J. Harris, and H. Yoshida (2008). Structure-analysis method for electronic cleansing in cathartic and noncathartic ct colonography. *Medical Physics* 35(7), 3259–3277. [p. 126]
- Callstrom, M., C. Johnson, J. Fletcher, J. Reed, D. Ahlquist, W. Harmsen, K. Tait, L. Wilson, and K. Corcoran (2001). Ct colonography without cathartic preparation: Feasibility study1. *Radiology* 219(3), 693–698. [p. 126], [p. 136]
- Cappell, M. et al. (2005). The pathophysiology, clinical presentation, and diagnosis of colon cancer and adenomatous polyps. *Med Clin North Am* 89(1), 1–42. [p. 10], [p. 19]
- Cardoso, M., M. Clarkson, M. Modat, and S. Ourselin (2011). On the extraction of topologically correct thickness measurements using khalimskys cubic complex. In G. Székely and H. Hahn (Eds.), *Information Processing in Medical Imaging*, Volume 6801 of *Lecture Notes in Computer Science*, pp. 159–170. Springer Berlin / Heidelberg. [p. 40]
- Carter, T., M. Serresant, D. Cash, D. Barratt, C. Tanner, and D. Hawkes (2005). Application of soft tissue modelling to image-guided surgery. *Medical engineering & physics* 27(10), 893–909. [p. 124]
- Castellano, S. A. (1999, September). *The Folding of the Human Brain: From Shape to Function*. Ph. D. thesis, University of London, Division of Radiological Sciences and Medical Engineering, King's College London. [p. 12], [p. 51], [p. 52]

- Chang, K., H. Zhang, S. Chen, L. Chen, and J. Chen (2011). Automatic colon segmentation using isolated-connected threshold. In *Robot, Vision and Signal Processing (RVSP), 2011 First International Conference on*, pp. 44–47. IEEE. [p. 126]
- Chowdhury, A., S. Tan, J. Yao, M. Linguraru, and R. Summers (2009). Two methods of haustral fold detection from computed tomographic virtual colonoscopy images. In *Proceedings of SPIE*, Volume 7260, pp. 72602U. [p. 28]
- Chowdhury, T. and P. Whelan (2011). A fast and accurate method for automatic segmentation of colons at ct colonography based on colon geometrical features. In *2011 Irish Machine Vision and Image Processing Conference*, pp. 94–100. IEEE. [p. 126]
- Christensen, G., X. Geng, J. Kuhl, J. Bruss, T. Grabowski, I. Pirwani, M. Vannier, J. Allen, and H. Damasio (2006). Introduction to the non-rigid image registration evaluation project (nirep). *Biomedical Image Registration*, 128–135. [p. 94], [p. 95]
- Christensen, G. and H. Johnson (2001, july). Consistent image registration. *Medical Imaging, IEEE Transactions on* 20(7), 568–582. [p. 94], [p. 105]
- Cignoni, P., M. Corsini, and G. Ranzuglia (2008). Meshlab: an open-source 3d mesh processing system. *ERCIM News* 73, 45–46. [p. 41]
- Cotin, S., H. Delingette, and N. Ayache (1999). Real-time elastic deformations of soft tissues for surgery simulation. *Visualization and Computer Graphics, IEEE Transactions on* 5(1), 62–73. [p. 124]
- Couprie, M., D. Coeurjolly, and R. Zrou (2007). Discrete bisector function and euclidean skeleton in 2d and 3d. *Image and Vision Computing* 25(10), 1543–1556. [p. 39], [p. 40]
- Crum, W., T. Hartkens, and D. Hill (2004). Non-rigid image registration: theory and practice. *British journal of radiology* 77(suppl 2), S140–S153. [p. 129]
- Dachman, A., J. Lieberman, R. Osnis, S. Chen, K. Hoffmann, C. Chen, G. Newmark, and J. McGill (1997). Small simulated polyps in pig colon: sensitivity of ct virtual colography. *Radiology* 203(2), 427–430. [p. 75], [p. 83]
- Davis, B., J. Norris, J. Bieszczad, J. Soto, and D. Kynor (2011). Fully automated prone-supine coregistration in computed tomographic colonography. In *Proceedings of SPIE*, Volume 7962, pp. 79621U. [p. 34]
- Day, J., A. Freeman, N. Coni, and A. Dixon (1993). Barium enema or computed tomography for the frail elderly patient? *Clinical radiology* 48(1), 48–51. [p. 17]
- de González, A., K. Kim, A. Knudsen, I. Lansdorp-Vogelaar, C. Rutter, R. Smith-Bindman, J. Yee, K. Kuntz, M. Van Ballegooijen, A. Zauber, et al. (2011). Radiation-related cancer risks from ct colonography screening: a risk-benefit analysis. *American Journal of Roentgenology* 196(4), 816–823. [p. 126]
- de Vries, A., R. Truyen, J. Van der Peijl, J. Florie, R. van Gelder, F. Gerritsen, and J. Stoker (2006). Feasibility of automated matching of supine and prone CT-colonography examinations. *Br. J. Radiol.* 79(945), 740–744. [p. 25], [p. 84]
- Deschamps, T. and L. Cohen (2001). Fast extraction of minimal paths in 3D images and applications to virtual endoscopy. *Med. Image Anal.* 5(4), 281–299. [p. 25], [p. 27], [p. 39]

- Deyhle, P. (1980). Results of endoscopic polypectomy in the gastrointestinal tract. *Endoscopy* (Suppl), 35. [p. 17]
- Feng, W., S. Reeves, T. Denney, S. Lloyd, L. Dell'Italia, and H. Gupta (2009). A new consistent image registration formulation with a b-spline deformation model. In *Biomedical Imaging: From Nano to Macro, 2009. ISBI'09. IEEE International Symposium on*, pp. 979–982. IEEE. [p. 105], [p. 110]
- Fenlon, H., D. Nunes, P. Schroy, M. Barish, P. Clarke, and J. Ferrucci (1999). A comparison of virtual and conventional colonoscopy for the detection of colorectal polyps. *N. Engl. J. Med.* 341(20), 1496–1503. [p. 18]
- Fink, M., A. Freeman, A. Dixon, and N. Coni (1994). Computed tomography of the colon in elderly people. *BMJ* 308(6935), 1018. [p. 17]
- Fischl, B., M. Sereno, R. Tootell, and A. Dale (1999). High-resolution intersubject averaging and a coordinate system for the cortical surface. *Human Brain Mapping* 8(4), 272–284. [p. 30]
- Floater, M. and K. Hormann (2005). Surface parameterization: a tutorial and survey. *Advances in multiresolution for geometric modelling*, 157–186. [p. 10], [p. 32], [p. 33], [p. 35], [p. 43], [p. 73]
- Fornefett, M., K. Rohr, and H. S. Stiehl (2001). Radial basis functions with compact support for elastic registration of medical images. *Image and Vision Computing* 19(1), 87–96. [p. 118]
- Fukano, E., M. Oda, T. Kitasaka, Y. Suenaga, T. Takayama, H. Takabatake, M. Mori, H. Natori, S. Nawano, and K. Mori (2010). Haustral fold registration in CT colonography and its application to registration of virtual stretched view of the colon. *SPIE Med. Imaging: Computer-Aided Diagnosis* 7624(1), 762420. [p. 27], [p. 84]
- Gene Coin, C., F. Wollett, J. Thaddeus Coin, M. Rowland, R. Deramos, and R. Dandrea (1983). Computerized radiology of the colon: a potential screening technique. *Computerized Radiology* 7(4), 215–221. [p. 17]
- Geng, X., G. Christensen, H. Gu, T. Ross, and Y. Yang (2009). Implicit reference-based group-wise image registration and its application to structural and functional mri. *NeuroImage* 47(4), 1341. [p. 130]
- Graser, A., P. Stieber, D. Nagel, C. Schaefer, D. Horst, C. R. Becker, K. Nikolaou, A. Lottes, S. Geisbuesch, H. Kramer, et al. (2009). Comparison of ct colonography, colonoscopy, sigmoidoscopy and faecal occult blood tests for the detection of advanced adenoma in an average risk population. *Gut* 58(2), 241–248. [p. 20]
- Gray, H. (1858). *Anatomy—descriptive and surgical*. JW Parker and Son. [p. 10], [p. 19], [p. 27], [p. 83]
- Gu, X., F. Luo, and S. Yau (2005). Tutorial on discrete ricci flow for global parameterizations. *Technique report, August*. [p. 43]
- Haker, S., S. Angenent, A. Tannenbaurn, and R. Kikinis (2000). Nondistorting flattening maps and the 3-D visualization of colon CT images. *IEEE Trans. Med. Imaging* 19(7), 665–670. [p. 33], [p. 73]
- Halligan, S. and H. Fenlon (1999). Virtual colonoscopy. *Bmj* 319(7219), 1249–1252. [p. 10], [p. 18]
- Halligan, S., R. J. Lilford, J. Wardle, D. Morton, P. Rogers, K. Wooldrage, R. Edwards, R. Kanani, U. Shah, W. Atkin, et al. (2007). Design of a multicentre randomized trial to evaluate ct colonography versus colonoscopy or barium enema for diagnosis of colonic cancer in older symptomatic patients: The siggar study. *Trials* 8(1), 32. [p. 20], [p. 21]

- Halligan, S., S. Taylor, J. Dehmeshki, H. Amin, X. Ye, J. Tsang, and M. Roddie (2006). Computer-assisted detection for ct colonography: external validation. *Clin. Radiol.* 61(9), 758–763. [p. 84]
- Hamilton, R. (1982). Three-manifolds with positive Ricci curvature. *J. Differential Geom.* 17(2), 255–306. [p. 43]
- Hampshire, T., H. Roth, D. Boone, G. Slabaugh, S. Halligan, and D. Hawkes (2012). Prone to supine ct colonography registration using a landmark and intensity composite method. *Abdominal Imaging. Computational and Clinical Applications*, 1–9. [p. 23], [p. 98]
- Hampshire, T., H. Roth, M. Hu, D. Boone, G. Slabaugh, S. Punwani, S. Halligan, and D. Hawkes (2011). Automatic prone to supine haustral fold matching in CT colonography using a markov random field model. *Medical Image Computing and Computer-Assisted Intervention–MICCAI 2011*, 508–515. [p. 23], [p. 28], [p. 85], [p. 96]
- Hampshire, T., H. R. Roth, E. Helbren, A. Plumb, D. Boone, G. Slabaugh, S. Halligan, and D. J. Hawkes (2013). Endoluminal surface registration for ct colonography using haustral fold matching. *Medical Image Analysis*. [p. 23], [p. 28], [p. 79], [p. 81], [p. 84], [p. 85], [p. 95], [p. 96], [p. 99], [p. 100], [p. 107], [p. 123], [p. 134]
- Hara, A., M. Kuo, M. Blevins, M. Chen, J. Yee, A. Dachman, C. Menias, B. Siewert, J. Cheema, R. Obregon, et al. (2011). National ct colonography trial (acrin 6664): comparison of three full-laxative bowel preparations in more than 2500 average-risk patients. *Am. J. Roentgenol.* 196(5), 1076–1082. [p. 17], [p. 84], [p. 86]
- Herman, G. (2009). *Fundamentals of Computerized Tomography: Image Reconstruction from Projections*. Springer Verlag. [p. 17]
- Holden, M. (2008). A review of geometric transformations for nonrigid body registration. *Medical Imaging, IEEE Transactions on* 27(1), 111–128. [p. 118]
- Hong, W., X. Gu, F. Qiu, M. Jin, and A. Kaufman (2006). Conformal virtual colon flattening. *Proc. 2006 ACM Symposium on Solid and Physical Modeling*, 85–93. [p. 11], [p. 33], [p. 35], [p. 39], [p. 44], [p. 73]
- Hoppe, H. (1999). New quadric metric for simplifying meshes with appearance attributes. *Proc. Article on Visualization'99: Celebrating Ten Years*, 59–66. [p. 41]
- Hounsfield, G. (1973). Computerized transverse axial scanning (tomography): Part 1. description of system. *British Journal of Radiology* 46(552), 1016–1022. [p. 17]
- Huang, A., D. Roy, M. Franaszek, and R. M. Summers (2005). Teniae coli guided navigation and registration for virtual colonoscopy. In *Visualization, 2005. VIS 05. IEEE*, pp. 279–285. IEEE. [p. 34]
- Huang, A., D. Roy, R. Summers, M. Franaszek, N. Petrick, J. Choi, and P. Pickhardt (2007). Teniae coli-based circumferential localization system for CT colonography: Feasibility study. *Radiology* 243(2), 551–560. [p. 27], [p. 34], [p. 84], [p. 104]
- Huysmans, T., J. Sijbers, and V. Brigitte (2010). Automatic construction of correspondences for tubular surfaces. *IEEE Trans. Pattern Anal. Mach. Intell.* 32(4), 636–651. [p. 30], [p. 56]
- Ikuta, K., K. Iritani, J. Fukuyama, and M. Takeichi (2000). Portable virtual endoscope system with force and visual display. In *Intelligent Robots and Systems, 2000.(IROS 2000). Proceedings. 2000 IEEE/RSJ International Conference on*, Volume 1, pp. 720–726. IEEE. [p. 124]

- Iordanescu, G. and R. Summers (2003). Automated centerline for computed tomography colonography. *Academic radiology* 10(11), 1291–1301. [p. 27]
- Ismail, M., S. Elhabian, A. Farag, G. Dryden, and A. Seow (2012). Fully automated 3d colon segmentation for early detection of colorectal cancer based on convex formulation of the active contour model. In *Computer Vision and Pattern Recognition Workshops (CVPRW), 2012 IEEE Computer Society Conference on*, pp. 58–63. IEEE. [p. 126]
- Jin, M., J. Kim, F. Luo, and X. Gu (2008). Discrete surface Ricci flow. *IEEE Trans. Vis. Comput. Graphics* 14(5), 1030–1043. [p. 32], [p. 33], [p. 43], [p. 44], [p. 45], [p. 46], [p. 73], [p. 85]
- Johnson, C., M. Chen, A. Toledano, J. Heiken, A. Dachman, M. Kuo, C. Menias, B. Siewert, J. Cheema, R. Obregon, et al. (2008). Accuracy of CT colonography for detection of large adenomas and cancers. *N. Engl. J. Med.* 359(12), 1207–1217. [p. 17], [p. 20], [p. 74], [p. 85], [p. 134]
- Johnson, K., C. Johnson, J. Fletcher, R. MacCarty, and R. Summers (2006). CT colonography using 360-degree virtual dissection: A feasibility study. *Am. J. Roentgenol.* 186, 90–95. [p. 35]
- Kilic, N. (2012). Automatic colon segmentation using cellular neural network for the detection of colorectal polyps. *IU-Journal of Electrical & Electronics Engineering* 7(2). [p. 126]
- Kirkpatrick, S., C. Gelatt, and M. Vecchi (1983). Optimization by simulated annealing. *science* 220(4598), 671. [p. 34]
- Knudsen, A. B., I. Lansdorp-Vogelaar, C. M. Rutter, J. E. Savarino, M. van Ballegooijen, K. M. Kuntz, and A. G. Zauber (2010). Cost-effectiveness of computed tomographic colonography screening for colorectal cancer in the medicare population. *Journal of the National Cancer Institute* 102(16), 1238–1252. [p. 20]
- Koenderink, J. (1990). *Solid shape*. Cambridge, Massachusetts: MIT Press. [p. 28], [p. 51], [p. 93]
- Koenderink, J. and A. van Doorn (1992). Surface shape and curvature scales. *Image and vision computing* 10(8), 557–564. [p. 28], [p. 93]
- Laghi, A., F. Iafrate, M. Rengo, and C. Hassan (2010). Colorectal cancer screening: The role of ct colonography. *World journal of gastroenterology: WJG* 16(32), 3987. [p. 126]
- Lai, Z., J. Hu, C. Liu, V. Taimouri, D. Pai, J. Zhu, J. Xu, and J. Hua (2010). Intra-patient supine-prone colon registration in ct colonography using shape spectrum. *Medical Image Computing and Computer-Assisted Intervention–MICCAI 2010*, 332–339. [p. 34], [p. 127]
- Laks, S., M. Macari, and E. Bini (2004). Positional change in colon polyps at ct colonography<sup>1</sup>. *Radiology* 231(3), 761–766. [p. 75]
- Lamy, J. and R. Summers (2007). Teniae coli detection from colon surface: extraction of anatomical markers for virtual colonoscopy. pp. 199–207. [p. 27], [p. 28]
- Lavery, I. (1996). Colonic fistulas. *Surgical Clinics of North America* 76(5), 1183–1190. [p. 39]
- Lee, M., S. Kim, H. Park, J. Lee, S. Joo, S. An, and B. Choi (2009). An anthropomorphic phantom study of computer-aided detection performance for polyp detection on ct colonography: a comparison of commercially and academically available systems. *American Journal of Roentgenology* 193(2), 445–454. [p. 75]

- Lee, S., G. Wolberg, and S. Shin (1997). Scattered data interpolation with multilevel b-splines. *Visualization and Computer Graphics, IEEE Transactions on* 3(3), 228–244. [p. 98], [p. 99]
- Levin, B., D. A. Lieberman, B. McFarland, R. A. Smith, D. Brooks, K. S. Andrews, C. Dash, F. M. Giardiello, S. Glick, T. R. Levin, et al. (2008). Screening and surveillance for the early detection of colorectal cancer and adenomatous polyps, 2008: A joint guideline from the american cancer society, the us multi-society task force on colorectal cancer, and the american college of radiology. *CA: a cancer journal for clinicians* 58(3), 130–160. [p. 20]
- Lévy, B., S. Petitjean, N. Ray, and J. Maillot (2002). Least squares conformal maps for automatic texture atlas generation. In *ACM Transactions on Graphics (TOG)*, Volume 21, pp. 362–371. ACM. [p. 10], [p. 33]
- Li, L., J. Zhao, L. Lu, D. Zhang, and Z. Wang (2009). Colon straightening based on a gravity field model. In *Information Science and Engineering (ICISE), 2009 1st International Conference on*, pp. 3621–3624. IEEE. [p. 32]
- Li, P., S. Napel, B. Acar, D. Paik, R. Jeffrey Jr, and C. Beaulieu (2004). Registration of central paths and colonic polyps between supine and prone scans in computed tomography colonography: Pilot study. *Med. Phys.* 31(10), 2912–2923. [p. 25], [p. 26], [p. 84]
- Liepa, P. (2003). Filling holes in meshes. In *Proceedings of the 2003 Eurographics/ACM SIGGRAPH symposium on Geometry processing*, pp. 200–205. Eurographics Association. [p. 41]
- Liu, M., L. Lu, J. Bi, V. Raykar, M. Wolf, and M. Salganicoff (2011). Robust large scale prone-supine polyp matching using local features: a metric learning approach. *Medical Image Computing and Computer-Assisted Intervention—MICCAI 2011*, 75–82. [p. 29]
- Lohsiriwat, V. (2010). Colonoscopic perforation: Incidence, risk factors, management and outcome. *World J. Gastroenterol.* 16(4), 425–430. [p. 17]
- Loop, C. (1987). Smooth subdivision surfaces based on triangles. *Master's thesis, University of Utah, Department of Mathematics*. [p. 41]
- Lorensen, W. and H. Cline (1987). Marching cubes: A high resolution 3d surface construction algorithm. In *ACM Siggraph Computer Graphics*, Volume 21, pp. 163–169. ACM. [p. 37], [p. 41]
- Lu, L., M. Wolf, J. Liang, M. Dundar, J. Bi, and M. Salganicoff (2009). A two-level approach towards semantic colon segmentation: removing extra-colonic findings. *Medical Image Computing and Computer-Assisted Intervention—MICCAI 2009*, 1009–1016. [p. 73], [p. 126]
- Lu, L., D. Zhang, L. Li, and Z. Jun (2011). Fully automated colon segmentation for the computation of complete colon centerline in virtual colonoscopy. *Biomedical Engineering, IEEE Transactions on* (99), 1–1. [p. 126]
- Lu, L., D. Zhang, L. Li, and J. Zhao (2012). Fully automated colon segmentation for the computation of complete colon centerline in virtual colonoscopy. *Biomedical Engineering, IEEE Transactions on* 59(4), 996–1004. [p. 61], [p. 126]
- Lu, L. and J. Zhao (2011). An automatic method for colon segmentation in virtual colonoscopy. In *Biomedical Engineering and Informatics (BMEI), 2011 4th International Conference on*, Volume 1, pp. 105–108. IEEE. [p. 126]

- Mertzaniidou, T., J. Hipwell, L. Han, Z. Taylor, H. Huisman, U. Bick, N. Karssemeijer, and D. Hawkes (2012). Intensity-based mri to x-ray mammography registration with an integrated fast biomechanical transformation. *Breast Imaging*, 48–55. [p. 124]
- Metz, C., S. Klein, M. Schaap, T. Van Walsum, and W. Niessen (2011). Nonrigid registration of dynamic medical imaging data using intensity-based b-splines and a groupwise optimization approach. *Medical Image Analysis* 15(2), 238–249. [p. 56]
- Modat, M., M. Cardoso, P. Daga, D. Cash, N. Fox, and S. Ourselin (2012). Inverse-consistent symmetric free form deformation. *Biomedical Image Registration*, 79–88. [p. 105], [p. 106], [p. 107], [p. 110]
- Modat, M., J. McClelland, and S. Ourselin (2010). Lung registration using the NiftyReg package. *Proc. MICCAI Medical Image Analysis for the Clinic: A Grand Challenge, EMPIRE10*. [p. 59]
- Modat, M., G. Ridgway, Z. Taylor, M. Lehmann, J. Barnes, D. Hawkes, N. Fox, and S. Ourselin (2010). Fast free-form deformation using graphics processing units. *Comput. Meth. Prog. Bio.* 98(3), 278–284. [p. 23], [p. 56], [p. 85], [p. 91], [p. 93], [p. 107]
- Moore, M. and J. Wilhelms (1988). Collision detection and response for computer animation. In *ACM Siggraph Computer Graphics*, Volume 22, pp. 289–298. ACM. [p. 125]
- Nain, D., S. Haker, W. Grimson, E. Cosman, W. Wells, H. Ji, R. Kikinis, and C. Westin (2002). Intra-patient prone to supine colon registration for synchronized virtual colonoscopy. *Proc. MICCAI*, 573–580. [p. 25]
- Näppi, J., M. Imuta, Y. Yamashita, and H. Yoshida (2012). Computer-aided detection for ultra-low-dose ct colonography. *Abdominal Imaging. Computational and Clinical Applications*, 40–48. [p. 126]
- Näppi, J., A. Okamura, H. Frimmel, A. Dachman, and H. Yoshida (2005). Region-based supine-prone correspondence for reduction of false-positive CAD polyp candidates in CT colonography. *Acad. Radiol.* 12, 695–707. [p. 27], [p. 73], [p. 84]
- Näppi, J. and H. Yoshida (2007). Fully automated three-dimensional detection of polyps in fecal-tagging ct colonography. *Academic radiology* 14(3), 287–300. [p. 61], [p. 126]
- Nguyen, T. B., S. Wang, V. Anugu, N. Rose, M. McKenna, N. Petrick, J. E. Burns, and R. M. Summers (2012). Distributed human intelligence for colonic polyp classification in computer-aided detection for ct colonography. *Radiology* 262(3), 824–833. [p. 20]
- Oda, M., Y. Hayashi, T. Kitasaka, K. Mori, and Y. Suenaga (2006). A method for generating virtual unfolded view of colon using spring model. In *Proceedings of SPIE*, Volume 6143, pp. 61431C. [p. 28], [p. 32]
- Oda, M., T. Kitasaka, Y. Hayashi, K. Mori, Y. Suenaga, and J. Toriwaki (2005). Development of a navigation-based cad system for colon. *Medical Image Computing and Computer-Assisted Intervention–MICCAI 2005*, 696–703. [p. 31]
- Oda, M., T. Kitasaka, K. Mori, Y. Suenaga, T. Takayama, H. Takabatake, M. Mori, H. Natori, and S. Nawano (2009). Haustral fold detection method for ct colonography based on difference filter along colon centerline. In *Society of Photo-Optical Instrumentation Engineers (SPIE) Conference Series*, Volume 7260, pp. 84. [p. 28]
- Ogden, R. W. (1998). *Nonlinear Elastic Deformations*. Dover. [p. 124]

- Passenger, J., O. Acosta, H. de Visser, S. Bauer, C. Russ, and S. Ourselin (2008). Texture coordinate generation of colonic surface meshes for surgical simulation. In *Biomedical Imaging: From Nano to Macro, 2008. ISBI 2008. 5th IEEE International Symposium on*, pp. 640–643. IEEE. [p. 32]
- Peterson, S., M. Brejl, and A. Gothandaraman (2011, April 19). Characteristic path-based colon segmentation. US Patent 7,929,748. [p. 126]
- Pickhardt, P., J. Choi, I. Hwang, J. Butler, M. Puckett, H. Hildebrandt, R. Wong, P. Nugent, P. Mysliwiec, and W. Schindler (2003). Computed tomographic virtual colonoscopy to screen for colorectal neoplasia in asymptomatic adults. *N. Engl. J. Med.* 349(23), 2191–2200. [p. 17]
- Pickhardt, P., M. Hanson, D. Vanness, J. Lo, D. Kim, A. Taylor, T. Winter, and J. Hinshaw (2008). Unsuspected extracolonic findings at screening ct colonography: Clinical and economic impact<sup>1</sup>. *Radiology* 249(1), 151–159. [p. 22]
- Pickhardt, P., C. Hassan, A. Laghi, A. Zullo, D. Kim, F. Iafrate, and S. Morini (2008). Small and diminutive polyps detected at screening ct colonography: a decision analysis for referral to colonoscopy. *American Journal of Roentgenology* 190(1), 136–144. [p. 111]
- Pickhardt, P. J., D. H. Kim, R. J. Meiners, K. S. Wyatt, M. E. Hanson, D. S. Barlow, P. A. Cullen, R. A. Remtulla, and B. D. Cash (2010). Colorectal and extracolonic cancers detected at screening ct colonography in 10 286 asymptomatic adults<sup>1</sup>. *Radiology* 255(1), 83–88. [p. 20]
- Piegl, L. and W. Tiller (1997). *The NURBS book*. Springer Verlag. [p. 123], [p. 129]
- Punwani, S., S. Halligan, D. Tolan, S. Taylor, and D. Hawkes (2009). Quantitative assessment of colonic movement between prone and supine patient positions during CT colonography. *Br. J. Radiol.* 82(978), 475–481. [p. 10], [p. 18], [p. 19], [p. 84], [p. 89]
- Qiu, F., Z. Fan, X. Yin, A. Kaufman, and X. Gu (2008). Colon flattening with discrete Ricci flow. *Proc. MICCAI workshop*, 97–102. [p. 33], [p. 43], [p. 73], [p. 91], [p. 127]
- Rabeneck, L., L. Paszat, R. Hilsden, R. Saskin, D. Leddin, E. Grunfeld, E. Wai, M. Goldwasser, R. Sutradhar, and T. Stukel (2008). Bleeding and perforation after outpatient colonoscopy and their risk factors in usual clinical practice. *Gastroenterology* 135(6), 1899–1906. [p. 17]
- Regge, D., C. Laudi, G. Galatola, P. Della Monica, L. Bonelli, G. Angelelli, R. Asnaghi, B. Barbaro, C. Bartolozzi, D. Bielen, et al. (2009). Diagnostic accuracy of computed tomographic colonography for the detection of advanced neoplasia in individuals at increased risk of colorectal cancer. *JAMA: the journal of the American Medical Association* 301(23), 2453–2461. [p. 20]
- Roth, H., D. Boone, S. Halligan, T. Hampshire, J. McClelland, M. Hu, S. Punwani, S. Taylor, and D. Hawkes (2012). External clinical validation of prone and supine ct colonography registration. *Abdominal Imaging. Computational and Clinical Applications*, 10–19. [p. 84]
- Roth, H., T. Hampshire, J. McClelland, M. Hu, D. Boone, G. Slabaugh, S. Halligan, and D. Hawkes (2012). Inverse consistency error in the registration of prone and supine images in ct colonography. *Abdominal Imaging. Computational and Clinical Applications*, 1–7. [p. 28], [p. 93], [p. 105]
- Roth, H., J. McClelland, M. Modat, D. Boone, M. Hu, S. Ourselin, G. Slabaugh, S. Halligan, and D. Hawkes (2010). Establishing spatial correspondence between the inner colon surfaces from prone and supine ct colonography. *Medical Image Computing and Computer-Assisted Intervention–MICCAI 2010*, 497–504. [p. 75]



- Roth, H. R., J. R. McClelland, D. J. Boone, M. Modat, M. J. Cardoso, T. E. Hampshire, M. Hu, S. Punwani, S. Ourselin, G. G. Slabaugh, S. Halligan, and D. J. Hawkes (2011). Registration of the endoluminal surfaces of the colon derived from prone and supine ct colonography. *Medical Physics* 38(6), 3077–3089. [p. 35], [p. 84], [p. 85], [p. 104], [p. 110], [p. 124]
- Rubinstein, J. and R. Sinclair (2005). Visualizing ricci flow of manifolds of revolution. *Experimental Mathematics* 14(3), 285–298. [p. 11], [p. 43]
- Rueckert, D., L. Sonoda, C. Hayes, D. Hill, M. Leach, and D. Hawkes (1999). Nonrigid registration using free-form deformations: Application to breast mr images. *IEEE Trans. Med. Imaging* 18(8), 712–721. [p. 30], [p. 56], [p. 59], [p. 93], [p. 105]
- Sadleir, R. and P. Whelan (2005). Fast colon centreline calculation using optimised 3d topological thinning. *Computerized Medical Imaging and Graphics* 29(4), 251–258. [p. 27], [p. 40]
- Sander, P., J. Snyder, S. Gortler, and H. Hoppe (2001). Texture mapping progressive meshes. In *Proceedings of the 28th annual conference on Computer graphics and interactive techniques*, pp. 409–416. ACM. [p. 127]
- Schroeder, W., L. Avila, K. Martin, W. Hoffman, and C. Law (2001). The visualization toolkit-users guide. *Kitware, Inc.* [p. 49]
- Slabaugh, G., X. Yang, X. Ye, R. Boyes, and G. Beddoe (2010). A robust and fast system for CTC computer-aided detection of colorectal lesions. *Algorithms* 3(1), 21–43. [p. 35], [p. 129], [p. 130]
- Slater, A., S. Taylor, D. Burling, L. Gartner, J. Scarth, and S. Halligan (2006). Colonic polyps: Effect of attenuation of tagged fluid and viewing window on conspicuity and measurement in vitro experiment with porcine colonic specimen1. *Radiology* 240(1), 101–109. [p. 75]
- Stephenson, K. (2005). *Introduction to circle packing: The theory of discrete analytic functions*. Cambridge University Press. [p. 43]
- Sudarsky, S., B. Geiger, C. Chefdhote, and L. Guendel (2008). Colon unfolding via skeletal subspace deformation. *Medical Image Computing and Computer-Assisted Intervention–MICCAI 2008*, 205–212. [p. 32], [p. 126]
- Suh, J. and C. Wyatt (2009). Deformable registration of supine and prone colons for computed tomographic colonography. *J. Comput. Assist. Tomogr.* 33(6), 902–911. [p. 29], [p. 72], [p. 84], [p. 104]
- Suh, J. W. and C. L. Wyatt (2008). Registration of prone and supine colons in the presence of topological changes. *SPIE Med. Imaging: Physiology, Function, and Structure from Medical Images* 6916(1), 69160C. [p. 29], [p. 61], [p. 72], [p. 84]
- Summers, R. (2002). Challenges for computer-aided diagnosis for ct colonography. *Abdominal imaging* 27(3), 268–274. [p. 22], [p. 30]
- Summers, R., J. Swift, A. Dwyer, J. Choi, and P. Pickhardt (2009). Normalized distance along the colon centerline: a method for correlating polyp location on ct colonography and optical colonoscopy. *Am. J. Roentgenol.* 193(5), 1296–1304. [p. 22], [p. 26], [p. 84], [p. 131]
- Sun, L., H. Wu, and Y. Guan (2008). Colonography by ct, mri and pet/ct combined with conventional colonoscopy in colorectal cancer screening and staging. *World journal of gastroenterology: WJG* 14(6), 853. [p. 131]

- Taimouri, V., X. Liu, Z. Lai, C. Liu, D. Pai, and J. Hua (2011). Colon segmentation for prepless virtual colonoscopy. *IEEE Transactions on Information Technology in Biomedicine* 15(5), 709. [p. 126]
- Taubin, G., T. Zhang, and G. Golub (1996). Optimal surface smoothing as filter design. *Computer Vision ECCV*, 283–292. [p. 41]
- Taylor, S., J. Bomanji, L. Manpanzure, C. Robinson, A. Groves, J. Dickson, N. Papathanasiou, R. Greenhalgh, P. Ell, and S. Halligan (2010). Nonlaxative pet/ct colonography: feasibility, acceptability, and pilot performance in patients at higher risk of colonic neoplasia. *Journal of Nuclear Medicine* 51(6), 854–861. [p. 18], [p. 131]
- Taylor, S., S. Halligan, W. Atkin, et al. (2010, October 2527). Clinical trials and experiences: Siggar. In *11th International Symposium on Virtual Colonoscopy. Westin Copley Place, Boston, MA. October*, pp. 25–27. [p. 20]
- Taylor, S., S. Halligan, B. Saunders, P. Bassett, M. Vance, and C. Bartram (2003). Acceptance by patients of multidetector CT colonography compared with barium enema examinations, flexible sigmoidoscopy, and colonoscopy. *Am. J. Roentgenol.* 181(4), 913–921. [p. 17]
- Taylor, S., A. Laghi, P. Lefere, S. Halligan, and J. Stoker (2007). European Society of Gastrointestinal and Abdominal Radiology (ESGAR): Consensus statement on CT colonography. *European Radiology* 17(2), 575–579. [p. 18], [p. 63], [p. 94]
- Thirion, J. (1998). Image matching as a diffusion process: an analogy with maxwell’s demons. *Medical image analysis* 2(3), 243–260. [p. 29]
- Thompson, W., D. Holland, et al. (2011). Bias in tensor based morphometry stat-roi measures may result in unrealistic power estimates. *Neuroimage* 57(1), 1. [p. 105]
- Thurston, W. and J. Milnor (1979). *The geometry and topology of three-manifolds*. Princeton University. [p. 43]
- Torresani, L., V. Kolmogorov, and C. Rother (2008). Feature correspondence via graph matching: Models and global optimization. *Computer Vision–ECCV 2008*, 596–609. [p. 34]
- Umemoto, Y., M. Oda, T. Kitasaka, K. Mori, Y. Hayashi, Y. Suenaga, T. Takayama, and H. Natori (2008). Extraction of teniae coli from ct volumes for assisting virtual colonoscopy. In *Proc. of SPIE Medical Imaging*, Volume 6916, pp. 69160D. [p. 28], [p. 29]
- USPSTF (2008). U.s. preventive services task force recommendation statement: Screening for colorectal cancer. *Annals of Internal Medicine* 149(9), 627–637. [p. 20]
- van Gelder, R., H. Venema, I. Serlie, C. Nio, R. Determann, C. Tipker, F. Vos, A. Glas, J. Bartelsman, P. Bossuyt, et al. (2002). Ct colonography at different radiation dose levels: Feasibility of dose reduction1. *Radiology* 224(1), 25–33. [p. 126]
- Van Uitert, R., I. Bitter, and R. Summers (2006). Detection of colon wall outer boundary and segmentation of the colon wall based on level set methods. In *Engineering in Medicine and Biology Society, 2006. EMBS’06. 28th Annual International Conference of the IEEE*, pp. 3017–3020. IEEE. [p. 27], [p. 61], [p. 126], [p. 128]
- Van Uitert, R. and R. Summers (2007). Automatic correction of level set based subvoxel precise centerlines for virtual colonoscopy using the colon outer wall. *Medical Imaging, IEEE Transactions on* 26(8), 1069–1078. [p. 27], [p. 61]

- Vercauteren, T., X. Pennec, A. Perchant, and N. Ayache (2008). Symmetric log-domain diffeomorphic registration: A demons-based approach. *Medical Image Computing and Computer-Assisted Intervention—MICCAI 2008*, 754–761. [p. 104], [p. 105]
- Vining, D., D. Gelfand, R. Bechtold, E. Scharling, E. Grishaw, and R. Shifrin (1994). Technical feasibility of colon imaging with helical ct and virtual reality. *Am J Roentgenol* 162. [p. 17]
- Von Renteln, D., H. Rudolph, A. Schmidt, M. Vassiliou, and K. Caca (2010). Endoscopic closure of duodenal perforations by using an over-the-scope clip: a randomized, controlled porcine study. *Gastrointestinal endoscopy* 71(1), 131–138. [p. 75]
- Wahba, G. (1990). *Spline models for observational data*, Volume 59. Society for Industrial Mathematics. [p. 118]
- Wan, M., Z. Liang, Q. Ke, L. Hong, I. Bitter, and A. Kaufman (2002). Automatic centerline extraction for virtual colonoscopy. *Medical Imaging, IEEE Transactions on* 21(12), 1450–1460. [p. 26]
- Wang, G., G. McFarland, B. Brown, and M. Vannier (1998). Gi tract unraveling with curved cross sections. *Medical Imaging, IEEE Transactions on* 17(2), 318–322. [p. 31]
- Wang, G., G. McFarland, B. Brown, and M. Vannier (2002). GI tract unraveling with curved cross sections. *IEEE Trans. Med. Imaging* 17(2), 318–322. [p. 73]
- Wang, J. and T. Jiang (2007). Nonrigid registration of brain mri using nurbs. *Pattern Recognition Letters* 28(2), 214–223. [p. 129]
- Wang, S., N. Petrick, R. Van Uitert, S. Periaswamy, Z. Wei, and R. Summers (2012). Matching 3-d prone and supine ct colonography scans using graphs. *Information Technology in Biomedicine, IEEE Transactions on* 16(4), 676–682. [p. 27]
- Wang, S., J. Yao, J. Liu, N. Petrick, R. Van Uitert, S. Periaswamy, and R. Summers (2009). Registration of prone and supine CT colonography scans using correlation optimized warping and canonical correlation analysis. *Med. Phys.* 36(12), 5595–5603. [p. 25], [p. 26], [p. 84], [p. 89]
- Wei, Z., S. Wang, N. Petrick, J. Yao, S. Periaswamy, and R. Summers (2012). Supine and prone ct colonography registration by matching graphs of teniae coli. In *Biomedical Imaging (ISBI), 2012 9th IEEE International Symposium on*, pp. 712–715. IEEE. [p. 27]
- Wei, Z., J. Yao, S. Wang, J. Liu, and R. M. Summers (2012). Automated teniae coli detection and identification on computed tomographic colonography. *Medical Physics* 39(2), 964. [p. 28], [p. 29]
- Wei, Z., J. Yao, S. Wang, and R. Summers (2011). Teniae coli extraction in human colon for computed tomographic colonography images. *Virtual Colonoscopy and Abdominal Imaging. Computational Challenges and Clinical Opportunities*, 98–104. [p. 28], [p. 29]
- West, J., C. Maurer Jr, and J. Dooley (2005). Hybrid point-and-intensity-based deformable registration for abdominal ct images. In *Proceedings of SPIE*, Volume 5747, pp. 204. [p. 128]
- WHO (2011, February). Cancer. <http://www.who.int/mediacentre/factsheets/fs297/en/>, Retrieved on July 11, 2013. [p. 17]
- Wyatt, C. and P. Laurienti (2006). Nonrigid registration of images with different topologies using embedded maps. In *Engineering in Medicine and Biology Society, 2006. EMBS'06. 28th Annual International Conference of the IEEE*, pp. 4823–4827. IEEE. [p. 29]

- Yao, J., A. Chowdhury, J. Aman, and R. Summers (2010). Reversible projection technique for colon unfolding. *Biomedical Engineering, IEEE Transactions on* 57(12), 2861–2869. [p. 32], [p. 126]
- Yee, J., N. Kumar, R. Hung, G. Akerkar, P. Kumar, and S. Wall (2003). Comparison of supine and prone scanning separately and in combination at ct colonography1. *Radiology* 226(3), 653–661. [p. 84]
- Yigitsoy, M., M. Reiser, N. Navab, and S. Kirchhoff (2012). Dynamic graph cuts for colon segmentation in functional cine-mri. In *Biomedical Imaging (ISBI), 2012 9th IEEE International Symposium on*, pp. 1268–1271. IEEE. [p. 126]
- Yoshida, H. and J. Nappi (2002). Three-dimensional computer-aided diagnosis scheme for detection of colonic polyps. *IEEE Trans. Med. Imaging* 20(12), 1261–1274. [p. 12], [p. 51], [p. 52], [p. 85], [p. 93]
- Zalis, M., M. Blake, W. Cai, P. Hahn, E. Halpern, I. Kazam, M. Keroack, C. Magee, J. Nappi, R. Perez-Johnston, et al. (2012). Diagnostic accuracy of laxative-free computed tomographic colonography for detection of adenomatous polyps in asymptomatic adults: A prospective evaluation. *Annals of internal medicine* 156(10), 692. [p. 126], [p. 136]
- Zalis, M. and P. Hahn (2001). Digital subtraction bowel cleansing in ct colonography. *American Journal of Roentgenology* 176(3), 646–648. [p. 17]
- Zeng, W., J. Marino, K. Chaitanya Gurijala, X. Gu, and A. Kaufman (2010). Supine and prone colon registration using quasi-conformal mapping. *IEEE Trans. Vis. Comput. Graphics* 16(6), 1348–1357. [p. 34], [p. 43], [p. 72], [p. 84], [p. 104]
- Zeng, W., X. Yin, Y. Zeng, Y. Lai, X. Gu, and D. Samaras (2008). 3d face matching and registration based on hyperbolic ricci flow. In *Computer Vision and Pattern Recognition Workshops, 2008. CVPRW'08. IEEE Computer Society Conference on*, pp. 1–8. IEEE. [p. 30]
- Zou, G., J. Hu, X. Gu, and J. Hua (2011). Area-preserving surface flattening using lie advection. *Medical Image Computing and Computer-Assisted Intervention–MICCAI 2011*, 335–342. [p. 127]